Title
Tissue Elasticity Tunes Immune Infiltration, Stress Response Activation, and Metabolic State in Breast Cancer

Author
Stashko, Connor

Publication Date
2022

Peer reviewed|Thesis/dissertation

Tissue Elasticity Tunes Immune Infiltration, Stress Response Activation, and Metabolic State in Breast Cancer

by

Connor Stashko

DISSERTATION

Submitted in partial satisfaction of the requirements for degree of

DOCTOR OF PHILOSOPHY

in

Bioengineering

in the

GRADUATE DIVISION

of the

UNIVERSITY OF CALIFORNIA, SAN FRANCISCO
AND
UNIVERSITY OF CALIFORNIA, BERKELEY

Approved:

DocuSigned by:
Valerie Weaver
48C0A2F0F26A4A7...

Valerie Weaver

Chair

DocuSigned by:
Hani Goodarzi
DocuSigned by:

Hani Goodarzi

Mohammad Mofrad
DocuSigned by:

Mohammad Mofrad

Zev Gartner
6E99B613A5754DD...

Zev Gartner

Committee Members

Dedicated to Tawni, Joanna, and Tirzah

Thank you to all those in the Weaver Lab who helped me become a scientist: Fuiboon Kai, Mary-Kate Hayward, Kevin Tharp, Johnathon Lakins, Roger Oria, Dhruv Thakar, Shelly Kaushik, Kevin Metcalf, Jason Northey, Bram Piersma, Allison Drain, Nadia Ayad, and Jonathon Muncie. Special thanks to my faculty support system that supported and guided my research: Valerie Weaver, Zev Gartner, Hani Goodarzi, and Mohammad Mofrad. Thank you to those who provided technical contributions to my research: Neil Pearson, Dylan Romero, and Xinmiao Yu.

Acknowledgment of Previously Published Materials: The text of chapters 3, 4, 5, and 6 are reprints of the material specified at the beginning of each chapter. The co-authors listed in chapters 4, 5, and 6 directed and supervised the research that forms the basis for this dissertation.

ABSTRACT

Tissue Elasticity Tunes Immune Infiltration, Stress Response Activation, and Metabolic State in Breast Cancer

by

Connor Stashko

Fibrosis is a risk factor for cancer in many tissues and accompanies tumor progression. Fibrosis-associated stiffening of breast tumors is linked with increased tumor growth, invasion, and metastasis. However, the mechanisms through which tissue stiffness imparts these phenotypes on a tumor are still poorly understood, due in part to limitations in existing in vitro culture systems and methods to discern mechanically soft and stiff regions within tumors. In this dissertation, I sought to better identify physiologically-relevant mechanisms through which fibrosis drives tumor aggression by emphasizing unbiased screening approaches and utilizing recently available clinical transcriptomic datasets. These projects identified metabolic state, glycocalyx content and bulkiness, and immune cell infiltration and phenotypes as a network of changes in the tumor microenvironment driven by and feeding back into tissue fibrosis. Moreover, my collaborators and I developed a novel method for characterizing tissue rigidity and identified shortcomings in existing cell culture models, thus facilitating future research into the impact of tissue mechanics in breast cancer. Altogether, these works apply state-of-the-art sequencing and machine learning methods to shed light on the impact of tissue fibrosis and mechanics in breast cancer development and aggression.

Contents

List of Figures

List of Tables

List of Abbreviations

- **ADAM**: A Disintegrin and Metalloproteinase
- **AFM**: Atomic Force Microscopy
- **ANXA2**: Annexin-2
- **APEX2**: Apurinic/Apyrimidinic Endodeoxyribonuclease 2
- **ARE**: Antioxidant Response Element
- **ATF**: Activating Transcription Factor
- **ATP**: Adenosine 5'-Triphosphate
- **AutoAFM**: Automated Atomic Force Microscopy
- **BCECF**: 2',7'-bis-(2-carboxyethyl)-5-(and-6)-carboxyfluorescein, acetoxymethyl ester
- **Bleb**: Blebbistatin
- **CAF**: Cancer-Associated Fibroblast
- **CKD**: Chronic Kidney Disease
- **CNA35-OG488**: Collagen-Binding Adhesion Protein 35-Oregon Green 488
- **CNN**: Convolutional Neural Network
- **Col1**: Collagen 1
- **CRISPR-I**: Clustered Regularly Interspaced Short Palindromic Repeats - Interference
- **Cryo-ET**: Cryo-Electron Tomography
- **DAPI**: 4',6-diamidino-2-phenylindole
- **DCIS**: Ductal Carcinoma in situ

- **DDR**: Discoidin Domain Receptor
- **DMEM**: Dulbecco's Modified Eagle Medium
- **DMSO**: Dimethyl Sulfoxyide
- **ECM**: Extracellular Matrix
- **EIF2a**: Eukaryotic Translation Initiation Factor 2A
- **EMT**: Epithelial-Mesenchymal Transititon
- **ERK**: Extracellular Signal-Regulated Kinase
- **ETC**: Electron Transport Chain
- **FAK**: Focal Adhesion Kinase
- **FCCP**: Trifluoromethoxy Carbonylcyanide Phenylhydrazone
- **FDA**: Food and Drug Administration
- **FFPE**: Formalin-Fixed, Paraffin-Embedded
- **FLMN**: Filamin
- **FOV**: Field of View
- **GFP**: Green Fluorescent Protein
- **GSVA**: Gene Set Variation Analysis
- **GZMB**: Granzyme B
- **HER2**: Human Epidermal Growth Factor Receptor 2
- **HPLM**: Human Plasma-Like Medium
- **HSE**: Heat Shock Elements

- **HSF1**: Heat Shock Transcription Factor 1
- **HSP60**: Heat Shock Protein Family D Member 1
- **HSR**: Heat Shock Response
- **IDC**: Invasive Ductal Carcinoma
- **IMS**: Inner Membrane Space
- **IPF**: Idiopathic Pulmonary Fibrosis
- **ISR**: Integrated Stress Response
- **ITH**: Intratumor Heterogeneity
- **ITIM**: Immunoreceptor Tyrosine-Based Inhibitory Motif
- **KRT**: Keratin
- **LLSM**: Lattice Light Sheet Microscopy
- **Luc**: Luciferasae
- **MEC**: Mammary Epithelial Cell
- **MLC**: Myosin Light Chain
- **MMP**: Matrix Metalloproteinase
- **MRE**: Magnetic Resonance Elastography
- **NANS**: N-Acetylneuraminate Synthase
- **OCR**: Oxygen Consumption Rate
- **OCT**: Optimal Cutting Temperature
- **OSR**: Oxidative Stress Response

- **PA**: Polyacrylamide
- **PBS**: Phosphate-Buffered Saline
- **PDAC**: Pancreatic Ductal Adenocarcinoma
- **PDMS**: Polydimethylsiloxane
- **PDO**: Patient-Derived Organoid
- **PDX**: Patient-Derived Xenograft
- **PERK**: PKR-like ER Kinase
- **PETG**: Glycol-Modified Polyethylene Terephthalate
- **PI**: Propidium Iodide
- **PI3K**: Phosphatidylinositol-3-Kinase
- **PIP2**: Phosphatidylinositol 4,5-bisphosphate
- **PLA**: Proximity Ligation Assay
- **PPP**: Pentose Phosphate Pathway
- **rBM**: reconstituted Basement Membrane
- **RFP**: Red Fluorescent Protein
- **RHAMM**: Receptor for Hyaluronan-Mediated Motility
- **RNA-i**: RNA-interference
- **RNA-seq**: RNA-sequencingg
- **ROCK**: Rho-Associated Protein Kinase
- **ROI**: Region of Interest

- **ROS**: Reactive Oxygen Species
- **RT-PCR**: Reverse Transcription - Polymerase Chain Reaction
- **scRNAseq**: single cell RNA sequencing
- **SEM**: Scanning Electron Microscope
- **SHG**: Second Harmonic Generation
- **shRNA**: short hairpin RNA
- **SIGLEC**: Sialic Acid-Binding Immunoglobulin-Type of Lectins
- **SLUG/SNAI2**: Snail Family Transcriptional Repressor 2
- **SMA**: Smooth Muscle Actin
- **SNA**: Sambucus Nigra Lectin
- **SNAIL1**: Snail Family Transcriptional Repressor 1
- **SOCE**: Store-Operated Calcium Entry
- **STIFMap**: Spatially Transformed Inferential Force Map- ping
- **TAM**: Tumor-Associated Macrophage
- **TAZ**: Tafazzin
- **TBS**: Tris-Buffered Saline
- **TCA**: Tricarboxylic Acid
- **TCGA**: The Cancer Genome Atlas
- **TDLU**: Terminal Ductal Lobular Unit
- **TFM**: Traction Force Microscopy

- **TGF-β**: Transforming Growth Factor-β
- **TME**: Tumor Microenvironment
- **TMRE**: Tetramethylrhodamine Ethyl-Ester
- **TN**: Triple Negative
- **TNBC**: Triple Negative Breast Cancer
- **TRAIL**: TNF Superfamily Member 10
- **TWIST1**: Twist Family BHLH Transcription Factor 1
- **UCSF**: University of California, San Francisco
- **UMAP**: Uniform Manifold Approximation and Projection
- **UPR**: Unfolded Protein Response
- **UPRmt**: Mitochondrial Unfolded Protein Response
- **VIM**: Vimentin
- **WSI**: Whole Slide Imaging
- **YAP**: Yes1 Associated Transcriptional Regulator
- **YME1L1**: YME1 Like 1 ATPase
- **ZEB1**: Zinc Finger E-Box Binding Homeobox 1

1 Chapter 1: Introduction

1.1 Fibrosis and Breast Cancer

It is well-documented that breast tumors are significantly dysregulated from normal, healthy tissues on a multitude of levels including genomic instability, metabolic rewiring, immune infiltration, and cell plasticity and motility, to name a few. However, in the 1930s, long before any of these associations were discovered, it was noted that the breast tumor microenvironment is highly fibrotic ([1]). The fibrotic tumor stroma is characterized by the excessive deposition, remodeling, and crosslinking of extracellular matrix (ECM) proteins by fibroblasts. These proteins include collagens, fibronectin, tenascin, vimentin, hyaluronic acid, and others. Fibroblast-mediated ECM remodeling in tumors leads to the formation of thick type I collagen fibers that are stiffer than those in a normal matrix ([2], [3], [4], [5], [6]). The observation that breast tumors are stiffer than regular tissues dates at least as far back as the Jin Dynasty (317-420 B.C.) when breast tumors were described as ”hard as stone” ([7]).

High levels of fibrosis are linked with poor prognosis in cancer. In breast cancer, more aggressive subtypes such as triple negative and HER2+ were found to be stiffer than the less aggressive LumA and LumB subtypes ([8]). Poor patient survival in breast cancer is associated with elevated expression of a stromal gene expression signature of fibrosis-associated genes as well as the presence of fibrotic foci, defined as regions within a tumor of increased fibroblast proliferation and collagen abundance ([9], [10]). Beyond just breast cancer, extracellular matrix deposition is significantly correlated with worse patient survival in PDAC tumors ([11]) as was the presence of thick, highly crosslinked collagen fibers adjacent to tumors ([12]).

Fibrosis has also been implicated as a risk factor for the development of cancer in many different tissues. 70-90% of worldwide hepatocellular carcinoma cases arise after the presence of cirrhosis, or fibrosis of the liver ([13]). Idiopathic pulmonary fibrosis (IPF) is a risk factor for lung carcinogenesis ([14]) and exposure to asbestos is thought to increase the risk of developing lung cancer through similar mechanisms to IPF ([15]). Chronic pancreatitis is associated with pancreatic

cancer, progressive fibrosis of the kidneys associated with chronic kidney disease (CKD) is a risk factor for renal cancer ([16], [17]), and fibrosis has also been reported as a risk factor for prostate cancer ([18]). Despite the fundamental association between fibrosis and cancer, there has been a marked inability to leverage this understanding into meaningful treatments that target the ECM to treat cancer, in large part because the causal relationship between a stiff, fibrotic ECM and the risks of cancer progression and aggression are still poorly understood.

1.2 Monitoring and Measuring Tissue Fibrosis

One hindrance for better understanding the causal relationship between tissue fibrosis and tumor progression is the limitations of existing methods to study ECM crosslinking, thickening, and stiffening in the TME. Collagen, the main component of the breast ECM (Compare the collagen, water, and lipid concentrations from [19] against the average breast density from [20]), can be visualized through second harmonic generation (SHG), and specific patterns of thick, highly linearized fibers were recognized in breast tumors ([21]), but this requires a highly-specific microscope and is not amenable to co-staining with other markers of tumor state since fluorescent markers exhibit substantially different emission-excitation behavior with SHG that vary between labs and microscopes ([22], [23]). Picrosirius red (PS red) is an imaging modality for visualizing collagen packing and thickness, though PS red signals depend on the orientation of the tissue section relative to a laser polarizer and is also not amenable to costaining for additional tissue markers. Methods such as magnetic resonance elastography (MRE) and shear rheology are able to characterize the elasticity of tissues, but are applied to bulk tissues and thus do not provide micron-scale information about the tissue. Atomic Force Microscopy (AFM) is the most direct means of measuring tissue elasticity by physically probing tissue directly, but is low-throughput, highly specialized, and also no pipeline currently exists for overlaying AFM data onto a costained tissue. Furthermore, AFM, shear rheology, and MRE all require fresh or cryopreserved tissue sections, thus preventing their usage with formalin-fixed paraffin embedded (FFPE) tissue sections that are

more common in the clinic. Improved methods for characterizing the mechanical properties of the TME with single-cell resolution are essential if we hope to utilize the ECM to target cancer.

1.3 The Influence of ECM Fibrosis on Cell Signaling in the Tumor Microenvironment

Cells possess various means for feeling and interacting with the surrounding ECM. Most directly, cells bind to the ECM via receptors such as integrins, syndecans, and DDRs. Integrins are a family of heteterodimeric transmembrane receptors that bind to specific ECM proteins based on which alpha and beta subunits are present ([24]). After integrin binding to the ECM, talin and kindlin are recruited to the integrins' cytoplasmic tails, which stabilizes integrins in their active, high-ECM affinity conformation. This process is known as outside-in signaling. Alternatively, intracellular signals such as phosphatidylinositol 4,5-bisphosphate (PIP2) enrichment at the membrane can disrupt talin auto-inhibition, promote binding to integrin intracellular domains, and drive integrins into their active conformation in a process termed inside-out signaling ([25]). Once talin is bound to an integrin it connects to intracellular actin and vinculin, thus physically tethering the ECM to the cell cytoskeleton. Through actomyosin-mediated pulling on these nascent integrin-ECM adhesions, the cell feels if the adhesion is stable and, if so, reinforces it with hundreds of other proteins necessary to form a focal adhesion (FA) ([26], [27]). FAs signal to the cell in part through autophosphorylation of focal adhesion kinase (FAK) Tyr397 at FAs, which activates FAK. FAK in turn activates Rho GTPases that regulate diverse cellular processes such as cell cycle progression, migration, survival, and polarity ([28]). Moreover, activated FAK regulates gene expression by binding to transcription factors in the nucleus ([29], [30]). High FAK activation and expression is associated with aggression in many types of cancer including melanoma, prostate, and breast ([31], [32], [33]). Through these mechanisms and others, FAs manage to convert mechanical interactions between the cell and ECM into biochemical cues culminating in gene expression changes. This process whereby cells sense and respond to mechanical cues from the matrix via biochemical perturbations is known as mechanotransduction.

Cells are also able to directly bind to the ECM via discoidin domain receptors (DDRs) and syndecans. DDRs are transmembrane receptor tyrosine kinases that are activated through binding with triple-helical collagen in the ECM. Activated DDRs interact with a host of binding partners including PI3K and Notch and promotes ERK signaling, leading to a pro-survival phenotype ([34]). DDR overexpression and mutation is associated with multiple types of cancer including breast, glioma, gastric, liver, and prostate ([35]). Syndecans are a family of transmembrane proteoglycans that bind with ECM components such as collagen, laminin, and fibronectin ([36]). Syndecans interact with integrins and growth factors to potentiate cell proliferation, differentiation, adhesion, and migration ([36]). In addition, cancer cells remodel the matrix through ECM cleavage with matrix metalloproteinases (MMPs) ([37]). Syndecans not only regulate the expression levels of MMPs, but serve as docking sites for MMPs on the cell surface ([38]). Syndecans themselves are cleaved by MMPs, releasing protein fragments that promote cancer cell metastasis, invasion, and proliferation ([38]). Altogether, integrins, DDRs, and syndecans are a highly complex network of proteins that drive cell signaling and disease-relevant behavior through interactions with the ECM.

Beyond direct ECM-receptor interactions, a number of other mechanosignaling mechanisms have also been characterized. PIEZO transmembrane ion channels are opened in response to membrane tension to allow the passage of cations such as sodium, potassium, and calcium ([7]). Cation homeostasis is critical during cell cycle progression and intracellular ion concentrations support the proliferation of tumor cells ([39]). Some novel cancer therapies even target ion homeostasis as a means of attenuating tumor growth ([40]). As elevated ECM stiffness associates with increased membrane tension, PIEZO indicates an indirect mechanism through which ECM stiffness may dictate cell cycle progression. Finally, the YAP/TAZ pathway is a well-studied mechanotransduction pathway in which the transcriptional coactivators YAP and TAZ experience nuclear translocation in response to high matrix stiffness ([41]). Nuclear YAP/TAZ promotes expression of genes associated with proliferation, growth, stress adaptation, and dedifferentiation ([42]). Altogher, these pathways represent a complex network of signals through which the ECM communicates with a cell and drives cellular behavior.

1.4 Phenotypic Impacts of the Fibrotic ECM on the Tumor Microenvironment

A stiff ECM potentiates a multitude of pathways associated with tumor development and progression. Most fundamentally, a stiff ECM promotes cell proliferation through a number of mechanisms mentioned above including ERK signaling, ion channel opening, and YAP/TAZ activity. However, abundant cancer cell proliferation in the presence of stiff, inflexible ECM leads to the build-up of compressive forces within a tumor, known as solid stress ([43]). This solid stress has been shown to inhibit the proliferation of cancer cell organoids in stiff 3D matrices ([44]), suggesting that high ECM stiffness may promote or inhibit tumor cell growth depending on the specific tissue context. Clustering transcriptomic data from >10,000 different cancer patients further revealed that fibrotic, matrix-rich tumors were not associated with a proliferation signature ([45]), and my own analyses of a patient datasets and soft/stiff collagen gels implanted into mice were in agreement that stiff tumors or tumors with greater expression of matrix signatures had significantly lower proliferation and cell-cycle signatures (GSE25066; [46], [47]). Nevertheless, it is well known in the Weaver Lab that any cell line cultured on soft and stiff 2D polyacrylamide gels will proliferate substantially faster on the stiff gels. The trade off in cancer cells between enhanced growth signaling via cell-ECM interactions versus growth inhibition due to the build-up of solid stresses remains a compelling and poorly understood question worthy of further investigation.

Another key mechanism whereby a stiff ECM may drive tumor invasion, dissemination, and metastasis is by driving an epithelial-mesenchymal transition (EMT). During an EMT, epithelial-like cancer cells lose apical-basal polarity and tight cell-cell junctions and adopt mesenchymal characteristics such as morphology, motility, and invasion ([48]). EMT occurs due to a number of transcription factors and chromatin remodeling proteins that cooperate to shut off epithelial transcriptional programs while inducing genes involved in mesenchymal pathways. One way in which an ECM can induce EMT is through induction of TWIST1, a pro-mesenchymal transcription factor. In response to high ECM stiffness, integrin-dependent phosphorylation drives release of TWIST1 from cytoplasmic G3BP2, which allows TWIST1 to enter the nucleus and serve

as a pro-mesenchymal transcription factor ([49]). SNAIL1, another mesenchymal-associated transcription factor, was also observed to accumulate in the nucleus in response to activation of DDR2 from collagen I signaling ([50]). This connection was observed *in vivo* as well, as DDR2 in breast tumors was associated with nuclear SNAI1 and the absence of E-cadherin ([50]).

Given the association between ECM stiffness and EMT, it is not surprising that high tissue tension is also associated with increased motility and invasion in cancer. The invasion of cancer cells in breast tumors correlates with increased deposition and stiffening of ECM proteins such as collagen ([8]). Cancer cells have been shown to invade along thick, stiffer collagen fibers, as they provide a stronger scaffold for cell motility ([51]). The morphology of collagen fibers is also a relevant feature of the tumor ECM, as SHG imaging has revealed that tumors with thick, linearized collagen fibers oriented radially outwards from the tumor have worse disease-free survival, likely due to the ability of cancer cells to migrate along these tracts ([21]). Mechanistically, a stiff matrix leads to enhanced tumor cell invasion through phosphorylation of paxillin by src family kinases ([52]). All of these behaviors contribute to the elevated disease progression and metastasis observed in mice with artificially stiffened ECMs ([53], [54]).

It is remiss to consider the interplay between cancer cells and the ECM in a tumor without including the contribution of other cell types such as fibroblasts and immune populations. It is well documented that immune function varies considerably between pro-wound healing vs pro-inflammatory microenvironments ([55], [56], [57], [58]). Fibroblasts and macrophages contribute to the ECM deposition and crosslinking observed in tumors. Stromal fibroblasts exhibited the highest levels of ECM crosslinking enzymes in miscrodissected human tumors, and ablation of tumor-associated macrophages (TAMs) decreased stromal crosslinking and stiffness while attenuating metastasis ([53]). Fibrotic breast tumors with poor prognosis were associated with low infiltration of CD8+ T cells and enriched for fibrotic foci ([59]). One mechanism of crosstalk between immune populations, fibroblasts, and cancer cells occurs in part via fibroblast-secreted TGF-β ([60]), which was associated with EMT, low immune infiltration, metastasis, and poor survival ([45]). TGF-β may actually inhibit tumor growth in early stages, but is well-documented to

promote metastasis in late tumors through induction of an EMT ([61], [62]). TGF-β signaling also activates non-inflammatory regulatory T cells (Tregs), that in turn feedback into a wound-healing microenvironment by secreting TGF-β themselves. TGF-β is one well-studied pathway linking immune function, fibrosis, and EMT in the TME, but is only the tip of the iceberg of complexity for how spaciotemporal cues influence the behavior and crosstalk of the multitude of celltypes and states present within a tumor.

1.5 Heterogeneity in Breast Cancer

Tumors, particularly breast cancers, are highly heterogeneous. Intratumor heterogeneity (ITH) is higher in tumors with greater risk of recurrence ([63]), thought to be because diversity in the TME allows for selection of more aggressive cancer cell phenotypes. At the level of cancer cells, variability in hormone receptor expression and HER2 copy number can predict treatment efficacy and patient survival ([64], [65]). Substantial variability also exists between and within breast tumors in terms of the immune populations present and their relative proportions ([66]). Azizi and colleagues found substantial heterogeneity in immune cell states and phenotypes within breast tumors, but not normal breast tissues, and attributed this finding to the diverse microenvironments within tumors in terms of inflammatory signaling, hypoxia, and nutrient availability. Extensive effort has gone into attempts at classifying these different immune tumor states to reveal clinical susceptibilities and therapeutic opportunities ([67]).

ECM heterogeneity within tumors and its impact on disease progression is an exciting, if largely unexplored, topic of research. Localization within tumors relative to the ECM can impact metabolic function and stress response induction in a tumor, as cancer cells at the tumor-stroma boundary exhibit elevated glycolytic metabolism and global histone de-acetylation compared to cells in the hypoxic tumor core ([68]). Moreover, scRNAseq has revealed variability in the populations and phenotypes of cancer-associated fibroblasts (CAFs), the ECM-controlling cell type, in breast cancer ([69]). Bartoschek and colleagues classified CAFs into populations for angiogenesis, ECM deposition, cell-cycle progression, and cell differentiation, though breast tumors contain

variable proportions of all four. How these subsets of CAFs contribute to mechanical heterogeneity in the TME is unknown. Thus far, our studies also suggest that fibrosis and tissue stiffness are heterogeneous within a tumor, as the Young's Modulus of the invasive front of breast tumors ranged from a few hundred pascals to several thousand ([8]). However, how ECM heterogeneity factors into other facets of tumor heterogeneity is still unknown, as no method currently exists to characterize the mechanical heterogeneity within a tumor or co-register ECM topology and stiffness with gene expression, protein levels, copy number genomics, and immune infiltration.

1.6 Clinical trials reveal the spatiotemporal importance of the ECM during tumor progression

An abundance of clinical trials have been conducted targeting various components of the extracellular matrix, but none have received FDA approval. Closer inspection reveals two trends that emerge from these studies. First, there are often unexpected off-target effects because ECM molecules have important functions in normal tissues. At doses high enough to curtail development of the tumor there are intolerable side effects elsewhere in the body. Second, ECM therapies tend to be efficacious only during a narrow window of tumor progression. There is a growing appreciation of a tumor as an organ that develops over time; therapies that reduce tumor size at one stage in its development may actually increase aggression at another stage. Third, tumors possess extensive heterogeneity in terms of inflammatory signaling, immune infiltration, and ECM stiffness. It's likely that the ECM may be pro-proliferation and growth inhibiting at different positions within the same tumor simultaneously.

Some of the earliest clinical trials aimed at perturbing the TME were for matrix metalloproteinases (MMPs). MMPs cleave ECM components and are used by cancer cells during invasion. Over 50 MMP inhibitors have been tried in clinical trials for various cancers, but none have progressed to market ([70]). Early MMP inhibitors were non-specific and resulted in musculoskeletal pain, likely due to cross-inhibition of disintegrin and metalloproteinase (ADAM) family proteins, which are ubiquitously involved in cellular adhesion, cell-matrix interactions, and reg-

ulating growth factor availability ([71]). Recent MMP inhibitors were more specific, but were generally administered too late to matter. MMP-mediated invasion happens early in cancer and tumor cells may have already undergone metastatic dissemination by the time patients were receiving MMP inhibitors ([70]). There is a continued interest in the role of MMPs in cancer and in the development of more specific MMP inhibitors, but the failure of early MMP clinical trials has left a lasting stigma against therapies targeting MMPs.

Hyaluronic acid (HA) is the main structural component of brain ECM and has been implicated in cancer as promoting tumor growth, metastasis, and angiogenesis ([72]). Therapies have been developed targeting HA synthases, receptors, and degradation proteins. BIWI-1, a drug targeting the HA receptor CD44 was terminated early in Phase I due to serious skin toxicity that was fatal in some patients ([73]). RHAMM, an HA receptor overexpressed in some acute leukemias, has been used as a target for immunotherapies ([74]). Although vaccination with the RHAMM-R3 peptide showed a partial clinical response in 35% of patients, it was found that leukemic stem cells had low RHAMM expression and the clinical trial was called off.

TGF-β has proven to be an especially interesting therapeutic target in cancer due to the promise of some therapies targeting TGF-β and the changing role of TGF-β over time in the tumor. In healthy epithelia, TGF-β plays a key role in maintaining homeostasis by regulating apoptosis, the cell cycle, and differentiation, making it antitumor ([75]). However, mutations impair the response of cancer cells to the antiproliferative and apoptotic roles of TGF-β, and in the late tumor TGF-β is associated with proliferation, angiogenesis, invasion, metastasis, recurrence after therapy, and poor survival. Due to its prominent role in cancer as a molecule mediating communication between the stroma, immune system, and cancer cells, TGF-β has been a target of cancer trials for over 15 years. While some patients have had complete or partial responses on these therapies, none have been approved due to overall intolerable toxicity or lack of efficacy. Nevertheless, the promise of these therapies in some tumors has led to a major interest in identifying patients whose tumors will respond to TGF-β inhibitors. Various patient stratification techniques are in the works regarding immunohistochemistry for p-Smad2, gene expression analysis for TGF-β response signatures,

and levels of TGF-β in the blood and tumor ([76], [77], [78]). Moreover, there is an interest in utilizing TGF-β inhibitors in combination therapies that enlist an immune response. For instance, Bintrafusp Alfa acts via simultaneous blockage of PD-L1 and TGF-β and has shown promising results in various types of tumors, but only months ago failed to meet efficacy standards necessary to obtain FDA approval ([79], [80]). TGF-β inhibitors have shown promising results in the clinic in large part because there is an appreciation that only a subset of tumors will respond if they are in a particular ECM and immune state.

A number of common themes emerge when evaluating the reasons that all of these clinical trials failed. For one, ECM molecules have important functions in normal issues, therefore therapies that target them tend to have severe unforeseen offtarget effects. This is especially evident in hyaluronic acid inhibitors and MMP inhibitors such as batimistat, tanomastat, and prinomastat, which exhibited severe musculoskeletal side effects ([72], [71]. Second, there appears to be a temporal element of therapies that target the ECM in that ECM ablation may have an anti-tumor effect in the early stage and a pro-tumor effect in later stages. Indeed, the abundances of macrophages, neutrophils, and dendritic cells have all been observed to differ between normal, DCIS, and IDC tissues ([81]). Particularly with therapies targeting TGF-β, researchers have emphasized that tumors must be targeted at the appropriate stage to possess a treatment-responsive immune microenvironment ([82], [75]). Third, researchers failed to account for the role of tumor heterogeneity when predicting patient responsiveness. By targeting therapies against specific oncogenic signaling targets not expressed by all cancer cells, subpopulations are able to evade treatment, acquire resistance, and expand, leading to relapse ([83]). Clearly, we require a better understanding of how the ECM acts spatially and temporally to potentiate or hinder tumor growth. However, to date there is no method that can characterize the heterogeneity in stiffness in the extracellular matrix or answer the question of the specific mechanical microenvironment that each cell within a tissue is experiencing.

Motivating Questions: Despite advances in our understanding of the role of the tumor microenvironment on cancer progression, a number of outstanding questions remain:

(1) What role does the ECM play at different stages of tumor progression?

(2) How does mechanical heterogeneity within the tumor microenvironment impact tumor progression?

(3) How do cells in a tumor behave based on their local mechanical microenvironment?

(4) How does the ECM modulate immune function in the TME?

My thesis aims to shed light on these questions by synthesizing findings from clinical datasets, experimental evidence, and a novel method that I developed for evaluating mechanical heterogeneity within the tumor extracellular matrix.

2 Chapter 2: STIFMaps Reveal Mechanical Heterogeneity in Breast Cancer

In collaboration with Mary-Kate Hayward[1,2], Jason J. Northey[1,2], Neil Pearson, Alastair J. Ironside[3], Johnathon N. Lakins[1,2], Marie-Anne Goyette[4], Lakyn Mayo[5], Hege Russness[6,7], E. Shelley Hwang[8], Matthew Kutys[5,9], Kornelia Polyak[4], Valerie M. Weaver[1,2,9,10]

[1]Department of Surgery, University of California, San Francisco, California, USA.

[2]Center for Bioengineering and Tissue Regeneration, University of California, San Francisco, San Francisco, CA.

[3]Department of Pathology, Western General Hospital, NHS Lothian, Edinburgh, UK

[4]Department of Medical Oncology, Dana-Farber Cancer Institute, Boston, MA

[5]Department of Cell and Tissue Biology, School of Dentistry, University of California, San Francisco, San Francisco, CA.

[6]Department of Pathology and Department of Cancer Genetics, Institute for Cancer Research, Oslo University Hospital, Oslo, Norway.

[7]Institute for Clinical Medicine, University of Oslo, Oslo, Norway.

[8]Department of Surgery, Duke University Medical Center, Durham, NC.

[9]UCSF Helen Diller Comprehensive Cancer Center, University of California, San Francisco, San Francisco, CA.

[10]Department of Radiation Oncology, Eli and Edythe Broad Center of Regeneration Medicine and Stem Cell Research, University of California, San Francisco, San Francisco, CA.

2.1 Introduction

Intratumor heterogeneity (ITH) is a feature of breast tumors ([63], [84], [85], [66]). Tumor heterogeneity predicts poor patient outcome as diversification of genetic, phenotypic and behavioral characteristics within a tumor supports progression, metastasis, and treatment resistance

([86], [83], [87]). Accordingly, much effort has been directed towards defining ITH and clarifying how it drives tumorigenesis ([45], [88]). Towards this goal, the ability to decipher the causal relationship between tumor heterogeneity and tumor behavior relies heavily on the availability of accurate and quantitative methods with which to measure and analyze individual features of the tumor.

Tumor tissue variability is mediated, in part, by intrinsic stochastic gene expression as well as by genetic and epigenetic differences in the transformed cells. Sophisticated approaches including genetic tags and high throughput sequencing have permitted researchers to detect genomic abnormality at the single cell level to provide important insights into clonal evolution and have linked these findings to patient survival ([89], [90], [91]). State of the art spatial RNA sequencing (RNAseq) analysis has revealed underlying spatial associations between stress response gene expression profiles in cancer cells and inflammatory fibroblast gene signatures [92]. Importantly, tumors are organs comprised of transformed cells interacting with a diverse cellular and acellular stroma. Consistently, in situ multiplexing approaches have revealed wide diversity with respect to the frequency and phenotype of tumor-infiltrating immune cells and have used these findings to predict patient outcomes as well as checkpoint inhibitor responsiveness [93]. In situ immunofluorescence has also illustrated wide variability in oncogenic signaling, cellular metabolism and stress responsiveness between the epithelial and stromal cells within the hypoxic tumor core, and those cells that localize to the fibrotic tumor periphery, to predict treatment response in patients ([94], [68]).

An important feature of all solid tumors is the remodeled and crosslinked extracellular matrix (ECM) that generates a stiffened, fibrotic stroma characterized by markedly reorganized interstitial collagens [95]. A stiff ECM modifies cell and nuclear shape, disrupts tissue organization, promotes cell growth, viability, and invasion, alters gene expression, and can even induce an epithelial to mesenchymal transition (EMT) in cells cultured in two- and three-dimensional substrates ([96]). Within experimental tumors *in vivo*, the stiffened tumor ECM promotes solid stress, disrupts vascular integrity to drive hypoxia and tumor aggression, and compromises drug

delivery [97]. The stiff tumor ECM also increases cytokine and chemokine expression to promote myeloid cell infiltration and can even impede CD8 T cell infiltration, migration, and function [98]. Clinically, the level of tissue fibrosis correlates with worse patient outcome, and in situ analysis of human breast cancer tissues revealed that a stiff, fibrotic ECM associates with tumor progression as well as clinical subtype ([8], [8], [53], [99]). Nevertheless, whether stromal stiffness tracks with human breast cancer aggression and, if so, how remains unclear.

To clarify links between stromal stiffness heterogeneity and tumor aggression, approaches are needed that can be combined with state-of-the-art spatial genomics, proteomics, and multiplexing protocols ([100], [101], [102]). Although techniques do exist with which to monitor ECM heterogeneity and organization including H&E, second harmonic generation (SHG), trichrome, and picrosirius red (PS red) staining, none can be directly combined with immunostaining on the same slide ([8], [103], [104]). Moreover, these protocols do not provide quantitative insight into mechanically soft and stiff regions within the tumor. Methods to directly measure ECM stiffness include shear rheology, Atomic Force Microscopy (AFM), Magnetic Resonance Elastography, Sonoelastography, and unconfined compression analysis ([105], [106], [107], [108]). However, these approaches do not provide high resolution spatial and morphology information, particularly with respect to the state of the collagenous ECM. Although stromal stiffness can be measured directly with sub-micron resolution using Atomic Force Microscopy (AFM), current AFM methods are time-consuming, poorly resolved spatially, and require specialized equipment not readily available to most research and clinical laboratories ([109], [110]). An automated AFM developed by Plodinec and colleagues can rapidly quantify the material properties of tumor biopsies, but the method does not provide imaging of the probed tissue nor the positions from where measurements are taken. Thus, while the approach is useful for characterizing cell and tissue biomechanical properties, it is not suitable for studies whose goal is to link elasticity of the ECM to biological markers of tumor and stromal phenotype, genotype, and heterogeneity [111]. Importantly, all of the currently available approaches to quantify cell and stromal stiffness require manipulation of either

fresh or cryopreserved tissue, precluding comprehensive spatial analysis of elasticity in archived formalin-fixed paraffin-embedded (FFPE) sections in tissue banks.

Here, we present a novel approach termed Spatially Transformed Inferential Force Mapping (STIFMap) that is able to visualize the heterogeneous stiffness landscape of normal and tumor breast tissues with micron-resolution and to spatially register this tension phenotype with biological markers of tumor aggression. The method works on both cryopreserved and FFPE tissues and employs a single quick, inexpensive collagen stain that is visualized with standard fluorescence microscopy. The approach permits simultaneous quantification of the tension landscape of the stromal ECM together with co-staining for cell or ECM biomarkers of interest, and lends itself to quick assessment of the impact of biophysical ECM heterogeneity on tumor aggression. The method can be readily integrated with spatial proteomics and genomics as well as standard protein marker multiplexing protocols. To illustrate the potential of the approach we applied STIFMap to explore the relationship between stromal stiffness and markers of tumor aggression in human breast cancers. We were able to link tissue mechanics with indicators of mechanosignaling and biomarkers of EMT previously implicated in tumor aggression and treatment resistance ([112], [113]). The results highlight the potential utility of using stromal biophysical features to predict tumor behavior and possibly even patient outcome.

2.2 Results

2.2.1 Design and development of an automated AFM system

AFM has emerged as the method of choice to spatially analyze stromal stiffness in tumors ([114], [115]). However, executing AFM analysis is cumbersome, specialized, and not easily amenable to spatial registration with sequential in situ analysis and imaging. To improve upon these pitfalls, we developed AutoAFM to facilitate high-throughput, spatially-resolved acquisition of AFM data. We automated AFM movements by affixing servo motors onto the X and Y translation knobs of the AFM stage with custom-made, 3D-printed motor mounts (Fig. 2.1 a, b, Table 8.1, Extended Fig. 8.1a, b, Methods). Scripts were developed to enable the AFM to move along a user-

specified path (Fig. 2.1c, d). The system was designed so that as the AFM moves from one point to the next, a feedback loop reports on the current position of the AFM and fine-tunes movements to poke the specimen within a user-designated tolerance of the desired positions. All movements and imaging were designed to be conducted using epifluorescence of propidium iodide-stained cells to guide the measurements. This strategy was chosen to remove artifacts from the cantilever shadow that could potentially be introduced into the images during stitching (Extended Fig. 8.1c). The system was engineered so that a completed AutoAFM scan will provide the location of each AFM force curve acquired over the tissue section being measured (Fig. 2.1e, f). The AutoAFM was designed such that scans can be acquired across as many points as the operator desires and are only spatially limited by the overall X-Y range of the AFM stage.

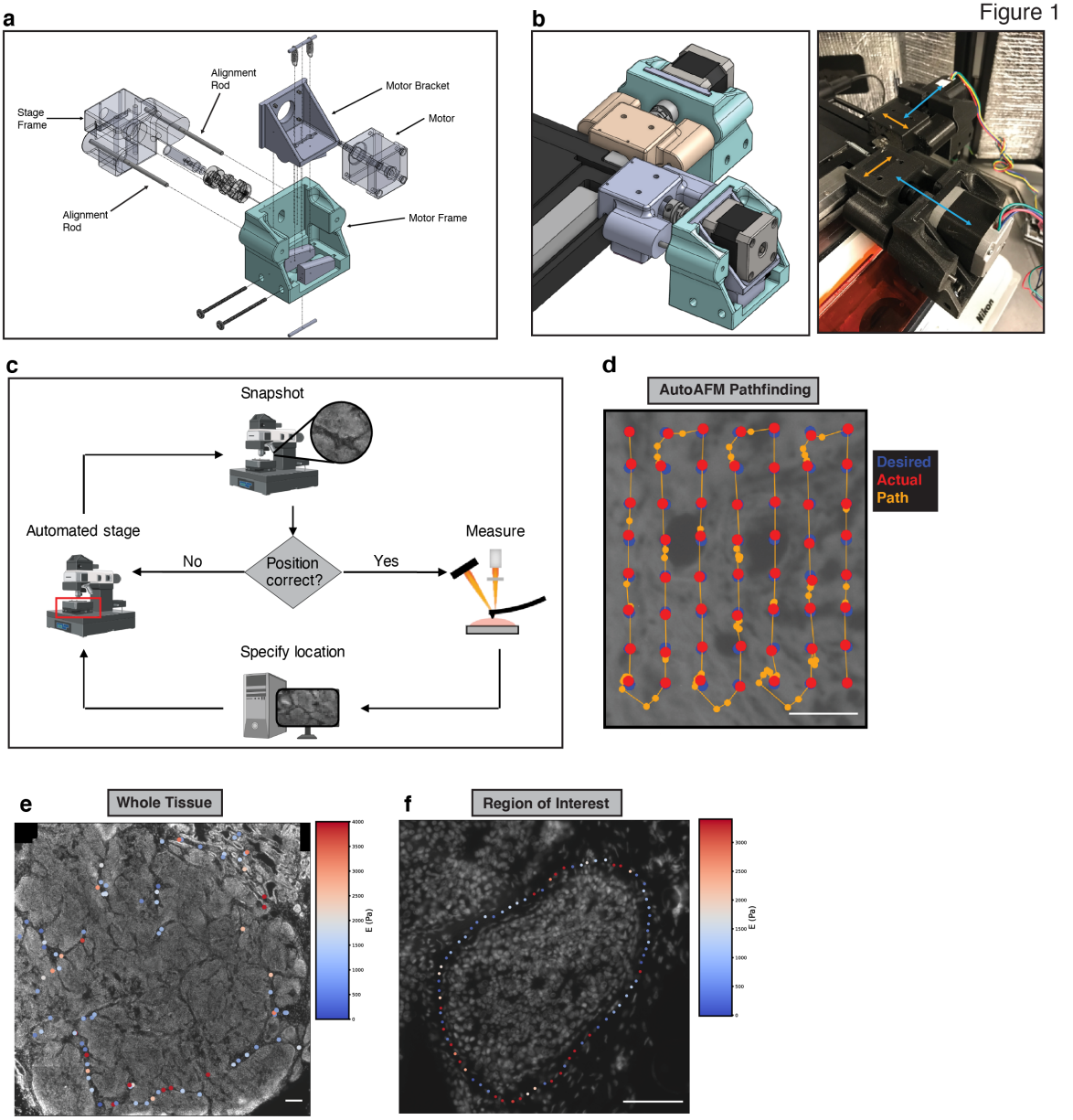

Figure 2.1: Overview of automated AFM acquisition system

a, Technical drawing of motor mount for interfacing servo motors with AFM translation knobs. b, Assembled motor mounts. The Stage Frame slides along the edge of the stage (orange arrows) while the Motor Frame slides along the Alignment Rods, towards and away from the Stage Frame as the knobs turn (blue arrows). c, Schematic of AutoAFM feedback system. d, Example of AutoAFM feedback with desired AFM sampling positions (blue), actual AFM positions (red), and AFM path of movement and positions outside of the desired (orange). e,f, Representative images of AutoAFM collecting AFM measurements over a whole tissue (e) and a region of interest (f) in a breast tumor section. Scale bar, 100 μm.

2.2.2 Assessment of AutoAFM precision and validation of AFM measurements

To validate movements of the AutoAFM, a series of elevated PDMS beams of varying widths were fabricated using photolithography followed by PDMS soft lithography (Extended Fig. 8.1d). Using this strategy, the height at which the AFM contacts the sample is known, so force curves collected on the beams registered as much higher than those collected on the surrounding PDMS surface. To determine the resolution limit of AutoAFM, we used the AFM to 'walk' along each beam and measured the accuracy of the AFM to contact the beam at each width. The measurements indicated that movements of the automated AFM are precise to within a few microns (Extended Fig. 8.1e).

The Young's Modulus of an AFM cantilever is calibrated before measurements are performed (Methods). Nevertheless, the cantilever modulus can change over the course of data collection due to protein and cell debris deposition onto the cantilever. To ensure that the stiffness of the cantilever remained consistent throughout the measurements, we measured the elasticity of polyacrylamide (PA) gels of known Young's Moduli before and after probing each sample. The elasticities of the PA gels used were validated using shear rheology (Extended Fig. 8.2a). AFM measurements on each tissue were collected over 1-2 hours. To verify that tissues did not degrade over the timespan of AFM measurements, we collected force curves at the same tissue positions over a defined length of time. AFM measurements collected in the same positions every 30 minutes for three hours revealed no noticeable differences in elasticity, indicating that tissue degradation does not occur over the timespan that AutoAFM measurements were acquired for this study (Extended Fig. 8.2b). Because tissues are viscoelastic substrates, the rate of force loading impacts the resulting force curve [116]. Accordingly, highly viscous substrates will appear stiffer when poked faster if they are assumed to be purely elastic. To address this potential anomaly an AFM velocity of 2 μ/s was chosen since Young's Moduli measurements were constant at this rate (Extended Fig. 8.2c).

To avoid any potential for tip fouling we chose AFM cantilevers that were triangular with 5 μm spherical beads incorporated onto the cantilever tip (Extended Fig. 8.2d; [117]). To

stitch together images taken during AutoAFM, the bead location was estimated for each image. To estimate the bead location within the image, the average image for each AutoAFM scan was taken, which revealed a faint but distinct outline of the cantilever (Extended Fig. 8.2e). This occurred because the stronger PI signals from the cells move during AutoAFM acquisition, but the faint cantilever image remains in the same position throughout. Five cantilevers with known bead locations were aligned with the average scan images to indicate the actual position of the bead during imaging (Extended Fig. 8.2f, g).

2.2.3 Overlaying AutoAFM Measurements onto Confocal Images

In an effort to ensure visual spatial alignment between tissue morphological features and elasticity measurements, the AutoAFM measurements were overlaid with nuclear staining via alignment with AutoAFM PI positions. DAPI measurements were collected via confocal imaging at either 40x or 63x magnification, while AutoAFM PI images were collected at 20x magnification. A pipeline was then developed to translate low-resolution AutoAFM images onto high-resolution DAPI imaging (code available on GitHub). To do so, the two images were first manually pre-aligned so that the fields of view were similar, and the confocal DAPI image was downsampled to more closely resemble the resolution of the AutoAFM image (Extended Fig. 8.3a). Thereafter, we applied a Fourier-Mellin Transform to determine the scale and rotation of the AutoAFM image relative to the DAPI image [118]. Finally, translation between the two images was computed using phase contrast cross-correlation. Using this transformation matrix, AFM positions were mapped onto the high-resolution images (Extended Fig. 8.3b). The average mapping error was found to be 2.57 μm, estimated by monitoring nuclei positions before and after transformation (95% confidence interval: 2.09 - 3.06 μm) (Extended Fig. 8.3c).

2.2.4 Deep learning model of tissue young's modulus from collagen morphology

Interstitial fibrillar collagens are the major structural component of breast tissue ([119], [20], [19], [120]). As such, we reasoned that the elasticity of breast tissue could be inferred based

on the morphology of interstitial collagen fibers, particularly given that stiff collagen fibers are thick and highly linear whereas more compliant collagen fibers are typically more dispersed, relaxed, and present as wavy fibers [121]. Although most investigators have used SHG imaging or PS red staining to visualize interstitial fibrillar collagens, collagen SHG imaging is susceptible to interference from additional fluorophores on co-stained tissues [122], and PS red coloring depends on the angle of the slide on the microscope relative to the polarizer [104]. Accordingly, we chose to stain the collagens using the collagen-binding adhesion protein 35-Orange Green 488 fusion protein (CNA35-OG488) ([123], [124]). CNA contains two subdomains, N1 and N2, which engage in a 'collagen hug' around triple helical collagen in the ECM [125]. CNA staining was selected because it is cheap to produce, plasmid sequences are freely available online, and the stain is not species specific [126]. The CNA stain is also rapid and easy to perform, and can be viewed on conventional fluorescent microscopes, lending itself to standard research laboratories as well as a clinical lab format.

To register collagen morphological features with tissue stiffness, a convolutional neural network (CNN) was applied using CNA and DAPI imaging as the inputs and the corresponding AFM measurements as the output (Fig. 2.2a). A CNN was chosen due to its superiority compared to alternative models with image classification tasks [127]. We reasoned that a CNN would be able to learn how factors such as collagen fiber linearity, thickness, and proximity to cells impacts elasticity better than alternative models. Different CNN architectures were applied to predict tissue elasticity including ResNet, DenseNet, and models discovered using Neural Architecture Search, but the best performance came from an AlexNet modified for a regression output instead of classification (https://github.com/pytorch/vision/blob/main/torchvision/models/alexnet.py).

Figure 2

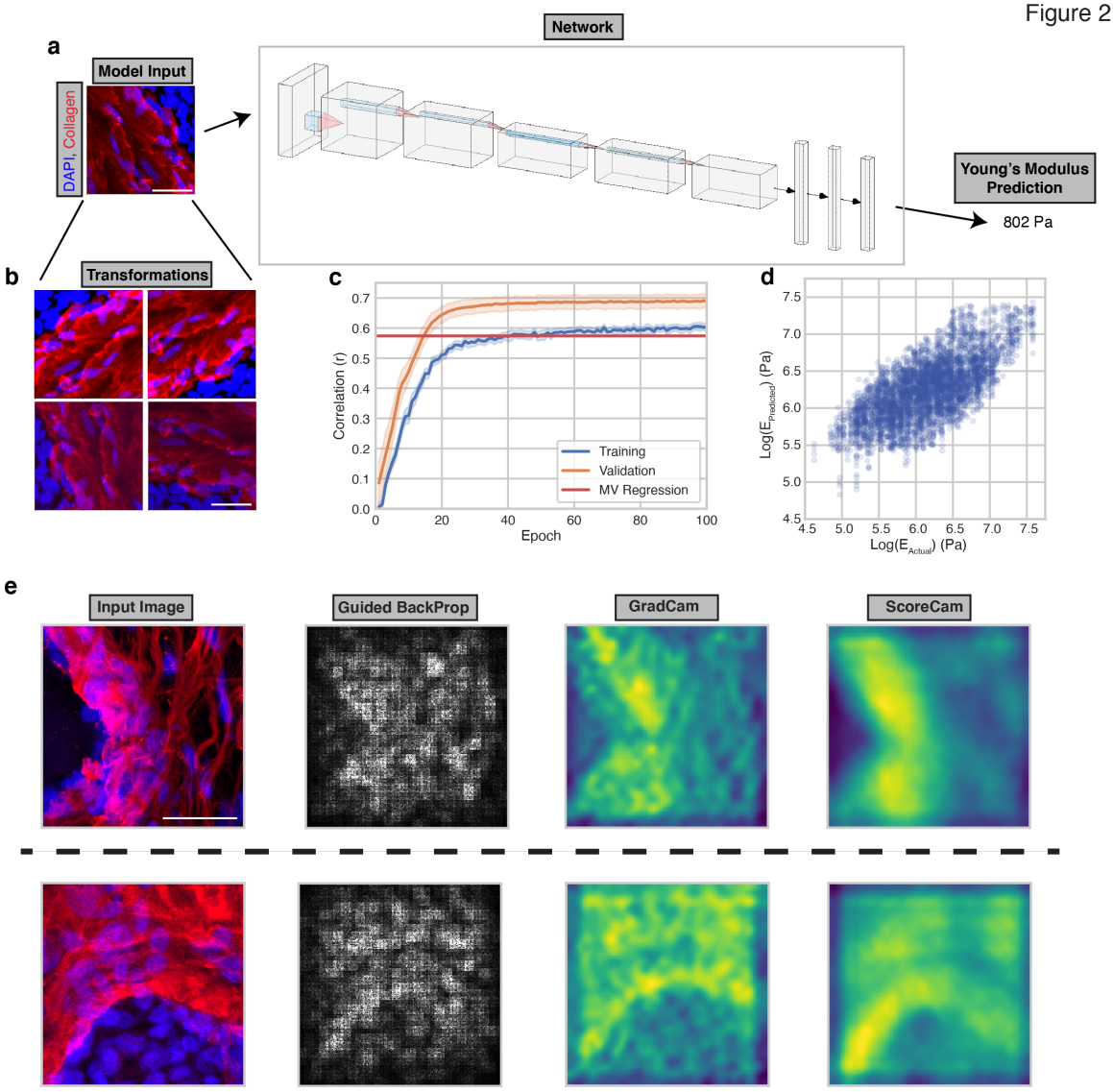

Figure 2.2: A convolutional neural network predicts the Young's Modulus of tissue. a, Example input-output relationships to the network with diagram depicting connectivity of different network layers. b, Example image transformations to increase the size of the network training dataset. c, Correlation between model predictions and actual Young's Modulus values for the training (blue line) and validation (orange line) datasets over the course of training. Error bars indicate 95% confidence intervals across 25 trained models. d, Dot plot of actual versus predicted Young's Modulus values for the validation datasets across 25 trained models. n = 4768, Pearson r = 0.687. e, Saliency maps reflecting image regions that influenced model predictions. Scale bar, 20μm.

Neural networks are data hungry, such that their performance is greatly improved when more data is utilized. When given a small amount of training data, neural networks tend to overfit the training dataset and emphasize features that do not generalize well. To address this, we

artificially enlarged our training dataset of a thousand data points by applying random rotations, mirroring, and adjustments to brightness, contrast, and sharpness (Fig. 2.2b). Based upon the fact that the Young's Modulus of the sample is independent of these manipulations, we reasoned this would allow the model to learn which features were the most informative while preventing overfitting. Consistently, we found that the model generalized much better to validation data when transformations were applied to the training data.

In the final model, we utilized both the DAPI and collagen channels. As dead cells are typically quite soft when probed using AFM, the additional information from the DAPI stain helped the model to learn and was included in our imaging studies. We also natural log-transformed elasticity measurements prior to training to alleviate the influence of outliers. At training completion, the correlation of predicted to actual Young's Moduli values was 0.689 (pearson R value; averaged across 25 trained models) when trained over 100 epochs (Fig. 2.2c, d), which performed significantly better than predicting elasticity based on the intensity of collagen and DAPI alone (multivariable (MV) regression line using all training and validation samples; r = 0.574; p(CNN over MV) = 5.23e-10). The validation data is predicted more accurately than the training data as a result of the transformations applied to the training dataset. Saliency maps indicating image regions that contribute to tissue stiffness demonstrated that the trained models were able to incorporate morphological information from nuclei as well as collagen when predicting stiffness (Fig. 2.2e) ([128], [129], [130], [131]).

2.2.5 Generation of STIFMaps

We next applied our trained CNNs to predict the elasticity of normal and tumor breast tissue sections across a region of interest using Spatially Transformed Inferential Force Maps (STIFMaps). We achieved this objective by segmenting the images into squares matching the input dimensions of the neural network and predicting the Young's Moduli for each square (Fig. 2.3a, Methods). We then colorized the original images to correspond to the predicted stiffness of each point (Fig. 2.3b). To validate the performance of these stiffness predictions, tissues were im-

munostained for two established markers of cellular mechanosignaling, activated $\beta 1$ integrin and phospho-Myosin Light Chain 2 (pMLC2) that are typically increased in cells in response to a stiff ECM ([132], [133]). We used the predicted STIFMaps to evaluate the correlation between expression of these markers and tissue elasticity (Fig. 2.3c). Since a large proportion of the ECM is not directly in contact with cells, we looked at the 99th percentile of stain intensity for each percentile of ECM elasticity (Fig. 2.3d, Extended Fig. 8.4a, b). This allowed us to remove low-intensity pixels where there were no cells or stain present. The intensity of both mechanosignaling markers was found to positively correlate with the predicted Young's Modulus of the local tissue region (Fig. 2.3e), but not with the intensity of collagen or DAPI alone (Fig. 2.3f). We also applied a mask to better identify pixels located at the cell-ECM interface and observed the same trend (Extended Fig. 8.4c, d). The findings indicate that STIFMaps can accurately identify mechanical 'hotspots' within breast tumor tissue sections, thus providing an additional layer of information about the mechanical landscape of breast tissue that was not previously possible.

2.2.6 Utilizing STIFMaps with Formalin-Fixed Paraffin-Embedded Tissue

FFPE tissues are frequently used for clinical analysis because this approach preserves cell and tissue morphology. Unlike cryopreserved tissues, which are needed for traditional AFM analysis, FFPE tissue are more readily available for research analysis and clinical translational studies. However, FFPE tissues are highly cross-linked due to formalin-fixation, and thus impossible to accurately measure stiffness by AFM. Accordingly, we asked if STIFMap could predict the elasticity of the original, unfixed tissue samples based solely on collagen morphology. We stained terminal duct lobular units (TDLUs) from cryo-preserved and FFPE breast tissues with CNA and DAPI. In consultation with a clinical breast cancer pathologist, we detected no discernable morphological differences between the collagen morphology detected using the CNA collagen stain in a patient-matched FFPE versus cryopreserved tissue (Extended Fig. 8.5). The results indicate that STIFMaps can be applied to predict the elasticity of FFPE tissues in which elasticity measurements are not currently possible.

2.2.7 A stiff, fibrotic collagenous ECM drives an EMT and tumor metastasis in mice.

STIFMaps revealed a spatial co-localization between tumor cells with activated $\beta 1$ integrin, elevated actomyosin contractility (pMLC) and high-tension regions in the stroma of breast cancer tissues (Fig. 2.3e). The findings illustrate the feasibility of this method to more directly demonstrate clinical links between known regulators of breast tumor aggression and tissue tension.

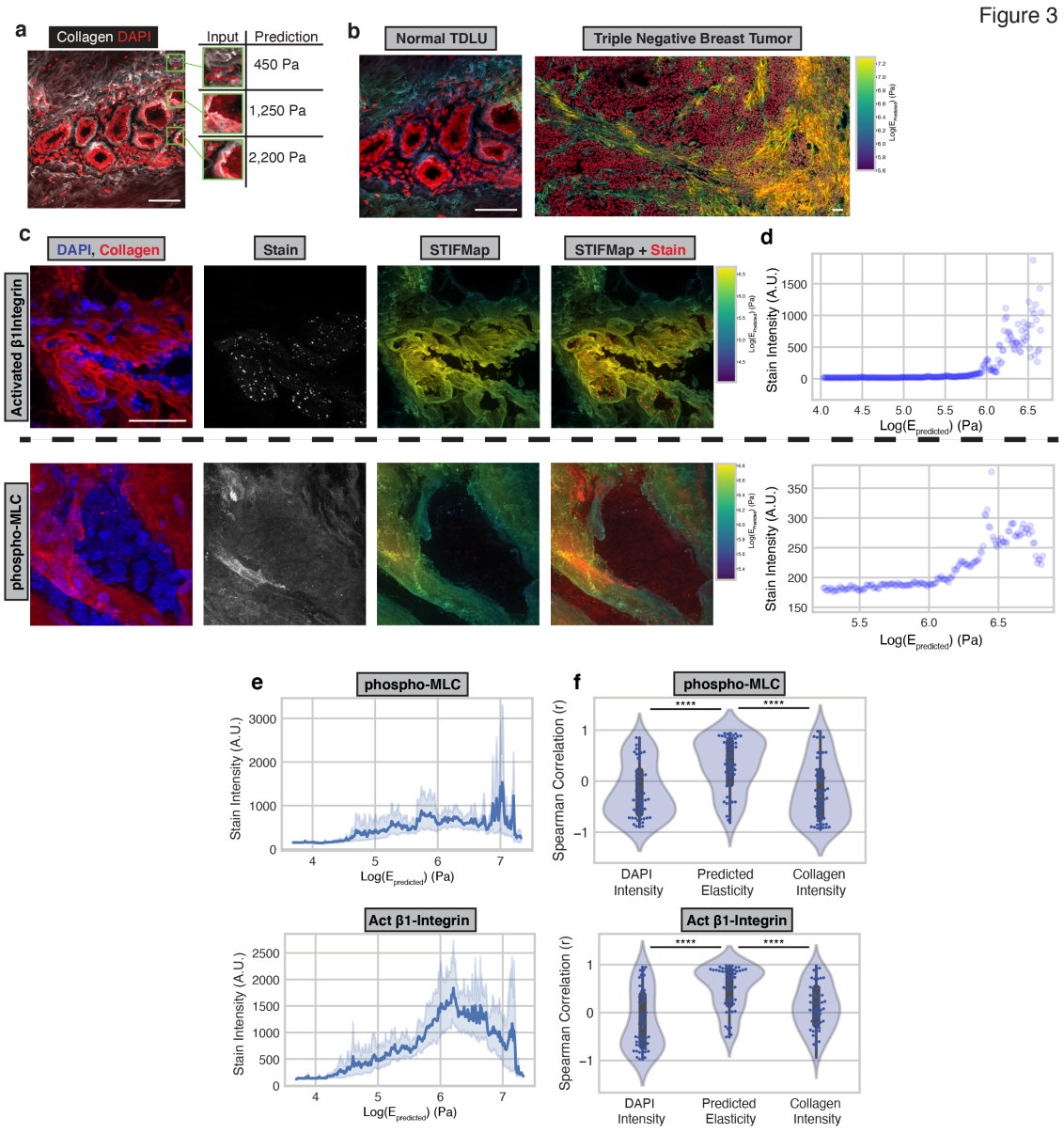

Figure 2.3: STIFMaps predict high elasticity regions within tissues.

a, Deconstruction of a CNA- and DAPI-stained image into squares of approximately 50 x 50 μm. The Young's Modulus of each square is predicted. b, Elasticity predictions are aggregated and overlaid over collagen to produce the overall STIFMap for both a normal TDLU and triple negative breast cancer. c, Representative images of immunofluorescent staining for pMLC (top) and activated β1 integrin (bottom). d, Scatterplots of STIFMap intensity vs stain intensity for each pixel shown in (c) indicating the 99th percentile of stain intensity for each STIFMap percentile. e, STIFMap percentiles versus the 99th percentile of stain intensity for all acquired fields of view (FOVs). Error bars indicate a 95% confidence interval. n = 60 FOVs from 10 different patient tumor samples. Median Spearman r values, activated β1 integrin = 0.696, pMLC = 0.364. f, Violin plots of the Spearman correlation for each FOV comparing the 99th percentile of staining intensity versus percentiles of DAPI, predicted elasticity, or collagen stain intensity. Internal gray bars indicate a Box-plot. n= 60 FOVs from 10 different patient tumor samples. Scale bar, 50μm. Statistical analyses were performed using Mann-Whitney U test, ****P¡10-5.

A stiff ECM can foster the growth, survival, and invasiveness of cultured premalignant and tumorigenic breast cancer cell lines by inducing an EMT ([52], [49], [134], [135]). A stiff, cross-linked collagenous stroma can also induce an EMT to promote tumor aggression and metastasis *in vivo* in experimental murine models of mammary cancer [136]. Nevertheless, there is currently no evidence to directly implicate a stiff, fibrotic tissue stroma in human breast cancer aggression and metastasis, nor to link this phenotype to induction of an EMT. Therefore, to directly test whether a stiff stroma could drive the aggressiveness and metastatic behavior of human breast cancers, and to determine if this is linked to an EMT, we manipulated HER2+ human breast cancer patient-derived xenografts (PDX) *in vivo*. We reasoned that PDXs are a model that more closely mirrors the heterogeneous phenotype of human breast tumors ([137], [138]). To assess this, we implanted three independent HER2+ human breast cancer PDXs (BCM-3963; BCM-3143B, HCI-012) embedded within control (SOFT; 140 Pa) and non-metabolizable L-ribose cross-linked (STIFF; 1,200-2,000 Pa) collagen gels into the fat pads (orthotopic) of NOD/SCID mice and monitored the impact on tumor phenotype and behavior (Fig. 2.4a). Immunofluorescence analysis revealed a significant increase in activated β1 integrin and phospho-Y397 focal adhesion kinase activity (Y397FAK) in the PDX tumors that developed within the stiffened collagen gels (Fig. 2.4b, c). We observed an increase in tumor outgrowth in all three independent HER2+ PDX tumors embedded within the stiffened collagen gels (Extended Fig. 8.6a-c). Markers of growth factor receptor signaling, as indicated by elevated phosphorylated MAP Kinase (pERK; Extended Fig. 8.6d), indicated

that tissue tension and integrin signaling promoted tumor cell growth. There was also a greater number of larger metastatic lesions quantified in the lungs of the mice harboring the stiff tumors (Fig. 2.4d-g). Consistent with a relationship between a stiff stroma, breast tumor aggression, and induction of an EMT, RNAseq analysis revealed a significant elevation of the 'Hallmark Epithelial Mesenchymal Transition' pathway in STIFF PDX tumors (Fig. 2.4h,i, MSIGDB pathway M5930). RT-PCR analysis validated the stiffness induction of the expression of several of the EMT genes including Vimentin (VIM), TWIST1, SLUG, and MMP2 (Fig. 2.4j-m, Extended Fig. 8.6f-k). These findings demonstrate that a stiff stroma induces integrin and growth factor receptor signaling to drive tumor aggression and metastasis of human breast tumor PDXs *in vivo*. The data also implicate stromal stiffness-dependent induction of an EMT in this phenotype.

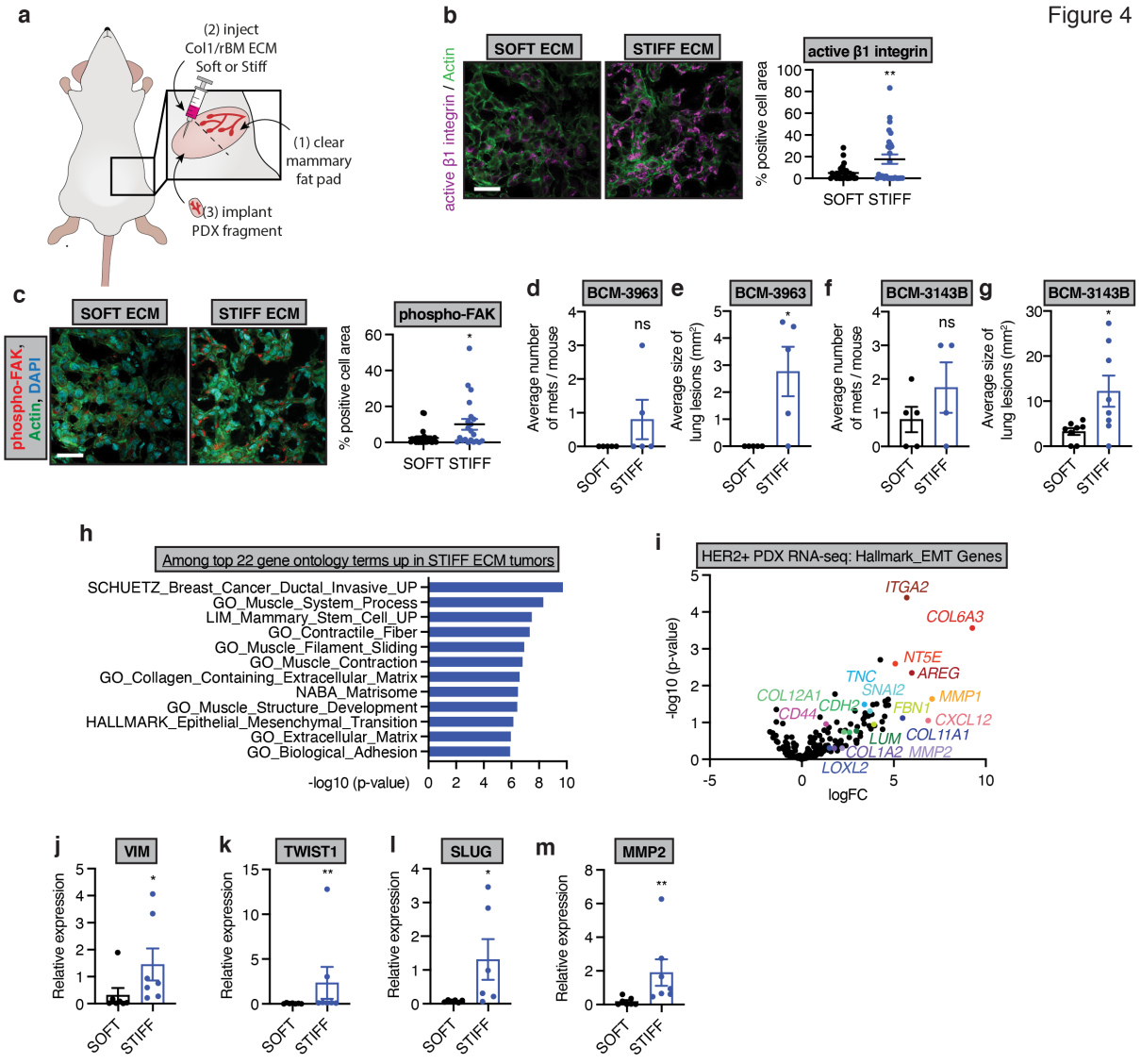

Figure 2.4: Matrix elasticity associates with EMT in a PDX model of HER2+ breast cancer. a, Schematic showing the strategy for implantation of HER2-positive patient-derived xenograft (PDX) breast cancer tissues in SOFT (Col1/rBM, no L-ribose) and STIFF (Col1/rBM, crosslinked with L-ribose) hydrogels. b,c, Representative images of immunofluorescent staining of active $\beta 1$ integrin (b) and phospho-FAK (c) in SOFT or STIFF HER2-positive PDX tumors (left). Scale bar, 50 μm. Quantification of average phospho-FAK (b) and active $\beta 1$ integrin (c) positive cell area for all HER2-positive PDX tumors (right). SOFT; n = 6, STIFF; n = 6. d, Average number of lung metastases for mice bearing BCM-3963 PDX tumors in SOFT and STIFF ECM stroma as determined by histological analysis. SOFT; n = 10, STIFF; n = 10. e, Average size of the metastatic lesions corresponding to the analysis in (d). f, Analysis as in (d) for mice bearing BCM-3143B PDX tumors. SOFT; n = 10, STIFF; n = 10. g, Analysis as in (e) for metastatic lesions corresponding to the analysis in (f). h, Gene ontology terms from among the top 23 most significantly upregulated, using RNAseq data derived from all HER2-positive PDX tumors generated

in SOFT (n=9) and STIFF (n=9) ECM stroma as above (n=3 for each PDX and condition). i, Volcano plot of p-value (-log10) vs. log fold change (logFC) for gene expression from the HALLMARK_epithelial-to-mesenchymal transition gene set for RNAseq data of HER2-positive PDX tumors developed in SOFT and STIFF ECM stroma. j-m, qRT-PCR arrays designed to examine Epithelial-to-mesenchymal transition related gene expression were used to analyze RNA isolated from PDX tumors developed in SOFT and STIFF ECM stroma. SOFT; n = 7, STIFF; n = 7. Bar plots for the average relative expression of the indicated mesenchymal genes are displayed. All graphs are presented as mean +/- S.E.M. Statistical tests used were Mann-Whitney U test (c, e, j-m) and unpaired t-test (b, d, f, g), *P¡0.03, **P¡0.002, ***P¡0.0002, ns=non-significant.

2.2.8 STIFMaps link stromal elasticity to EMT in patient tumors.

Having established that high ECM tension can drive the aggressiveness and metastasis of HER2+ PDX breast tumors in association with induction of an EMT, we next applied STIFMaps to look for clinical evidence supporting this relationship. We previously showed using AFM and immunofluorescence analysis that the more aggressive triple-negative breast cancer (TNBC) and HER2+ human breast cancer subtypes have higher levels of activated $\beta 1$ integrin and a stiffer invasive front ([8], [53]). We applied STIFMaps to explore if there was a significant association between stromal tension and EMT markers in clinical FFPE samples of TNBC and HER2+ breast tumors. We first looked within patient transcriptomic data and found that expression of collagen genes highly correlated with expression of EMT genes (Fig. 2.5a, b). Collagen genes were removed from all gene sets to not bias this analysis. We then stained TNBC FFPE tissue sections for ZEB1 and SLUG, two transcription factors induced by a stiff stroma previously implicated in EMT [139]. We detected expression of both ZEB1 and SLUG and found their levels to be significantly positively correlated with the predicted elasticity of the interstitial collagens in the stroma, but not individually with total collagen or DAPI intensity (Fig. 2.5c-e). A trend was also observed when a mounted TNBC tissue was subjected to a full imaging scan (Extended Fig. 8.7a, b). To determine the broader relevance of these clinical findings we next applied STIFMaps to a cohort of 21 HER2+ breast tumors with associated clinical follow-up data [65]. We co-stained these FFPE tissue sections with HER2 and ZEB1 as well as with CNA35 to stain tissue collagens and had a pathologist outline the tumor in each whole slide image. The predicted tissue elasticity

from STIFMaps was significantly associated with ZEB1 stain intensity, but not with HER2, when compared to the correlation with collagen intensity alone (Fig. 2.5f, g, Extended Fig. 8.7c, d). We then looked at the spatial autocorrelation of each stain in each tissue by calculating Moran's I, which revealed a trend showing that greater clustering of HER2, ZEB1, and elasticity associated with metastatic recurrence (Fig. 2.5h). This observation is consistent with worse overall survival among patients with high expression of EMT and collagen gene expression signatures (Fig. 2.5i, j). These findings demonstrate, for the first time, a spatial link between high stromal collagen elasticity and biomarkers of EMT in both TNBCs and HER2+ human breast tumors. Together with our PDX findings, these data link EMT to ECM stiffness and implicate tension-induced EMT in human breast tumor metastasis. The findings also suggest a stiff ECM could promote tumor aggression and compromise breast cancer patient outcome.

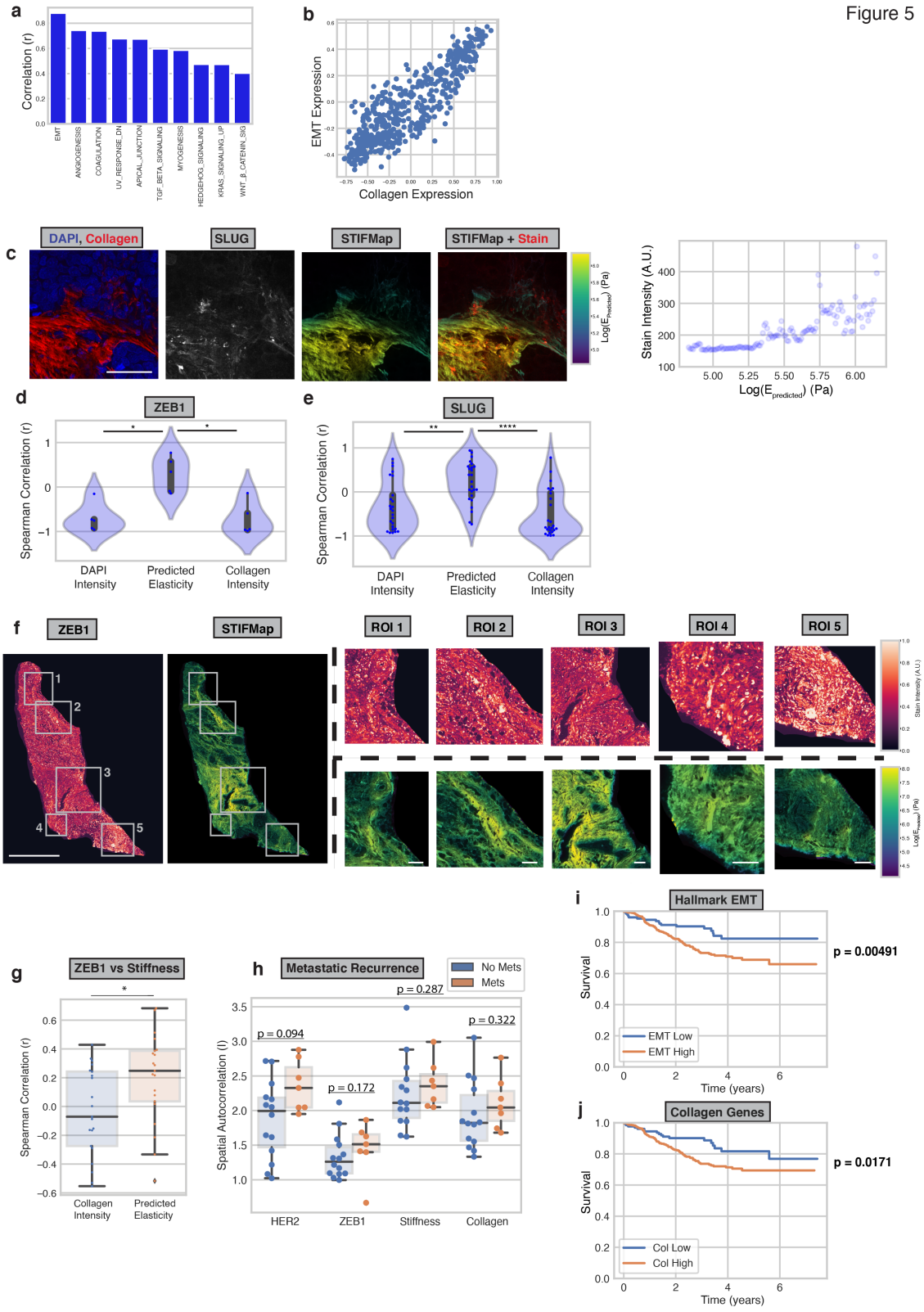

Figure 2.5: EMT markers spatially overlap with high tension matrix and associate with poor survival in patient tumors.

a, Pearson correlation between GSVA scores for collagen genes and hallmark pathway genes in the Nuvera dataset. b, Scatterplot of GSVA scores for collagen genes and hallmark EMT genes. Each point represents one patient. n = 508 patients. Pearson r = 0.880. c, Representative FOVs for SLUG staining within FFPE tumors. Scale bar, 50 μm. d,e, Violin plots of the Spearman correlation for each FOV comparing the 99th percentile of staining intensity versus percentiles of DAPI, predicted elasticity, or collagen stain intensity. Internal gray bars indicate a Box-plot. n = 5 ZEB1 FOVs and n = 25 SLUG FOVs. f, Representative whole slide image (WSI) and regions of interest (ROIs) of ZEB1 stain with STIFMap in HER2+ breast cancer cohort. Scale bar (WSI), 1 mm. Scale bar (ROIs), 100 μm. g, Spearman correlation for each whole tissue section comparing the 99th percentile of staining intensity versus percentiles of predicted elasticity and collagen stain intensity. n = 21 patient tumor samples. h, Box and whiskers plots to show the association between metastatic recurrence and spatial autocorrelation (Moran's I) for tissue markers and STIFMaps in the HER2+ breast cancer cohort. i,j, Kaplan-Meier curves comparing survival between the upper and lower quartiles of EMT (i) and collagen (j) GSVA scores within the Nuvera cohort. n = 127 patients in each group. Statistical analyses were performed using Mann-Whitney U, *P¡0.05, **P¡0.01, ****P¡10-5.

2.3 Discussion

Here we present a new method we term Spatially Transformed Inferential Force Mapping, STIFMap, which permits the spatial resolution and quantification with micron-resolution of the mechanical heterogeneity of the collagenous stroma within normal and tumor breast tissues. The method works on both cryopreserved and FFPE tissues and employs a quick, inexpensive staining protocol via CNA35 and DAPI. The approach permits simultaneous quantification of the tension landscape of the stromal ECM together with standard biomarker immunostaining approaches, and could be integrated with spatial proteomics and genomics as well as protein marker multiplexing protocols ([100], [101], [102]). Although methods do exist to broadly quantify tissue elasticity across a tissue section, they do not provide high-resolution spatial information [111]. AFM is a technique that directly probes tissue elasticity at the single cell scale [140]. However, standard AFM methods are not high throughput, require fresh or cryopreserved tissue, rely upon specialized equipment and operators, are time-consuming, and only collect sparely spaced data points over focused sections of a tissue ([109], [110]). In the absence of the AutoAFM algorithms presented herein, it is also challenging to overlay AFM data with biomarker staining, and the use of cryopreserved or fresh tissue compromises simultaneously conducting spatial genomic, transcriptomic,

or proteomic analyses. STIFMaps overcomes current shortcomings of conventional AFM methods and can rapidly annotate the elasticity landscape of an entire tissue section with a simple collagen stain. The method is also amenable to FFPE tissue thereby expanding the scope and application of the method. Indeed, using STIFMap we were able to link, for the first time in clinical biopsies of human breast cancer, tissue mechanics with indicators of mechanosignaling and biomarkers of an EMT previously implicated in tumor aggression ([112], [113]). The results highlight the potential utility of using STIFMaps to quantify stromal biophysical features to predict tumor behavior and ultimately patient outcome.

We and others showed both *in vitro* and in experimental models *in vivo* that a stiff ECM increases integrin mechanosignaling to foster tumor cell growth, survival, invasion and metastasis, and that this is accompanied by induction of an EMT ([52], [141], [49]). Here we demonstrate, for the first time using human breast tumor PDX biospecimens, that a stiff stroma can induce an EMT *in vivo* and that this is accompanied by metastasis. By correlating stromal tension with biomarkers of an EMT in human clinical specimens of TNBC and HER2+ breast cancer, we found clinical evidence that such a relationship also exists within human tumors, thereby providing validation of the experimental manipulations. Furthermore, we showed that expression of either collagen genes or an EMT signature associates with significantly worse patient outcome. The findings thereby directly link stromal tension to human breast cancer aggression and directly implicate induction of an EMT in this phenotype. Although STIFMaps provides researchers with a versatile tool to explore the role of stromal stiffness in clinical specimens, additional studies will be necessary to further clarify mechanisms through which a stiff ECM drives an EMT in tumors. Moreover, more work will be needed to assess the clinical relevance of stromal stiffness on patient outcome.

There is growing interest in the application of artificial intelligence methods to classify clinical histological images ([142], [143], [144]). While early deep learning algorithms focused on routine tasks such as nuclei segmentation, current state-of-the-art algorithms are beginning to rival pathologists at tasks such as tumor grading and cancer detection [142]. Moving beyond what pathologists are able to detect, some new algorithms are even able to predict tumor recurrence and

invasive potential in cohorts for which there is currently no means available for evaluating risk to progression [145]. Notwithstanding these advances, a number of caveats hinder development in this area such as suboptimal network architectures, the requirement for large numbers of samples, the immense computational processing power necessary to train highly sophisticated models, overfitting data that is generated by only one individual or group, and the difficulty in interpreting why deep learning models classify results in one group or another [146]. Nevertheless, improvements in deep learning such as neural architecture search to find more optimal networks and advancements in computational power continue to make computational pathology more mainstream and accessible in the clinic. While there are still issues to overcome, deep learning algorithms appear to be the future of histopathological analysis and tissue classification [147].

Tumors are highly heterogeneous at the genomic, transcriptomic, and proteomic levels ([63], [66]). Regions within human and murine tumors have been identified in which immune infiltration, cancer cell metabolism, and stress response pathways exhibit diverse phenotypes. Given that patient prognosis and outcomes have been linked to genomic heterogeneity, as well as variability in immune infiltration and hormone receptor expression, it is perhaps not surprising that there is a growing interest in understanding the relevance of and drivers of tumor heterogeneity [64]. In this regard, the level of tissue fibrosis also predicts patient outcome and recent data suggest the level and organization of tissue collagens and stromal stiffness varies widely within a patient's tumor ([12], [59], [8]). Yet, to date there are no tools with which to spatially resolve the mechanical stromal heterogeneity within a tumor and none that are amenable to scanning across a full tissue section of a tumor. With STIFMaps, it is now possible to evaluate the association between a biomarker or pathway of interest and the local and heterogeneous elasticity of the collagen-rich stroma within a given normal or malignant tissue. Moreover, the STIFMap method can be combined with spatial sequencing, in situ gene expression, metabolomics, and even proteomics to allow for unbiased screening of correlations between molecular heterogeneity and mechanically regulated pathways in clinical samples. Accordingly, STIFMaps opens the door for clinicians and

translational researchers to explore the impact that tissue elasticity has on cancer cells in their native tissue microenvironments.

3 Chapter 3: Fibrosis Correlates with Myeloid Cell Immune Evasion and Immunosuppressive Glycoproteins in the Tumor Microenvironment

This chapter is a reprint of the peer-reviewed article titled "Immunosuppressive glycoproteins associate with breast tumor fibrosis and aggression" by Kevin James Metcalf, Mary-Kate Hayward, Eric Berens, Alastair J Ironside, Connor Stashko, E Shelley Hwang, and Valerie M Weaver in Matrix Biology Plus (2022).

3.1 Introduction

Many tumor types exhibit elevated levels of sialoglycoproteins that correlate with increased proliferation and metastasis, and poor prognosis [148]. The glycocalyx, the layer of glycoproteins and proteoglycans that covers all cells, is abnormal on cancer cells and features increased sialic acid content [149]. We previously showed that a collective effect of glycocalyx dysregulation is increased bulkiness, defined as a denser, thicker glycocalyx and includes increases in number of glycoconjugates and glycoconjugate sites, and elaboration of glycan structures. A bulkier glycocalyx enhances integrin signaling, promotes cell cycle progression, increases metastatic potential, and sterically hinders macrophage phagocytosis [150], [141], [151], [152]. These findings indicate that the increased expression of glycoproteins including sialoglycoproteins in tumor cells likely play a causal role in tumor progression and aggression.

One mechanism by which sialoglycoproteins regulate tumor progression is by inducing immune suppression by acting as ligands to the Siglec family of receptors that are expressed on most immune cell types and contain immunoreceptor tyrosine-based inhibitory motif (ITIM) domains [153]. Siglec signaling—in particular Siglec-7, Siglec-9, Siglec-10, and Siglec-15 expressed on macrophages, monocytes, NK cells, and activated T cells—inhibits cancer cell killing *in vitro* and promotes tumor growth *in vivo* [154], [155], [156], [157], [158], [159], [160]. Shed sialogly-

coproteins originating from the cancer cell glycocalyx are also immunosuppressive and promote differentiation of Siglec-7- and Siglec-9-positive monocytes to pro-tumor macrophages in pancreatic ductal adenocarcinoma (PDAC) [161]. These findings emphasize the critical role played by sialoglycoproteins in immune modulation and suggest that inhibition of the sialic acid-Siglec axis could improve cancer treatments including checkpoint inhibitor responses [162]. Nevertheless, factors that modulate sialoglycoprotein expression and their relationship to tumor aggression and anti-tumor immunity remain poorly defined.

Solid tumors are characterized by a desmoplastic response that associates with fibrosis, involving increased deposition, remodeling and crosslinking of extracellular matrix proteins. In breast cancer and PDAC, fibrosis associates with more aggressive subtypes [8], [12]. Tumor fibrosis can promote malignancy by fostering cancer cell growth and survival, enhancing invasion and migration, and inducing immune suppression [95], [53], [163]. Highly fibrotic cancers are often defined as immune deserts defined by poor infiltration of tumoricidal GzmB+CD8+ T cells [59]. What is not clear, however, are the mechanisms by which fibrosis induces immune suppression. Fibrosis induces multiple changes in tumors, including metabolic changes that lead to dysregulated anabolism of many different complex molecules, including glycoproteins [164].

We hypothesized that an association between fibrosis and increased production of immunosuppressive sialoglycoproteins could provide a functional link for fibrosis-induced immune suppression. In this study, we performed a comprehensive histological analysis and cellular census of human breast tumors to assess the link between fibrosis, tumor aggression, and the sialic acid-Siglec axis. We found that sialoglycans, including Siglec-7, Siglec-9, and Siglec-10 ligands, are produced by cancer cells and are increased in regions of high fibrosis and more aggressive breast cancer subtypes. In addition, more aggressive breast cancer subtypes feature greater infiltration of SIGLEC7-, SIGLEC9-, and SIGLEC10-positive myeloid cells. Our findings demonstrate an association of tumor fibrosis and tumor aggression with sialoglycoprotein expression and infiltration of immunosuppressive Siglec-positive myeloid cells. Additionally, our data predict that the highly

aggressive triple-negative (TN) subtype as the most likely to benefit from therapeutic targeting of the sialic acid-Siglec axis.

3.2 Results

3.2.1 Acidic glycoprotein content is elevated in high fibrosis regions and associates with breast cancer aggression

We first sought to investigate whether a link exists between acidic glycoprotein expression and fibrosis. We stained a cohort of human breast tumors for total collagen (Trichrome blue), fibrillar collagen (Picrosirius red), and polyacidic molecules including sialoglycoproteins, hyaluronic acid, and sulfated proteoglycans (Alcian blue). Serial tissue sections were stained and whole slide imaging (WSI) was used to evaluate acidic glycoprotein content in regions of varying levels of fibrosis. High and low fibrosis regions within each tumor were identified by a breast pathologist in parallel hematoxylin and eosin (H&E) stained tissue (Fig. 3.1A). These identified regions of high and low fibrosis defined by collagen abundance were confirmed by Trichrome blue and Picrosirius red staining (Fig. 3.1B-C). Analysis revealed that Alcian blue staining was significantly higher in the high fibrosis regions within the tumor tissue as compared to the low fibrosis regions. Sialidase pretreatment decreased Alcian blue staining (Extended Fig. 8.8), indicating that the Alcian blue staining represents sialoglycoproteins. These findings suggest there may be a link between fibrosis and levels of sialoglycoproteins in human breast tumor tissue (Fig. 3.1D).

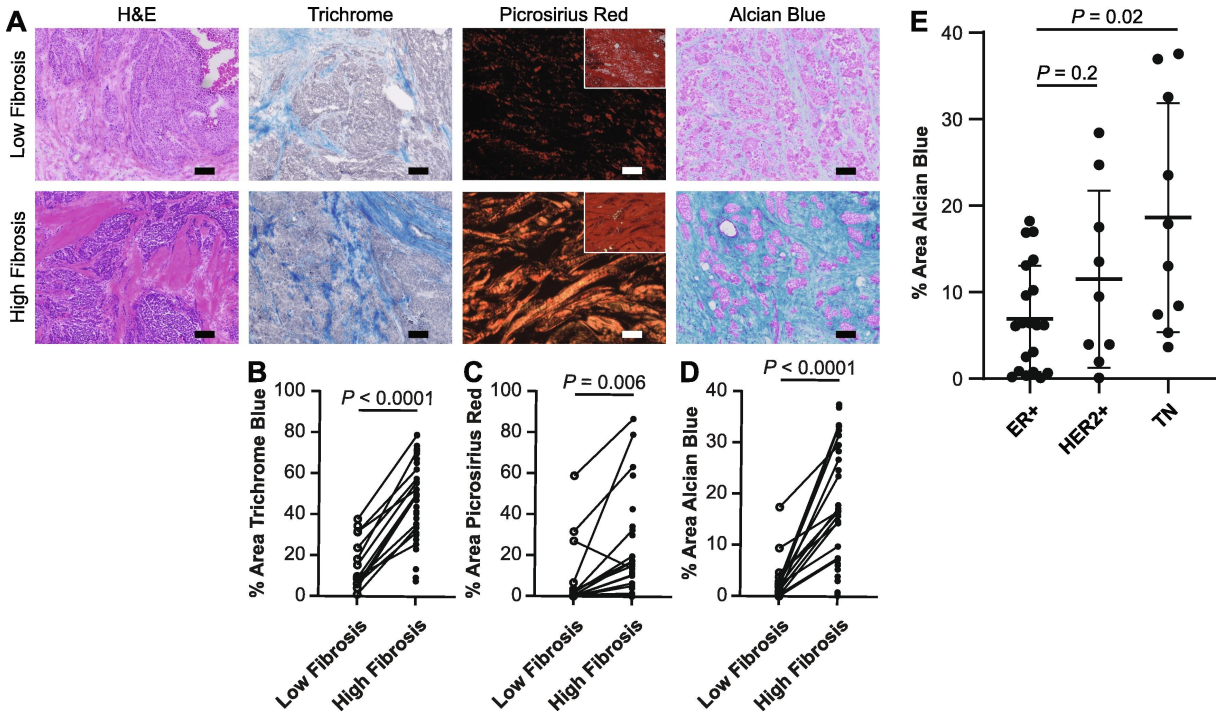

Figure 3.1: High fibrosis regions have greater acidic glycoprotein content[1]

A. Representative images of patient-matched low and high fibrosis regions of human breast tumors stained with H&E, Trichrome, Picrosirius red (polarized image; inset brightfield), and Alcian Blue. Scale bar is 100 micron. B-D. Quantification of positively stained area of B. Trichrome, C. Picrosirius red, and D. Alcian blue in low and high fibrosis regions. E. Quantification of Alcian blue-positive area across whole tumor tissues by subtype. The mean is plotted and the error bars represent 1 standard deviation. (For interpretation of the references to color in this figure legend, the reader is referred to the web version of this article.)

Human breast cancers can be divided into histological subtypes that predict tumor aggression with ER+ reflecting lower grade, HER2+ reflecting higher grade, and TN reflecting highest grade. We reported previously that the level of tissue fibrosis associated with the more aggressive HER2+ and TN breast cancer subtypes [8]. To determine whether the correlation between acidic glycoproteins and tissue fibrosis reflected tumor aggression, we next compared the level of Alcian blue staining across whole tissues according to breast cancer subtype. Alcian blue staining was highest in TN tumors and lowest in ER+ tumors with the highest intensity of Alcian blue staining found in the regions within these tumors with the greatest intensity of fibrosis (Fig. 3.1E and Ex-

[1]This figure was generated by co-authors.

tended Fig. 8.8). These data reveal a link between tumor aggression, fibrosis, and sialoglycoprotein content.

3.2.2 Cancer cells express a sialoglycoprotein biosynthetic gene program that is the most abundant in the more aggressive breast cancer subtypes

To understand the cellular source of the increased acidic glycoprotein in fibrotic and aggressive breast tumors, we quantified expression of sialoglycoprotein biosynthetic genes from a publicly available scRNAseq dataset [165]. We first clustered 34 breast tumors (20 HR+ including 19 ER+ and 1 PR+, 6 HER2+, and 8 TN) (Fig. 3.2A and Extended Fig. 3.2) and extracted the epithelial cell clusters based on KRT19 expression (Extended Fig. 8.9). We also performed the clustering and extraction of epithelial cell clusters based on KRT14 and KRT18 expression from 12 normal breast tissues (Extended Fig. 8.10). We then merged the tumor and normal epithelial cell datasets. Our analysis revealed that cells clustered by malignancy and subtype in UMAP space (Extended Fig. 8.11).

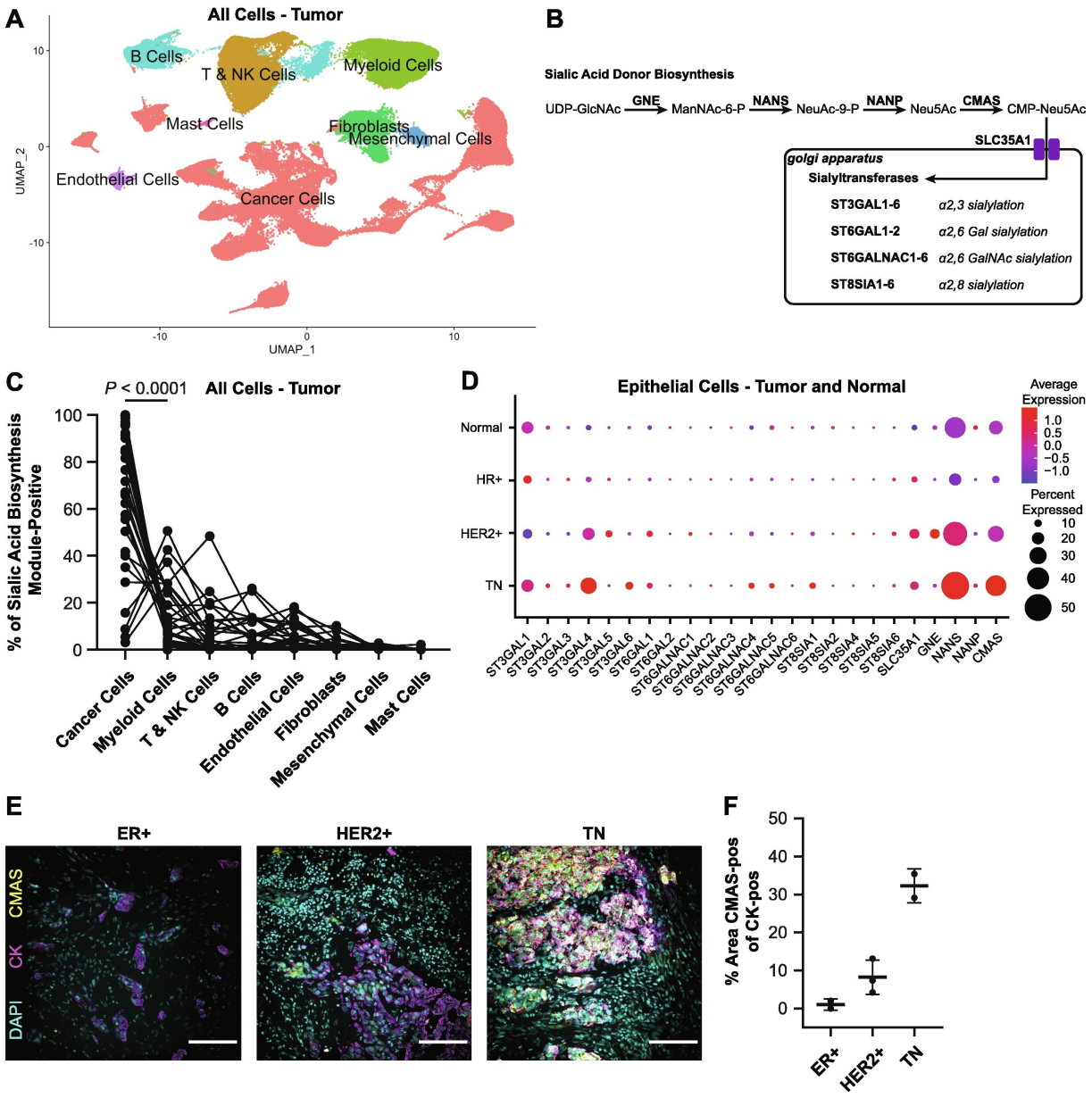

Figure 3.2: Sialoglycoprotein biosynthetic gene programs are found in cancer cells and elevated in aggressive breast cancers.[1]

A. UMAP projection of all cells from scRNAseq data of 34 breast tumors [95]. B. Diagram of sialylglycoprotein biosynthetic pathway. C. Plot of percent sialic acid biosynthesis module-positive (CMAS and NANS) by cell type for each patient. D. Dot plot showing expression of all sialoglycoprotein biosynthetic genes in epithelial cells extracted from normal breast, and HR+, HER2+, and TN tumors. E. Representative images of multicolor IF of CMAS and CK. Scale bar is 100 micron. F. Quantification of CMAS staining in CK-positive cells. For each subtype n = 2–3 patient samples were quantified. The mean is plotted and the error bars represent 1 standard deviation.

[1]This figure was generated by co-authors.

We then identified the cell clusters responsible for sialoglycoprotein biosynthesis based on gene expression. We evaluated expression of 20 sialyltransferase genes (ST3GAL1-6, ST6GAL1-2, ST6GALNAC1-6, ST8SIA1-6) and 5 sialic acid biosynthetic genes (SLC35A1, GNE, NANS, NANP, CMAS) per cluster for the tumor and normal tissues (Fig. 3.2B and Extended Figs. 8.9, 8.10). We found elevated expression of CMAS, a N-acylneuraminate cytidylyltransferase and the last step in CMP-sialic acid biosynthesis, in cancer cells in tumors (Extended Fig. 8.9) and in secretory L1-type luminal epithelial cells, marked by SPLI [166], in normal breast tissue (Extended Fig. 8.10). In addition, multiple clusters had high expression of NANS, a sialic acid synthase, including cancer cells, myeloid cells, and B cells in tumors and basal epithelial cells, mesenchymal cells, and immune cells in normal breast. Importantly, limitations in sequencing depth associated with scRNAseq protocols are likely responsible for the low detected expression we quantified in these data sets for many of the sialoglycoprotein biosynthetic genes [167]. Nevertheless, within tumor tissues, cancer cells featured higher expression of the NANS and CMAS gene module, relative to all other cell clusters (Fig. 3.2C). These data suggest that cancer cells are likely the major source of the increased level of sialylation that characterizes human breast tumors.

Next, we asked if sialoglycoprotein biosynthetic gene expression within the breast epithelial cells varied by clinical cancer subtype. We found elevated expression of NANS, CMAS, ST3GAL4, a beta-galactoside alpha2-3 sialyltransferase, and ST6GAL1, a beta-galactoside alpha2-6 sialyltransferase, in more aggressive tumor subtypes (i.e., HER2+ and TN tumors), relative to HR+ tumors and normal breast tissues (Fig. 3.2D). Interestingly, epithelial cells from HR+ tumors did not have elevated expression of any sialoglycoprotein biosynthetic genes, relative to HER2+ and TN tumors and normal breast epithelium. There was substantial interpatient heterogeneity in the expression of sialoglycoprotein biosynthetic genes (Extended Fig. 8.12). We confirmed elevated expression of CMAS on the protein level using immunofluorescence staining of breast tumor sections. We observed the fraction of cancer cells, marked by pan-cytokeratin (CK-positive), that are CMAS-positive was highest for TN tumors and lowest for ER+ tumors, consistent with the scRNAseq results (Fig. 3.2E-F).

We next confirmed that an individual cell would have potential for sialoglycoprotein biosynthesis through coexpression of NANS and CMAS. We identified coexpression of NANS in 55% of CMAS-positive epithelial cells, and coexpression of CMAS in 31% of NANS-positive epithelial cells as CMAS-positive (Extended Fig. 8.12). These data suggest that sialoglycoprotein biosynthesis may be elevated in the more aggressive breast cancer clinical subtype. The findings are also consistent with the increased Alcian blue staining we quantified in the more aggressive breast cancer subtypes (Fig. 3.1E).

3.2.3 Tumor sialylation is increased in high fibrosis regions

To understand if changes in sialic acid biosynthetic gene expression contributes to the changes in sialic acid content we and others observed in these human breast cancers, we next used quantitative lectin immunofluorescence. We first stained the human breast cancer tissue with Sambucus nigra lectin (SNA), which binds preferentially to alpha2,6-sialylated glycoproteins (Fig. 3.3A). For the less aggressive ER+ tumors, SNA staining did not change between low and high fibrosis regions (Fig. 3.3B). Interestingly however, in the more aggressive HER2+ and TN breast cancer subtypes, we quantified an increase in the SNA-positive area in high fibrosis regions as compared to the low fibrosis regions (Fig. 3.3C). Increased SNA staining in HER2+ and TN breast cancer subtypes is consistent with elevated expression of ST6GAL1 in these subtypes (Fig. 3.2D).

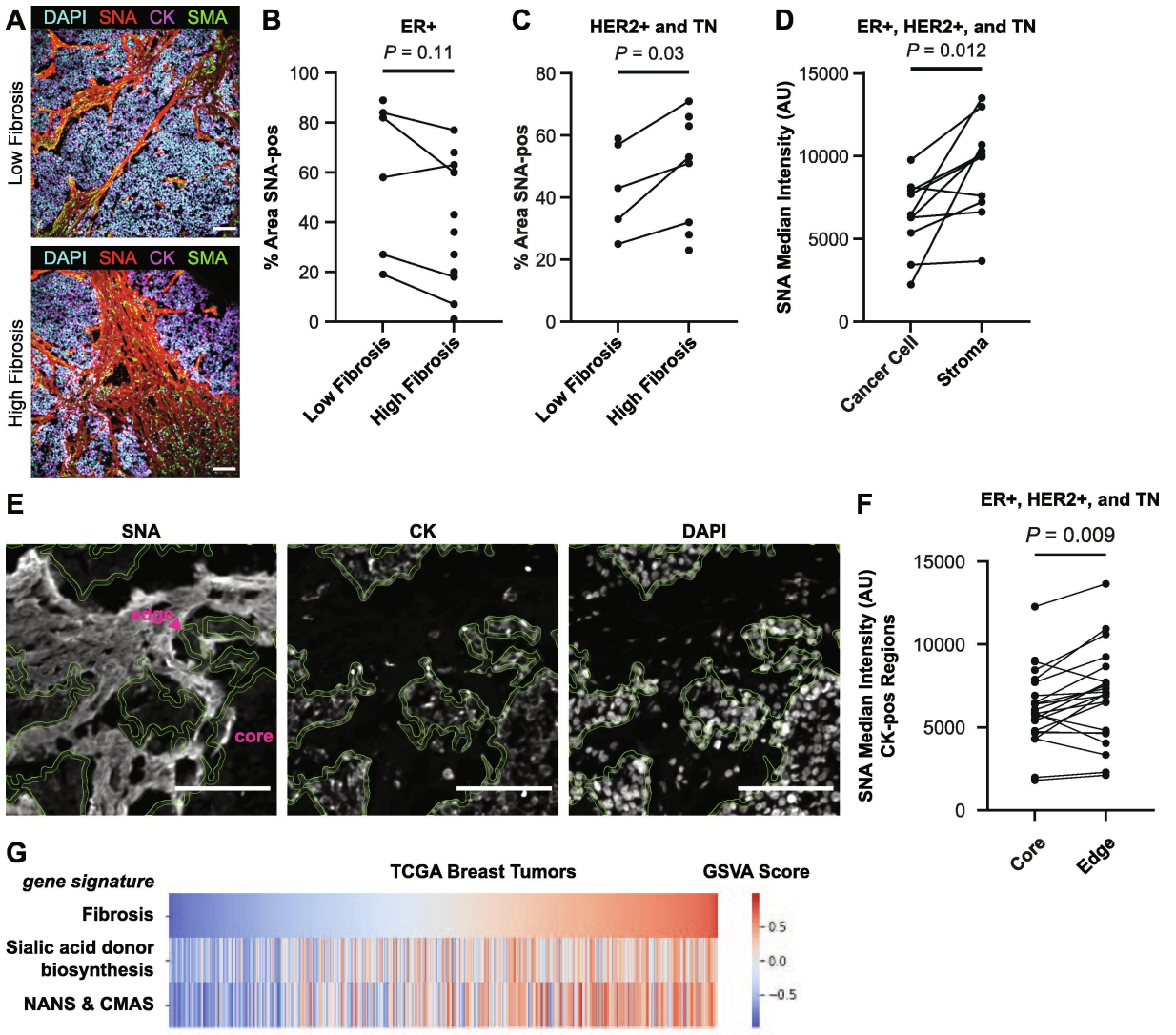

Figure 3.3: Sialic acid levels are elevated in the cancer cell glycocalyx and stroma within high fibrosis regions of aggressive breast tumors.[1]

A. Representative IF images of a TN tumor in high and low fibrosis regions stained with DAPI, SNA lectin, pan-CK, and SMA. Scale bar is 100 micron. B-C. Quantification of SNA-positive area in low and high fibrosis regions in B. ER+ and C. HER2+ and TN tumors. D. Quantification of SNA intensity in cancer cell and stromal regions. E. Representative IF images of SNA staining of tumor edge and core regions. The 5 micron thick region bounded by the green lines represents the tumor edge. DAPI and CK inserts are from the same image. Scale bar is 100 micron. F. Quantification of SNA intensity in tumor core and edge regions. G. Heatmap showing the expression of gene signatures in RNAseq data from breast tumors from TCGA. Patients were ordered by the fibrosis signature.

SNA-positive regions were found throughout the tumor (Fig. 3.3A) and could represent sialoglycoproteins found in the glycocalyx, sialylated extracellular matrix proteins, sialylated se-

[1]This figure was generated by co-authors. I analyzed the TCGA data and contributed panel (G).

creted proteins, and sialylated shed proteins [168]. Based on lectin staining localization, we identified two regions containing sialoglycoproteins—cancer cell and the stromal regions. We used smooth muscle actin (SMA), which marks stromal fibroblasts to identify stromal regions [95]. SNA intensity was greatest in SMA-positive regions, relative to CK-positive regions (Fig. 3.3D). The elevated SNA staining in stromal regions was consistent with the elevated Alcian blue staining we quantified earlier in the stromal regions of the breast tumors (Fig. 3.1A).

Sialyation of the cancer cell compartment, which includes the glycocalyx, was determined by quantifying SNA intensity within CK-positive regions. To begin with we failed to observe any differences in sialylation of the cancer cell compartment between high and low fibrosis regions within the breast cancer tissue (Extended Fig. 8.13). Accordingly, given that the tumor invasive front displays a strikingly reorganized collagenous stroma that we previously showed was stiffer [8], we next compared the SNA lectin staining of the cancer cell compartment between the tumor invasive front and tumor core. We classified CK-positive edge regions using a 5 micron circle erosion of CK-positive regions (Fig. 3.3E). The tumor front featured elevated SNA lectin staining, compared to the CK-positive core (Fig. 3.3F). These data reveal that the cancer cell compartment is less sialylated than proximal stromal regions, and that cancer cells on the tumor front feature a greater level of sialylation than cancer cells in the tumor core.

To confirm that the lectin staining results were not specific to SNA ligands, we also stained tumor tissues with MAL-II lectin, which binds preferentially to alpha2,3-sialylated glycoproteins. We observed a similar staining pattern between SNA and MAL-II lectins, suggesting that the sialoglycoprotein distribution does not vary by sialic acid linkage (Extended Fig. 8.13).

The presence of sialoglycoprotein in fibrotic stroma and at the tumor edge suggests a causal link between fibrosis and sialoglycoprotein content in human breast tumors. To test this correlation, we queried breast tumor RNAseq data deposited in The Cancer Genome Atlas (TCGA) for evidence of any correlation of sialic acid biosynthesis gene programs with level of tumor fibrosis using a previously described fibrosis gene signature [169] (Fig. 3.3G). We found that the sialic acid donor biosynthesis gene program (GNE, NANS, NANP, CMAS, and SLC35A1) was

positively correlated with the fibrosis gene signature (r = 0.465, P = 3.51e-60). The sialic acid biosynthesis module used in Fig. 3.2C, which consisted of NANS and CMAS, was even more highly correlated with the fibrosis gene signature (r = 0.566, P = 3.01e-94). These data support a causal link between fibrosis and sialic acid donor biosynthesis in breast cancer.

3.2.4 Aggressive breast tumor subtypes feature elevated infiltration of SIGLEC7, SIGLEC9, and SIGLEC10-positive myeloid cells

We next explored potential links between the increased sialoglycoprotein content we observed in the high fibrosis regions of the tumor stroma as compared to the tumor invasive edge to markers of immune modulation. We focused on tumor-infiltrating Siglec-positive cells which have been implicated in immune inhibition [162]. Human Siglecs are a family of 14 receptors that are primarily expressed on immune cells, bind to sialoglycoprotein ligands, and have activating and/or inhibiting signal transduction functions [170]. In breast cancer, inflammation and macrophage infiltration correlate positively with tumor aggression and with the more aggressive breast cancer histophenotypes [8]. To further assign the cell types that express SIGLEC genes, we applied the human breast cancer scRNAseq dataset [165] analyzed in Fig. 3.2 to quantify SIGLEC expression. We focus our analysis here on SIGLEC7, SIGLEC9, and SIGLEC10, which have the greatest evidence of pro-tumor functions in breast cancer [154], [156], [159], [161], [170], [171], [172]. After first confirming that SIGLEC expression is found primarily in immune cell types we thereafter extracted the data on the immune cells for further analysis (Extended Fig. 8.14). We also performed the same analysis on the normal breast samples, and similarly found SIGLEC expression primarily in immune cells (Extended Fig. 8.15). We assigned cell types to each cluster based on marker genes (Figs. S7-S8). Analysis revealed that myeloid cells were the predominant cell type with expression of SIGLEC7, SIGLEC9, and SIGLEC10 in the human breast tumors (Extended Fig. 8.14). In normal breast tissues, we did not observe any SIGLEC7 expression, and identified myelomonocytic cells had the highest expression of SIGLEC9 and SIGLEC10 (Extended Fig. 8.15), although a lower percentage of cells from this cluster were positive compared to the myeloid cell cluster in

the tumor samples. We continued our analysis of SIGLEC expression within the extracted immune cells to further characterize SIGLEC-positive immune cells. We extracted and reclustered the immune cells from all tumor samples (Fig. 3.4A and Extended Fig. 8.14) and found that SIGLEC7, SIGLEC9, and SIGLEC10 expression was highest in the myelomonocytic and macrophage cells in tumors (Fig. 3.4B). In normal breast tissue, we failed to observe SIGLEC7 expression in any of the immune cell types, and discerned lower expression of SIGLEC9 and SIGLEC10 within the myeloid population relative to breast tumors (Extended Fig. 8.15). Recently, Siglec-15 has also been shown to have pro-tumor functions [160]. We observed high SIGLEC15 expression in the macrophage cluster, but not the myelomonocytic cluster.

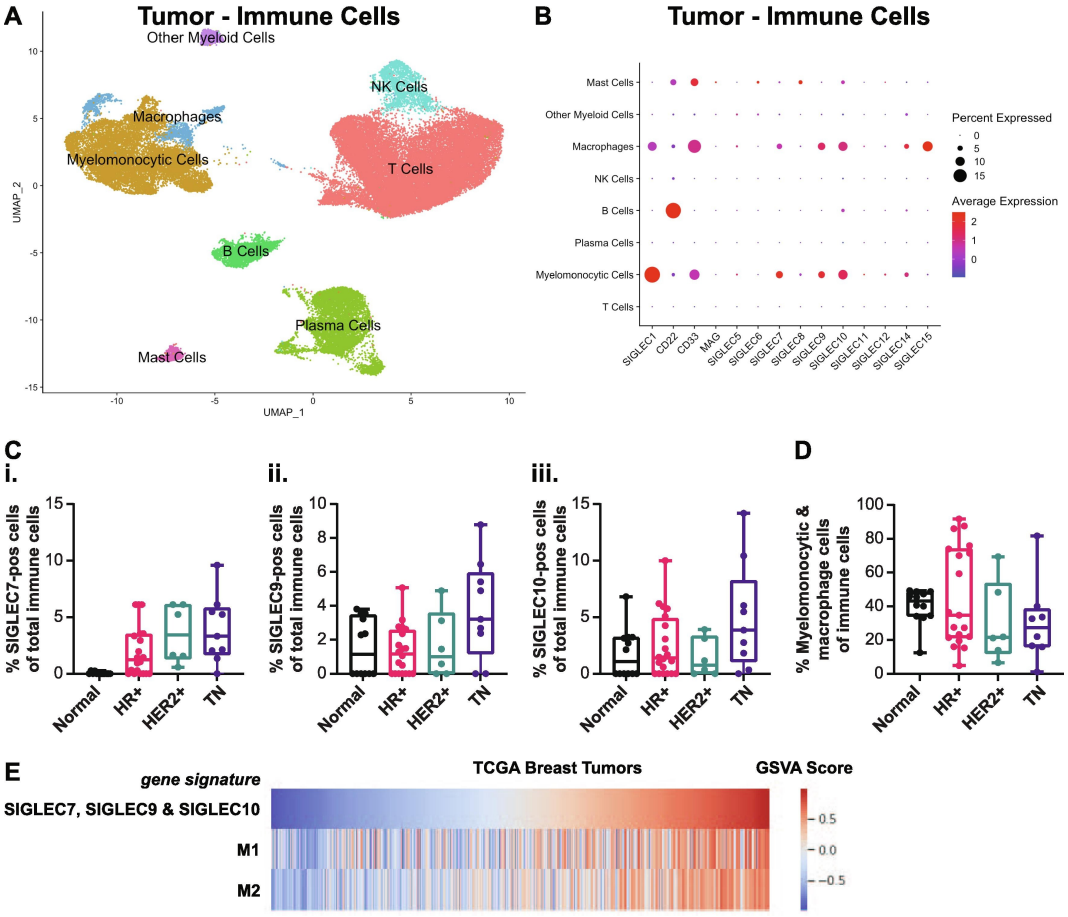

Figure 3.4: SIGLEC7, SIGLEC9 and SIGLEC10-positive myeloid infiltration is increased in breast tumors and correlates with aggression.[1]

[1]This figure was generated by co-authors. I analyzed the TCGA data and produced panel (E).

A. UMAP projection of immune cells from scRNAseq data of 34 breast tumors [95]. B. Dot plot of SIGLEC expression in immune cell clusters in breast tumors. C. Quantification of i. SIGLEC7, ii. SIGLEC9, and iii. SIGLEC10-positive inflammation as a percentage of total inflammation in normal breast and breast cancer subtypes. D. Quantification of myeloid infiltration as a percentage of total inflammation in normal breast and breast cancer subtypes. E. Heatmap showing the expression of gene signatures in RNAseq data from breast tumors from TCGA. Patients were ordered by the immunosuppressive Siglec signature.

The percentage of SIGLEC7-, SIGLEC9-, and SIGLEC10-positive cells of all immune cells increased with subtype aggression (Fig. 3.4C). Importantly, SIGLEC7 expression was not observed in normal human breast tissue, indicating that SIGLEC7-positive cells may be a feature of human breast cancer. The increased infiltration of SIGLEC7-, SIGLEC9-, and SIGLEC10-positive myeloid cells was not simply due to increased myeloid inflammation. The immune infiltration and myeloid infiltration as a percentage of total cells increased with breast cancer aggression subtype (Extended Fig. 8.16), which we and others have previously reported [8]. However, the amount of infiltrating myeloid cells as a percentage of infiltrating immune cells did not vary by subtype in this dataset (Fig. 3.4D). We interpreted this to mean that the infiltrating myeloid cells in the more aggressive breast cancer subtype likely have increased SIGLEC7, SIGLEC9, and SIGLEC10 expression, relative to the myeloid cells in the less aggressive breast cancer subtype and to normal human breast tissue.

Prior work showed Siglec-7, Siglec-9, and Siglec-10 have immunosuppressive and pro-tumor functions using a functional-based approach [154], [156], [159], [161], [170], [171], [172]. Here, we sought to explore links between these Siglecs and an immunosuppressive phenotype using transcriptomic data. As illustrated in Fig. 3.3G, we queried breast tumor RNAseq data deposited in TCGA for evidence of a correlation between an immunosuppressive Siglec gene signature, consisting of SIGLEC7, SIGLEC9, and SIGLEC10, with previously described M1 (anti-tumor) and M2 (pro-tumor) macrophage gene signatures [169] (Fig. 3.4E). Macrophages are phenotypically plastic, and anti-tumor and pro-tumor macrophage classifications represent phenotypes of a spectrum of states [173], [174]. Although the immunosuppressive Siglec gene signature correlated positively with both the anti-tumor and pro-tumor gene signatures, we noted a stronger

correlation with the pro-tumor gene signature (r = 0.758, P = 2.27e-206) as compared to the anti-tumor gene signature (r = 0.563, P = 3.68e-93). These data further support the classification of SIGLEC7, SIGLEC9, and SIGLEC10-positive myeloid cells as immunosuppressive.

3.2.5 Association of Siglec ligands with regions of fibrosis

While Siglec receptors bind to sialylated ligands, they do possess unique substrate specificities [159], [171], [175], [176]. To better understand the location and quantify immunoinhibitory Siglec ligands within human breast tumors, we stained our cohort of breast cancer tissue with Siglec receptor-Fc fusion proteins (Fig. 3.5A). Siglec ligands stained positively in all breast cancer tissues. However, there was significant heterogeneity in Siglec ligand-positive area and intensity. As with the plant lectins, we observed higher staining intensity in stromal regions within the tumor tissue as compared to the cancer cell region. However, unlike the relatively uniform staining of SNA and MAL-II lectin in stromal regions, Siglec ligand staining was heterogeneous in these regions. These data demonstrate the different specificities between Siglecs and plant lectins.

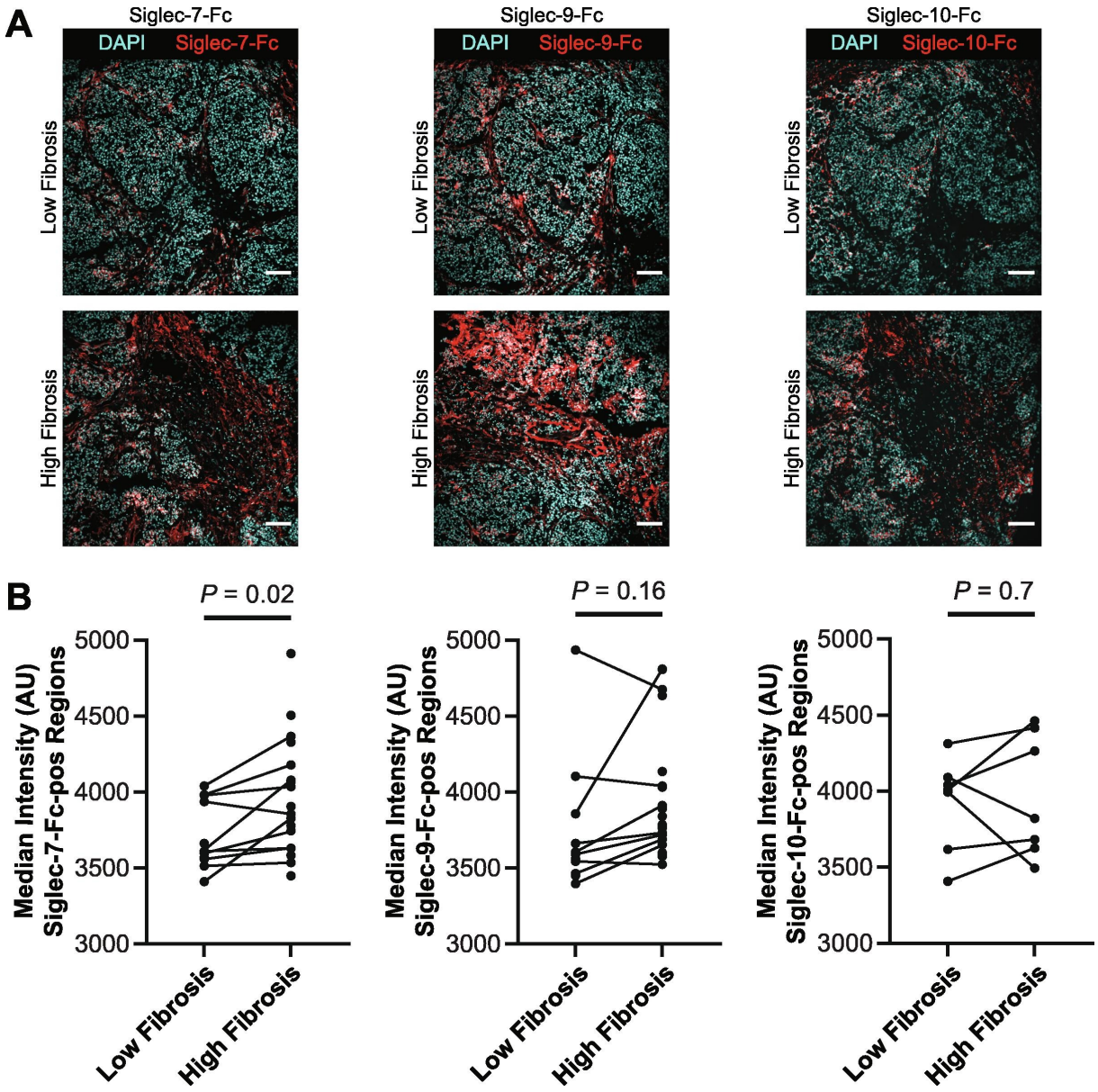

Figure 3.5: Association of Siglec ligands with fibrosis.[1]

A. Representative images from a TN tumor of Siglec-7, Siglec-9, and Siglec-10 staining in low and high fibrosis regions. Scale bar is 100 micron. B. Quantification of median intensity within Siglec ligand-positive regions for Siglec-7-Fc, Siglec-9-Fc, and Siglec-10-Fc.

To clarify the relationship between Siglec ligand content and local fibrosis, we calculated the fraction of area with Siglec ligand-positive staining. There did not appear to be a difference in Siglec ligand-positive area between high and low fibrosis regions for the three Siglec-Fc reagents tested (Extended Fig. 8.17). However, we did quantify higher intensity of Siglec ligand-positivity

[1]This figure was generated by co-authors.

for Siglec-7 ligands in regions within the breast cancer tissue that had high levels of fibrosis (Fig. 3.5B). We similarly observed increased Siglec-9 ligand levels in regions within the breast tumors that had high amounts of fibrosis. However, we failed to observe any association between levels of Siglec-10 ligand and tumor tissue fibrosis. These data suggest there may be a relationship between the level of the ligands Siglec-7 and Siglec-9 and tissue fibrosis in human breast cancer.

3.3 Discussion

Our data establish an association between breast cancer fibrosis, sialoglycoprotein content and human breast cancer aggression as indicated by the HER2+ and TN subtypes. Increased sialylation is found in multiple tumor types, including breast, and increases metastatic potential in multiple mouse tumor models [162]. While recent studies have focused on the functional consequences of hypersialylation in tumors, less is known about the causes of increased sialylation. Our study provides evidence there may be a functional link between cancer fibrosis and the increased sialylation found in tumors. We found greater acidic glycoprotein content in high fibrosis regions and in more aggressive breast tumor subtypes. We also found increased sialylation in high fibrosis regions for HER2+ and TN tumors. Finally, we observed greater Siglec-7 ligand levels in high fibrosis regions.

We found that cancer cells are the main producers of sialoglycoprotein biosynthesis within tumors. In addition, cancer cells in TN tumors have elevated expression of the sialoglycoprotein biosynthesis genes ST3GAL4, NANS, and CMAS. Although we found increased expression of sialoglycoprotein biosynthesis genes in HER2+ and TN tumors, relative to ER+ tumors, we still observed high levels of tumor sialylation in ER+ tumors. One explanation for this observation is that the greater biosynthetic flux of sialoglycoproteins in TN tumors could be matched by greater consumption fluxes, such as greater recycling of surface sialoglycoproteins and greater cellular uptake of shed sialoglycoproteins.

While recent studies have elucidated the immune suppressive role of glycocalyx sialoglycans at immunological synapses, our data showed greater sialoglycans abundance in the stroma.

Given the greater sialylation of the stroma, we propose that cancer cells secrete and shed sialoglycoproteins that become physiochemically adsorbed to the extracellular matrix in the tumor microenvironment. Soluble shed sialoglycoproteins can serve as Siglec ligands that drive monocyte differentiation to immune suppressive macrophages [161], which suggests that stromal sialoglycoproteins could serve as Siglec ligands and contribute to an immunosuppressive phenotype in the tumor microenvironment. Greater fibrosis involves increased collagen accumulation [163] and could provide for more binding sites for sialoglycoprotiens. More work is needed to attribute cancer cells as the source of stromal sialoglyoproteins and to elucidate the functional consequences of stromal sialylation in cancer.

Sialoglycoproteins suppress cytotoxic immune responses in tumors [172]. High expression of sialyl-Tn antigen is correlated with lower tumor infiltration of CD8+ T cells in human endometrial cancer [177], and therapeutic desialylation of EMT6 xenografts increases tumor infiltration of GZMB+ CD8+ cytotoxic T cells [178]. Mechanistically, immune inhibition by Siglec receptors requires the presence of both ligands and receptor-positive cells. We found that TN tumors have increased infiltration of SIGLEC7-, SIGLEC9-, and SIGLEC10-positive myeloid cells, which have been shown previously to have immunosuppressive functions [157], [158], [159], [161], [178]. Interesting, these TN tumors also feature greater synthesis of sialoglycoproteins, which could serve as Siglec ligands. Thus, among breast tumor subtypes, TN tumors may be best targeted with inhibitors of the sialic acid-Siglec axis.

3.4 Contribution

I contributed to the bioinformatics portion of this project through analysis of the TCGA dataset. This analysis established the correlation between expression of sialic acid genes and a fibrosis transcriptional program. Moreover, this identified that the expression of SIGLECs elevated in more aggressive breast cancer subtypes correlates with macrophage-mediated immunosuppression. I generated panels where specified, wrote the associated methods, and edited the manuscript.

4 Chapter 4: ECM Dimensionality Influences Endoplasmic Reticulum Stress and Protein Trafficking

This chapter is a reprint of the peer-reviewed article titled "Extracellular matrix dimensionality modulates endoplasmic reticulum function to regulate organoid phenotype by tuning actin tension" by FuiBoon Kai, Guanqing Ou, Richard W. Tourdot, Connor Stashko, Guido Gaietta, Mark F. Swift, Niels Volkmann, Alexandra F. Long, Yulong Han, Hector H. Huang, Jason J. Northey, Andrew M. Leidal, Virgile Viasnoff, David M. Bryant, Wei Guo, Arun P. Wiita, Ming Guo, Sophie Dumont, Dorit Hanein, Ravi Radhakrishnan, Valerie M. Weaver published in The EMBO Journal (2022).

4.1 Introduction

Human tissue fragments cultured within (3D) a reconstituted basement membrane (rBM; which resembles the laminin/collagen IV-rich basement membrane found in tissues) as patient-derived organoids (PDOs) retain many of the differentiated features of their native tissue including their apical–basal polarity, vectorial protein secretion, and resistance to exogenous stress ([179], [180], [181]). Similarly, recapitulation of the tissue-like differentiated spheroid phenotype of primary and immortalized cells and the retention of their long-term viability and stress resilience are supported by culturing the cells within rBM ([182]; [179]). It remains unclear why culturing cells within (3D) as opposed to on top (2D) of rBM directs tissue-specific structure and homeostasis.

Primary and immortalized mammary epithelial cells (MECs) embedded within rBM (3D) assemble into growth-arrested, apoptosis-resistant spheroids, secrete, and assemble an endogenous BM and upon stimulation express tissue-specific differentiated gene expression ([182]). The tissue-specific differentiation of MECs depends upon the engagement of laminin receptors and a rounded cell phenotype that direct the signaling required to induce differentiated gene expression ([183]). A compliant extracellular matrix (ECM) supports MEC rounding and stabilizes the cell–cell adhesions required to build and maintain the differentiated spheroid structure ([184]; [132]). Nev-

ertheless, cells cultured on top of rBM (2D) do not establish a stress resilient phenotype and do not assemble into polarized spheroids surrounded by their own assembled endogenous basement membrane. Why deposition and assembly of a polarized basement membrane and acquisition of long-term viability and treatment resistance in MEC spheroids require interaction with rBM in 3D is poorly understood.

Organelles are subcellular structures that execute specialized cellular functions such as energy production, protein secretion, and the recycling and degradation required for cell and tissue homeostasis. The endoplasmic reticulum (ER), in particular, is a multifunctional organelle essential for protein folding that is critical for protein secretion and for the stress regulation required to support normal cell and tissue function. The ER is especially important for intracellular calcium storage, synthesis and folding of nascent transmembrane and secretory proteins, and for lipid metabolism. ER function is compromised when ER calcium levels are depleted, resulting in protein misfolding, induction of ER stress and activation of an ER stress response ([185]). Not surprisingly, cells have a surveillance system to monitor and ensure efficient ER activity. Upon ER calcium depletion, the ER rapidly establishes ER-plasma membrane contact sites that activate store-operated calcium entry (SOCE) to replenish intracellular calcium storage that restore ER function ([186]). Accordingly, the ER plays a critical role in maintaining cell and tissue homeostasis and operates key mechanisms that facilitate this function. Given the profound impact of the ER on protein secretion and cell stress regulation, we asked whether differential engagement of the ECM, in either 2D or 3D, could regulate protein secretion and cellular stress resilience by altering organelle homeostasis. We specifically asked whether basement membrane deposition and assembly and stress resilience in MECs interacting with rBM in 2D was compromised through perturbations in ER structure and/or function, and, if so how?

4.2 Results

4.2.1 Ligation of rBM in 3D modulates expression of molecules implicated in endoplasmic reticulum function

In marked contrast to MECs grown as a monolayer on top of a thin layer of a laminin-rich rBM (2D), spontaneously immortalized nonmalignant MCF10A and HMT-3522S-1 MECs grown within rBM (3D) generate growth-arrested spheroids ([187]). Growth-arrested polarized HMT-3522S-1 MEC spheroids embedded within rBM (3D) increase the expression of genes implicated in collagen-containing ECM proteins and plasma membrane surface protein localization (Fig. 4.1A and B, and Extended Fig. 8.18A; Dataset EV1 and EV2). The spheroids generated by both of these MECs generated within rBM also acquire apical–basal polarity (shown is staining in MCF10A MECs for cell–cell localized basal-lateral β4 integrin; Fig. 4.1C; top panels; and apical-lateral E-cadherin ([188])) and demonstrate vectorial secretion of proteins. This includes the basal deposition and assembly of an endogenous basement membrane, as indicated by laminin-5 (Fig. 4.1C; bottom panels), and upon stimulation with lactogenic hormones, the apical secretion of whey acidic protein and β-casein, as has been previously reported ([189]; [182]; [180]). The HMT-3522S-1 polarized MEC spheroids generated within rBM are also highly resistant to exogenous stresses including to treatment with agents such as Paclitaxel, TRAIL, and Doxorubicin, as well as gamma radiation exposure, when compared with the same MECs interacting with rBM in only two dimensions (2D; Fig. 4.1D). Indeed, we found that the HMT-3522 S-1 MECs interacting with rBM in 2D exhibit an ER stress phenotype when treated with agents such as TRAIL, as illustrated by enhanced expression of genes reflecting the ER chaperone complex, response to ER stress and PERK-mediated unfolded protein response (UPR) (Fig. 4.1E).

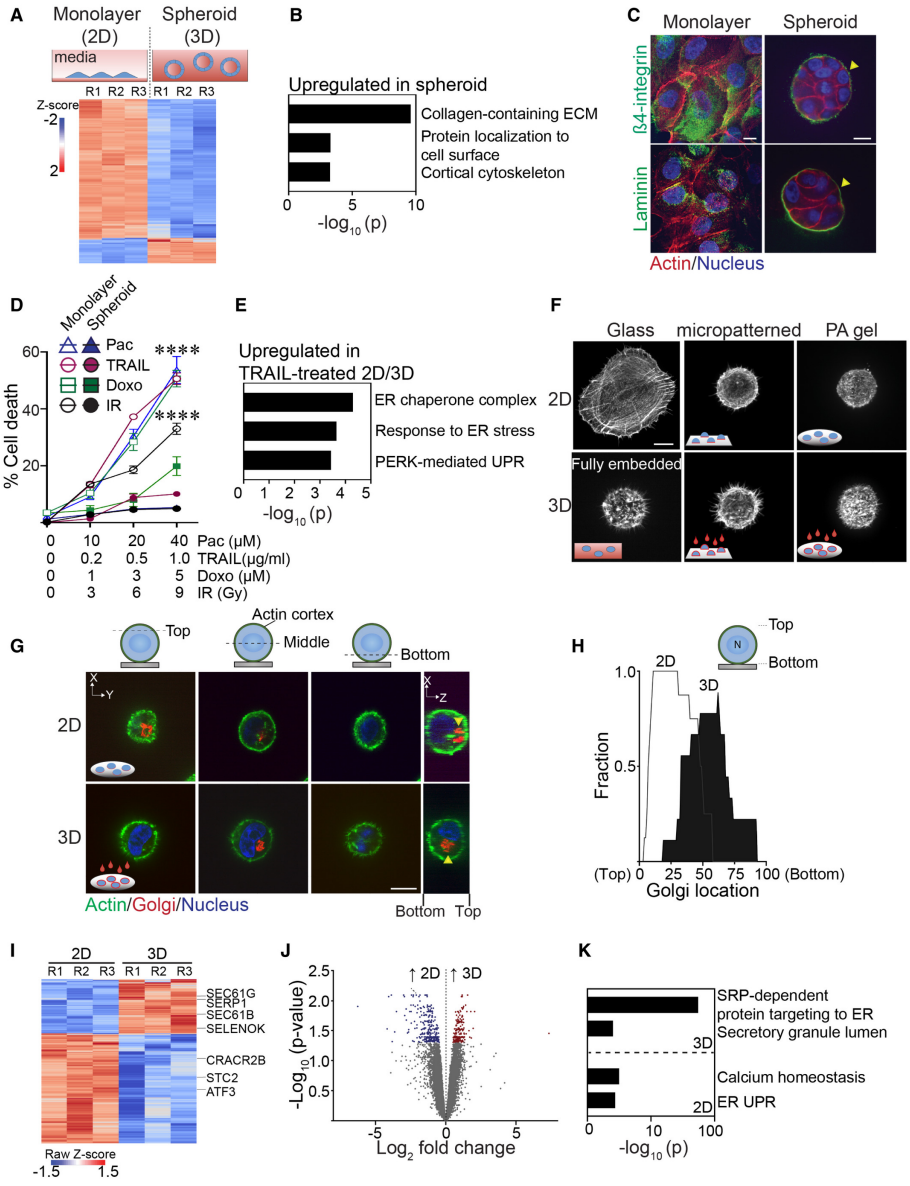

Figure 4.1: Ligation of rBM in 2D versus 3D regulates expression of molecules implicated in ER function[1]

A. Schematic of experimental setup depicting MECs grown as monolayers on a rigid rBM (two-dimensional culture model, 2D; top left) or within a compliant rBM to generate multicellular spheroid structures with apical-basal polarity (three-dimensional culture model, 3D) top right). Heatmap of microarray analysis of gene expression in HMT-3522 S-1 MECs cultured either as a 2D monolayer or as spheroids (Bottom). Expression of the top 200 differentially expressed genes between the two experimental conditions (n = 3 independent biological replicates; R = replicate). B. Gene Ontology (GO) analysis of genes upregulated in HMT-3522 S-1 spheroids. C. Samples were stained with antibodies for β4-integrin or laminin (green; yellow arrows). The actin and nucleus were counterstained with phalloidin (red) and DAPI (blue), respectively. Scale bar, 10 μm. D.

[1]This figure was generated by co-authors. I analyzed the RNAseq and microarray data described and generated panels (A), (B), (E), (I), (J), and (K).

HMT-3522 S-1 MECs plated as monolayers on a rigid rBM (2D) or as spheroids within rBM (3D) were treated with increasing doses of Paclitaxel (Pac), TRAIL, Doxorubicin (Doxo) and irradiation (IR). Percent cell death was quantified by immunofluorescence as percentage of cells stained positive for cleaved caspase-3 at 48 h posttreatment (mean ± SEM; n = 3 independent biological replicates). ****P ¡ 0.0001 (Student's t-test). E. Gene ontology (GO) analysis of genes significantly upregulated in TRAIL-treated HMT-3522 S-1 MEC monolayers (2D) relative to TRAIL-treated spheroid cultures (3D). F. Representative immunofluorescence microscopy images of MCF10A MECs plated in the indicated conditions for 18 h and stained with phalloidin to reveal F-actin organization. Cells were plated as single cells on rigid glass coverslips (2D glass; top left) or fully embedded within rBM (3D fully embedded; bottom left). Cell spreading was inhibited by plating cells on either laminin-111 conjugated, 10-μm micropatterned glass (2D/micropatterned, rigid substrate; top middle) or on compliant 75 Pa rBM-laminated polyacrylamide (PA) gels (2D/PA, soft substrate; top right). The single 2D cells were overlaid with either purified laminin-111 (bottom middle) or rBM (bottom right) to create a 3D ECM microenvironment. Images show maximum intensity z-projections of confocal stacks for F-actin phalloidin staining. Scale bar, 10 μm. G. Representative immunofluorescence microscopy images of MCF10A MECs stably expressing recombinant mCherry-tagged golgi marker (mCherry-GalT; red; yellow arrows) ligated with rBM in either 2D or 3D for 18 h. The actin cortex and nucleus were counterstained with phalloidin (green) and DAPI (blue), respectively. Images show the cross-sectional view of each cell compartment (dashed lines; xy plane) and side view of confocal stacks (xz plane) in individual MCF10A MECs. Scale bar, 10 μm. H. Golgi staining was assessed within non-spread MCF10A MECs ligated with rBM in 2D and 3D for 18 h and values were plotted as a function of subcellular localization (2D, n = 8; 3D, n = 9 cells from two independent experiments). I. Heatmap of RNA-seq experiment from MCF10A MECs ligated with rBM in 2D and 3D 12 h post-plating. Data show the expression of the top 200 genes that are differentially expressed between the 2D and 3D rBM conditions. (n = 3 independent biological replicates). J. Volcano plot of differentially expressed genes from RNA-seq of MCF10A MECs ligated to rBM in 2D and 3D harvested 12 h post-plating. Significantly downregulated genes (blue; log 2 $>$ 0.5) and upregulated genes (red; log 2 $>$ 0.5) are highlighted (n = 3 independent biological replicates). K. GO analysis of genes significantly upregulated in non-spread MCF10A MECs ligated to rBM in 3D relative to those interacting with a rBM in 2D.

To clarify whether the dimensionality of ECM ligation modulates spheroid phenotype by altering the ER, we studied the impact of engaging MCF10A MECs with laminin-111 or rBM in either 2D or 3D on ER structure and function. To avoid potential contributions induced by cell–cell junctions and multicellularity, we conducted the studies using single cells. To recapitulate the "non-spread—rounded cell" spheroid phenotype exhibited by MECs embedded within rBM, we restricted cell spreading using either micropatterned borosilicate glass (diameter 10 μm) or by plating the cells on top of a compliant (75 Pascal) polyacrylamide (PA) gel (which fails to support cell spreading) ([132]). Cell ligation in 2D was achieved by plating the cells on top of

laminin-111-conjugated borosilicate glass or on top of a laminin-111 or a rBM-laminated PA gel (Fig. 4.1F; compare 2D nonpatterned glass to micropatterned glass and PA gels). The third ECM dimension was induced by overlaying the MECs with either purified laminin-111 or a dilute solution of rBM (1:100; Fig. 4.1F; compare 2D to 3D). We evaluated the impact of ECM compliance on cell phenotype by comparing actin organization in the non-spread MECs plated on the rigid laminin-111-conjugated micropatterned glass to the cells that were plated on top of the compliant PA gels laminated with laminin-111 or rBM to the same cells overlaid with laminin-111 or diluted rBM (3D). We noted that the rounded single cells consistently reconstituted an actin phenotype reminiscent to that demonstrated by single MECs fully embedded within rBM, irrespective of whether they were plated on top of a compliant laminin-111 or rBM-laminated PA gels or on top of a micropatterned laminin-conjugated rigid glass substrate (Fig. 4.1F). The impact of ECM dimensionality was monitored by observing the loss of forced apical–basal polarity in the MECs plated on the rBM PA gels overlaid with rBM (3D). The non-polarized phenotype was indicated by the absence of Golgi apparatus orientation in the MECs ligated with the rBM in 3D, and the uniform apical localization of this organelle in the MECs plated on top of rBM-laminated PA gels (2D; Fig. 4.1G and H).

Global transcriptome analysis revealed that within 12 h, of 489 differentially expressed genes, 201 genes were significantly induced, and 288 genes were significantly repressed in the single non-spread MECs interacting with rBM in 3D, as compared with the single non-spread MECs interacting with rBM in 2D (Fig. 4.1I, J, and Extended Fig. 8.18B and Dataset EV3). Gene set enrichment analysis revealed that the MECs engaging rBM in 3D, that exhibited cortically localized actin, were enriched for genes implicated in the regulation of protein insertion into the ER (e.g., SEC61B and SEC61G) as well as protein secretion (Fig. 4.1I and K and Dataset EV4). Those MECs engaging rBM in 3D also upregulated genes previously shown to protect cells from ER stress including SERP1 and SELENOK ([190]; [191]). By contrast, the MECs encountering rBM in 2D were enriched for genes implicated in calcium homeostasis as well as those activated by ER UPR (e.g., CRACR2b, ATF3, and STC2) (Fig. 4.1I and K and Dataset EV4) ([192]; [193];

[194]). The findings suggest that how a cell ligates its ECM, whether in 2D or in 3D, influences its ER-dependent phenotype.

4.2.2 Ligation of rBM in 3D alters ER function

We next explored whether cell ligation to its ECM in 2D versus 3D influences ER function. Building upon our GO analysis (Fig. 4.1K), we monitored secretory protein trafficking to examine the impact of ligating rBM in 2D versus 3D on ER function. RT-PCR analysis confirmed that MECs interacting with rBM in 3D had higher levels of SEC61B, a subunit of the channel-forming translocon complex responsible for targeting proteins to the secretory pathway by directing their insertion either into the ER membrane or lumen (Fig. 4.2A). Temperature-induced pulse chase monitoring for secretory protein trafficking further revealed a significant increase in plasma membrane-associated VSVG-ts045 in MECs interacting with rBM in 3D, consistent with efficient secretory protein trafficking (Fig. 4.2B and C).

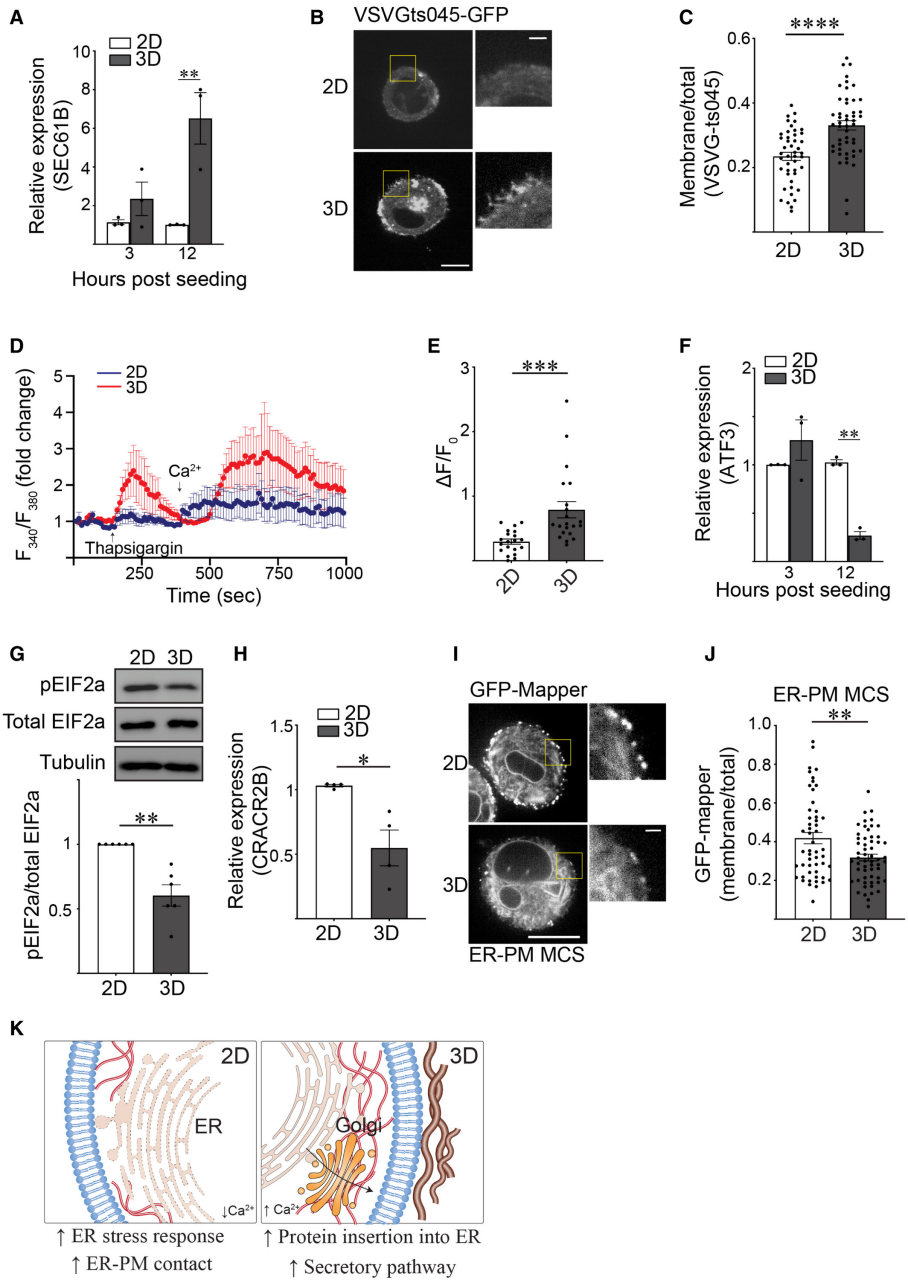

Figure 4.2: Ligation of rBM in 3D alters ER function[1]

A. Bar graph showing qPCR quantification of SEC61B level in MCF10A MECs ligated with rBM in 2D and 3D 12 h post-plating (mean ± SEM; n = 3 independent biological replicates). Statistical analysis by one-way ANOVA followed by Uncorrected Fisher's LSD, **P = 0.0022. B. MCF10A MECs expressing VSVGts045-EGFP were ligated to rBM in 2D or 3D and incubated at 40°C for 16 h to trap VSVGts045-EGFP protein in the ER. Cells were shifted to 32°C for 2 h to release VSVGts045-EGFP into the secretory pathway. Representative fluorescence microscopy images of MECs expressing VSVGts045-EGFP 2 h post incubation at 32°C. Scale bar (whole cell), 10 μm; Scale bar (magnified), 2 μm. C. Scatter plot of the secretory trafficking efficiency of VSVGts045-

[1]This figure was generated by co-authors. My analysis identified the regulated pathways shown in (K).

EGFP based on the fluorescence of VSVGts045 at the plasma membrane versus total fluorescence measured in cells from Panel B (mean ± SEM; 2D, n = 45; 3D, n = 49 cells from three independent experiments). ****P ¡ 0.0001 (Student's t test). D. Representative line graph showing the changes in cytosolic [Ca2+] levels of MCF10A MECs under different treatment. Fura-2-loaded MECs ligated to 2D (blue) or 3D rBM (red) were pre-incubated with EGTA to chelate extracellular Ca2+ in the bath solution, challenged with 2 μM thapsigargin to induce ER Ca2+ release, and replenished with 4 mM Ca2+ in bath solution at the indicated time. F340/F380 values for each cell were quantified over the course of imaging (mean ± SD; 2D, n = 7; 3D, n = 7 cells from one experiment). E. Quantification of the amplitude of the Ca2+ response induced by thapsigargin (δF=F-F0), where F0 is the basal fluorescence before thapsigargin treatment (mean ± SEM (2D, n = 20; 3D, n = 21 cells from three independent experiments). ***P = 0.0007 (Student's t test). F. Bar graph showing qPCR of the relative level of ATF3 mRNA in MCF10A MECs ligated with rBM in 2D and 3D 12 h post-plating (mean ± SEM; n = 3 independent biological replicates). Statistical analysis by one-way ANOVA followed by Uncorrected Fisher's LSD, **P = 0.0037. G. Representative immunoblots of phosphorylated EIF2a (pEIF2a), total EIF2a and alpha-tubulin in cell lysate from MCF10A MECs ligated to a rBM in 2D or 3D and corresponding quantification data (mean ± SEM; n = 6 independent biological replicates). Statistical analysis by Student's t-test, **P = 0.0049. H. Bar graph of qPCR data measuring the relative levels of CRACR2B mRNA in MCF10A MECs ligated with rBM in 2D and 3D 12 h post-plating (mean ± SEM; n = 4 independent biological replicates). *P = 0.0371 (Student's t-test). I. Representative fluorescence microscopy images of the ER-plasma membrane contact site reporter GFP-MAPPER in MCF10A MECs ligated with rBM in 2D or 3D 18 h post plating. Scale bar (whole cell), 10 μm; Scale bar (magnified), 1 μm. J. Graph of the levels of GFP-MAPPER at the plasma membrane relative total cellular GFP-MAPPER fluorescence in MCF10A MECs ligated with rBM in 2D or 3D in Panel I (mean ± SEM; 2D, n = 52; 3D, n = 57 cells from three independent experiments). **P = 0.0032 (Student's t test). K. Model of how ECM dimensionality affects ER structure/function.

GO analysis indicated MECs ligating rBM in 2D upregulated genes implicated in calcium homeostasis and an ER stress response (Fig. 4.1K). Given ER calcium depletion can activate ER stress, we investigated whether ligating MECs in 2D versus 3D differentially regulated intracellular ER Ca2+. ER calcium dynamics were assessed in FURA-2-loaded MECs interacting with rBM in 2D and 3D and impact on ER Ca2+ release was examined following thapsigargin treatment. Compared to MECs ligating rBM in 3D, FURA analysis revealed that the MECs ligating rBM in 2D had a relatively low ER calcium content, indicated by a truncated amplitude of intracellular calcium release following thapsigargin treatment (smaller δF/F0 in 2D condition) (Fig. 4.2D and E). Functionality of this phenotype was assessed by examining SOCE which becomes activated following thapsigargin-induced ER Ca2+ depletion. We assessed cellular SOCE activity by adding back Ca2+ to the culture medium and monitoring for an increase in intracellular Ca2+ levels.

Measurements revealed lower ER Ca2+ storage content and reduced SOCE activity in the MECs ligating rBM in 2D, consistent with compromised ER homeostasis (Fig. 4.2D).

Perturbed calcium homeostasis can lead to the accumulation of unfolded protein in the ER that in turn can activate an ER stress response ([195]). RNA-seq analysis revealed that ATF3, which is part of the PERK-pEIF2a-ATF4-ATF3 stress signaling axis, was one of the top candidate genes significantly upregulated in the MECs ligating rBM in 2D (Dataset EV3). Quantitative analysis of RNA demonstrated that ATF3 levels were indeed higher in the MECs interacting with rBM in 2D (Fig. 4.2F). The effect on the ER stress phenotype was further verified by detecting higher levels of phosphorylated EIF2a protein in the MECs interacting with rBM in 2D (Fig. 4.2G).

In response to calcium depletion, cells activate SOCE at ER-PM contact sites to replenish their intracellular calcium stores ([196]). RNA-seq analysis revealed that MECs interacting with rBM in 2D as compared with 3D, expressed higher levels of CRACR2B, which regulates Ca2+ release-activated Ca2+ channels that mediate SOCE (Dataset EV3; validated in Fig. 4.2H). Upon further investigations, we observed that despite a compromised SOCE, when we used the GFP-MAPPER marker to report ER-PM junctions, we quantified a significant increase in the number of ER-PM sites throughout the cells ligating rBM in 2D (Fig. 4.2I and J, and Extended Fig. 8.19). The findings are consistent with the possibility that the increase ER-PM contact sites comprise an adaptive feedback mechanism that compensates for the reduced cellular ER Ca2+ content found in MECs interacting with rBM in 2D. The data indicate ECM-MEC ligation configuration can influence cellular ER structure and function (Fig. 4.2K).

4.2.3 Ligation of rBM in 3D modulates filamin to alter ER function

ER-PM contact site assembly is mediated by interaction between the actin cross-linker filamin and the ER stress sensor PERK ([197]). We therefore assessed whether ligating rBM in 2D versus 3D influenced ER organization and function by modulating filamin levels and cellular distribution. Immunostaining revealed prominent cortically localized filamin aggregates in the MECs engaging rBM in 2D, whereas by contrast, filamin was diffusely localized throughout the

MECs interacting with rBM in 3D (Fig. 4.3A). Immunoblot analysis also revealed that filamin protein levels (but not another actin crosslinker such as actinin) were significantly lower in the MECs interacting with rBM in 3D (Fig. 4.3B). Consistent with a functional link between filamin and ER-PM junctions, the GFP-MAPPER reporter revealed that shRNA-mediated knockdown of filamin reduced the number of ER-PM junctions in the MECs interacting with rBM in 2D (Fig. 4.3C and D). Furthermore, depleting filamin in the MECs ligating rBM in 2D ameliorated ER stress signaling, as indicated by lower levels of phosphorylated EIF2a protein (Fig. 4.3E) and reduced expression of the stress regulator ATF3 (Fig. 4.3F). Conversely, overexpression of filamin in the MECs interacting with rBM increased their pEIF2a levels indicating the cells now exhibited ER-mediated cell stress (Fig. 4.3G). The findings indicate that the context of ECM engagement (2D versus 3D) influences filamin-ER interactions to regulate ER organization and function that in turn modulates cell phenotype (Fig. 4.3H).

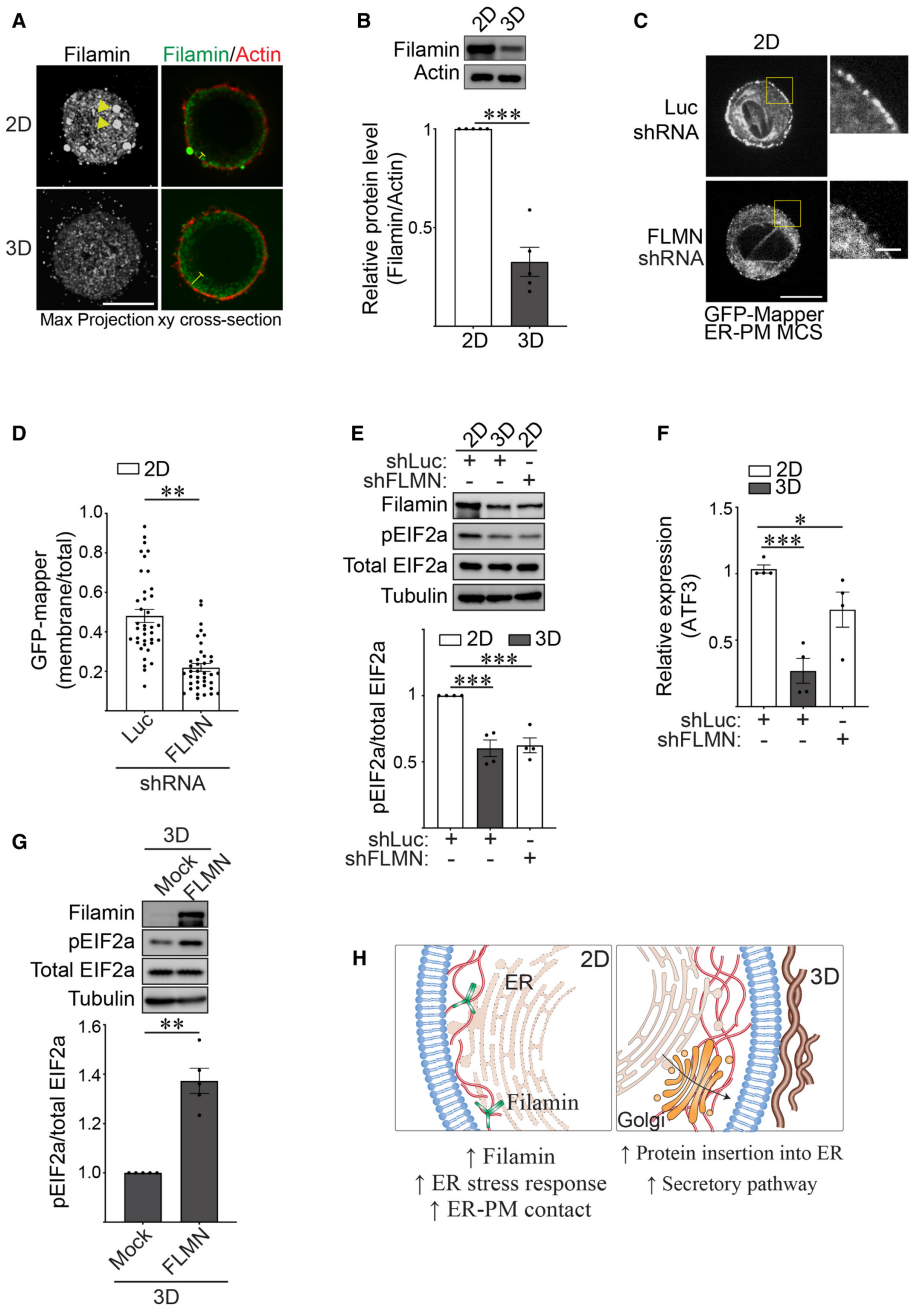

Figure 4.3: Ligation of rBM in 3D modulates filamin to alter ER function[1]

A. Representative immunofluorescence microscopy images of MCF10A MECs ligated with either a rBM in 2D or 3D for 18 h and stained with antibody targeting filamin (green). F-actin was counterstained with phalloidin (red). Images show maximum intensity z-projections of xy confocal stacks (left) and middle focal plane of confocal stacks from MECs (right). Yellow arrows indicate filamin aggregates in individual MECs ligated to rBM in 2D. Yellow blunt-end lines highlight the extent of filamin distribution away from the cell edge. Scale bar, 10 μm. B. The expression level of filamin in MCF10A MECs ligated to rBM in 2D and 3D for 18 h was assessed via immunoblot and

[1]This figure was generated by co-authors. My analysis identified the regulated pathways shown in (H).

quantified relative to actin loading control (mean ± SEM; n = 5 independent biological replicates). ***P = 0.0008 (Student's t-test). C. Representative fluorescence microscopy images of MCF10A MECs co-expressing the ER-plasma membrane contact site reporter GFP-MAPPER and shRNA targeting filamin (FLMN) or luciferase (Luc) ligated to rBM in 2D for 18 h. Scale bar (whole cell), 10 μm; Scale bar (magnified), 2 μm. D. Quantification of the levels of GFP-MAPPER at the plasma membrane versus total cellular fluorescence in MCF10A MECs stably expressing an shRNA targeting filamin (FLMN) or luciferase (Luc) ligated to rBM in 2D (mean ± SEM; 2D + shLuc, n = 38; 2D + shFLMN, n = 39 cells from three independent experiments). **P ¡ 0.0021 (Student's t-test). E. Representative immunoblots of filamin, phosphorylated EIF2a (pEIF2a), total EIF2a and alpha-tubulin in cell lysate from MCF10A MECs that express shRNA targeting filamin (shFLMN) or luciferase (shLuc) and ligated to a rBM in 2D or 3D for 18 h and corresponding quantification data (mean ± SEM; n = 4 independent biological replicates). Statistical analysis by one-way ANOVA followed by Uncorrected Fisher's LSD. 2D-shLuc versus 3D-shLuc, ***P = 0.0003. 2D-shLuc versus 2D-shFLMN, ***P = 0.0004. F. Bar graph of the relative levels of ATF3 mRNA as measured by qPCR in MCF10A MECs expressing shRNA targeting filamin (shFLMN) or luciferase (shLuc) and ligated with rBM in 2D or 3D for 18 h (mean ± SEM; n = 4 independent biological replicates). Statistical analysis by one-way ANOVA followed by Uncorrected Fisher's LSD. 2D-shLuc versus 3D-shLuc, ***P = 0.0005. 2D-shLuc versus 2D-shFLMN, *P = 0.0359. G. Representative immunoblots of filamin, phosphorylated EIF2a (pEIF2a), total EIF2a and alpha-tubulin in cell lysate from MCF10A MECs ligated to rBM in 3D and treated with ethanol (mock) or doxycycline (FLMN) for 18 h to induce filamin expression and corresponding quantification data (mean ± SEM; n = 5 independent biological replicates). **P = 0.0018 (Student's t-test). H. Model of how ECM dimensionality affects ER function via filamin.

4.2.4 Ligation of rBM in 3D reduces actin tension

Filamin is a mechanosensitive actin cross-linker ([198]). Given our findings that the dimensionality of ECM ligation by a cell influences the expression and spatial organization of filamin, we asked whether a cell interacting with ECM in 2D versus 3D exhibits differences in actin cytoskeletal tension. We used atomic force microscopy (AFM) to measure the tension of the actin cortex in MECs plated on top of laminin-111-coated micropatterned borosilicate glass (10 μm), and generated the third dimension of ECM binding using a dilute concentration of laminin-111. We chose this strategy to limit nonspecific binding and to prevent potential interference of measurements induced by overlay with a thick rBM. AFM force-distance curves confirmed that the laminin-111 overlay did not impair AFM indentation measurements (Extended Fig. 8.20A). AFM indentation revealed that the MECs engaging laminin in 2D had a significantly stiffer actin cortex than MECs overlaid with laminin-111 to generate the third dimension of laminin-111 engagement

(Fig. 4.4A; compare 2D to 3D). Treatment of the MECs with blebbistatin confirmed that actin cortex stiffness was due to myosin-II activity (compare 2D to 3D with and without blebbistatin treatment). Furthermore, inducing ROCK activity to increase actomyosin tension restored cortical actin tension in the MECs engaging ECM in 3D toward that measured in the MECs engaging rBM ECM in 2D (Fig. 4.4A; compare 2D to 3D + ROCK; Extended Fig. 8.20B). Consistent with our earlier observations, increasing filamin prevented the drop in cortical actin stiffness induced in the MECs engaging rBM ECM in 3D (Fig. 4.4A; compare 3D to 3D + FLMN). Traction force microscopy (TFM) measurements, that quantify actomyosin contractility, revealed that MECs ligating rBM ECM in 3D exerted lower traction stress against the basal ECM substrate, likely through a redistribution of traction forces around the cell cortex (Fig. 4.4B and Extended Fig. 8.20C). Moreover, inhibiting myosin-II activity, by treating the cells with blebbistatin, uniformly abolished traction stresses in the MECs regardless of whether the cells were engaging rBM in 2D or 3D (Fig. 4.4B). To assess whether cortical actin tension associated with altered cellular rheology, we used optical tweezers to measure the cytoplasmic modulus in the MECs ([199]; [200]). Measurements revealed that the MECs engaging the rBM ECM in 3D had a lower cytoplasmic modulus as compared with the MECs engaging rBM in 2D (Fig. 4.4C).

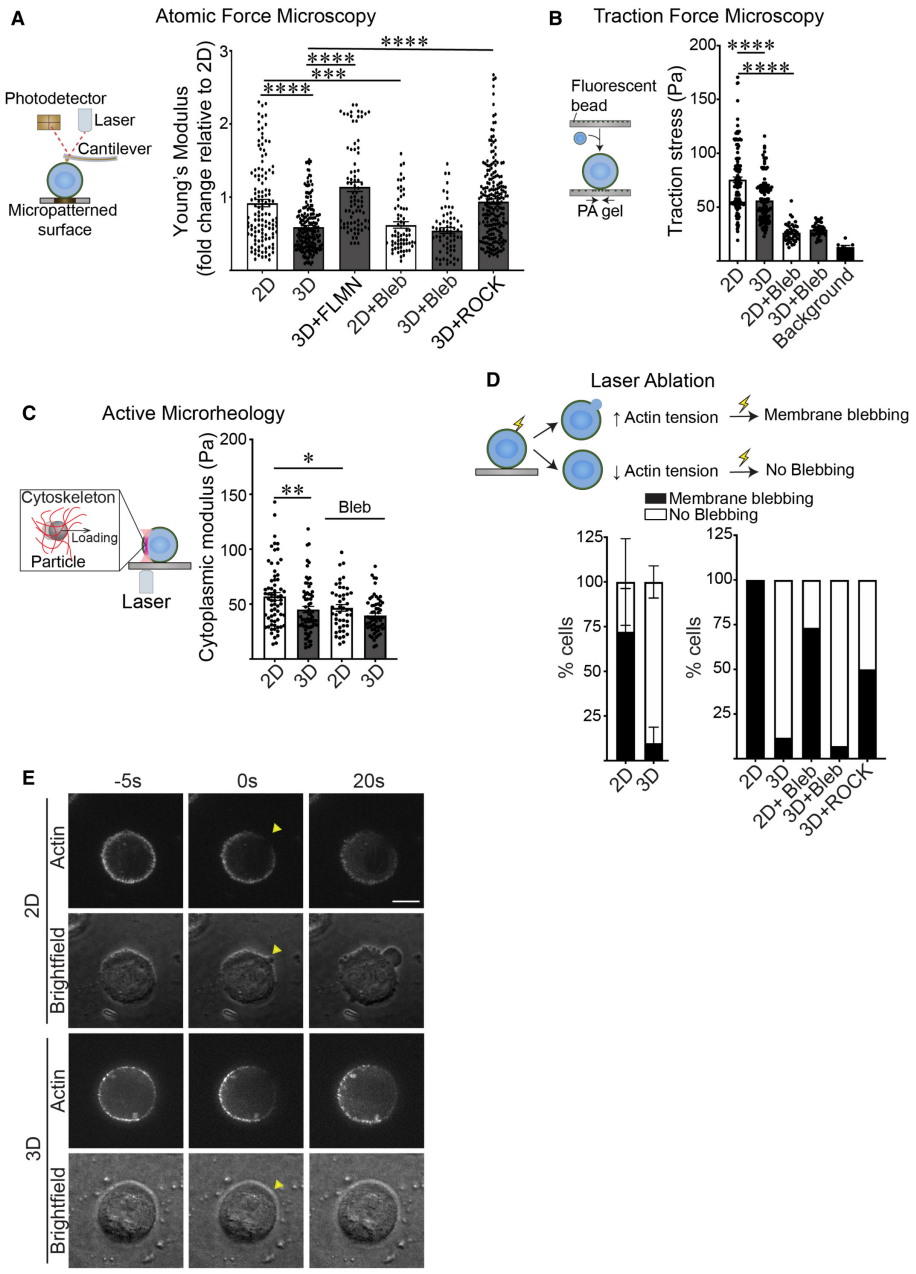

Figure 4.4: Ligation of rBM in 3D reduces actin tension[1]

A. Schematic showing the principles behind Atomic Force Microscopy (AFM) (left). A cantilever at the end of the microscope probe is deflected when it is in contact with the cell surface. Cell cortex-mediated resistance to indentation alters the path of the laser beam focused on the cantilever that is then reflected onto a photodetector to enable measurement of cellular cortical actin tension. AFM was used to measure the cortical actin tension in MCF10A MECs ligated to a laminin-111 substrate in 2D or 3D (right) and treated with blebbistatin (Bleb) to reduce cortical actin tension, induced to overexpress filamin expression (FLMN), or activated ROCK (ROCK) to increase cortical actin tension. MECs were indented using a 2-μm beaded tip on the AFM cantilever and the

[1]This figure was generated by co-authors.

Hertz model was used to fit each indentation curve to extract the Young's modulus of the cell cortex (mean ± SEM; 2D, n = 123; 3D, n = 184; 3D + FLMN, n = 83; 2D + Bleb, n = 66; 3D + Bleb, n = 65; 3D + ROCK, n = 212; n = AFM indentation from >30 cells from three independent experiments). Statistical analysis by one-way ANOVA followed by Tukey's multiple comparisons test. 2D versus 3D, ****P ¡ 0.0001; 3D versus 3D + FLMN, ****P ¡ 0.0001; 3D versus 3D + ROCK, ****P ¡ 0.0001; 2D versus 2D + Bleb, ***P = 0.0004. B. Schematic of the principles behind traction force microscopy (left). MECs are plated on compliant polyacrylamide gels containing 100 nm fluorescent beads (close to the cell-polyacrylamide gel interface). Traction stresses are calculated based on the bead displacement induced by substrate deformation and relaxation. Quantification of the traction stresses in individual MCF10A MECs ligated with rBM in 2D and 3D and treated in the absence and presence of blebbistatin (Bleb) for 18 h (right; mean ± SEM; 2D, n = 139; 3D, n = 124; 2D + Bleb, n = 42; 3D + Bleb, n = 43 cells from three independent experiments). The background bead displacement was measured from gel areas that lacked ligated cells (n = 8 fields from one experiment). Statistical analysis by one-way ANOVA followed by Tukey's multiple comparisons test. ****P ¡ 0.0001. C. Schematic of the principle of active microrheology (left). MCF10A MECs endocytosed 0.5 μm polystyrene particles, which were trapped and oscillated using laser optical tweezers to measure the cytoplasmic modulus. The cytoplasmic modulus was measured for MECs ligated to a rBM in 2D or 3D and treated in the absence or presence of blebbistatin (Bleb) to reduce cortical actin tension (right); individual modulus values were calculated based on the slope in the linear range of the normalized force-displacement curve (mean ± SEM; 2D, n = 66; 3D, n = 69; 2D + Bleb, n = 46; 3D + Bleb, n = 60 cells from three independent experiments). Statistical analysis by one-way ANOVA followed by Uncorrected Fisher's LSD. 2D versus 3D, **P = 0.0028. 2D versus 2D + Bleb, *P = 0.0182. D. Schematic depicting strategy used to measure cortical tension using laser ablation. (Top) Cells with high cortical tension exhibit plasma membrane blebbing when cortical actin is severed by a pulsed laser, whereas cells with lower cortical tension do not. (Bottom left) Bar graph of the laser ablation response of MCF10A MECs ligated to a rBM in 2D or 3D (mean ± SD; 2D, n = 35; 3D, n = 40 cells from three independent experiments). (Bottom right) Bar graph showing the laser ablation response of MCF10A MECs ligated to a rBM in 2D or 3D and treated in the absence or presence of blebbistatin (2D + Bleb and 3D + Bleb) or expressing constitutively active ROCK (3D + ROCK) (mean; 2D, n = 14; 3D, n = 15; 2D + Bleb, n = 17; 3D + Bleb, n = 14; 3D+ ROCK, n = 10 cells from one experiment). E. Representative fluorescence and brightfield images of bleb formation induced by laser ablation in MECs stably expressing LifeAct-RFP. Arrowhead: the site of laser ablation. Scale bar, 10 μm.

Cells with high actin tension can nucleate blebs rapidly in response to local laser ablation of the actin cortex ([201]). We therefore used laser ablation to disrupt the actin cortex and monitored the bleb behavior of the untethered plasma membrane to examine whether the context of ECM ligation (2D versus 3D) influenced cortical actin tension. Consistently, laser ablation of cortical actin induced rapid bleb formation in the MECs interacting with rBM in 2D in an actomyosin-dependent manner (Fig. 4.4D and E). By contrast, laser ablation failed to elicit blebs in MECs interacting with rBM in 3D (Fig. 4.4D and E). Importantly, expressing a constitutively

active ROCK to elevate actomyosin activity restored laser ablation-induced membrane bleb activity in the MECs engaging rBM in 3D, implicating actomyosin tension in this phenotype and ruling out the possibility that the ECM overlay physically impeded bleb formation (Fig. 4.4D; right panel; compare 3D and 3D + ROCK).

4.2.5 Ligation of rBM in 3D reduces actin tension-dependent filamin unfolding and filamin-ER binding

To determine whether the context of ECM ligation influences ER function by tuning cortical actin tension, we treated MECs engaging rBM in 2D with blebbistatin and assessed whether this treatment rescued ER calcium depletion phenotype and reduced ER stress. FURA calcium dynamic analysis revealed that inhibiting actomyosin activity increased ER Ca2+ store content (Fig. 4.5A and B), reduced levels of pEIF2a protein (Fig. 4.5C), and decreased levels of the stress-regulated transcription factor ATF3 in MECs engaging rBM in 2D (Fig. 4.5D). Reducing actomyosin tension also decreased the number of ER-PM junctions, reflecting improved ER calcium homeostasis (Fig. 4.5E).

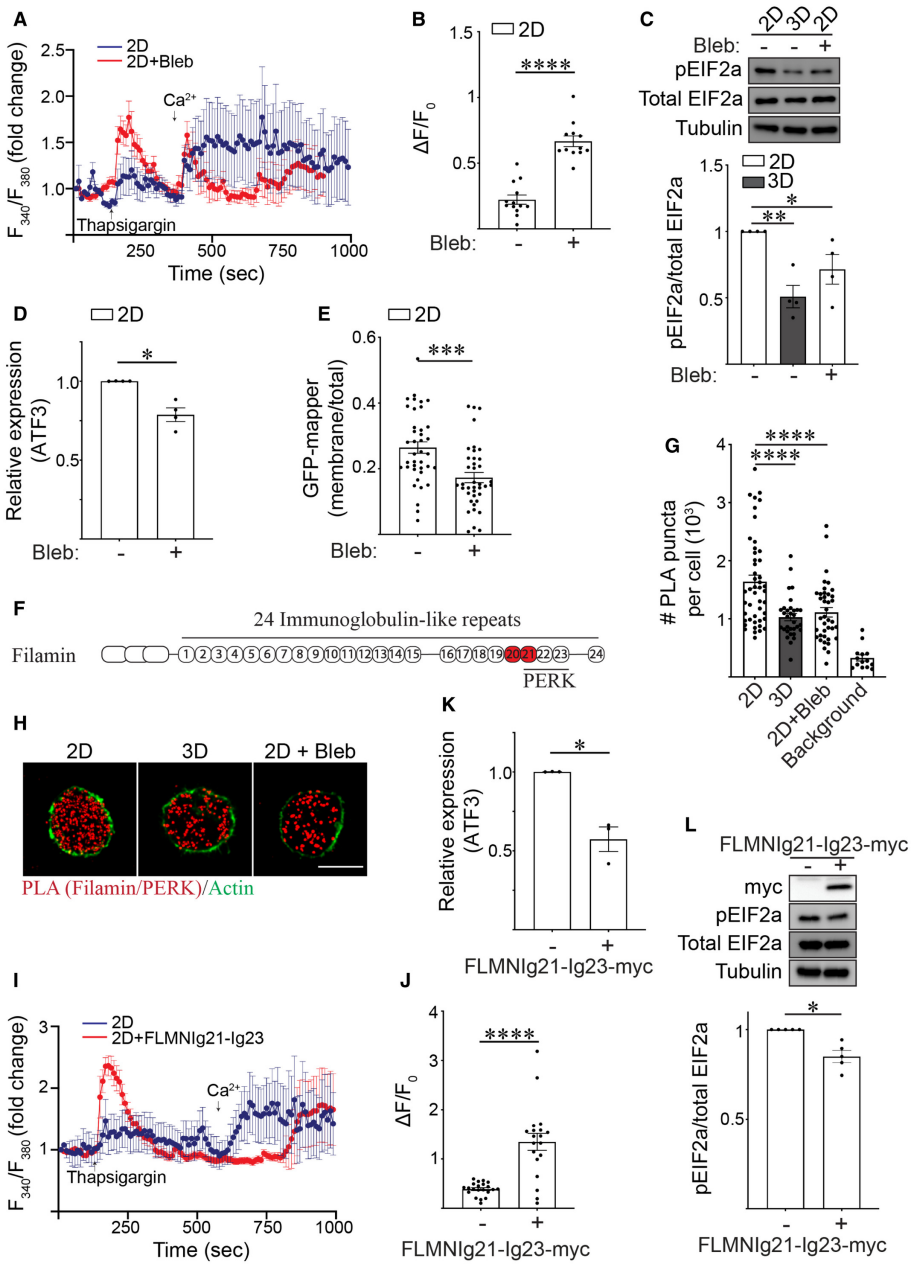

Figure 4.5: Ligation of rBM in 3D reduces actin tension-dependent filamin-ER binding to regulate ER function[1]

A. Representative line graph showing the changes in cytosolic [Ca2+] levels of MCF10A MECs in response to treatment. Fura-2-loaded MECs ligated with rBM in 2D were treated with DMSO (2D; blue) or with blebbistatin (2D + Bleb; red) and preincubated with EGTA to chelate extracellular Ca2+ in the bath solution, challenged with 2 μM thapsigargin to induce ER Ca2+ release, and replenished with 4 mM Ca2+ in bath solution at the indicated times. F340/F380 values for each cell were quantified over the course of imaging and plotted (mean ± SD; 2D, n = 7; 2D + Bleb, n = 7 cells from one experiment). B. Quantification of the amplitude of the Ca2+ response

[1]This figure was generated by co-authors.

(δF=F-F0) induced by thapsigargin, where F0 is the basal fluorescence before thapsigargin treatment. The data shown indicated mean ± SEM (2D, n = 13; 2D + Bleb, n = 12 cells from two independent experiments). ****P ¡ 0.0001 (Student's t-test). C. Representative immunoblots of phosphorylated EIF2a (pEIF2a), total EIF2a and alpha-tubulin in cell lysate from MCF10A MECs ligated to a rBM in 2D or 3D and treated in the absence or presence of blebbistatin (Bleb). Corresponding quantification data are shown at bottom (mean ± SEM; n = 4 independent biological replicates). Statistical analysis by one-way ANOVA followed by Uncorrected Fisher's LSD. 2D versus 3D, **P = 0.0022. 2D versus 2D + Bleb, *P = 0.0248. D. Bar graph of qPCR data measuring the relative levels of ATF3 mRNA in MECs ligated with rBM in 2D and treated in the absence or presence of blebbistatin (Bleb) (mean ± SEM; n = 4 independent biological replicates). *P = 0.0158 (Student's t-test). E. Graph of the levels of GFP-MAPPER at the plasma membrane relative total cellular GFP-MAPPER fluorescence in MCF10A MECs ligated with rBM in 2D and treated in the absence or presence of blebbistatin (Bleb) (mean ± SEM; 2D, n = 39; 2D + Bleb, n = 39 cells from three independent experiments). ***P = 0.0002 (Student's t-test). F. Schematic showing the immunoglobulin(Ig)-like repeats within filamin and the PERK-interacting domains identified within this repeat region (Ig21-23). The mechanosensitive domains Ig20-21 is highlighted in red. G. Scatter plot of the number of proximity ligation assay (PLA) puncta within individual cells expressing myc-PERK that were ligated to rBM in 2D or 3D, treated in the absence or presence of blebbistatin (Bleb) for 25 h and stained with PLA antibody probes specific for endogenous filamin and myc-PERK. Representative images of PLA staining from these experiments can be found in Panel H. Background PLA signal was measured from cells stained in the absence of primary antibodies (mean ± SEM; 2D, n = 47; 3D, n = 32 cells; 2D + Bleb, n = 39; background, n = 14 cells from three independent experiments). Statistical analysis by one-way ANOVA followed by Uncorrected Fisher's LSD. ****P ¡ 0.0001. H. Representative fluorescence microscopy images of cells expressing myc-PERK that were ligated to rBM in 2D or 3D, treated in the absence or presence of blebbistatin (Bleb) for 25 h and stained with PLA antibody probes specific for endogenous filamin and myc-PERK (red puncta). F-actin was stained with phalloidin to outline the cell (green). Scale bar, 10 μm. Puncta quantification data for this experiment is plotted in Panel G. I. Representative line graph showing the changes in cytosolic [Ca2+] levels of MCF10A MECs in response to treatment. Fura-2-loaded MCF10A MECs ligated with rBM in 2D and expressing filamin repeats 21–23 (2D + FLMNIg21-Ig23) or vector control (2D) were pre-incubated with EGTA to chelate extracellular Ca2+ in the bath solution, challenged with 2 μM thapsigargin to induce ER Ca2+ release, and replenished with 4 mM Ca2+ in bath solution at the indicated time. F340/F380 values of individual cells were quantified over the course of imaging (mean ± SD (2D, n = 8; 2D + FLMNIg21-Ig23, n = 7 cells from one experiment). J. Quantification of the amplitude of the Ca2+ response (δF=F-F0) induced by thapsigargin, where F0 is the basal fluorescence before thapsigargin treatment. The data shown indicated mean ± SEM (2D, n = 21; 2D + FLMNIg21-Ig23, n = 19 cells from three independent experiments). ****P ¡ 0.0001 (Student's t-test). K. Bar graph of qPCR data measuring the relative levels of ATF3 mRNA in MCF10A MECs expressing luciferase control or filamin repeats 21–23 (FLMNIg21-Ig23) ligated with rBM in 2D for 18 h (mean ± SEM; n = 3 independent biological replicates). *P = 0.032 (Student's t-test). L. Representative immunoblots of phosphorylated EIF2a (pEIF2a), total EIF2a and alpha-tubulin in cell lysate from MCF10A MECs expressing luciferase (control) or filamin repeats 21–23 (FLMNIg21-Ig23-myc) that were ligated with rBM in 2D. Corresponding quantification data are shown at bottom (mean ± SEM; n = 5 independent biological replicates). *P = 0.0112 (Student's t-test).

We next investigated how ECM ligation dimensionality tunes actin tension to regulate ER function. ER resident proteins including PERK can interact with filamin ([197]). Furthermore, the domain of filamin that interacts with ER resident proteins including PERK, overlaps with the mechanosensitive immunoglobulin-like repeats 20–21 in the molecule (Fig. 4.5F) ([198]). To investigate this relationship between filamin and PERK, we used the in situ proximal ligation assay (PLA; an antibody-based technique used to determine whether two proteins are in proximity with each other; ¡40 nm). We examined whether filamin interacts with PERK in the MECs ligating rBM in 2D, and if so, whether the interaction was actin tension-dependent. Quantification of PLA signal revealed that PERK and filamin interact in MECs interacting with rBM in 2D, and revealed that this interaction is actomyosin-dependent because treatment with blebbistatin reduced this interaction (Fig. 4.5G and H; quantification of apical, mid and basal focal planes in Extended Fig. 8.21A). By contrast, MECs interacting with rBM in 3D had a significantly lower PLA signal, likely because they exhibited reduced actin tension and lower filamin levels (Fig. 4.3B and Fig. 4.5G and H).

To examine whether tension-dependent filamin-PERK interactions modulate the ER phenotype of the MECs ligating the ECM in 2D, we overexpressed the PERK-interacting, mechanosensitive domain of filamin (FLMNIg21-Ig23), which prior studies indicate can inhibit filamin/PERK interactions and thus function as a dominant negative ([197]) (Extended Fig. 8.21B). Studies revealed that decoupling filamin-PERK interaction using FLMNIg21-Ig23 in the MECs ligating rBM in 2D ameliorated ER stress, as indicated by restoration of ER calcium store content (Fig. 4.5I and J), reduced ATF3 levels (Fig. 4.5K) and lower pEIF2a levels (Fig. 4.5L). The findings indicate that how the cell ligates its ECM, whether in 2D or 3D, influences its ER function and thereby its cell phenotype by tuning tension-dependent filamin-PERK interactions.

4.2.6 Cortical actin tension modulates plasma membrane topology

ER stress can impede protein secretion ([202]). To explore this possibility, we asked whether actin tension influenced secretory protein trafficking in the MECs engaging rBM in 3D. Upon investigation, we observed that inhibiting actomyosin tension in the MECs engaging the

ECM in 2D reduced their ER stress signaling and concomitantly increased SEC61B expression (Fig. 4.5A–E and Fig. 4.6A), consistent with a relationship between cortical tension and ER-dependent secretory protein trafficking.

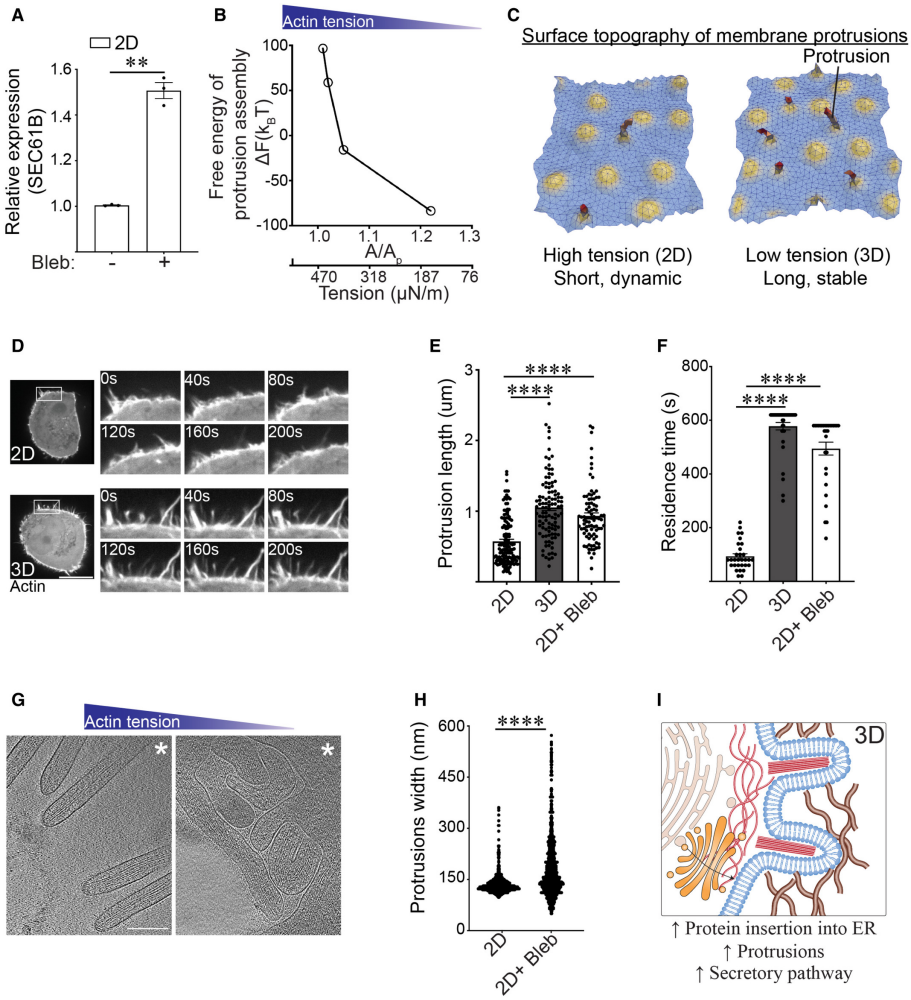

Figure 4.6: Cortical actin tension modulates plasma membrane topology[1]
A. Bar graph of qPCR data measuring the levels of SEC61B mRNA in MECs ligated with rBM in 2D and treated in the absence and presence of blebbistatin (Bleb) (mean ± SEM; n = 3 independent biological replicates). **P = 0.0046 (Student's t-test). B. Change in the Helmholtz free energy of membrane protrusion assembly (δF) as a function of cell membrane excess area (A/Ap), which is the variable conjugate to the cortical actin tension. C. Representative snapshots from a typical membrane patch with properties of the plasma membrane showing that protrusion length is higher in low-tension (3D) conditions compared to high-tension (2D) conditions. The model predicts that cells interacting with a rBM in 2D that experience high actin tension will form shorter and/or more dynamic membrane protrusions. In contrast, cells that experience low actin tension, as is the case for MECs interacting with a rBM in 3D (3D), are predicted to form longer and more stable

[1]This figure was generated by co-authors. My analysis identified the regulated pathways shown in (I).

membrane protrusions. D. Representative time-lapse confocal microscopy images of MECs stably expressing LifeAct-RFP that were ligated to a rBM in 2D (2D) or 3D (3D). Time in seconds (s) is indicated in each inset; scale bar, 10 μm. E. Bar graph of protrusion length measurements in MECs ligated to rBM in 2D, 3D, or in 2D treated with blebbistatin (2D + Bleb) (mean ± SEM; 2D, n = 139; 3D, n = 106; 2D + Bleb, n = 88 protrusions from three independent experiments). Statistical analysis by one-way ANOVA followed by Uncorrected Fisher's LSD. ****P ¡ 0.0001. F. Bar graph of protrusion residence time measurements in MECs ligated to rBM in 2D (2D), 3D (3D), or in 2D treated with blebbistatin (2D + Bleb) (mean ± SEM; 2D, n = 30; 3D, n = 30; 2D + Bleb, n = 38 protrusions from three independent experiments). Statistical analysis by one-way ANOVA followed by Uncorrected Fisher's LSD. ****P ¡ 0.0001. G. 30-nm thick slice through a cellular tomogram focusing on protrusions emanating from a vitrified no-spread MECs cultured on a rBM in the absence (left, 2D) or in the presence of blebbistatin (right, 2D+ Bleb). The position of the cell body is toward the upper right-hand corner (marked with white asterisk). Scale bars, 200 nm. Note: under conditions of low cortical actin tension (blebbistatin treatment) the protrusions visualized in these MECs appeared to be highly interdigitated with sharp kinks, consistent with a compliant phenotype. By contrast, the protrusions observed in the 2D samples (higher cortical actin tension) were predominantly straight and outwardly projected, suggesting they were stiffer than the protrusions formed in the MECs with lower cortical actin tension (e.g., blebbistatin treated). H. Quantification of membrane protrusion width in tomograms from non-spread MECs interacting with rBM treated with (2D + Bleb) and without blebbistatin (2D). n $>$ 2,000 protrusions. Statistical significance of differences between the distributions was assessed using Mann–Whitney rank tests. ****P ¡ 0.0001. I. Model of how reduced cortical tension influences membrane protrusion phenotype.

Secretory proteins are synthesized in the ER, transported through the Golgi and thereafter are delivered to the plasma membrane. Cortical actin physically attaches to the plasma membrane and by so doing influences membrane topology ([203]). Membrane topology regulates the binding of curvature-associated proteins that reinforce membrane organization and influence cell signaling and protein secretion or recycling ([204]). We therefore explored whether the context of ECM engagement facilitates protein secretion by regulating cortical actin tension-dependent plasma membrane topology. We used dynamically triangulated Monte Carlo simulations to explore the morphological conformational space of planar to highly curved membranes ([205]; [206]; [207]). The method incorporates (a) thermal fluctuations that play a key role in the self-organization of membranes, (b) the fluid nature of the membrane, and (c) membrane physical environment variables such as tension, osmotic stress, stiffness, and excess area. Using this framework, we quantified the surface deformations induced by membrane proteins as curvature fields, and studied the emergent morphologies of the membrane using isotropic and anisotropic curvature models. This mesoscale

model is broadly applicable and appropriate for modeling systems with different tension values. We simulated membrane patches with different excess area (A/Ap), which is the variable conjugate to the membrane tension and depends on cortical actin tension ([207]). Our free energy simulations for the formation of cellular protrusions were computed from the Helmholtz free energy change of the protrusion assembly (δF) and were plotted as a function of membrane excess area (proxy for cortical actin tension) (Fig. 4.6B), and thereafter presented as representative cartoons of membrane deformation and protrusion phenotype (Fig. 4.6C). The model predicted that the protrusions that assemble in the MECs engaging the ECM in 2D, that experience high cortical actin tension, herein depicted as being under small excess area (A/Ap), would be shorter and/or more transient (Fig. 4.6C). By contrast, the model indicated that the membrane protrusions that assemble in the MECs engaging the ECM in 3D, that experience low cortical actin tension, would be longer and/or more stable. Consistent with these predictions, kymographs of MECs expressing LifeAct-RFP showed that MECs interacting with rBM in 2D formed highly dynamic, short membrane protrusions, whereas the MECs interacting with rBM in 3D formed longer and more stable protrusions (Fig. 4.6D), quantified as increased protrusion length (Fig. 4.6E) and residence time (Fig. 4.6F). Causal links between cortical actin tension, membrane protrusions, and membrane topology was demonstrated by showing that reducing myosin activity in the MECs engaging rBM in 2D (high cortical actin tension) stabilized their plasma membrane protrusions. Furthermore, the MECs engaging rBM in 2D treated with myosin inhibitor phenocopied the larger, long-lived plasma membrane protrusions exhibited by MECs engaging rBM in 3D (low cortical actin tension) (Fig. 4.6E and F).

We next used in-situ cryogenic cellular tomography (cryo-ET) to explore causal associations between cortical actin tension, plasma membrane protrusions, and plasma membrane topology of non-spread cells. Cryo-ET imaging of selected MEC cells plated on top of rBM-coated electron microscopy compatible substrates (EM grids, 2D) revealed that the actin-based plasma membrane protrusions were sparsely distributed and predominantly directionally oriented and radially distributed from the cell body (Fig. 4.6G). By contrast, following actomyosin inhibition

through blebbistatin treatment, the density of actin-based plasma membrane protrusions in the MECs was increased and the morphology of the protrusions was modified such that they were heavily interdigitated and convoluted, and the protrusions sprouted randomly extending from the cell body with no preferred directionality (Fig. 4.6G). Cryo-ET analysis of the membrane protrusions showed a central bundle of actin filaments, with an approximate average distance between the filaments of 117 nm, consistent with tight bundles mediated by cellular actin-binding proteins such as fimbrin or fascin ([208]; [209]). Thus, although lowering cortical actin tension does not appear to influence the distance between actin filaments within the protrusions, statistical analysis of protrusion width revealed the protrusions in the MECs with low cortical tension were on average significantly wider and appeared more compliant, consistent with their reduced protrusion activity and greater dwell time (Fig. 4.6G and H). The observations suggest that ECM engagement context (2D versus 3D) could influence protein secretion by modulating cortical actin tension and plasma membrane topology (Fig. 4.6I).

4.2.7 Cortical actin tension modulates plasma membrane protein composition

Plasma membrane protrusions are cylindrically shaped structures comprised of a protrusion, an annulus and a basal component that combine to generate negative and positive curvature in the associated membrane (Fig. 4.7A). While the neck or annulus of the protrusion generates positive membrane curvature, the entire cytoplasmic length of the protrusion compartment generates a negatively curved membrane. Membrane curvature regulates the binding affinity of membrane curvature-associated proteins that can exert profound effects on cell behaviors including endocytosis, protein secretion and recycling, organelle function and actin dynamics ([210]). To explore the relationship between cortical actin tension, plasma membrane protrusions and plasma membrane topology, we extended our Monte Carlo model to predict protein recruitment dynamics. We computed the excess chemical potential (or the free energy to add/recruit a protein) to these three spatial regions of the membrane (protrusion, annulus, and basal) as a function of excess membrane area (A/Ap) (proxy for cortical actin tension) (Fig. 4.7B) ([211]). Our calculations revealed

that a lower value of the excess chemical potential signifies the favorable recruitment of a protein to a given membrane location and curvature to enhance its local protein density. As shown in Fig. 4.7B, our computational analysis revealed that the excess chemical potential of negative curvature-binding protein domains is preferentially localized to the cytosolic site of the membrane protrusions, and predicted that this protein domain binding behavior will segregate more favorably under conditions of low cortical actin tension (3D). Our energetics calculations further predicted that conditions in which cell tension is low (MECs engaging the ECM in 3D), the recruitment of positive curvature-inducing proteins would be hindered (Extended Fig. 8.22A).

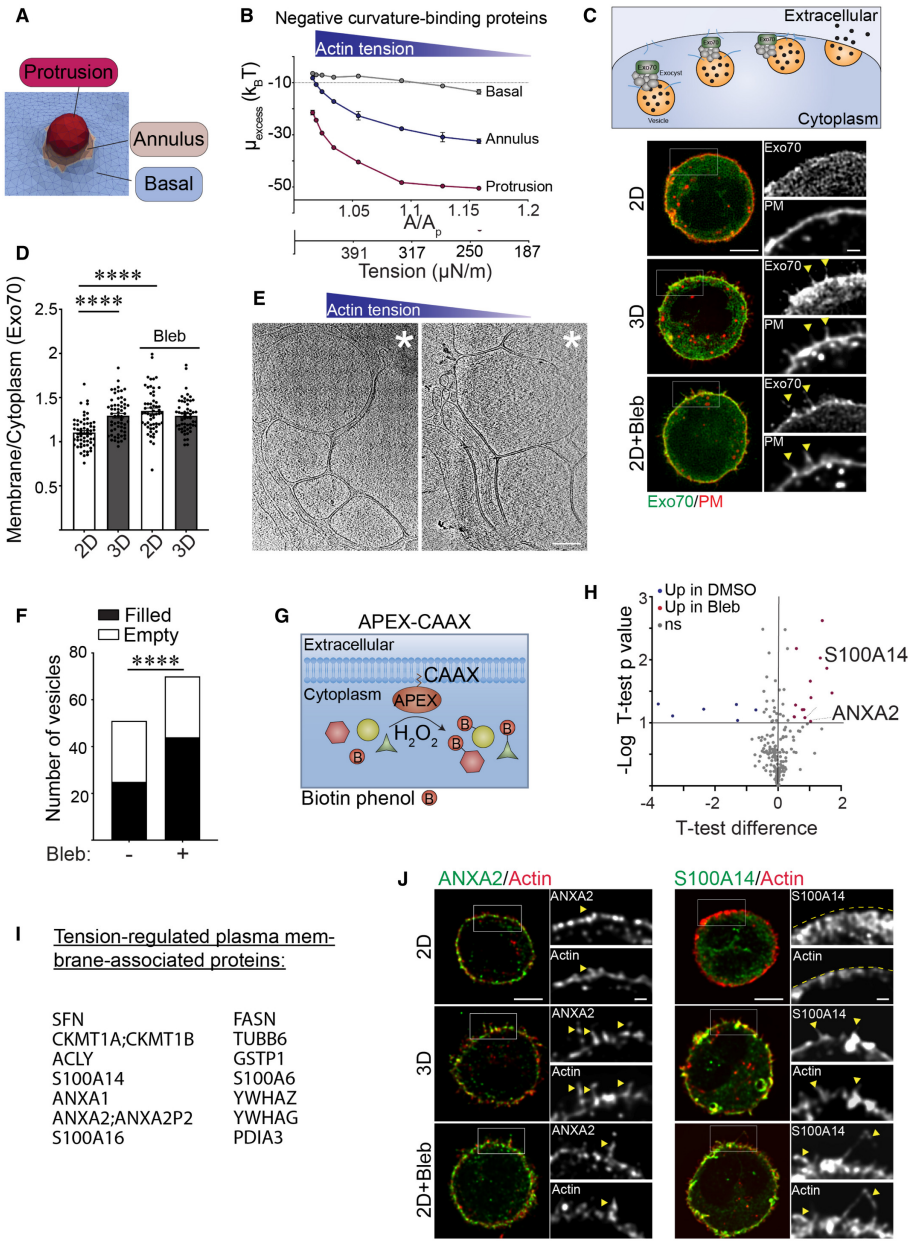

Figure 4.7: Cortical actin tension modulates plasma membrane protein composition[1]

A. Diagram showing spatial regions associated with plasma membrane actin-associated projections including the basal domain, the annulus and the protrusion. B. Line graph of the excess chemical potential required to recruit negative curvature sensing domain proteins to the basal, annulus, and protrusion region of the plasma membrane as a function of excess membrane area (A/Ap), which is the variable conjugate to the cortical actin tension. C. (Top) Model of how exocyst components (including Exo70) tether vesicles during exocytosis. Representative fluorescence microscopy images of MECs stably co-expressing EGFP-Exo70 (Exo70) and the plasma membrane reporter farnesylated mCherry (PM) ligated to rBM in 2D, 3D, and treated with blebbistatin (2D + Bleb). Fluorescent images of whole cells are shown (left) and cell-edge protrusions are magnified within

[1]This figure was generated by co-authors. My analysis identified the proteins shown in (I).

inset (right). Colocalization of Exo70 and membrane protrusions are highlighted with yellow arrows. Scale bar (whole cell), 5 μm; Scale bar (magnified inset), 1 μm. D. Bar graph of the relative level of EGFP-Exo70 at the plasma membrane versus cytoplasm in MECs ligated to rBM in 2D or 3D in the absence and presence of blebbistatin (Bleb). Membrane localization of EGFP-Exo70 was quantified as a ratio of plasma membrane to cytoplasmic fluorescence (mean ± SEM; 2D, n = 59; 3D, n = 60; 2D + Bleb, n = 57; 3D + Bleb, n = 54 cells from three independent experiments). Statistical analysis by one-way ANOVA followed by Uncorrected Fisher's LSD. ****P ¡ 0.0001. E. 30-nm thick slices through a cellular tomogram focusing on subplasmalemmal regions enriched with membrane-encased compartments of vitrified MECs cultured on rBM treated with (2D, right panel) or without (2D + Bleb, left panel) blebbistatin. The position of the cell body is toward the upper right-hand corners (marked with white asterisk). Scale bars, 200 nm. F. Quantification of the number of membrane-enclosed compartments (vesicles) proximal to the plasma membrane that were classified as either "filled" (black) or "empty" (white), based on the absence or presence of encapsulated macromolecules. Membrane-enclosed compartments were independently classified by three cryo-EM experts using 28 tomograms per condition. The resulting standard deviation for assigning "empty" versus "filled" was 10.3% (n = 3 independent expert classifications). Statistical significance of differences between the distributions was assessed using Mann–Whitney rank tests. ****P ¡ 0.0001. G. Schematic of the proximity-based biotinylation assay used to label proteins localized to the plasma membrane under different ECM ligation conditions. Expression of a recombinant APEX2-CAAX probe within cells facilitated biotin labeling of proteins in close proximity to the plasma membrane upon addition of biotin-phenol and H2O2. H. Volcano plot showing differentially associated proteins in MECs ligated to rBM in 2D treated with vehicle (DMSO; blue; log 2 $>$ 0.5; high cortical actin tension) versus blebbistatin (Bleb; red; log 2 $>$ 0.5; low cortical actin tension). Differentially expressed genes with an adjusted P-value ¡ 0.1 and log2 (fold change) $>$ 0.5 are shown (n = 2 biological replicates). I. List of proteins enriched at the plasma membrane in cells ligated to rBM in 2D and treated with blebbistatin (low cortical actin tension). J. Representative immunofluorescence microscopy images of MECs ligated to rBM in 2D, 3D, or 2D treated with blebbistatin (2D+ Bleb) and immunostained with antibodies targeting ANXA2 or S100A14 (green). Cellular F-actin was counterstained using phalloidin (red) and actin-rich protrusions are highlighted with yellow arrows. Fluorescent images of whole cells (left) and actin-rich protrusions containing ANXA2 or S100A14 are magnified in the inset (right). The edge of the actin cortex in MECs ligated to rBM in 2D was marked with a yellow dashed line. Scale bar (whole cell), 5 μm; Scale bar (magnified insets), 1 μm.

Given that Exo70 is a negative curvature binding/inducing protein that is also a component of the exocyst complex targeting secretory vesicles to the plasma membrane (Fig. 4.7C; top panel), we predicted that Exo70 could be a candidate protein regulated by cortical actin tension to facilitate secretory protein trafficking ([212]). In keeping with our energetics model prediction, EGFP-tagged Exo70 showed greater plasma membrane localization in the MECs engaging the rBM in 3D (low actin tension), as revealed by a higher colocalization of the EGFP-Exo70 with membrane-tagged farnesylated mCherry, as compared with lower plasma membrane associations observed in

the MECs engaging the rBM ECM in 2D (Fig. 4.7C and D; quantification of apical, mid and basal focal planes in Extended Fig. 8.22B). The differential plasma membrane localization did not reflect changes in Exo70 expression between the MECs interacting with rBM in 2D and 3D (Extended Fig. 8.22B). Reducing myosin activity using blebbistatin in the MECs engaging rBM ECM in 2D, not only recapitulated the membrane protrusion behavior of the MECs engaging rBM ECM in 3D, but also significantly enhanced the level of plasma membrane-associated Exo70 (compare Fig. 4.7C and D; compare 2D top to 2D + Bleb bottom panels). Consistently, statistical analysis of the cryo-ET regions containing membrane-enclosed compartments revealed that the MECs with reduced cortical tension (2D + Bleb) had more membrane-enclosed compartments proximal to the plasma membrane region than MECs with high cortical tension (2D; Fig. 4.7E). The analysis further revealed that a higher fraction of the membrane compartments in the MECs with reduced actin tension were enriched with macromolecular content, whereas a higher fraction of vesicle-like structures adjacent to the plasma membrane in the MECs with high actin tension appeared emptier (Fig. 4.7E and F), suggesting defective secretory pathway cargo loading. RT-qPCR analysis also demonstrated that the MECs with high cortical actin tension expressed lower levels of SEC61B, an important protein required for protein insertion into the ER (Fig. 4.6A). The data suggest cortical actin tension regulates secretory protein trafficking to the plasma membrane, potentially by modulating plasma membrane protrusion activity and topology. This possibility accords with the RNA-seq data comparing gene expression in the MECs engaging rBM in 2D versus 3D that revealed a significant increase in the expression of several ER protein insertion regulators and secretory pathway regulators in the MECs with low cortical actin tension (ligating ECM in 3D/2D; Fig. 4.1K).

To explore the possibility that cortical actin tension modulates plasma membrane protein composition, we used an unbiased proximity-based biotinylation assay to identify a broader repertoire of cell cortex-associated proteins whose localization is regulated by myosin activity. Using membrane-targeting ascorbate peroxidase (APEX2-CAAX) as a bait, we mapped the proteomic landscape at the actin cortex in MECs with high and low myosin activity (Fig. 4.7G; MECs in

2D with and without blebbistatin treatment). We used APEX2-CAAX to mark the cellular cortex and immunoblotting to verify APEX biotinylation efficiency (Extended Fig. 8.22C and D). Quantitative mass spectrometry analysis identified 14 candidate proteins whose plasma membrane associations were modulated by myosin activity (Extended Fig. 8.22E and Fig. 4.7H and I). Gene enrichment analysis revealed that these tension-sensitive membrane-associated proteins were predominantly localized at either the extracellular region of the cell, at cellular vesicles, or at the cell-substrate interface (Extended Fig. 8.22F). Immunofluorescent staining verified that the localization of the APEX2-CAAX identified protein ANXA2 was enriched at the plasma membrane as well as within plasma membrane protrusions in the MECs with low cortical actin tension (Fig. 4.7J; compare ANXA2 2D to 3D and 2D + Bleb panels). ANXA2 can form heterodimeric structures with S100 family members, which are extracellular secreted proteins known to form a bridge between two membranes to facilitate vesicle docking during exocytosis ([213]). Consistently, immunofluorescence staining for S100A14 showed abundant plasma membrane and membrane protrusion localization in the MECs with low cortical actin tension (Fig. 4.7J; compare S100A14 2D to 3D and 2D + Bleb panels).

The increased ANXA2 and Exo70 plasma membrane localization we observed is not only consistent with the molecular dynamic simulations that predicted the plasma membrane binding of negative curvature-binding proteins, such as ANXA2 and Exo70, but also suggest that this binding could induce and stabilize negative plasma membrane curvature ([212]; [214]). Accordingly, the findings suggest that cortical actin tension regulates membrane protrusion activity and plasma membrane topology to modulate the spatial distribution of negative curvature-binding proteins implicated in secretory protein trafficking.

4.2.8 Actin tension regulates MEC spheroid phenotype

Our results thus far implied that how a cell ligates its ECM (in 2D versus 3D) has a profound effect on ER function and possibly also on protein secretion. We implicated filamin-dependent cortical actin tension as a key regulator of this ECM ligation-mediated ER homeostasis

phenotype. Unresolved or prolonged ER stress responses compromise cell viability, and impeding secretory protein trafficking can severely compromises ER function ([215]). Therefore, we examined whether the context of ECM ligation regulates MEC viability at the single cell level and influences stress resilience at the multicellular spheroid level, and if this is mediated through the tuning of cortical actin tension. To begin with, calcein/ethidium homodimer live/dead staining revealed the single non-spread MECs with high cortical actin tension that engaged rBM in 2D had significantly reduced cell viability as compared to non-spread MECs engaging rBM in 3D with low cortical actin tension (Fig. 4.8A; left). However, and importantly, the viability of the non-spread MECs engaging rBM in 2D could be significantly extended if their myosin activity was reduced by blebbistatin treatment (Fig. 4.8A; right). Consistently, reducing filamin, but not alpha actinin, using shRNA, or overexpressing the PERK-interacting domain of filamin FLMNIg21-Ig23, simultaneously enhanced cellular viability in MECs engaging rBM in 2D (Fig. 4.8B and C). Importantly, manipulating cortical actin tension either by inhibiting myosin activity or through filamin knockdown had no measurable impact on cell adhesion or cell spreading on compliant PA gels, implying cell viability regulation occurred through another distinct mechanism. Indeed, decreasing cellular filamin significantly ameliorated ER stress signaling in the MECs interacting with the ECM in 2D, as indicated by reduced peIF2a and ATF3 levels (Fig. 4.3E and F). Consistently, knocking down the negative curvature membrane binding protein Exo70, which has been implicated in protein secretion and membrane topology regulation, compromised the viability of MECs interacting with rBM in 3D (Fig. 4.8D and E). The data therefore suggest that filamin-dependent cortical actin tension modulates ER function to regulate MEC viability.

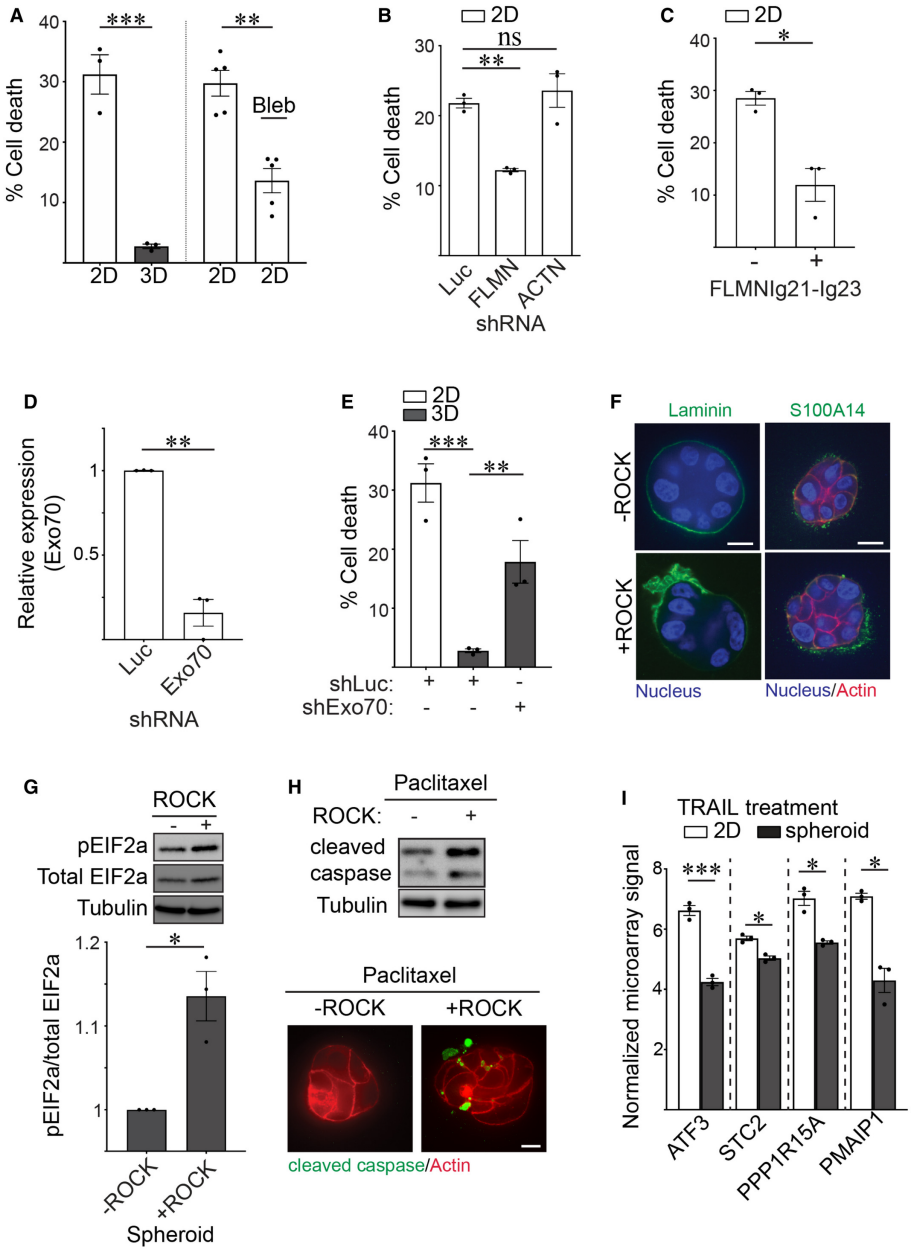

Figure 4.8: Cortical actin tension regulates MEC spheroid phenotype[1]

A. Graph of the percent cell death measured in MCF10A MECs ligated to rBM in 2D and 3D (left) and in 2D treated with blebbistatin (2D + Bleb) 48 h post-plating (right) that was quantified using calcein AM and ethidium homodimer staining (mean ± SEM; 2D, n = 3; 3D, n = 3 independent experiments; 2D + DMSO, n = 5; 2D + Bleb, n = 5 independent experiments). 2D versus 3D, ***P = 0.0010, 2D versus 2D + Bleb, **P = 0.0248 (Student's t-test). B. Bar graph of the percent cell death measured in MCF10A MECs stably expressing shRNAs targeting Luciferase (Luc), filamin (FLMN) or actinin (ACTN) and ligated to rBM in 2D. Cell death was assessed at 48 h post-plating via calcein AM and ethidium homodimer staining (mean ± SEM; n = 3 independent biological replicates). **P = 0.0034; ns = not significant (Student's t-test). C. Bar graph of the percent

[1]This figure was generated by co-authors.

cell death in MCF10A MECs expressing luciferase control or filamin repeats 21–23 (FLMNIg21-Ig23) that were ligated with rBM in 2D. Cell death was assessed at 48 h post-plating via calcein AM and ethidium homodimer staining (mean ± SEM; n = 3 independent biological replicates). *P = 0.0489 (Student's t-test). D. Bar graph of the levels of endogenous Exo70 in MECs stably expressing shRNA against Exo70 or luciferase (Luc) (mean ± SEM; n = 3 independent biological replicates). **P = 0.0086. E. Bar graph of the percent cell death measured in MECs expressing shRNA targeting Exo70 (shExo70) or luciferase (control) and ligated with rBM in 2D or 3D. Cell death was assessed at 48 h post-plating via calcein AM and ethidium homodimer staining (mean ± SEM; n = 3 independent biological replicates). Statistical analysis by one-way ANOVA followed by Uncorrected Fisher's LSD. 2D versus 3D, ***P = 0.0004. 3D + shLuc versus 3D + shExo70, **P = 0.0091. F. Spheroids were induced to express constitutively active ROCK or left uninduced (control) and co-stained with antibodies for laminin or S100A14 (green), phalloidin (red) and DAPI (blue). Scale bar, 10 μm. G. Representative immunoblots of phosphorylated EIF2a (pEIF2a), total EIF2a and alpha-tubulin in cell lysate from MCF10A MEC spheroids induced to express constitutively active ROCK or left uninduced (control). Corresponding quantification data are plotted at bottom (mean ± SEM; n = 3 independent biological replicates). *P = 0.0442 (Student's t test). H. Spheroids were induced to express constitutively active ROCK or left uninduced (control), treated with Paclitaxel (2 nM), lysed and immunoblotted for cleaved caspase-3 and alpha-tubulin (top). In parallel, spheroids were stained with antibody and phalloidin to evaluate the levels of caspase-3 (green) and actin organization (red), respectively. Scale bar, 10 μm. I. Bar graph of the relative mRNA levels of ER stress response genes including ATF3, STC2, PPP1R15A, and PMAIP1 in microarray analyses of TRAIL treated HMT-3522 S-1 MECs plated as monolayers on a rigid rBM (2D) or as spheroids (3D) (mean ± SEM; n = 3 independent experiments). ATF3, ***P = 0.0006; STC2, *P = 0.0353; PPP1R15A, *P = 0.0254; PMAIP1, *P = 0.0127 (Student's t-test).

We next explored whether the reduction in cortical actin tension induced by ligation of rBM in 3D could account for the polarized basement membrane (BM) protein secretion and the stress resilience phenotype of multicellular MEC spheroids within rBM (3D). We ectopically increased actomyosin tension in preassembled MEC spheroids within rBM (3D) by expressing an inducible, constitutively active ROCK, and then monitored effects on endogenous BM deposition, polarized protein secretion and resistance to exogenous stress. Consistent with a causal association between cortical actin tension and ER homeostasis, confocal imaging revealed that increasing cortical tension through activated ROCK compromised the deposition of an endogenous, polarized basement membrane, as indicated by randomly deposited laminin-111 (Fig. 4.8F; left panels). Furthermore, elevating ROCK activity also disrupted the level and membrane association of S100A14 secreted protein (Fig. 4.8F; right panels). Importantly, increasing cortical tension in the spheroids by activating ROCK increased levels of phosphorylated EIF2a (pEIF2a) which together

with the compromised protein secretion we observed imply high cortical actin tension increases ER stress (Fig. 4.8G). To further explore the relationship between actin tension and ER function, we monitored the chemotherapy response of MEC spheroids embedded within rBM. Results showed that increasing actomyosin tension mediated by expressing the activated ROCK sensitized the MEC spheroids to the chemotherapy agent Paclitaxel, as quantified by increased levels of cleaved caspase-3 (Fig. 4.8H). Similarly, bioinformatics analysis revealed that many genes significantly induced in the TRAIL-treated MEC monolayers interacting with rBM in 2D, with high cortical actin tension, as compared with those MEC spheroids interacting with rBM in 3D with low cortical actin tension, were genes implicated in PERK-dependent ER stress regulation including ATF3, STC2, PPP1R15A and PMAIP1 (Fig. 4.8I, Dataset EV5 and EV6). The findings suggest high filamin-dependent cortical actin tension compromises ER homeostasis to perturb protein secretion and activate an ER stress response activity and implicate PERK-dependent signaling in this phenotype.

4.3 Discussion

Our studies underscore the importance of cellular context in regulating organelle homeostasis and tissue phenotype. Our data demonstrate that the context of cell-ECM ligation regulates ER function including ER stress response signaling and secretory protein trafficking and does so by modulating cellular cortical actin tension. Our findings reveal that cortical actin and actin-binding molecules, which regulate cellular tension, are critical effectors of the tissue-like behavior of cells interacting with an ECM in 3D. Our observations that ECM topology affects ER homeostasis are consistent with prior findings showing stress-resilient, enhanced protein secretion and deposition by spheroids and patient-derived organoids embedded within rBM (3D) and offer a plausible explanation for why these tissue-like structures exhibit such profound treatment resistance and are such useful models for drug testing ([216]). These findings also clarify why organoids cultured within rBM (3D) are able to faithfully reconstitute self-organization phenotypes and tissue behaviors such as branching morphogenesis and tubulogenesis.

Our results revealed that secretory protein trafficking is perturbed when cortical actin tension is elevated. Cortical actin has been shown to regulate secretory protein trafficking ([217]). To begin with, the actin cortex can hinder vesicle docking to the plasma membrane and thus can serve as a barrier to efficient protein secretion ([218]). In the current studies, we found that cortical actin tension can influence protein secretion, in part, by modulating ER homeostasis. This is consistent with the previous work showing that secretory protein synthesis and trafficking is impaired during ER stress ([202]). Surprisingly, we found that actin tension can also influence secretion by affecting plasma membrane topology to alter the localization/composition of targeting secretory effectors at the plasma membrane. In particular, membrane protrusion formation and the recruitment of negative curvature binding proteins including Exo70 and ANXA2, which serve important functions in membrane trafficking and protein secretion, require low cortical actin tension and are in fact inhibited by high actin tension ([213]; [219]). The findings also raise the intriguing possibility that high actin tension impedes protein secretion, and that in turn, this leads to the accumulation of proteins in the ER that exacerbates ER stress.

Our studies showed how ER function is sensitive to cortical actin tension and suggest that the ER harbors mechanosensitive elements. Indeed, recent evidence suggest that numerous calcium channels localized to the ER (e.g., Pannexin-1 and Piezo) can be activated by extracellular mechanical stimuli such as uniaxial stretch, focused ultrasound, and laser-tweezer-traction at the plasma membrane ([220]; [221]; [222]). We consistently found that cells ligated to an ECM in 2D generate high actin tension and simultaneously develop dysregulated calcium homeostasis. These findings raise the possibility that the high actin tension in cells interacting with an ECM in 2D aberrantly activate mechanosensitive ER calcium channels, ultimately compromising calcium homeostasis, ER function, and cell viability.

So how does the actin cortex influence ER function? Our data suggest that the actin cross-linker filamin is an important regulator of this process. Filamin is not only an actin cross-linker required for the maintenance of cortical actin tension but it is also a critical adaptor protein that operates at ER-PM contact sites ([197]). SOCE at the ER-PM contact sites is a key regulator of

cellular calcium homeostasis. When ER calcium stores are depleted, the ER rapidly establishes ER-PM contact to promote calcium influx across the plasma membrane to replenish the cellular ER calcium repository. Surprisingly, we determined that the higher numbers of ER-PM contact sites in the cells interacting with the ECM in 2D (high actin tension) was not accompanied by increased levels of intracellular calcium (Fig. 4.2D and E). We speculate that this phenotype is likely due to the ER calcium stores being chronically depleted in these cells and that this eventually compromises calcium homeostasis. Indeed, we observed lower levels of ER calcium storage in the cells ligating ECM in 2D. Our observations are consistent with prior published work that show that mechanical stretch can activate ER calcium leakage into the cytoplasm ([222]). Accordingly, we interpret our findings to mean that the higher number of ER-PM sites is a cellular mechanism induced in the cells in an attempt to restore calcium homeostasis to compensate for low levels of ER calcium. Tension-regulated filamin-mediated actin cross-linking likely influences the ER function we documented via one of the following two mechanisms. First, filamin is required to maintain actin cortex integrity and tension, and high cortical actin tension appears to stabilize cellular filamin, possibly by preventing its turnover. In turn, high filamin-mediated cortical tension may activate mechanosensitive calcium channels in the ER via filamin-PERK interaction to modulate calcium homeostasis and thereby ER function. Alternatively, given that we observed that high actin tension impaired Exo70 recruitment to the plasma membrane, a stiffer filamin cross-linked actin cortex in the cells engaging ECM in 2D may be less amenable to secretory activity, possibly leading to aberrant accumulation of proteins in the ER and activation of ER stress responses. Regardless of how filamin regulates the ER, our studies present compelling evidence that cortical actin composition and tension play a critical role in regulating ER structure/function and homeostasis. Our results also suggest that conditions which increase cortical actin tension, including a pathologically stiffened ECM or elevated actomyosin tension induced by oncogene expression such as activated Ras, would similarly activate ER stress response signaling in cells. Indeed, tumors that develop within a stiffened fibrotic ECM and those that express oncogenic Ras,

which increases ROCK activity and actomyosin tension, consistently demonstrate compromised ER stress regulation ([223]).

Interestingly, external stresses such as hypoxia, nutrient deprivation, and loss of cell-ECM adhesion also trigger ER stress and regulate cell viability and survival. For example, suspended cells that are devoid of ECM ligation activate PERK-dependent phosphorylation of EIF2a, selectively upregulate ATF4 expression and undergo anoikis (apoptosis) ([224]). Notably, our studies demonstrate that actin tension is necessary and sufficient to modulate ER function, cell stress and apoptosis. We found that ER stress signaling and cell viability can be alleviated by agents that reduce cortical actin tension without affecting cell-ECM ligation, and that increasing cortical actin tension promotes ER stress and compromises cell viability even in the presence of ECM ligation. Thus, cortical actin tension, via its ability to influence ER structure and function and modulate stress, is a key regulator of stress-dependent viability and survival. Accordingly, molecules that regulate actin cortex composition and mechanics may comprise attractive drug targets to manipulate ER function and for antitumor therapeutic intervention.

4.4 Contribution

I contributed the bioinformatics portions of this project, generated the corresponding panels indicated in each figure, wrote the associated text and methods, and edited the manuscript. Moreover, I optimized the RNAseq protocol used to obtain the sequencing libraries contained herein. Using the RNAseq data, we identified ER stress and the associated secretory pathways as compelling differences between 2D and 3D, which motivated follow-up studies described throughout the manuscript.

5 Chapter 5: ECM Stiffness Perturbs Metabolic Function via an HSF1-Mediated Stress Response

This chapter is a reprint of the peer-reviewed article titled "Adhesion-mediated mechanosignaling forces mitohormesis" by Kevin M Tharp, Ryo Higuchi-Sanabria, Greg A Timblin, Breanna Ford, Carlos Garzon-Coral, Catherine Schneider, Jonathon M Muncie, Connor Stashko, Joseph R Daniele, Andrew S Moore, Phillip A Frankino, Stefan Homentcovschi, Sagar S Manoli, Hao Shao, Alicia L Richards, Kuei-Ho Chen, Johanna Ten Hoeve, Gregory M Ku, Marc Hellerstein, Daniel K Nomura, Karou Saijo, Jason Gestwicki, Alexander R Dunn, Nevan J Krogan, Danielle L Swaney, Andrew Dillin, Valerie M Weaver in Cell Metabolism (2021).

5.1 Introduction

Alterations in mitochondrial function permit cancer cells to rapidly proliferate and metastasize and aging cells to regulate senescence phenotypes induced by DNA damage. Mitochondria provide a privileged metabolic compartment where oxidative phosphorylation (OxPhos) consumes oxygen and reducing equivalents to produce ATP. While OxPhos provides an efficient means to produce ATP, it can create collateral cellular damage through the release of reactive oxygen species (ROS), which can oxidize proteins, lipids, and nucleic acids. In response to elevated mitochondrial ROS exposure, cancer and aging cells activate adaptive stress responses that allow them to harness ROS-mediated proliferation and migration effects without activating ROS-mediated cell death ([225]; [226] ; [227]; [228]). These types of oxidative stress resilience (OxSR) programs alter cellular metabolism to enhance ROS buffering in the cytosol to limit damage caused by mitochondrial ROS.

The overproduction of ROS via mitochondrial dysfunction is thought to occur because of the biochemical composition of the aged or tumor microenvironment (TME) ([229]; [230]; [231]; [232]). However, the physical characteristics of the cellular microenvironment are also altered by cancer and aging—and can affect cell fate, function, and metabolism by regulating the

activity of stress- and ROS-associated transcription factors ([229]; [233]; [234]; [235]). Sensing the mechanical properties of the extracellular matrix (ECM) can also affect cellular metabolism by regulating the levels and/or activity of cytoplasmic enzymes responsive to mechanosignaling-induced cytoskeletal dynamics ([236]; [14]; [237]). Cellular mechanosignaling relies on adhesion receptors, such as integrins, transducing signals that mechanically entrain the cytoskeleton to the ECM, and these cytoskeletal remodeling events can affect the topological distribution of metabolic organelles, cargoes, and enzymes ([238]; [234]; [234]; [239]). Cytoskeletal dynamics also play a critical role in the regulation of mitochondrial structure ([240]; [241], [242]), and mechanosensitive transcription factors can alter mitochondrial gene expression ([243]). Because mitochondrial structure influences mitochondrial function, we sought to determine whether and how adhesion-mediated mechanosignaling affects mitochondrial function (Fig. 5.1A).

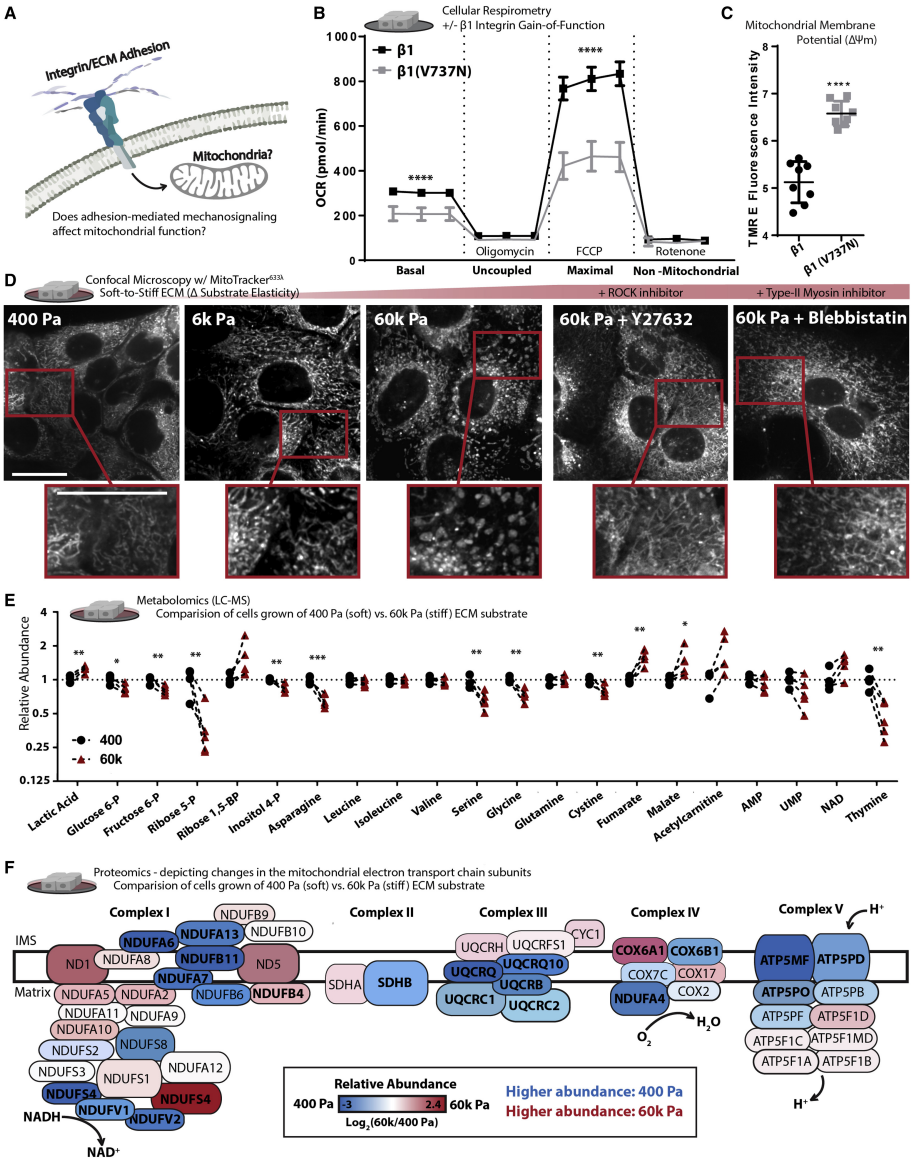

Figure 5.1: Adhesion-mediated mechanosignaling alters mitochondrial structure and function of human mammary epithelial cells (MECs)[1]

(A) Graphical representation of the experimental question. (B) Mitochondrial oxygen consumption rate (OCR) of β1-integrin or β1(V7373N)-expressing MECs (100k cells per well, n = 5 wells, 3 replicate measures, repeated 3 times). Mitochondrial stress test conditions: uncoupled, 1 μM oligomycin; maximal, 1 μM trifluoromethoxy carbonylcyanide phenylhydrazone (FCCP); non-mitochondrial, 1 μM antimycin A and 1 μM rotenone. (C) Mitochondrial membrane potential, measured after 1 h treatment of 10 nM tetramethylrhodamine ethyl-ester (TMRE) (n = 2 wells, repeated 4 times). (D) Confocal microscopy depicting mitochondrial network structure in PFA-fixed cells cultured on varied soft-to-stiff fibronectin-coated (6 μM/cm2) polyacrylamide hydrogels (soft-to-stiff ECM), for 24 h ± 10 μM Y27632 or 10 μM blebbistatin, stained with 100 nM MitoTracker (deep red FM). Scale bar, 10 μm. MitoMAPR quantification: 400 (18), 6k (20),

[1]This figure was generated by co-authors. I analyzed the metabolomics data and generated panel (F).

60k (7), 60k + Y27632 (15), and 60k + blebbistatin (12) junctions per network. (E) Selection of metabolites measured with LC-MS from MECs cultured on soft or stiff ECM for 24 h; fold change relative to 400 Pa (n = 4–5 biological replicates; LC-MS run together, repeated 2 times). (F) Relative abundance (fold change) of mitochondrial ETC subunits measured via timsTOF LC-MS of MECs cultured on soft or stiff ECM for 24 h (n = 3 biological replicates). Bolded text indicates *p $\leq$ 0.05; locations and sizes of ETC subunits graphically depicted are approximate and not to molecular scale.

5.2 Results

5.2.1 Mechanosignaling alters mitochondrial structure and function

We investigated the relationship between adhesion-dependent mechanosignaling and mitochondrial function by exogenously expressing a β1-integrin "gain-of-function" mechanosignaling model in nonmalignant human mammary epithelial cells (MECs; MCF10A). Expression of the β1-integrin (V737N, point mutation) promotes focal adhesion assembly, phosphorylation of focal adhesion kinase (FAK) (Extended Fig. 8.23A), cytoskeletal remodeling, actomyosin tension ([132]), and the suppression of mitochondrial oxygen consumption (Fig. 5.1B). Cellular respiration is primarily a product of OxPhos, in which the mitochondrial electron transport chain (ETC) consumes oxygen and reducing equivalents to produce ATP. Contrary to the paradigm that suppressed mitochondrial function (e.g., reduced respiration) occurs owing to the loss of the mitochondrial membrane potential ($\delta\ \psi$m), the β1(V737N)-integrin-expressing MECs had higher, not lower, mitochondrial membrane potential (Fig. 5.1C). To ensure that these phenotypes were not due to an indirect effect of β1(V737N)-integrin expression, we varied the surface density coating of fibronectin, an ECM component and integrin adhesion ligand that increases mechanosignaling via β1-integrin ([27]). MECs plated on a higher density of a fibronectin surface coating (60 μM/cm2) also showed repression of mitochondrial oxygen consumption, similar to β1(V737N)-integrin expression (Extended Fig. 8.23B). Furthermore, activating integrin mechanosignaling with acute exposure to manganese (Mn2+) ([244]) suppressed mitochondrial oxygen consumption (Extended Fig. 8.23C). The data indicate that increased integrin mechanosignaling impacts mitochondrial function.

Integrin mechanosignaling is highly sensitive to the stiffness of the adhesion substrate, which affects mitochondrial respiration (oxygen consumption). Accordingly, we examined the mitochondrial morphology of MECs cultured for 24 h on fibronectin-coated (6 μM/cm2) polyacrylamide hydrogel surfaces ranging in elasticity (stiffness) between normal breast (400 Pa) and tumor (6–60k Pa) ECM ([245]; [246]) (note: tissue culture polystyrene elasticity is supraphysiological, $\sim$3G Pa). MECs cultured on this range of biologically relevant ECM elasticities displayed a variety of mitochondrial morphologies, ranging from thin interconnected filaments (400 Pa), to thickened filaments (6k Pa), and then $\sim$300-nM diameter fragments with toroidal shapes (60k Pa) (Fig. 5.1D and Extended Fig. 8.23D, E). Cells respond to ECM stiffness by ligating ECM adhesion receptors that induce Rho-GTPase and Rho-associated protein kinase (ROCK) cytoskeletal remodeling and increase actomyosin tension via type-II myosins ([247]). We therefore bypassed the adhesion receptor ligation step and induced downstream mechanosignaling via an inducible ROCK, ROCK::ER ([248]), which was sufficient to suppress mitochondrial oxygen consumption (Extended Fig. 8.23A, F). In contrast, pharmacological inhibition of ROCK with Y27632 or type-II myosins with blebbistatin reduced the prevalence of the thick or toroidal mitochondrial fragments in MECs plated on the stiff ECM (Fig. 5.1D) and restored mitochondrial oxygen consumption in the ROCK::ER cells (Extended Fig. 8.23G). Finally, β1(V737N)-integrin-expressing cells displayed a fragmented/toroidal mitochondrial morphology, even on the soft ECM (Extended Fig. 8.23H) in direct contrast to MECs expressing a wild-type β1 integrin. The data indicate that mitochondrial structure and function is sensitive to the stiffness of the ECM through integrin- and ROCK-mediated mechanosignaling.

Mitochondrial function affects many aspects of cellular metabolism; therefore, we broadly examined the steady-state levels of polar metabolites present in MECs cultured on ECM surfaces that mimic the soft normal ECM (400 Pa) or stiff tumor ECM (60k Pa) (Fig. 5.1E; Videos S1, S2, and S3). MECs cultured on the stiff ECM possessed higher levels of lactate and lower levels of upstream glycolytic or pentose phosphate pathway (PPP) intermediates, which may indicate increased flux through those pathways. We also noted lower levels of serine ([249]) and

increased levels of tricarboxylic acid (TCA) cycle intermediates such as malate and fumarate, an oncometabolite ([250]), which could indicate that TCA cycle flux has reduced. Indeed, previous studies have indicated that TCA cycle impairment can affect mitochondrial structure ([251]). Since TCA cycle flux is largely dependent on the activity of the ETC, we mapped the compositional changes in ETC subunit abundance with mass-spectrometry-based proteomics (Fig. 5.1F). We found that a number of critical ETC subunits changed in abundance due to ECM stiffness and their relative levels can alter properties of mitochondrial function ([252]). These mechanosignaling-induced compositional changes in the ETC could explain the reduction of mitochondrial oxygen consumption, and the increased $\delta\ \psi$m observed when integrin mechanosignaling is high due to decreased entry of electrons via NADH (complex I) and proton flow from the inner membrane space (IMS) into the mitochondrial matrix (MM) through ATP synthase (complex V).

5.2.2 Hyperglycemia and stiff ECM facilitate similar mitochondrial responses

Hyperglycemia (>5 mM glucose) is a biochemical stress that induces mitochondrial fragmentation, raises intracellular pH (pHi) ([253]), lowers extracellular pH (pHe), and increases mitochondrial membrane potential in cultured cells ([254]). To explore whether the fragmented/toroidal mitochondrial morphologies induced by high cytoskeletal tension were similar to those induced by hyperglycemia, we increased the media glucose concentration from 5 mM ("low glucose") to 25 mM ("high glucose") for MECs plated on the soft ECM (400 Pa) and examined changes in mitochondrial organization. Lattice light sheet microscopy (LLSM), which permits live cell imaging with limited phototoxicity ([255]), revealed that exposing MECs to hyperglycemia induced a rapid transition of mitochondrial morphology from a filamentous network into fragmented/toroidal structures (Extended Fig. 8.23I; Video S4), comparable with MECs cultured on stiff ECM (Fig. 5.1D and Extended Fig. 8.23D). Moreover, cells exposed to hyperglycemia or plated on stiff ECM express similar gene profiles that have been implicated in the mitochondrial unfolded protein response (UPRmt) ([256]; [257]) (Extended Fig. 8.23J). Since both hyperglycemia and stiff ECM

induce these mitochondrial stress response genes, we hypothesized that the reorganization of the mitochondria may reflect a pro-survival stress response ([258]; [259]).

Because ECM stiffness induces mitochondrial reorganization by inducing cytoskeletal tension (Fig. 5.1D) and the similarities between hyperglycemia and ECM stiffness induced mechanosignaling, we asked if hyperglycemia was sufficient to increase cellular elasticity. Atomic force microscopy (AFM) indentation revealed that hyperglycemia significantly enhanced cortical tension in MECs (Extended Fig. 8.23K). These findings were confirmed in a second cell line, the MDA-MB-231 MECs, which is a model of triple-negative human breast cancer. Finally, similar to the reduced respiration rate induced by manipulating cytoskeletal tension, hyperglycemia also reduced mitochondrial oxygen consumption (Extended Fig. 8.23L). These findings demonstrate that biochemical and physical cues appear to stimulate similar changes in mitochondrial structure and function, and these changes may occur through the same stress response.

Mitochondrial fragmentation is thought to coordinate with mitophagy (autophagosome-mediated degradation of mitochondria) to repair dysfunctional mitochondria that have reduced mitochondrial membrane potential or increased ROS production/leak ([260]; [261]; [262]). However, our data indicated that the mitochondrial fragmentation induced by stiff ECM had elevated mitochondrial membrane potential (Fig. 5.2A and B). Thus, we reasoned that large mitochondrial fragments with toroidal morphologies likely arise through a different mechanism than has been previously described. Mitochondrial membrane potential reflects a pH differential between the mitochondrial IMS and the MM, but its measurement with lipophilic cations (TMRE) can be sensitive to changes in intracellular pH (pHi) ([263]). Since we found higher levels of lactate in the MECs cultured on stiff ECM, we were concerned that these cells may have a transiently lower pHi, which could influence the mitochondrial localization of TMRE. To verify that pHi was not confounding our measurement of $\delta\ \psi$m, we measured pHi of MECs cultured on the stiff ECM or exposed to hyperglycemia and found that both stresses increased pHi (Fig. 5.2C). One possible explanation for the mechanosensitive elevation of pHi despite elevated glycolytic metabolism could be that ROCK, a key mechanosignaling kinase, regulates the activity of SLC9A1 (Na+/H+ exchanger 1 [NHE1]).

SLC9A1 is responsible for the efflux of H+ from the cytoplasm necessary for regulating the pH of the adhesion-proximal cytosol to facilitate pH-dependent conformational changes in FAK critical for its phosphorylation and mechanosignaling downstream of integrin adhesions ([264]; [265]).

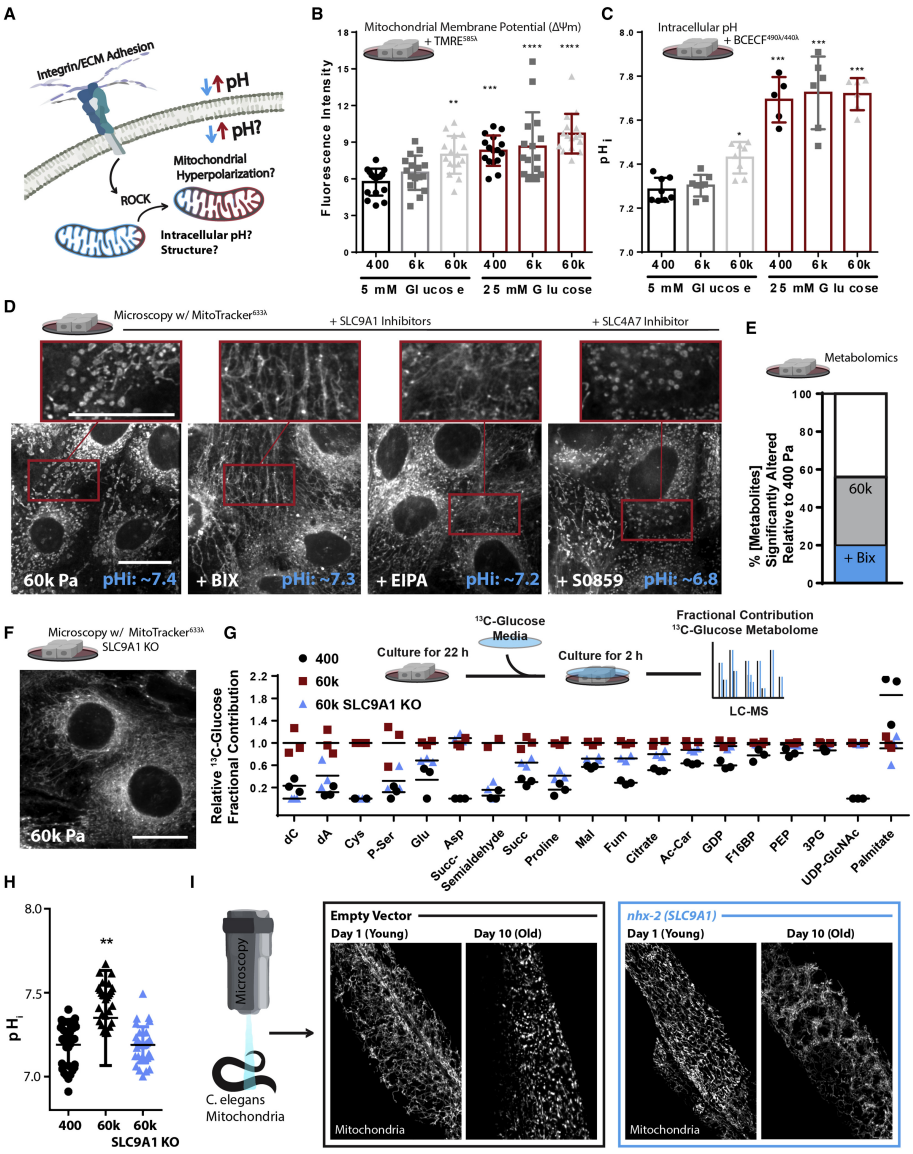

Figure 5.2: SLC9A1 facilitates stiff-ECM-induced mitochondrial programming[1]
(A) Graphical representation of the experimental question. (B) Mitochondrial membrane potential, measured after 1 h treatment of 10 nM tetramethylrhodamine ethyl-ester (TMRE) (n = 4 replicates, repeated 4 times, shown together). (C) Intracellular pH (pHi) of cells grown on soft-to-stiff ECM ± 25 mM glucose, measured via 1 μM 2',7'-bis-(2-carboxyethyl)-5-(and-6)-carboxyfluorescein, acetoxymethyl ester (BCECF) (n = 2 replicates, repeated 3 to 4 times, shown together). (D) Confocal microscopy depicting mitochondrial network structure and caption depicting pHi measurements

[1]This figure was generated by co-authors.

(mean of n = 5) in MECs on 60k Pa surfaces treated with 500 nM BIX, 10 μM EIPA, 50 μM S0859, or vehicle for 24 h; 100 nM MitoTracker (deep red FM) and 1 μM BCECF (n = 2 replicates, repeated 3 times). Scale bar, 10 μm. MitoMAPR quantification: 60k (9), BIX (20), EIPA (20), and S0859 (7) junctions per network. (E) Metabolomics (LC-MS) of cells cultured on 400 or 60k ECM for 24 h; percent (%) metabolites significantly altered relative to 400 Pa ± 500 nM BIX (n = 4–5 biological replicates; LC-MS run together, repeated 2 separate times). (F) Confocal microscopy depicting mitochondrial network structure of SLC9A1 KO cells on 60k Pa surfaces for 24 h; 100 nM MitoTracker (deep red FM). Scale bar, 10 μm. MitoMAPR quantification: WT (8) and SLC9A1 KO (21) junctions per network. (G) Fractional contribution of 13C6-glucose to a selection of pertinent metabolites. Two hour labeling (n = 3 biological replicates; LC-MS run together). (H) Intracellular pH (pHi) of WT or SLC9A1 KO cells grown on soft-to-stiff ECM measured via 1 μM 2',7'-Bis-(2-carboxyethyl)-5-(and-6)-carboxyfluorescein, acetoxymethyl ester (BCECF) (n = 6 replicates, repeated 4 times, shown together). (I) Representative microscopy depicting mitochondrial network structure of live C. elegans-expressing MLS::mRuby (mitochondrial matrix) grown on empty vector or nhx-2 (SLC9A1 ortholog) RNAi from hatch of 5- or 15-day-old animals.

5.2.3 SLC9A1-mediated ion exchange affects mitochondrial structure and function

To test if the elevated pHi was responsible for the altered mitochondrial morphology observed in MECs cultured on stiff ECM, we lowered pHi by inhibiting SLC9A1 with BIX and EIPA, and SLC4A7 (Na+/HCO3$\sim$ cotransporter) with S0859. While all of these interventions lowered pHi in MECs on stiff ECM to levels equivalent or lower than soft ECM, only SLC9A1 inhibition restored the filamentous mitochondrial morphology (Fig. 5.2D and Extended Fig. 8.24A). These data suggest that a pHi-independent effect of SLC9A1 may be responsible for the mitochondrial morphology induced by stiff ECM. SLC9A1 inhibition also restored the concentrations of approximately 60% of the significantly altered polar metabolites we measured in MECs plated on the stiff ECM back to the concentrations observed in MECs on soft ECM (Fig. 5.2E). SLC9A1 inhibition also rescued the impaired mitochondrial oxygen consumption caused by β1(V737N)-integrin or ROCK::ER expression (Extended Fig. 8.24B–D). Since both hyperglycemia and ROCK activity have been shown to increase pHi ([253]; [266]), we assayed whether the proportional decrease in pHe occurred (extracellular acidification, H+ pumped out of the cell) and found that the pHi:pHe dynamics induced by hyperglycemia were sensitive to inhibition ROCK or SLC9A1 (Extended Fig. 8.24E).

CRISPR-mediated knockout of SLC9A1 in MECs (SLC9A1 KO) resulted in MECs that maintained a filamentous mitochondrial morphology on stiff ECM (Fig. 5.2G and Extended Fig. 8.24F). SLC9A1 KO was sufficient to normalize mitochondrial respiration in MECs exposed to hyperglycemia, as well as those on high-density fibronectin coating (Extended Fig. 8.24G and H). SCL9A1 KO cells cultured on stiff ECM metabolized glucose similarly to wild-type (WT) cells cultured on soft ECM (Fig. 5.2G) and did not increase pHi when cultured on stiff ECM (Fig. 5.2H). To explore the physiological relevance of these findings, we examined the ability of SLC9A1 to affect mitochondrial morphology in C. elegans, a model organism that is amenable to live microscopy of mitochondria and genetic manipulations ([267]) that has been used extensively to study OxSR ([268]). RNAi-mediated knockdown of nhx-2 (SLC9A1 ortholog) prevented the mitochondrial fragmentation/toroidal phenotype typically found in the aged gut epithelium of this organism (Fig. 5.2I) and instead promoted an abundant and hyperfused mitochondrial network (Extended Fig. 8.24I–L).

As a byproduct of H+ efflux (raising pHi, lowering pHe) SLC9A1 facilitates Na+ import that subsequently reverses the directionality of the Na+/Ca2+ exchangers (NCX, SLC8A1-3), a process which ultimately causes mitochondrial ROS production via mitochondrial calcium (Ca2+) overload ([269]; [270]). Additionally, cellular Na+ can affect the solubility of mitochondrial calcium phosphate precipitates, fluidity of the mitochondrial inner membrane, and ROS production from Complex III of the ETC ([271]). To determine whether adhesion-dependent cytoskeletal tension regulates mitochondrial Ca2+ content through SLC9A1 activity, we measured mitochondrial and total cellular Ca2+ levels in MECs plated on a range of soft-to-stiff ECM. Imaging of Rhod2-AM, calcium green-1 AM, and Fura 2 AM revealed that mitochondrial Ca2+ concentration was highest on the stiff ECM and could be reduced either by inhibiting or knocking out SLC9A1 (Fig. 5.3B and Extended Fig. 8.25A). SLC9A1 inhibition was also able to suppress the mitochondrial ROS production induced by mitochondrial Ca2+ loading in the CGP37157 (7-Chloro-5-(2-chlorophenyl)-1,5-dihydro-4,1-benzothiazepin-2(3H)-one)-treated cells (Fig. 5.3C, Extended Fig. 8.25B, C).

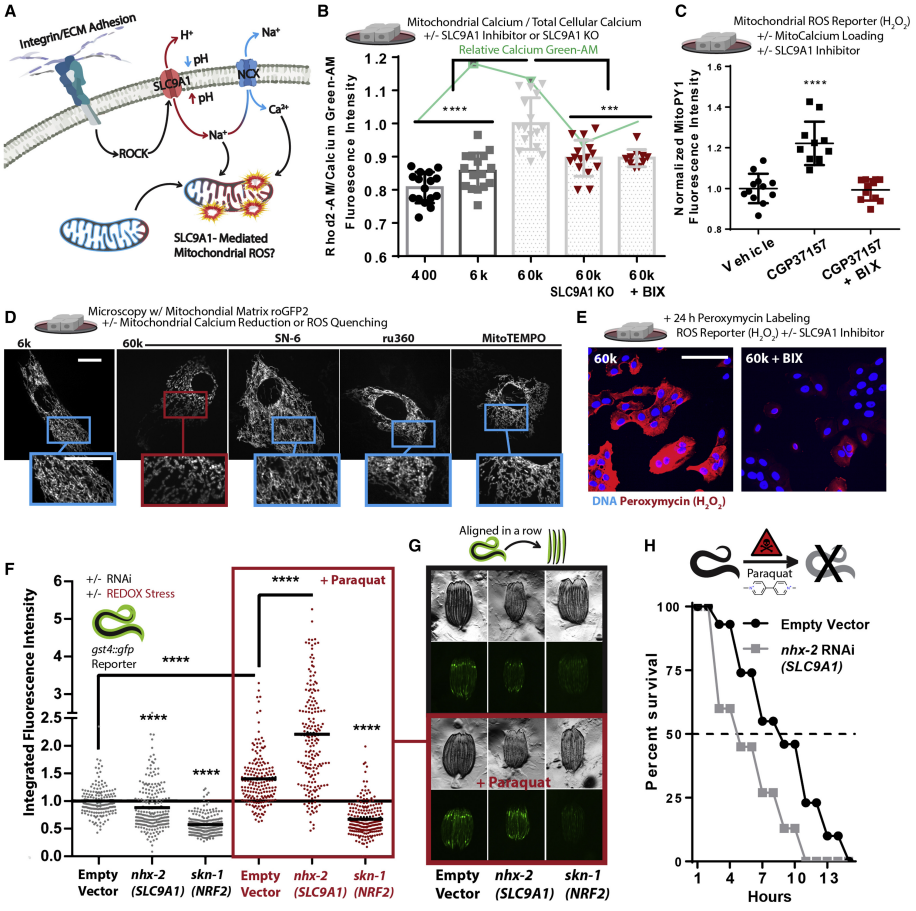

Figure 5.3: SLC9A1 facilitates mitochondrial oxidative stress[1]

(A) Graphical schematic indicating how SLC9A1 affects mitochondrial oxidative stress. (B) Calcium content of MECs cultured on soft-to-stiff ECM for 24 h, treated with 2 μM Rhod2-AM (mitochondrial) and 2 μM calcium green-1-AM (intracellular) (n = 4 replicates, repeated 4 times). (C) Mitochondrial H2O2 production of cells cultured on 6k Pa surfaces and treated with 500 nM BIX or vehicle for 24 h and then 5 μM MitoPy1 and vehicle or 1 μM CGP37157 for 1 h (n = 6, repeated 2 times). (D) Confocal microscopy depicting mitochondrial network structure of PFA-fixed MECs on 6 or 60k Pa ECM treated with 1 μM ru360 (MCU inhibitor), 10 μM SN-6 (NCX reverse mode inhibitor, opposite direction of CCP37157), and 2 μM mitoTEMPO for 24 h. Scale bar, 10 μm. MitoMAPR quantification: 6k (21), 60k (6), 60k + SN-6 (27), 60k + Ru360 (13), and 60k + MitoTEMPO (12) junctions per network. (E) Confocal microscopy of peroxymycin (H2O2) ([249]) staining over 24 h on 60k Pa ECM ± 500 nM BIX; quantitated in Figure S3I. (F and G) gst-4p::gfp reporter fluorescent intensity of C. elegans measured with a large particle cytometer ± 50 mM paraquat (n = 177, 206, 190, 187, 191, and 215 animals in order, left to right) with representative images (G) of C. elegans quantified, repeated 3 times. (H) C. elegans survival in 50 mM paraquat at 1 day; animals grown from hatch on nhx-2 RNAi versus empty-vector control (80 worms per condition, repeated 3 times).

[1]This figure was generated by co-authors.

Increased fibronectin surface density (Extended Fig. 8.25D–F), hyperglycemia (Extended Fig. 8.25G), and Mn2+ treatment altered mitochondrial structure, increased mitochondrial Ca2+, and enhanced mitochondrial ROS production, in part through the activity of SLC9A1 (Extended Fig. 8.25H and I). Consistently, treating cells with CGP37157 or kaempferol (mitochondrial calcium uniporter [MCU] activator) to increase mitochondrial Ca2+ content was sufficient to induce the fragmented/toroidal mitochondrial morphology in MECs plated on the soft ECM (Extended Fig. 8.25J). Suppression of mitochondrial ROS with 2-(2,2,6,6-tetramethylpiperidin-1-oxyl-4-ylamino)-2-oxoethyl)-triphenylphosphonium chloride (MitoTEMPO), or suppression of the mitochondrial Ca2+ loading via selective inhibition of the reverse mode of NCX exchangers with SN-6 (ethyl 2-[[4-[(4-nitrophenyl)methoxy]phenyl]methyl]-1,3-thiazolidine-4-carboxylate), and the MCU, with ru360 (oxo-bridged dinuclear ruthenium ammine), was also sufficient to prevent the fragment/toroid formation on stiff ECM (Fig. 5.3D and Extended Fig 8.25K; Videos S5 and S6), providing additional evidence that Ca2+ overload and ROS were causative of mitochondrial remodeling.

To directly test whether ECM stiffness could impact ROS production, we next monitored the ROS production in MECs on a range of soft-to-stiff ECM over the course of 24 h ([249]). As expected, we found that cells seeded on stiff ECM produced more ROS than those on soft ECM, in an SLC9A1-dependent fashion (Fig. 5.3E and Extended Fig. 8.25L). Additionally, ROS production in ROCK:ER cells was also suppressed by SLC9A1 inhibition (Extended Fig. 8.25M). Finally, to determine whether the functional role of SLC9A1 on ROS-mediated oxidative stress was conserved in a whole organism, we tested its impact on oxidative stress in C. elegans. Using an reporter for oxidative stress (gst-4p::gfp), we found that nhx-2 (SLC9A1) knockdown reduced the expression of the reporter, indicating a lower basal level of ROS production/response in these animals (Fig. 5.3F and G). In agreement with the free radical theory of aging, which postulates that lifespan is shortened due to accumulated oxidation-mediated damage, we found that the lifespan of the C. elegans nhx-2 knockdown was dramatically extended (Extended Fig. 8.25N).

Since oxidative stress primarily regulates the expression of gst-4p through the transcriptional activity of skn-1 (NRF-2 ortholog), which facilitates the canonical oxidative stress response (OSR) by prompting transcription of genes with antioxidant response elements (ARE) in their promoters (e.g., gst-4p), we used a knockdown of skn-1/NRF-2 as a negative control. As a positive control, we treated the gst-4p::gfp reporter animals with paraquat, an herbicide that promotes mitochondrial ROS leak/production ([272]), which increased oxidative stress reporter activity. Surprisingly, paraquat treatment induced a more robust gst-4p::gfp reporter response to paraquat in nhx-2 knockdown animals (Fig. 5.3F and G). This result suggests that nhx-2 knockdown exacerbated paraquat-induced mitochondrial oxidative stress, likely because OxPhos could not be throttled. To test the difference in oxidative stress sensitivity of nhx-2 knockdown animals, we assayed the survival of these animals in response to paraquat-induced oxidative stress. Corroborating the gst-4p::gfp reporter measurements (Fig. 5.3F and G), the nhx-2 knockdown animals were more sensitive to paraquat exposure than control animals (Fig. 5.3H). Accordingly, these results indicate that SLC9A1 activity may induce OxSR via adhesion-mediated production of sub-lethal mitochondrial ROS, which promote mitochondrial reorganization (toroid/fragment formation) and may prepare cells and animals to overcome subsequent oxidative stresses.

The greater induction of gst-4p::gfp and the rapidity of death observed in the nhx-2 knockdown animals suggested that they were less adapted to manage the ROS-mediated oxidative stress induced by paraquat. Since greater SLC9A1 activity appeared to promote mitochondrial ROS production (Fig. 5.3C, E, and Extended Fig. 5.3G, I, and J) we hypothesized that because the nhx-2 knockdown animals experienced lower basal levels of ROS exposure, they were not pre-adapted to survive the paraquat exposure. It has been reported that mitochondrial stresses, particularly ROS production and respiratory dysfunction, promote adaptive reprogramming of mitochondrial function and OxSR through a process described as “mitohormesis” ([273]; [274]; [275]). In biological systems, hormesis describes a biphasic dose response in which a stress/signal is moderated by a compensatory response ([276]). For example, cancer cells produce more ROS than healthy cells produce, but the oncogene-induced overproduction of ROS elicits compensatory ROS quenching

response mediated by the transcriptional activity of NRF2 (nuclear factor erythroid-2-related factor 2). This NRF2-mediated ROS quenching OSR facilitates metabolic remodeling that provides cancer cells with OxSR requisite to harness ROS-mediated proliferation and migration effects without succumbing to ROS-mediated cell death ([226]). OxSR in cells and animals can be the product of NRF2-mediated OSR or other adaptive programs, which are less well defined.

5.2.4 Stiff ECM forces HSF1-mediated mitochondrial reprogramming

Since MECs cultured on stiff ECM experienced a greater amount of ROS stress as they adapted to the environment via integrin adhesion, we sought to determine if they had induced the NRF2-mediated OSR to survive and adapt (Fig. 5.4A). To test this, we used RNA sequencing (RNA-seq) to characterize the transcriptional state of MECs cultured on soft-to-stiff ECM or soft ECM with hyperglycemia for 24 h. We compared the transcriptional programs induced by hyperglycemia and adhesion substrate elasticity because they both affect cytoskeletal tension, mitochondrial reorganization (fragment/toroid), and mitochondrial oxygen consumption. Unsupervised hierarchical clustering demonstrated that the greatest transcriptomic signature overlap occurred in MECs plated on the soft ECM (400 Pa) that were exposed to extreme hyperglycemia (25 mM) and MECs plated on the stiff ECM (60k Pa) with physiological glucose (5 mM) (Fig. 5.4B). Gene ontology analysis indicated that the categories that were downregulated in response to stiff ECM included oxidation-reduction process, oxidoreductase activity, ion transport, mitochondrion, and mitochondrial inner membrane (Extended Fig. 8.26A). We also found that of all mitocarta 2.0 ([277]) annotated mitochondrial genes encoded by the nuclear genome, which change (up or down) in response to hyperglycemia or stiff ECM, the vast majority of these changes were conserved between both stresses (Fig. 5.4C). Specifically, a number of ETC subunits were downregulated (NDUFA7, ATP5B, ATP5D, COX6b1, etc.), while mitochondrial-localized chaperones and proteases, which facilitate mitochondrial import, protein folding, and structural remodeling of the mitochondria during UPRmt, were upregulated (YME1L1, HSPE1, DNAJC10 [hsp40], HSPD1, HSPA9, HSPB11, etc.) ([278]). With regard to NRF2 and the OSR it facilitates, unexpectedly, cells

cultured on stiff ECM had downregulated many canonical ARE-containing target genes (HMOX1, TXN, GPX2, GPX4, NQ01, etc.).

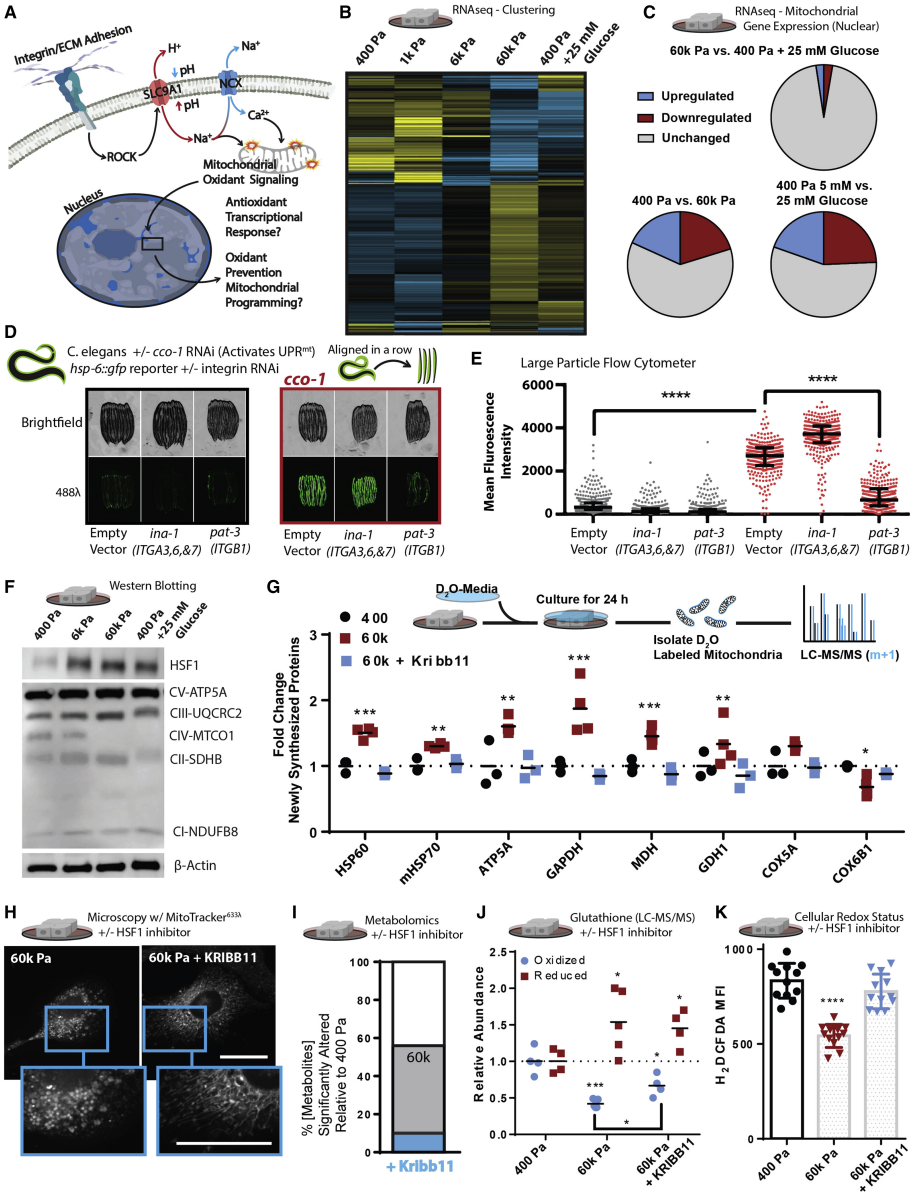

Figure 5.4: Mechanosignaling facilitates mitochondrial stress response via HSF1[1]

(A) Graphical representation of the paradigm and remaining questions. (B) Heatmap depicting unsupervised hierarchical clustering of RNA-seq of cells cultured on soft-to-stiff ECM for 24 h ± 5 or 25 mM glucose (n = 2 duplicate libraries of 3 biological replicates, 10 million reads per library). (C) Comparison of significantly altered MitoCarta 2.0 cataloged genes from the 400 Pa, 60k, and 400 Pa + 25 mM glucose conditions shown in (B). (D) hsp-6::gfp reporter fluorescent intensity representative images of C. elegans, quantified in (E). RNAis were mixed at a 5:1 ratio of

[1]This figure was generated by co-authors. I analyzed the RNAseq data and contributed panels (B) and (C).

ev, ina-1, or pat-3 RNAi to ev or cco-1 RNAi as depicted (hsp-6 is the HSPA9/mtHSP70 ortholog). (E) Quantification of hsp-6::gfp reporter fluorescent intensity of C. elegans measured with a large particle cytometer, ± cco-1 RNAi (n = 387, 309, 377, 326, 312, and 294 animals in order, left to right, repeated 3 times). (F) Western blot depicting relative protein abundance of HSF1, ETC components, or β-actin within 5 μg of total protein derived from lysates of MECs cultured on soft-to-stiff ECM for 24 h ± 5 or 25 mM glucose. (G) Stable isotope mitochondrial proteomics of crude mitochondrial fraction of MECs grown 400 or 60k Pa ECM for 24 h ± 2 μM KRIBB11 (n = 4 biological replicates; LC-MS run together, repeated 2 times) (H) Confocal microscopy of 100 nM MitoTracker (deep red FM) stained and fixed (PFA) cells cultured on 60k Pa ECM surfaces for 24 h ± vehicle or 2 μM KRIBB11. MitoMAPR quantification: 60k (7) and 60k + Kribb11 (12) junctions per network. (I) Metabolomics (LC-MS) of cells cultured on 400 or 60k Pa ECM for 24 h; percent (%) significantly altered relative to 400 Pa ± 2 μM KRIBB11 (n = 4–5 biological replicates; LC-MS/MS run together, repeated 2 times). (J) Oxidized/reduced glutathione (NEM protected) measurements of MECs grown on 400 or 60k Pa ECM for 24 h ± 2 μM KRIBB11 (n = 4 biological replicates, repeated two times) (n = 4–5 biological replicates; LC-MS run together, repeated 2 times). (K) Oxidative stress indicator intensity of cells after 1 h. MECs cultured on varied 400 or 60k Pa ECM for 24 h ± vehicle or 2 μM KRIBB11, measured with 2 μM 2',7'-dichlorodihydrofluorescein diacetate (H2DCFDA) (n = 4, repeated 3 times, shown together).

It was paradoxical that genes with AREs in their promoters were not upregulated in MECs cultured on stiff ECM, since they had experienced a greater amount of redox stress. However, this result could indicate that the transcriptomes measured reflected a post OSR state, in which oxidants were not actively produced, and therefore, ARE-mediated gene expression was downregulated. To address this possibility, we compared the transcriptional signature of MECs cultured on stiff ECM with other known stress responses ([279]) that can remediate damage resulting from oxidative stress, such as protein misfolding ([280]). We found that the majority of genes, which characterize the integrated stress response (ISR), were downregulated; heat shock response (HSR) genes were upregulated; and genes ascribed to the OSR and UPRmt were inconsistently up- and downregulated. However, when comparing the upregulated genes of the UPRmt, OSR, and HSR, we noted that the upregulated genes associated with all of these stress responses were primarily heat shock proteins (HSPs) regulated by heat shock factor 1 (HSF1) (See Table 8.3) ([279]).

Activation of UPRmt is thought to occur in response to mitochondrial respiratory dysfunction, so we tested if integrin signaling affected the activation of the UPRmt to the same degree as stiff ECM. UPRmt has been most well defined in C. elegans, so we used an established model of cytochrome c oxidase-1 subunit Vb (cco-1/COX4) knockdown, which robustly induces a flu-

orescent UPRmt reporter, hsp-6::gfp (HSPA9/mtHSP70 ortholog), in C. elegans. We performed double RNAi of cco-1 in conjunction with knockdown of ina-1 (ITGA ortholog, most similar to ITGA3,6, and 7) or pat-3 (ITGB1 ortholog). We found that pat-3/ITGB1 knockdown robustly attenuated cco1-mediated UPRmt, which suggests that integrin signaling is an important input to the activation of UPRmt (Fig. 5.4D and E). We then determined that HSF1 is required for the maximal activation of cco1-mediated UPRmt in C. elegans, as RNAi knockdown of hsf-1 partially suppressed UPRmt induction (Extended Fig. 8.26B). Since C. elegans activate UPRmt primarily through atfs-1 ([281]), which does not have a conspicuous mammalian ortholog ([282]), the data suggest that HSF1 may play a larger role in the mammalian UPRmt ([283]) or may resolve a UPRmt-overlapping aspect of mitochondrial dysfunction ([284]) that promotes OxSR.

HSF1 is primarily known to regulate a transcription program that facilitates the survival of cells experiencing heat stress ($\sim$43°C), but it may have an unappreciated role in OxSR since its transcriptional activity is regulated by ROS (H2O2) ([285]). Upregulation of HSF1 expression is an outcome of the NRF2-mediated OSR because the HSF1 promoter ($\sim$1.5k to $\sim$1.7k bp) is heavily enriched with AREs ([286]). Indeed, we found that HSF1 abundance increased in response to stiff ECM or hyperglycemia, as was mitochondrial ATP5A, but not the mitochondrial encoded subunit of oxygen consuming ETC complex IV subunit, MTC01 (Fig. 5.4F). Inhibiting SLC9A1 in MECs cultured on stiff ECM repressed the expression of HSF1 and its downstream targets (Extended Fig. 8.26C). Treatment with MitoTEMPO, a mitochondria-targeted antioxidant, suppressed stiff ECM or paraquat-induced HSF1 and HSF1-target gene expression (Extended Fig. 8.26D and E). Overall, these data indicate that ROS induced by the stiff ECM via SLC9A1 activity promotes HSF1 expression and activity (Fig. 5.3E and Extended Fig. 8.25I).

We postulated that HSF1 could modify mitochondrial structure/function by influencing the expression of the mitochondrial import machinery, such as mtHSP70 (HSPA9) ([287]), or by regulating mitochondrial biogenesis in collaboration with peroxisome-proliferator-activated receptor gamma coactivator 1-alpha (PGC-1α) ([288]). To test these possibilities, we measured the incorporation of newly synthesized proteins into the mitochondria with stable isotope incorporation

mass spectrometry, which revealed that the stiff ECM enhanced the incorporation of newly synthesized proteins in an HSF1-dependent fashion (Fig. 5.4G). Consistent with the hypothesis that an HSF1-mediated response facilitated the stiff ECM-induced mitochondrial adaptation, HSF1 inhibition was sufficient to prevent the altered mitochondrial morphology induced by stiff ECM (Fig. 5.4H). Inhibition of HSF1 also restored $\sim$80% of the metabolite concentrations measured in MECs plated on stiff ECM to that of MECs cultured on soft ECM (Fig. 5.4I). Overall, these findings suggest that ECM mechanosignaling alters mitochondrial reorganization and metabolic programing through a heat-stress-independent HSF1-mediated program ([289]).

To explore if adhesion-mediated mechanosignaling facilitates a HSF1-dependent OxSR program, we quantified the levels of reduced and oxidized glutathione, the primary cellular oxidant detoxification and redox (reduction:oxidation) management system, which becomes oxidized in the presence of ROS. MECs cultured on stiff ECM had lower levels of oxidized glutathione than those on soft ECM. HSF1 inhibition was sufficient to significantly increase the levels of oxidized glutathione in MECs on stiff ECM (Fig. 5.4J). Metabolomics allowed us to observe that many metabolite changes that reflect OxSR ([290]), such as PPP activity, which generates reduced nicotinamide adenine dinucleotide phosphate (NADPH) required to regenerate reduced glutathione and mitigate oxidative stress, were also elevated in response to stiff ECM, and could be normalized by inhibiting HSF1 (Extended Fig. 8.26F). Indeed, HSF1 inhibition abolished the enhanced reducing capacity of MECs that had been cultured on stiff ECM for 24 h prior to the measurement of redox stress (Fig. 5.4K). The data indicate that while MECs experience more redox stress in response to stiff ECM, they adapt and acquire an OxSR through HSF1-dependent changes in cellular metabolism facilitated by mitochondrial reprogramming via compositional changes (Fig. 5.1D, Fig. 5.4E and F).

To examine how HSF1 influences mitochondrial metabolic flux, we traced the metabolic fate of isotopic glucose metabolism in cells grown on soft or stiff ECM with or without HSF1 inhibition (Fig. 5.5A). We allowed the cells to metabolize the labeled glucose for 2 h to ensure robust labeling of mitochondrial TCA cycle intermediates ([291]). Consistently, we found that

stiff ECM dramatically alters the relative abundance of the whole metabolome, and also the flux of glucose metabolism (Fig. 5.5B and C). Of note, we observed increases in the fractional labeling (enrichment of isotopic carbon derived from glucose) in many metabolites of the TCA cycle, urea cycle, and purine and pyrimidine metabolism pathway (Extended Fig. 8.27), which could indicate a concerted remodeling of metabolism to support mechanosignaling or OxSR (Fig. 5.6A). Interestingly, the oncometabolite fumarate ([250]) is a metabolic intermediate between the urea cycle and the TCA cycle that may also be a driver of the altered mitochondrial morphologies observed ([292]) in cells adapting to stiff ECM.

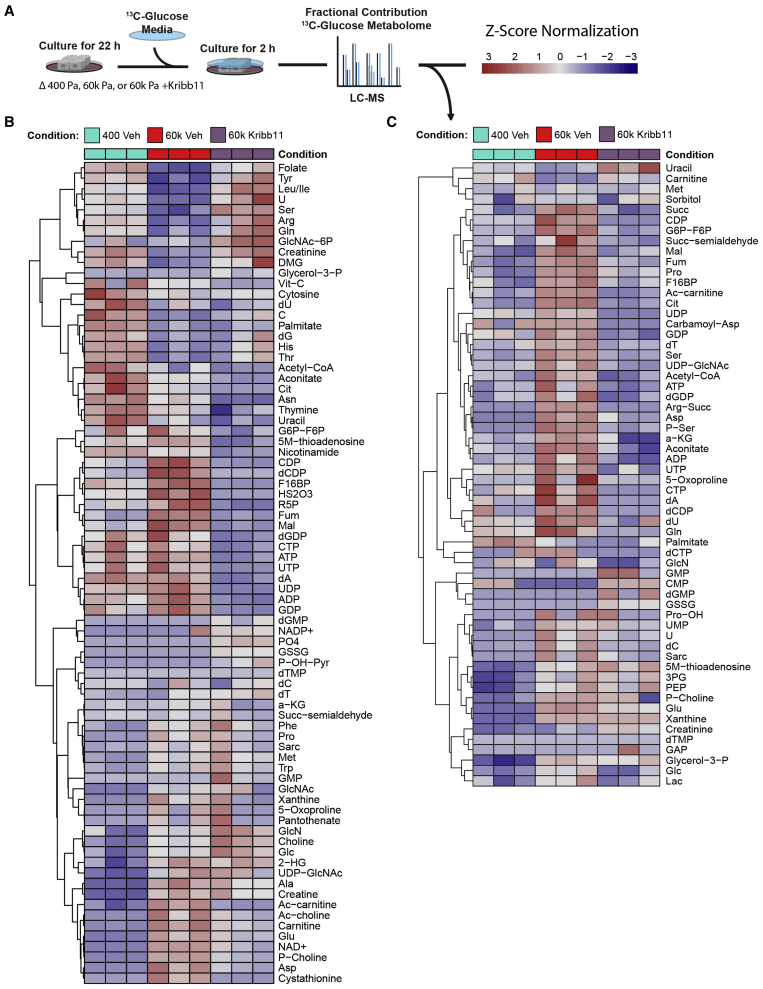

Figure 5.5: HSF1 facilitates mechanosignaling-mediated metabolic reprogramming[1]
(A) Graphical depiction of experimental design. (B) Heatmap of relative metabolite levels of MECs cultured on 400 or 60k Pa vehicle (DMSO treated) or 60k Pa ECM with 2 μM Kribb11 for

[1]This figure was generated by co-authors. I pre-processed the metabolomics data shown here.

22 h followed by media exchanged for 13C6-glucose containing media for 2 h and then harvested for LC-MS analysis (n = 3 biological replicates). (C) Heatmap of fractional contributions of 13C6-glucose to the metabolome of MECs cultured on 400 Pa or 60k Pa vehicle (DMSO treated) or 60k Pa ECM with 2 μM Kribb11 over the course of 2 h. MECs were previously cultured for 22 h in the same conditions with unlabeled glucose media (n = 3 biological replicates; LC-MS analysis).

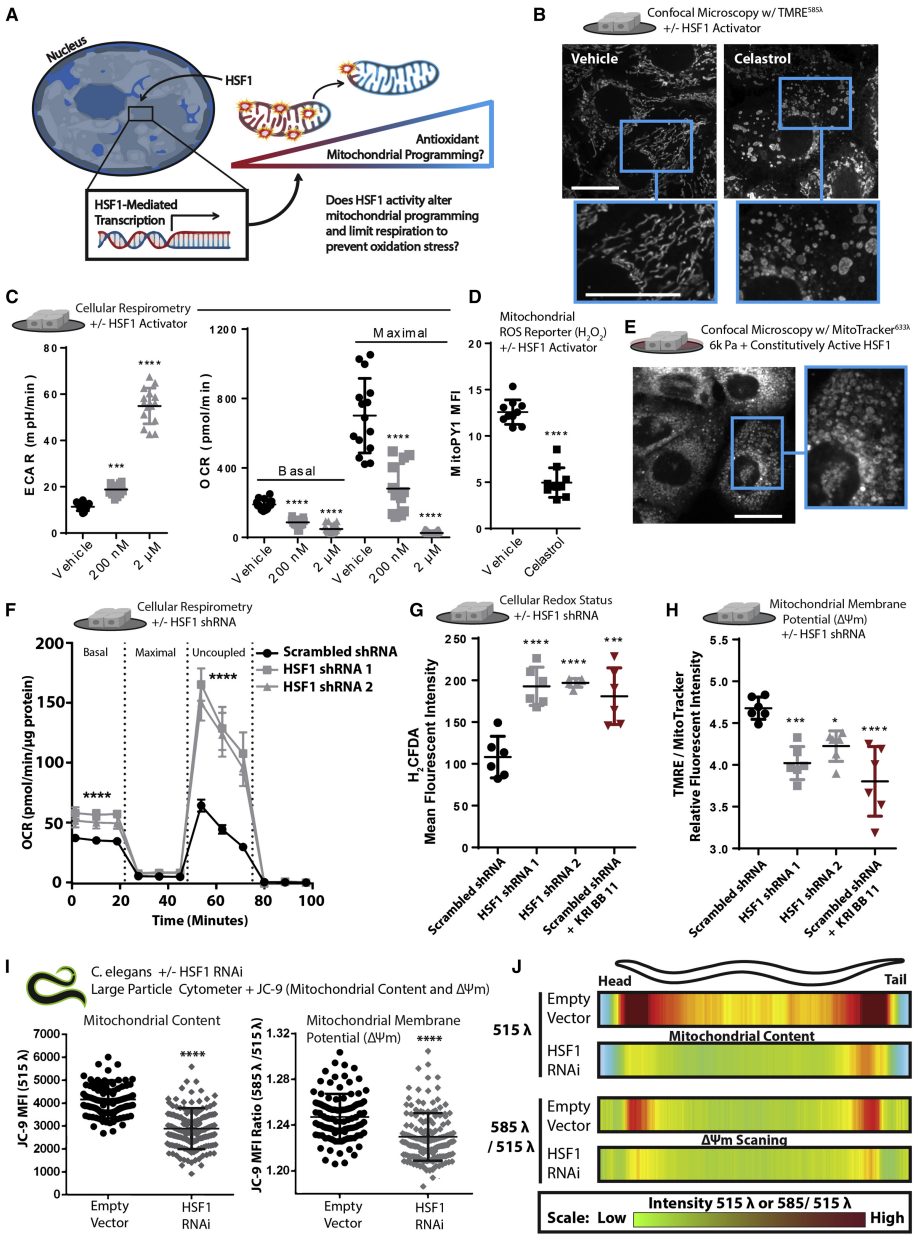

Figure 5.6: HSF1 induces mitochondrial reprogramming[1]

(A) Graphical depiction of experimental question. (B) Confocal microscopy depicting morphology and mitochondrial membrane potential staining of live cells via 10 nM TMRE staining ± vehicle or 2 μM celastrol treatment for 40 min prior to imaging. MitoMAPR quantification: vehicle (10)

[1]This figure was generated by co-authors.

and celastrol (6) junctions per network. (C) Extracellular acidification rate (ECAR) and OCR of MECs treated ± vehicle or 200 nM celastrol for 24 h or 2 μM celastrol for 40 min (n = 5 wells, 3 replicate measures, repeated 3 times). (D) Mitochondrial H2O2 production of cells treated with 2 μM celastrol treatment for 40 min, measured with 1 μM MitoPY (n = 5, repeated 2 times). (E) Confocal microscopy depicting mitochondrial morphology of PFA-fixed cells expressing constitutively active HSF1 and cultured on 6k Pa ECM for 24 h, stained with 100 nM MitoTracker (deep red FM). (F) OCR of MECs expressing a scrambled shRNA or two different shRNAs targeting HSF1 (n = 5 wells, 3 replicate measures, repeated 3 times). (G) Oxidative stress indicator intensity after 1 h in MECs cultured on TCPS expressing a scrambled shRNA ± 2 μM KRIBB11 or two different shRNAs targeting HSF1, measured with 2 μM 2',7'-dichlorodihydrofluorescein diacetate (H2DCFDA) (n = 6 wells, repeated 3 times). (H) Mitochondrial membrane potential of MECs cultured on TCPS expressing a scrambled shRNA ± 2 μM KRIBB11 or two different shRNAs targeting HSF1, measured with 1 nM TMRE and 100 nM MitoTracker after 1 h staining (n = 6, repeated 3 times). (I) Mean fluorescent intensity of 150 per condition JC-9-stained C. elegans grown on empty vector or hsf-1 RNAi from hatch, depicting mitochondrial mass (515 λ alone) or mitochondrial membrane potential (585 λ/515 λ), spatially quantified in Fig. 5.5J. (J) Heatmap depicting mitochondrial content (515 λ alone) or mitochondrial membrane potential (585 λ/515 λ) across the body length (head [left] to tail [right]) of 150 C. elegans animals grown on empty vector or hsf-1 RNAi from hatch; JC-9 staining via administration of JC-9 loaded C. elegans food (E. coli) (repeated 3 times).

HSF1 can be pharmacologically activated using celastrol, a reactive electrophile derived from the "Thunder of God" vine (Tripterygium wilfordii) ([293]), which was sufficient to induce mitochondrial fragmentation/toroids in MECs on all substrates (Fig. 5.6B and Extended Fig. 8.28A). HSF1 activation also increased extracellular acidification rate (ECAR), a proxy measure of glycolytic flux, and reduced mitochondrial oxygen consumption (Fig. 5.6C). A mitochondria-localized ROS (H2O2) reporter (MitoPY1) revealed that MECs treated with Celastrol had significantly suppressed mitochondrial ROS production (Fig. 5.6D). Expression of a constitutively active HSF1 induced fragmented/toroidal mitochondria in MECs plated on the soft ECM (Fig. 5.6E and Extended Fig. 8.28B) and increased mitochondrial membrane potential (Extended Fig. 8.28C). Conversely, HSF1 knockdown increased mitochondrial respiration (Fig. 5.6F), induced oxidative stress (Fig. 5.6G and Extended Fig. 8.27D), and decreased mitochondrial membrane potential (Fig. 5.6H and Extended Fig. 8.28E) in both the MCF10A (nonmalignant) and MDA-MB-231 (aggressive and malignant) MECs (Extended Fig. 8.28F–I). The physiological relevance of these findings was confirmed by reducing hsf-1 expression in C. elegans, which decreased mitochondrial content and membrane potential throughout the whole organism (Fig. 5.6I and J). This indicates

that increased HSF1 activity reduces mitochondrial oxygen consumption and increases the mitochondrial membrane potential because proton flow from IMS to MM is reduced, which may limit ROS produced as a byproduct of OxPhos, mediating an enhanced OxSR by suppressing the mitochondrial contribution to net oxidative stress.

5.2.5 ECM mechanosignaling engenders mitochondrial OxSR via HSF1 and YME1L1

Thus far, the data suggested that adhesion-mediated mechanosignaling stimulates a heat-stress-independent HSF1 transcriptional program, previously implicated in cancer, that alters mitochondrial structure/function and restricts mitochondrial respiration and oxidant production. Accordingly, we next stress-tested if the OxSR adaptation was sufficient to oppose mitochondrial ROS-mediated apoptosis, a trait associated with many tumors ([294]). We treated MECs cultured on soft-to-stiff ECM, with paraquat and assayed for apoptosis ([258]). Consistent with the hypothesis that mechnosignaling promotes OxSR via HSF1, MECs cultured on stiff ECM were less sensitive to paraquat treatment. This OxSR phenotype could be further enhanced via expression of constitutively active HSF1 and ablated by HSF1 knockdown or inhibition (Fig. 5.7A and B, Extended Fig. 8.29A and B). Functional links between mechanosignaling and mitochondrial OxSR adaptation were verified by determining that mitochondrial depletion negated the impact of ECM stiffness on redox sensitivity to paraquat (Extended Fig. 8.28C).

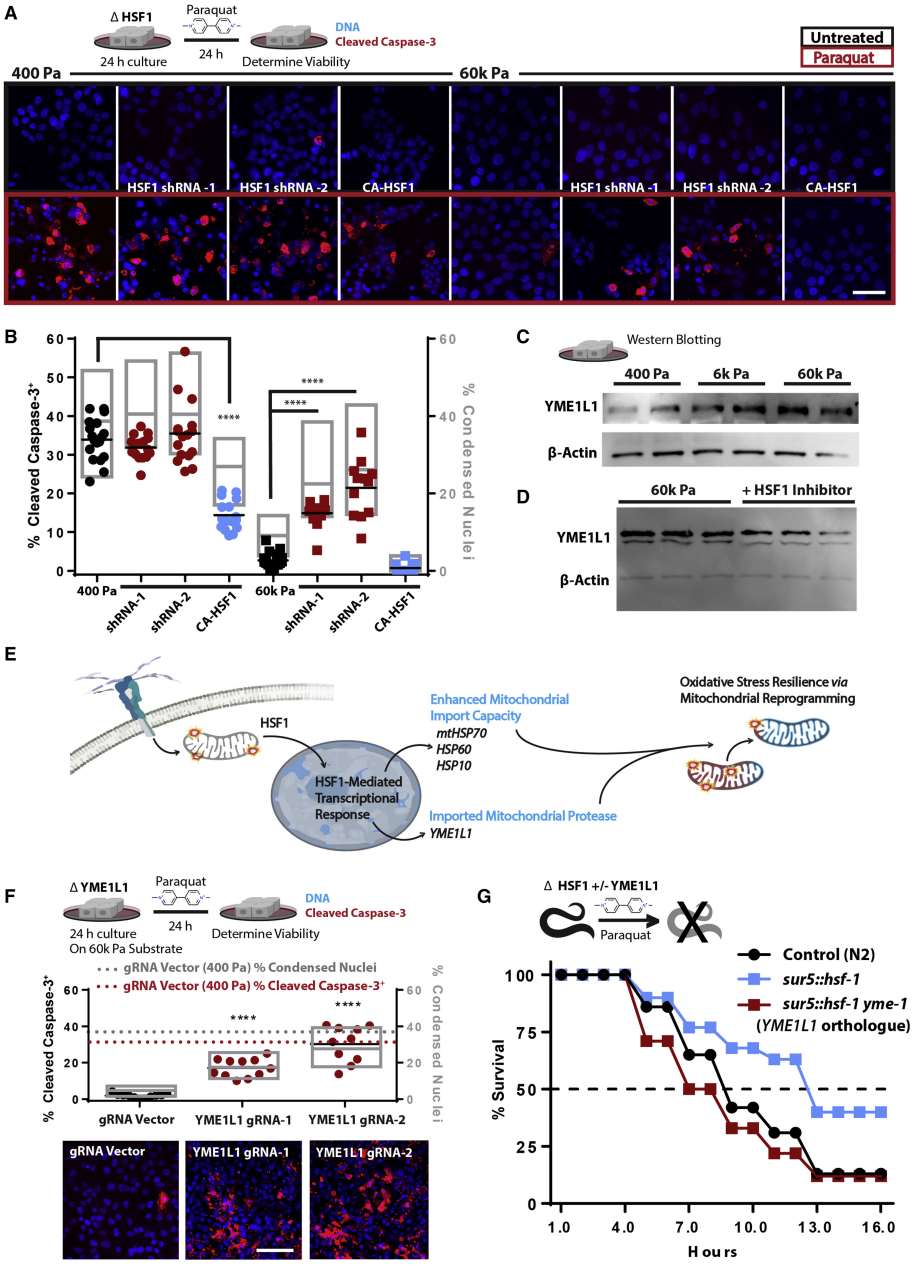

Figure 5.7: ECM-mediated mechanosignaling controls OxSR via HSF1 and YME1L1[1]
(A) Confocal microscopy of indicators of apoptosis with cleaved caspase-3 staining (red) and nuclear condensation (DAPI) of MECs cultured on 400 or 60k Pa ECM for 24 h with subsequent 24 h ± 10 mM paraquat treatment. 100k cells/well of 24-well plate (n = 4 replicates, repeated 3 separate times). (B) Quantitation of cells from 16 field views depicted in (G) for condensed nuclei and cleaved caspase-3-positive cells (1,653–575 cells counted per condition, repeated 3 times). (C) Western blot of YME1L1 and β-actin from 5 μg of protein derived from cells cultured on soft-to-stiff ECM for 24 h (2 biological replicates shown, repeated 3 times). (D) Western blot of YME1L1 and β-actin from 5 μg of protein derived from cells cultured on 60k Pa ECM for 24 h

[1]This figure was generated by co-authors.

± 2 μM KRIBB11 (3 biological replicates shown, repeated 2 times). (E) Graphical representation of the conceptual paradigm pertaining to this figure. (F) Quantitation of MECs with YME1L1 knockdown via CRISPR-I compared with CRISPR-I and empty guide vector expressing cells on 400 Pa (dashed lines) or 60k Pa ECM, 11 field views quantified for condensed nuclei and cleaved caspase-3-positive cells (923–2,880 cells counted per condition, repeated 3 times). (G) C. elegans survival in 50 mM paraquat, with C. elegans overexpressing hsf-1 (sur-5p::hsf-1) compared or control line (N2) grown on either empty vector or ymel-1 RNAi from hatch (n = 80 animals per condition, repeated 3 times).

Due to the fact that stiff ECM and HSF1 altered mitochondrial protein turnover rates and mitochondrial import is required for mitochondrial protein turnover, we next assessed whether cytoskeletal tension mediated OxSR was dependent upon mitochondrial protein import. Nuclear-encoded mitochondrial proteins are imported into the mitochondria ([295]), a process that requires a number HSF1 target genes to efficiently occur (e.g., HSPD1 [HSP60], HSPE1 [HSP10], and HSPA9 [mtHSP70]; [296]; [297]). To test if cytoskeletal tension enhanced mitochondrial import was critical for OxSR, we used JG-98, an inhibitor of HSP70 that enriches in mitochondria ([298]; [299]). JG-98-treated cells grown on stiff ECM were not apoptotic but were hyper-sensitized to paraquat-induced death (Extended Fig. 8.28D). To identify the specific mediators of the HSF1-dependent OxSR, we cross-referenced conserved nuclear-encoded mitochondrial genes containing heat shock elements (HSEs) in their promoters with genes whose expression was upregulated by cytoskeletal tension (Fig. 5.3B). We found one likely candidate, mitochondrial escape 1 like 1 (YME1L1), a zinc-dependent metalloprotease of the AAA+ protein family (ATPases with diverse cellular activity), which is a hallmark of UPRmt and regulates mitochondrial morphology ([300]; [301]). We verified that YME1L1 protein levels were regulated by HSF1 and were upregulated in response to mechanosignaling via stiff ECM (Fig. 5.7C and D).

Since HSF1 resolves mitochondrial import stress ([284]) by regulating the expression mitochondrial import machinery, we hypothesized that dysfunctional or ROS-producing mitochondria elicit a adaptive response to potentiate mitochondrial import capacity and facilitate the import of certain nuclear-encoded mitochondrial proteins that mediate mitochondrial repair/reprogramming (Fig. 5.7E). To determine if YME1L1 played a role in stiff-ECM-induced OxSR, we utilized CRISPR-I to downregulate YME1L1 expression. YME1L1 knockdown

sensitized MECs cultured on stiff ECM to paraquat-induced death to a similar degree as cells plated on soft ECM (Fig. 5.7F). Attenuated YME1LI expression in MECs increased cellular redox stress and lowered mitochondrial membrane potential (Fig. 5.7F) and was dependent on HSF1-mediated transcription (Extended Fig. 8.29F). To verify that HSF1 activity conferred OxSR through YME1L1, we examined the paraquat sensitivity of hsf-1-overexpressing C. elegans with or without reduced expression of yme-1 (YME1L1 ortholog). Overexpression of hsf-1 rendered C. elegans more resistant to paraquat-induced death, to a greater extent than that observed in other long-lived strains (e.g., daf-2 knockdown) and potentiated the skn-1-mediated adaptation to redox stress (Extended Fig. 8.29G and H). Impressively, yme-1 knockdown completely abolished the OxSR conferred to C. elegans through the overexpression of hsf-1 (Fig. 5.7G). Overall, these data indicate that YME1L1 plays an essential role in the HSF1-mediated OxSR that is induced by stiff-ECM-induced adhesion-mediated mechanosignaling.

Mechanosignaling has been established as a key driver of aggressive characteristics in breast cancers ([96]), and HSF1 has also been identified as a key driver of aggressive characteristics of metastatic breast cancer ([289]; [302]; [303]). Therefore, we sought to determine whether the fibrotic, stiffened tissue microenvironment that develops in experimental breast tumors regulates the transcriptional activity of HSF1. We examined nuclear localization of HSF1 in the murine PyMT mammary tumors excised from mice treated with and without the lysyl oxidase inhibitor (β-aminopropionitrile, BAPN), which reduces tissue fibrosis, collagen crosslinking, and stromal stiffening of mammary tumors ([136]). BAPN treatment reduced tissue fibrosis (Extended Fig. 8.29I) and nuclear localization of HSF1 in the mammary tumor cells (Extended Fig. 8.29J–K). HSF1 and YME1L1 have been shown to be involved in many tumor types; however, breast cancer cells appear to be most dependent on HSF1 or YME1L1 (Extended Fig. 8.29K).

5.3 Discussion

We identified a mechanism whereby the physical properties of the microenvironment alter mitochondrial composition, structure, and function to tune cellular metabolism through a me-

chanical stress adaptation. We demonstrate that SLC9A1 and HSF1 alter mitochondrial function to support OxSR by regulating the levels of YME1L1 ([301]). The mechano-responsiveness of HSF1 and its ability to limit mitochondrial respiration may explain why oncogene-driven Warburg metabolism has been so difficult to observe *in vitro*. The rigid tissue culture polystyrene substrates (3G Pa) elevate mechanosignaling and chronically activate HSF1, regardless of oncogene transformation, and this effect obscures any comparative measurements of mitochondrial function in normal and oncogene-transformed cells. Instead, prudent use of model systems with biomimetic properties (physically and chemically similar to the relevant biological system) is needed to uncover oncogene-driven alterations in mitochondrial metabolism ([304]; [305]).

Our findings here demonstrate that HSF1-driven redox management not only suppresses the production of ROS by limiting mitochondrial respiration, but it also opposes oxidant damage by promoting mitochondrial biogenesis/protein turnover and enhancing reducing equivalents (reduced glutathione/NADPH). Previous studies have indicated that cell-detachment/attachment-associated signaling elicits redox stress ([306]; [307]; [308]). With that in mind, coupling redox stress management to a molecular rheology sensor would be a rational design principle to promote cell survival. HSF1 is a logical candidate to serve as such a molecular rheology sensor because it facilitates cellular stress responses to the accumulation of misfolded proteins in the cytosol. Misfolded proteins can accumulate owing to changes in pH, ion concentrations, osmolality, osmotic pressure, molecular crowding, adhesion-associated forces (mechanotransduction), enthalpy (heat), entropy (order), and redox balance ([285]; [309]; [310]; [199]; [311])—all of which are cellular conditions associated with HSF1 activation. By surveying the physical state of the proteome, HSF1 is poised to temper diverse environmental perturbations that elicit mitochondrial dysfunction and oxidant leak. Indeed, HSF1 could mitigate the redox stress induced by conditions that deform mitochondrial structure ([240]), such as the physical stresses cells encounter in tumors with high interstitial pressure, mechanically stressful metastatic sites ([312]), rigid ECMs, or oncogene-induced ROCK activity ([313]; [314]; [315]).

HSF1 levels are elevated in the majority of tumors and are implicated in cancer aggression and metastasis ([289]; [302]; [303]). Because tumors are stiffer than healthy adjacent tissues, our findings offer a tractable explanation for why HSF1 and its target genes are so frequently upregulated in tumors ([8]; [53]). The heat-shock-independent activation of HSF1 and its target genes would provide the tumor cells with a metabolic adaptation to this chronic mechanical stress. Since metastatic cancer cells require redox stress management adaptations to disseminate to metastatic sites ([316]) and ECM stiffness promotes metastasis ([96]; [54]), our findings may describe an important molecular mechanism by which ECM tension promotes metastatic disease. In this regard, therapeutic approaches to disrupt HSF1 and its target genes have focused on cytosolic and nuclear targets but can incur difficult-to-tolerate systemic effects in humans ([317]). We postulate that targeting the specific mediators (e.g., YME1L1, HSP60, mtHSP70, etc.) of the metabolic adaptations conferred by HSF1 could be more tractable anti-tumor therapeutic ([301]) than inhibition of HSF1 directly. Overall, our data demonstrate that the physical properties of the microenvironment play a critical role in facilitating adaptive stress responses that may contribute to metastatic characteristics of solid tumors ([316]) or altered metabolism and pathology observed in structurally altered tissues (e.g., aged or fibrotic).

Our studies reveal a critical role for HSF1 in OxSR; however, other HSFs (e.g., HSF2) may be involved in regulating these phenotypes ([318]). We performed our *in vitro* experiments with DMEM:F12- or DMEM-based media classically used to culture our chosen cell line models. However, we strongly believe that our experiments would be more informative if we were to use the human-plasma-like medium (HPLM) ([319]; [304]; [320]). It is clear that the biochemical milieu influences metabolic programing, especially mitochondrial function. We hope to incorporate HPLM in our future work to more faithfully model cellular metabolic responses to physical cues in the cellular microenvironment. In this manuscript, we have demonstrated that extreme hyperglycemia affects cellular mechanosignaling and metabolic adaptations. We postulate that physiologically irrelevant glucose concentrations found in DMEM are likely one of many

metabolic substrates that obfuscate our ability to translate *in vitro* findings to *in vivo* models or clinical success.

5.4 Contribution

I contributed bioinformatics analysis to this project by analyzing the included RNAseq and metabolomics datasets. This analysis identified the transcriptional downregulation of electron transport chain components in soft substrates, which is the foundational observation of the metabolic changes explored between soft and stiff gels. I provided the processed data for plotting, consulted on clear and correct visualization of the data, wrote the corresponding methods, and edited the manuscript.

6 Chapter 6: Conclusions and Future Directions

There is growing appreciation for the role of mechanics in directing cancer cell behavior and tumor development. In this dissertation, I attempted to shed light on novel mechanisms through which the ECM can drive disease-relevant phenotypes, specifically in regards to matrix rigidity and dimensionality. Together with my colleagues, I explored the impact of tissue rigidity on metabolic state, stress response induction, and immune infiltration in the TME, finding exciting new connections between a fibrotic tumor stroma, metabolic rewiring to resist mitochondrial stress, and glycocalyx-mediated immune suppression. I also identified and improved upon shortcomings in the existing methods used to study breast cancer; from deficiencies in our means of recapitulating tumors with *in vitro* gel culture systems to limitations in our ability to study tissue mechanics using AFM. These findings will be useful for informing future studies on the impact of tissue fibrosis on cancer onset and development. Moreover, by developing a method to better elucidate soft and stiff tissue regions, I have provided a platform for future researchers to more easily evaluate the physiological relevance of ECM-cell relationships observed *in vitro*. The key findings and future directions of each of the major projects contained herein are summarized below.

6.1 STIFMaps reveal mechanical heterogeneity in breast cancer

A multitude of methods have been applied to emulate the TME *in vitro* including various types of gels, scaffolds, and co-culture systems ([321], [322], [323], [324], [325], [245], [326]). No model perfectly emulates *in vivo* conditions and there are advantages and limitations to each of the models. Oftentimes, results from these model systems can conflict with one another. For example, rigidity was found to enhance proliferation in 2D polyacrylamide gel culture systems, but lead to slower proliferation in rigid 3D agarose gels ([327], [324]). Given that both model systems have drawbacks, it can be difficult to determine which finding more closely emulates physiological behavior. By developing STIFMaps, I have provided researchers with a tool to quickly and easily evaluate *in vivo* whether or not a given signaling pathway or cell type associates with ECM tension.

In doing so, my intention is to provide greater clarity as to which experimental findings have translational potential by being observed *in vivo*.

STIFMaps applies machine learning to predict the stiffness of collagen fibers utilizing only their morphology and the morphology of nearby nuclei. This technology characterizes mechanical variability in the TME with precision and accuracy unrivaled by any other technique. I validated the performance of STIFMaps using co-localization of predicted stiff ECM regions with known markers of mechanical activation, then applied the technique to discover for the first time a spatial overlap between ECM rigidity and induction of an EMT in cancer cells. Evaluating this overlap would not have been possible with any other method in existence today, and has major clinical applications as it demonstrates a clear connection between tissue fibrosis and a cellular process known to result in downstream metastasis and poor patient outcomes. Moreover, STIFMaps clarifies a longstanding assumption in the field of cancer mechanics: That stiffer collagen fibers are thicker and more linear. This assumption has been applied to assert that various pathways are mechanically activated ([328]), but more abundant collagen alone does not mean that tissue is stiffer. Through STIFMaps, we have provided researchers with an improved tool to study whether of not their pathway of interest correlates with the mechanical microenvironment of breast cancer *in vivo*.

In the process of developing STIFMaps, I was able to develop an automated AFM (AutoAFM). AFM is an extremely powerful tool for studying mechanics in the TME, but its usefulness in biology is limited because AFMs were originally designed for materials science, which characterizes materials at the nanometer to micron scale. At the scale of tissues and tumors, it's more relevant to ask how mechanical properties vary across hundreds of microns, even up to millimeters. Moreover, a myriad of spatial techniques are available to study biological tissues such as staining, in situ hybridization, mass spectrometry imaging, and spatial RNAsequencing that are not relevant in materials science. Therefore, AFM was not developed to interface with these techniques and no method existed to register spatial co-localization of AFM data with any of these assays. Through AutoAFM, we managed to overcome both of these shortcomings by developing a technique that can probe tissue sections across millimeters while outputting data that is readily overlapped with

subsequent spatial assays performed on the tissue slide. This requires only a nuclei stain or visualization, which is standard in all of these techniques. Through AutoAFM, we have expanded the realm of what is possible to analyze and evaluate using AFM on biological tissues.

Though I was able to demonstrate how STIFMaps can be utilized to register co-localization of tissue stiffness with an EMT pathway predicted to be elevated in stiff regions using patient data and previous findings, this only scratches the surface of what is possible with this new method. There is a growing interest in spatially-resolved, non-biased tissue screening approaches such as spatial RNAseq and highly multiplexed proteomics ([92], [100], [101], [102]). With these new technologies comes the ability to characterize tissue heterogeneity on scales never before explored, and preliminary findings indicate that this heterogeneity factors into cancer risk to progression, patient outcome, and treatment responsiveness. How variability in the mechanical microenvironment factors into these phenomena is completely unexplored. By integrating STIFMaps with additional spatial multiplexing technologies, we will advance our understanding of the interplay between tissue mechanics and the cell phenotypes that it regulates.

6.2 Mechanics perturbs immune infiltration in the tumor microenvironment

The glycocalyx is thicker and more abundant in tumors, altered in approximately 95% of cancer cells ([329], [330]). We and others have explored the impacts of the glycocalyx on tumor progression in the hopes of informing the development of therapeutics that can leverage these findings to better treat aggressive tumor subtypes that are currently lacking in treatment options ([331], [141], [150], [332]). Indeed, tissue rigidity leads to a greater abundance of thicker glycoproteins on the surface of cancer cells ([150]). Sialoglycoproteins, one component of the glycocalyx composed of glycoproteins bound with sialic acid, are associated with poor survival by serving as ligands for immunosuppressive Siglec-7, -9, and -10 expressed by most immune cells ([333]). By attenuating Siglec-7 and -9 activity through function-blocking antibodies, researchers managed to restore the tumor killing capacity of NK cells ([154]). Given that tumors with a high

fibrosis signature were also stratified with an 'immune desert' phenotype ([59]), we asked whether tissue fibrosis might contribute to an immunosuppressive microenvironment through changes to the glycocalyx.

To test the association between fibrosis, sialoglycoprotein content, and immunosuppression in the TME, we stained clinical samples from different types of breast cancer and found that sialoglycoprotein content was greater in fibrotic regions as well as in more aggressive tumors. This was verified through additional staining for α2,6-sialylated glycoproteins, which revealed greater expression in high-fibrosis regions of HER2+ and triple negative tumors. scRNAseq analysis revealed that cancer cells themselves were the predominant source of sialoglycoprotein biosynthesis genes in the TME, and immunostaining revealed that expression of genes within this set were elevated in more aggressive subtypes of breast cancer. As sialoglycoproteins are the ligands for immunosuppressive Siglec-7, -9, and -10 expressed by most immune cells, we found a similar elevation of Siglec-positive immune cells in these more aggressive tumor subtypes. Finally, staining revealed that Siglec-7 expression was significantly elevated in high fibrosis regions of triple negative tumors. Altogether, these findings indicate that tumor fibrosis may contribute to Siglec-mediated immunosuppression by elevating expression of sialoglycoprotein biosynthesis within cancer cells.

These data have implications for furthering our understanding of the interplay between the glycocalyx, fibrosis, and immune function in tumors. In recent years, there has been an emphasis on developing therapies that utilize the body's existing defense system, the immune system, in order to fight cancer ([334], [174], [335]). One of the main hindrances to the development of these therapies has been that immune cells within the tumor microenvironment experience a host of signals that attenuate their tumor-fighting capacity, including FasL, Siglecs, and TGF-β ([335], [336], [337]). Extending our understanding of the mechanisms through which the TME attenuates immune function, specifically in more aggressive subtypes that are more difficult to treat, is crucial for immune therapies to prevail. The role of fibrosis cannot be ignored in this field, as a myriad of studies have demonstrated a direct association between elevated fibrosis and reduced immune

function in breast tumors ([338], [339], [340], [341]). By demonstrating a link between fibrosis, sialoglycoproteins, and immunosuppressive siglecs in breast tumors, we shed light on a potential therapeutic opportunity for targeting breast tumor subtypes that have been proven difficult to treat.

6.3 ECM dimensionality influences stress responses in cells in culture

One of the major challenges of developing therapies against breast cancer is in the establishment of models systems that accurately recapitulate the state of a tumor *in vivo*. A plethora of culture systems have been applied using various gels and scaffolds to mimic the tumor ECM ([321], [322], [323], [324], [325], [245], [326]). Nevertheless, a great deal of cancer research continues to be done in culture on tissue-culture plastic. When considering which variables are important to account for in these systems, one longstanding observation has been that ECM dimensionality (whether the cells interact with the ECM in a single plane vs all around) can drastically alter cell phenotype. For example, mammary epithelial cells (MECs) cultured in 3D develop proper apical-basal polarity and are more resistant to apoptosis than the same cell lines cultured on 2D substrates ([179]). This observation has critical implications for drug discovery and exploration, as it suggests that cells in their native tissue environments are able to endure stresses such as Paclitaxel, TRAIL, and Doxorubicin to a greater degree than what is exhibited in 2D culture systems ([342]). However, the underlying mechanisms culminating in the death-resistance phenotype in 3D remained poorly understood.

To explore the differences between MECs cultured in 2D and 3D substrates, we began by performing RNAseq and found an endoplasmic reticulum (ER) stress signature elevated in 2D substrates. RNAseq also indicated that 2D substrates had greater unfolded protein response while cells in 3D were elevated for protein insertion into the ER, protein secretion, and genes known to protect against ER stress. These findings were validated by demonstrating low calcium content in 2D, a known activator of ER stress, in contrast with a significant increase in secretory protein trafficking in 3D. Cells cultured in 2D were shown to have significantly higher cell contractility, and by attenuating cell contractility we were able to restore calcium homeostasis, improve ER function,

and reduce ER stress. As the ER is bound directly to the plasma membrane (PM), this led us to ask whether the extent and rigidity of ER-PM contacts might contribute to the ER stress observed on stiff substrates. By attenuating expression of filamin, an actin crosslinker, we both reduced the number of ER-PM junctions in 2D as well as lowered ER stress signaling. We determined that filamin interacts with PERK, an ER stress response sensor, in a tension-dependent manner, and that by knocking down filamin we reduced cell death, presumably by relieving ER stress. Moreover, we found that high membrane tension impaired the activity of the membrane binding protein Exo70, thus impairing membrane trafficking and protein secretion. Attenuation of Exo70 in 3D substrated resulted in more cell death, likely by perturbing protein trafficking to the membrane and causing a buildup of ER stress.

Taken altogether, these findings clarify the role of substrate dimensionality on promoting drug resistance and improving viability for cells cultured in 3D systems. 2D substrates have greater actomyosin tension, which causes worse protein trafficking to the cell surface and the accumulation of unfolded proteins in the ER to elicit a stress response. More broadly, these findings indicate that many studies done in 2D may be experimenting of pre-stressed cells with worse viability that are easier to kill using drug therapies. This accentuates the importance of considering variables such as dimensionality when extrapolating findings from *in vitro* culture systems to the clinic. Moreover, since these experiments were all performed *in vitro*, this paper motivates the need for technologies like STIFMap that can be applied *in vivo* to determine whether or not these results are physiologically relevant to a tumor system.

6.4 Tissue tension influences cell metabolism and mitochondrial dynamics

The metabolism of cancer cells is drastically different compared to that of cells in a healthy tissue. In particular, cancer cells are known to attenuate mitochondrial respiration via the electron transport chain (ETC) and instead favor anaerobic glycolysis that produces lactate that acidifies the TME, otherwise known as a Warburg metabolism ([343], [344]). Acidification of the TME leads to invasion, proliferation, drug resistance, and immune escape in cancer cells ([345],

[346], [347]). It has long been known that hypoxia tumor regions are highly acidic due to HIF1-alpha-mediated induction of a Warburg metabolism. However, it was recently shown that breast tumors have large acidic regions located at the tumor-stroma interface that are not acidic, which also corresponded with high proliferation and expression of invasive MMPs ([68]). We sought to explore the hypoxia-independent mechanism through which stromal interactions cause metabolic rewiring and induction of aggressive characteristics in breast cancer cells.

We found that MECs cultured in stiff environments not only exhibited attenuated ETC activity and extracellular acidification associated with a Warburg metabolism, but also that mitochondria took on a fragmented, toroidal morphology compared to a thin, filamentous morphology on soft substrates. We demonstrated that the toroidal mitochondria were dysfunctional and produced large quantities of reactive oxygen species (ROS), which resulted in the induction of a mitochondrial unfolded protein response (UPRmt) to prevent cell death by attempting to repair dysfunctional mitochondria and stress-adapting cells against damage from ROS. Through loss- and gain-of-function studies, we established that mitochondrial reorganization and metabolic rewiring was done through HSF1 to reduce mitochondrial oxygen consumption and induce expression of YME1L1 to drive toroidal mitochondrial morphology. Cells in stiff environments were more robust than those in soft environments against apoptosis from ROS, but knockdown of either HSF1 or YME1L1 sensitized the cells in stiff environments to ROS-mediated death, suggesting that both are required for the stress-adaptation needed to survive in stiff environments. These findings illuminate a novel mechanism through which a stiff ECM causes metabolic reprogramming in cancer cells to promote an aggressive phenotype.

The impact of a fibrotic ECM on cellular metabolism is fundamental, as it explains how cancer cells are able to obtain fuel, utilize inputs, and achieve processes related to growth, survival, and tumor development. It's important when studying cellular processes to not simply focus on the impact that one gene has on a phenotype, but rather consider the entire cellular system of interweaving pathways and processes that are utilized to ultimately achieve cellular goals like motility or proliferation. Here, we utilized proteomics and RNAseq to perform unbiased profiling

of the metabolic and transcriptional landscapes in cells cultured on soft or stiff ECMs, which allowed us to observe the interplay between metabolic pathways such as the ETC and pentose phosphate pathway (PPP) with stress responses such as the UPRmt. This multi-omics approach is a powerful means of studying cancer, as it allows researchers to consider an entire cellular network of genes, proteins, and organelles.

6.5 Broad Implications and Final Comments

Although the studies herein have helped to elucidate some of the disease-relevant pathways impacted by fibrosis and ECM stiffening in breast tumors, a number of outstanding questions remain:

(1) How does mechanical heterogeneity in the TME contribute to patient outcome and treatment response?

(2) Through what mechanism does fibrosis cause an elevation in glycocalyx thickness and sialoglycoprotein abundance in triple-negative breast tumors?

(3) What inconsistencies are there between MECs grown in 3D rBM gels compared to MECs *in vivo*?

(4) Does the metabolic rewiring undergone by cancer cells in stiff environments contribute to the immunosuppressive glyocalyx observed by cancer cells in these environments?

(5) Can HSF1-targeted therapies prevent stress-adaptation and induction of a Warburg metabolism in cancer cells *in vivo*?

To answer these questions, it will be necessary not only to demonstrate spaciotemporal associations *in vivo*, but also to establish causal relationships through mouse studies and *in vitro* culture systems. While some novel culture systems provide additional, crucial advancements such as co-culturing cancer cells with additional cell types that affect disease behavior *in vivo*, many

systems continue to overlook essential details such as by presenting a matrix that is realistically crosslinked with ligands that are physiologically relevant ([135], [348]). The crux of our ability to leverage these findings to develop therapies that succeed in curing cancer and saving lives relies on developing culture systems that adequately and sufficiently emulate all of the relevant axes that operate within a tumor *in vivo*. This entails representing cell types at proper ratios, integrating realistic tissue stromas or scaffolds, and presenting nutrients at physiological amounts, to name only a few variables.

The studies presented in this thesis illustrate the interplay between tissue fibrosis and disease-relevant phenotypes in breast cancer. We explored the impacts of ECM tension at the molecular level on processes such as metabolism, stress signaling in the ER and mitochondria, and protein trafficking, but we also worked on larger length scales to study co-localization of immune cells with fibrotic tissue regions. STIFMaps manages to provide information across length scales, as it can identify the mechanical microenvironment experienced by a single cell within a tissue and also depict mechanical heterogeneity across an entire tissue section. Through these studies, we aimed to illuminate pathways through which the fibrotic ECM can lead to disease progression, identify potential therapeutic susceptibilities in tumor subtypes that are difficult to treat, and also to provide researchers with a tool to clarify physiological relevance for cellular responses to tissue fibrosis that are identified *in vitro*. These works along with a better overall understanding of the impact of tissue fibrosis on cancer initiation and development will help to benefit cancer therapies and improve patient outcome.

7 Chapter 7: Methods

7.1 Chapter 2

DATA AVAILABILITY

The authors declare that all data supporting the findings of this study are available within this publication and its extended data. PDX RNAseq data has been deposited in NCBI's Gene Expression Omnibus [349] and are accessible through GEO Series accession number GSE179983 (https://www.ncbi.nlm.nih.gov/geo/query/acc.cgi?acc=GSE179983). Neural networks, training data, stain imaging, and STIFMaps are available at https://github.com/cstashko/STIFMaps. AutoAFM part files and assembly instructions are available at https://github.com/cstashko/AutoAFM.

CODE AVAILABILITY STATEMENT

All code necessary to implement STIFMaps is available via the Github repository https://github.com/cstashko/STIFMaps. AutoAFM code is available at https://github.com/cstashko /AutoAFM. All other code used in the preparation of this manuscript is publicly available from software and commercial sources.

Atomic Force Microscopy (AFM)

AFM measurements were performed using an MFP-3D BIO Inverted optical AFM (Asylum Research, Santa Barbara, CA) mounted on a Nikon TE2000-U inverted fluorescent microscope (Melville, NY) and placed on a vibration-isolation table (Herzan TS-150). Silicon nitride cantilevers were used with a nominal spring constant of 0.06 N m-1 and a borosilicate glass spherical tip with 5 μm diameter (Novascan Tech). Cantilevers were calibrated using the thermal fluctuation method and verified by probing polyacrylamide gels of known elasticity. The specimens used were 20 μm thick OCT-embedded frozen human breast tissue sections thawed and equilibrated to room temperature by immersion in PBS for 5 minutes. Thawed sections were immersed in PBS containing phosphatase inhibitor (GenDEPOT Xpert #P3200-001), protease inhibitor cocktail (GenDEPOT Xpert # P3100-001), 5 μg/mL propidium iodide (ACROS, Cat# 440300250), and 3 μg/mL of CNA35-OG488. Specimens were indented at 2 μm per second loading rate. The

Young's Moduli of the samples were determined by fitting force curves with the Hertz model using a Poisson ratio of 0.5.

AFM Forceplot Fitting Algorithm

AFM force plots were post-processed to obtain Young's Moduli using a homemade algorithm (see GitHub repository). Briefly, force plots were smoothed using a moving average convolution across 100 datapoints to remove noise and then baseline-corrected using the first third of the AFM indentation curve. The contact point of each force curve was estimated as the point at which the derivative of the force curve increased above an empirically-determined threshold. Then, a more precise contact point was determined by applying a minimization function to fit a flat baseline plus a 1.5-power curve (Hertz Model) onto the AFM data using the estimated contact point as an initial guess. With the contact point determined, the Young's Modulus was calculated to minimize the squared error between the AFM data and the fit curve

AutoAFM Design

The AutoAFM assembly's function is to ensure proper alignment of the motor relative to the microscope stage's adjustment knob in order to allow the motor to accurately control the knob's rotation and thus the movement of the microscope stage. It does this by supporting the weight of the motor and controlling its position, while allowing the motor to freely slide along its shaft axis. It also allows the operator to fine-tune the motor's position and orientation in space, ensuring good alignment with (and therefore accurate control of) the stage's adjustment knob.

The assembly has three main components: the Stage Frame, the Motor Frame, and the Motor Bracket. The motors screw into the Motor Brackets via the four Motor Screws. The Motor Bracket sits in the Motor Frame and is pulled down against the Bracket Adjusters by the springs hooked around the Tensioning Pins. By turning the Bracket Adjusting Screws, the Bracket Adjusters can be individually moved forward and backwards, adjusting both the pitch and the roll of the Motor Bracket relative to the axis of the motor shaft. This allows easy manual adjustment of the motor to ensure good alignment between the motor shaft and the stage knob.

The Stage Frame is hooked over the lip of the microscope stage, enclosing the stage's fine adjustment knob (not shown), and is able to slide freely along the edge of the stage. The Alignment Rods are press-fit into the Stage Frame and slip-fit into the Motor Frame, allowing the Motor Frame to slide freely towards and away from the Stage Frame along the motor shaft axis. The Motor Coupling joins the motor shaft to the Knob Adapter, which is screwed into the fine adjustment knob via the Adapter Screw. The Y Stage Frame has rollers attached to reduce friction with the AFM stage as it slides side-to-side.

Motor mount components were 3D printed on either a Prusa MINI+ or LulzBot Mini 2 with PETG. A high infill was used for ease of sanding. Some dimensions were slightly oversized so that they could be gradually sanded to fit snugly. See https://github.com/cstashko/AutoAFM/STL for a full list of part STL files. Other components were ordered from McMaster-Carr. See Table 8.1 for a full Bill of Materials. Motors were driven via an Arduino Mega 2560 Rev3 Classic microcontroller interfacing with RAMPS 1.4 (https://reprap.org/wiki/RAMPS_1.4).

AutoAFM operates by moving the AFM cantilever to user-defined positions and acquiring an AFM force curve at each point. Within MicroManager, the user draws a path via the Freehand Line or Segmented Line tools and specifies the step size between points as well as the initial cantilever position [350]. For each point, the motors attempt to move to the desired location. An image is taken at the new location and stitched together with existing images using Phase Cross-Correlation to determine the actual AFM movement that occurred [351]. If the AFM cantilever is within tolerance of the desired position, then a force curve is acquired. Otherwise, the motors make additional movements until the cantilever position is within tolerance (Fig. 2.1c). At completion, AutoAFM returns force curves and positions for each of the user-specified points. Full code and a complete pipeline for AutoAFM acquisition is available via https://github.com/cstashko/AutoAFM/.

Polyacrylamide hydrogels

Polyacrylamide (PA) hydrogels of varying rigidities were prepared as described ([352], [324]). Briefly, PA gels of specified rigidities were mixed according to previously reported ratios

[324], omitting 1% potasium persulfate (PPS). Solutions were degassed for 20 minutes, then PPS was added and 300 μL was quickly deposited onto a Rain-XTM-coated 60 mm coverslip and sandwiched with a glutaraldehyde-activated coverslip. After one hour of polymerization, Rain-XTM-coated coverslips were removed. Gels were stored in PBS. For shear rheology studies, gels were cast directly onto the baseplate of an AR 2000 rheometer (TA Instruments) and immediately compressed to a barrel shape using a 25 mm diameter probe. Gels polymerized for two hours at room temperature with a 1% applied strain at a frequency of 1 rad*s-1 as previously described [353]. A Poisson's Ratio of 0.457 was used when calculating the Young's Modulus of PA gels [354].

Micropatterned substrates for AFM control studies

Photolithography and soft lithography were used to generate polydimethylsiloxane (PDMS, Dow Silicones Corporation) substrates with defined ridge topographies (15 μm height, 100 μm length, and widths ranging from 12 μm to 0.5 μm) for use in AFM control studies. Briefly, a silicon wafer was plasma treated (5 minutes, Harrick Plasma) and a 2 μm tall adhesive layer of SU-8 2002 (Kayaku Advanced Materials) was cast onto the wafer surface using a spin coater (Laurell Technologies). A 4 cm square was UV patterned onto the adhesive layer using the PRIMO photopatterning system (Alvéole). A second 15 μm layer of SU-8 2010 (Kayaku Advanced Materials) was then cast onto the wafer, and ridge arrays (100 μm length, 12 μm-0.5 μm width, 30 μm spacing) were subsequently photopatterned. Patterned wafers were developed using propylene glycol monomethyl ether acetate (PGMEA, Sigma-Aldrich), cleaned with isopropyl alcohol (IPA, Sigma-Aldrich), and dried with n-pentane (Acros Organics) and N2 gas. PDMS was poured over wafer patterns and cured for 15 minutes at 100oC to generate a negative mold. The negative mold was silanized overnight by vapor deposit of trichloro(1H,1H,2H,2H-perfluorooctyl)silane (TFPS, Sigma-Aldrich). A second layer of PDMS was poured over the silanized negative mold, and a glass coverslip was applied to sandwich the layer of PDMS. This PDMS was cured at 100oC for 20 hours to generate a positive mold of ridges adhered to a glass coverslip, which was then used for AFM control studies. Fluorescent beads 1.0 μm in

diameter (ThermoFisher F8814, 1:500 dilution in water) were allowed to settle into the PDMS for visualization purposes during AutoAFM.

Image Registration

Registration for images with the same scale and orientation was computed using the phase_cross_correlation function from skimage [351]. For images with different scales and orientations, transformations were found by applying a Fourier Mellin Transform [118]. Briefly, images were applied with a band-pass filter followed by a Hanning Window. Images were then transformed using a Fast Fourier Transform (FFT) and magnitudes were log-polar transformed. Translations between these transformed images were calculated using phase_cross_correlation, which can then be used to calculate the rotation and scaling differences in the original images.

Neural Network Design

Networks were designed in Pytorch. Input images were used of size 224x224x3 pixels in which the three channels are DAPI, CNA35, and a layer of zeros, which was incorporated for ease of use with existing Python machine learning image loading functions. Within the training dataset, images were loaded with size 448x448x3 pixels, transformed via random rotation of 0-180 degrees, randomly flipped with probability 0.5, received adjustments to brightness, contrast, and sharpness, and cropped to 224x224x3 to remove any zero pixels resulting from rotation. A mini batch size of 16 was used throughout. For each round of training, samples were randomly split by patient with a training:validation ratio of 0.8:0.2 so that the validation dataset only contained samples from patients that were not included in the training set. Mean squared error was used as a loss function. Learning rate and weight decay were set at 4e-6 and 4e-7, respectively. A dropout rate of 0.5 was used for fully-connected layers. Networks were trained for 100 epochs since this is when accuracy for the validation set converges. Code for network visualizations was modified from https://github.com/utkuozbulak/pytorch-cnn-visualizations#gradient-visualization.

Human breast tissues

All human breast tissue specimens were collected prospectively from consenting patients (informed consent provided prior to surgery) undergoing surgery at the University of California,

San Francisco, (UCSF) or Duke University Medical Center between 2010 and 2020. Samples were stored and analyzed with deidentified labels to protect patient data in accordance with the procedures outlined in the Institutional Review Board Protocol #10-03832, approved by the UCSF Committee of Human Resources and the Duke University IRB (Pro00054515). Tissue specimens were flash frozen in OCT (Tissue-Tek) by slow immersion in liquid nitrogen or placement on dry ice and stored at $\sim$80°C until ready for sectioning. H&Es were performed on an adjacent slide and were scanned using a ZEISS Axio Scan.Z1 digital slide scanner equipped with CMOS and color cameras, 10x, 20x and 40x objectives. H&E-stained tissues were assessed by a pathologist (A.J.I.) to identify regions of interest for AFM measurements.

CNA35 Transformation and Purification

pET28a-EGFP-CNA35 was a gift from Jan Liphardt [126] (Addgene plasmid # 61603). CNA35 was expressed and purified as previously described [355]. Briefly, bacteria were incubated with 5 mL of 2YT media + 100 μg/mL ampicillin + 25 μg/mL kanamycin + 1% wt/v glucose overnight at 30°C in a shaking incubator. The next day, the culture was diluted in 50 mL of 2YT media + kanamycin for three hours. The culture was then centrifuged and the supernatant discarded. Then, the sample was digested for cell wall removal for 30 min using 500 μL of lysis buffer (50 mM Sodium Phosphate dibasic, 20 mM Imidazole, 300 mM NaCl, pH 8.0) supplemented with 0.125 mg Lysozyme and 1 mM DTT. The sample was sonicated and centrifuged, then CNA35 was isolated from the solubilized supernatant via affinity chromatography (Qiagen Ni-NTA Agarose) according to manufacturer's instructions. The purified protein was supplemented with 40% glycerol and stored at -20°C. Under typical isolation conditions we obtained a final concentration of approximately 1.5 mg/mL CNA35.

Collagen/rBM hyrdrogels with orthotopic implantation of tumor cells

Rat tail collagen-1 (High concentration, Corning, Cat. #: 354249) was incubated with 0.1% acetic acid (non-crosslinked; SOFT) or 0.1% acetic acid with 500 mM L-ribose (Chem Impex International, Cat. #: 28127) (cross-linked; STIFF) for at least 10 days before preparation of Col1/ rBM hydrogels for orthotopic implantation of tumor cells or tumor fragments ([136],

[356]). Col1 mixtures were then combined with basement membrane extract (R&D Systems, Cultrex BME, type 2, Pathclear, Cat. #: 3532-005-02) (20% final volume), PBS, and 1N NaOH to a slightly acidic pH (pH 6.5) as determined by pH strips. Col1/rBM with and without L-ribose was injected orthotopically into a cleared inguinal fat pad and allowed to set for 3-5 minutes prior to implantation of a PDX tissue fragment approximately 2x2 mm in size.

Breast cancer Patient-Derived Xenografts (PDXs)

PDX tissues were obtained from Dr. Alana Welm at the Huntsman Cancer Institute, University of Utah, Utah (HCI-012) or Dr. Michael Lewis at Baylor College of Medicine, San Antonio, Texas (BCM-3143B and BCM-3963) ([137], [138]). For the PDX study, 2x2 cm breast tumor specimens were collected as fresh tissue with immersion in media (phenol red free-DMEM/F12) with 10% charcoal-stripped fetal bovine serum (FBS Benchmark, Cat. #: 100-106) and GlutaMAX (Gibco, Cat. #: 35050-061) supplementation for transportation to the Weaver laboratory at UCSF. PDX fragments were established from frozen and maintained in NOD-SCID immunodeficient mice. Once established tumors reached experimental endpoint, mice were sacrificed, and tumor tissue was divided into pieces for formalin fixation and paraffin embedding, embedding and freezing in OCT, and flash freezing in liquid nitrogen and cryopreservation in 95% FBS: 5% DMSO. Flash frozen tumor pieces were used for RNA and protein isolation for the downstream applications indicated.

Animals and Animal Care

Animal husbandry and all procedures on mice were carried out in Laboratory Animal Resource Center (LARC) facilities at UCSF Parnassus in accordance with the guidelines stipulated by the Institutional Animal Care Use Committee (IACUC) protocols, #AN133001 and #AN179766, which adhere to the NIH Guide for the Care and Use of Laboratory Animals. NOD/SCID mice were purchased from Jackson Laboratories for orthotopic implantation assays. Mice were sacrificed twelve weeks after injection or at humane endpoint, and the tumors were excised and examined for tumor volume using calipers, histology by H&E of fixed tissue sections, proliferation and

growth factor and integrin signaling via immunofluorescence in tissue sections, and gene expression using RNAseq and RT-PCR.

Monitoring of Tumor growth and metastasis

Tumor growth was monitored by palpation and caliper measurement weekly or biweekly. Lung metastases were quantified by counting of surface lesions at time of animal sacrifice, and by examination of histological lung sections stained by H&E. Lungs were scanned using a ZEISS Axio Scan.Z1 digital slide scanner equipped with CMOS and color cameras, 10x, 20x and 40x objectives, and lesion area was determined by tracing metastatic lesions in QuPath [357].

Quantitative Reverse Transcriptase-polymerase chain reaction (qRT-PCR)

RNA was prepared from flash-frozen and pulverized mammary tumor tissues using TRI-Zol reagent (Invitrogen). Reverse transcription reactions were performed using M-MLV reverse transcriptase (Biochain, Cat. #: Z5040002) with random hexamer primers. cDNA was mixed with PerfeCTa SYBR Green FastMix (Quantibio, Cat. #: 95072-05K) for qPCR analysis using an Eppendorf realplex2 epgradient S mastercycler. Thermal cycling conditions were 10 min at 95 °C, followed by 40 cycles of 15s at 95 °C and 45 s at 65 °C. Melting curve analysis was used to verify primer pair specificity. Relative mRNA expression was determined by the δ δCT method with normalization to GAPDH, 18S or KRT8.

Quantitative polymerase chain reaction (qPCR) Arrays

Human EMT qPCR arrays were purchased from Qiagen (Cat. #: PAHS-021Z), performed as described using RNA from PDX mammary tumors grown in SOFT and STIFF Col1/rBM hydrogels, and analyzed using available product resources from Qiagen. Selected genes were plotted for presentation in Fig. 2.4 4 and Extended Fig. 8.6.

Immunofluorescence

Immunofluorescence was performed using the following specific antibodies: phospho-FAK (Y397) (Cell Signaling Technology, Cat. #: 8556, 1:200), phospho-p44/42 MAPK (ERK1/2) (T202/Y204) (Cell Signaling Technology, Cat. #: 9101, 1:200), Integrin β1, activated (Sigma-Aldrich, clone HUTS-4, Cat. #: MAB2079Z, 1:400), phospho-Myosin Light Chain 2 (Ser19)

(Cell Signaling Technology, Cat. #: 3671, 1:200), SLUG (C19G7) (Cell Signaling Technology, Cat. #: 9585, 1:200), ZEB1 (E2G6Y) (Cell Signaling Technology, Cat. #: 70512), and Anti-ErbB2 / HER2 [3B5] (ab16901). For cryopreserved samples, frozen sections were fixed in 2-4% paraformaldehyde, prior to permeabilization with 1-3% triton-x-100 and incubation with primary antibodies overnight at 4°C with 3 μg/mL CNA35 where specified. Sections were then incubated with species-specific secondary antibodies conjugated to different fluorophores (AF-555, -647, Invitrogen). All washes were carried out using Phosphate-buffered saline (PBS) with 0.5% Tween-20 and nuclei and/or actin filaments were counterstained using 4',6-diamidino-2-phenylindole (DAPI, Cat. #: D1306) and Phalloidin-AF488 conjugate (Thermo Fisher Scientific, Cat. #: A12379), respectively. For FFPE samples, antigen retrieval was accomplished by boiling sections in 10 mM citrate buffer in a pressure cooker on high power for 3 minutes. Following blocking with 10% goat serum and 1% BSA in Tris-Buffered Saline (TBS), sections were incubated with primary antibodies overnight at 4oC with 3 μg/mL CNA35. Sections were incubated for 1 hour with species-specific secondary antibodies conjugated to different fluorophores (AF-555, -647, Invitrogen). All washes were carried out using TBS with 0.025% Triton X-100 and nuclei were counterstained using DAPI. Images of stained sections were acquired on either a Leica TCS SP5 Confocal microscope or an inverted Eclipse Ti-E Nikon microscope with CSU-X1 spinning disk confocal (Yokogawa Electric Corporation), 405 nm, 488 nm, 561, 635 nm lasers; a Plan Apo VC 60X/1.40 Oil or an Apo LWD 40X/1.15 Water-immersion λS objective; electronic shutters; a charge-coupled device (CCD) camera (Clara; Andor) and controlled by Metamorph.

Image Analysis

For STIFMap generation, immunostaining images are first resized to the same resolution as the panels used to train the neural networks. Then, the image is decomposed into squares the same dimensions as the network training panels and separated by a user-defined step size that is smaller than the panel side length. The elasticity of each square is predicted using five independently trained models with different brightness, sharpness, and contrast transformations. Since elasticity predictions only apply to panel centers where the AFM cantilever would make contact,

the elasticity of pixels between panel centers is inferred using cubic spine interpolation. STIFMaps are depicted as collagen pseudocolored to reflect the predicted elasticity of each position.

Image analysis of percent positive area in PDX samples was performed using ImageJ and QuPath software ([357], [358]). For comparison, immunofluorescence images were subjected to same-level thresholding based on a determined range of positive fluorescence intensity in each channel and antibody staining panel and the threshold area was expressed as a percentage of whole cell or nuclear area using DAPI staining measured in the same manner.

RNA-seq library preparation, sequencing, and analysis

RNA was isolated using TRIzol (Invitrogen, Cat. #: 15596018) followed by chloroform extraction. RNAseq library preparation was performed by the Functional Genomics Laboratory (FGL), a QB3-Berkeley Core Research Facility at UC Berkeley. Total RNA samples were checked on a Bioanalyzer (Agilent) for quality and only high-quality RNA samples (RIN $>$ 8) were used. At the FGL, Oligo (dT)25 magnetic beads (Thermofisher) were used to enrich mRNA, and the treated RNAs were rechecked on the Bioanalyzer for their integrity. The library preparation for sequencing was done on Biomek FX (Beckman) with the KAPA hyper prep kit for RNA (now Roche). Truncated universal stub adapters were used for ligation, and indexed primers were used during PCR amplification to complete the adapters and to enrich the libraries for adapter-ligated fragments. Samples were checked for quality on an AATI (now Agilent) Fragment Analyzer. Samples were then transferred to the Vincent J. Coates Genomics Sequencing Laboratory (GSL), another QB3-Berkeley Core Research Facility at UC Berkeley, where Illumina sequencing libraries were prepared. qPCR was used to calculate sequence-able molarity with the KAPA Biosystems Illumina Quant qPCR Kits on a BioRad CFX Connect thermal cycler. Libraries were pooled evenly by molarity and sequenced on an Illumina NovaSeq6000 150PE S4. Raw sequencing data were converted into fastq format, sample-specific files using the Illumina bcl2fastq2 software on the sequencing centers local Linux server system. RNAseq fastq files were mapped to the primary assembly of the Gencode v33 human genome using Rsubread (version 2.0.1) and counted using featureCounts. Lowly expressed genes were filtered out if they did not have at least one count per

million (CPM) in at least 4 samples. Data normalization was performed using calcNormFactors in edgeR (version 3.28.1). Gene ontology was performed using Gage (version 2.36.0) with gene lists from MSigDB version 7.2.

Nuvera Dataset Analysis

Nuvera patient microarray data was obtained from GSE25066 using GEOquery (v2.60.0) [359]. Expression intensities were normalized between patients using the 'normBetweenArrays' function in the R package limma (v3.48.3) [360]. Gene set enrichment scores were computed using GSVA (v1.40.1) to estimate the abundance of each 'Hallmark' ('H' collection) gene set from MSIGDBR (v7.4.1) as well as a list of the 12 most highly expressed collagen genes [361]. All collagen genes were removed from Hallmark gene sets to prevent artifactually high correlations due to the same gene being included in both sets. Correlations between GSVA scores were plotted in Python using Seaborn (v0.11.2) and Matplotlib (v3.5.1). Kaplan-Meier curves and statistical testing was conducted in Python using the 'lifelines' package (v.0.27.0). All analysis code is available via GitHub repository https://github.com/cstashko/STIFMaps.

Statistical Analysis

Unless otherwise stated, statistical analyses were performed using GraphPad Prism Version 9.1.2 or SciPy Version 1.7.3. Statistical tests used as well as significance is noted in the corresponding figure legends. Tests of normality were used to determine the appropriate statistical test. All independent variables are described in the text with measurements always from distinct samples (biological replicates) unless otherwise stated. All tests are two-tailed unless otherwise indicated.

Illustrations

The AutoAFM feedback system schematic (Fig. 2.1c) was created using BioRender (licensed to V.M.W.). The AlexNet visualization (Fig. 2.2a) was created using NN-SVG (http://alexlenail.me/NN-SVG/AlexNet.html).

7.2 Chapter 3

Human breast tumor tissues

Tumor tissues were obtained from patients with breast cancer from University of California, San Francisco, (UCSF) or Duke University Medical Center between 2010 and 2020. Tissue specimens were flash frozen in OCT (Tissue-Tek) by slow immersion in liquid nitrogen or placement on dry ice and stored at $\sim 80\ ^{\circ}$C until ready for sectioning. Samples were stored and analyzed with deidentified labels to protect patient data in accordance with the procedures outlined in the Institutional Review Board Protocol #10–03832, approved by the UCSF Committee of Human Resources and the Duke University IRB (Pro00054515). HER2+ subtype included all HER2+ patients regardless of ER status.

Picrosirius red staining and quantification

Frozen OCT tissue sections were fixed in 4% PFA for 10 min at RT, and then washed three times with PBS for 5 min each. Tissues were then stained with 0.1% picrosirius red (Direct Red 80, Sigma-Aldrich, 365,548 and picric acid solution, Sigma-Aldrich, P6744) for 1 hr and counterstained with Weigert's hematoxylin (Thermo Scientific, 88,028 and 88029) for 10 min at RT. Polarized light images were acquired using an Olympus IX81 microscope fitted with an analyser (U-ANT) and a polarizer (U-POT, Olympus) oriented parallel and orthogonal to each other. Images were quantified using an ImageJ macro to determine percentage area coverage per field of view using one to five fields of view per tissue region. The ImageJ macro is available at https://github.com/northcottj/picrosirius-red.

Trichrome blue staining

Frozen OCT tissue sections were fixed in 4% PFA for 10 min at RT, and then washed three times with PBS for 5 min each. Tissues were then stained with Masson Trichrome Stain (Thermo Scientific) according to the manufacturer's instructions.

Alcian blue staining

Frozen OCT tissue sections were fixed in 4% PFA for 10 min at RT, and then washed three times with PBS for 5 min each. Tissues were then placed in alcian blue (Sigma, B8428) for 1

hr and counterstained with nuclear fast red (Vector, H-3403) for 5 min at RT. Whole-slide images were obtained with a ZEISS Axio Scan.Z1 digital slide scanner equipped with CMOS and color cameras, with a 10x objective.

Quantification of Trichrome blue and Alcian blue staining

For whole-slide images of trichrome blue and alcian blue staining, one to three images at 1218x809 pixels were selected per tissue region. Each image was color deconvoluted using https://github.com/landinig/IJ-Colour_Deconvolution2 [39] and a minimal threshold was set for blue pixels and maintained for all images. The area of region that was covered by the minimal threshold was calculated and one to three images per tissue region were then pooled and averaged.

Sialidase treatment of tumor sections

Frozen OCT tissue sections were fixed in 4% PFA for 10 min at RT, and then washed three times with PBS for 5 min each. Sections were then incubated with 0.25 U/mL Vibrio cholerae sialidase (Roche #11080725001) in glycosidase buffer (50 mM sodium acetate, 5 mM CaCl2, pH 5.5), or glycosidase buffer alone, in a humid chamber at 37 °C for 1 h. Slides were then washed with PBS and stained with Alcian blue as above.

scRNAseq analysis

We took advantage of a recently published human breast cancer atlas [25] that was publicly available on the Gene Expression Omnibus (GSE161529). We predominantly focused our SeuratV4 analysis [40] on merged data for 34 distinct breast tumors representing different disease subtypes, that we compared to merged data for 12 normal mammary glands. Prior to merging, we first processed each file individually in Seurat and retained cells based on RNA features, removing outliers that were always below 200 and generally above 5,000, as well as any cells exhibiting $>$10% mitochondrial DNA. The UMAP plot resulting from the merged data was produced using 20 principal components during the dimensional reduction step and with a resolution of 0.1. Cluster annotation proceeded via attributing to clusters the expression of core classification genes (e.g., B cells = IGKC, IGLC2, MS4A1; Cancer/Epithelial cells = KRT19, KRT18, KRT8; Endothelial cells = VWF, CLDN5, PECAM1; Fibroblast cells = COL1A1, COL1A2, TAGLN; Mast cells =

TPSAB1, TPSB2, Kit; Mesenchymal cells = IGFBP7, ACTA2, TAGLN, PDGFRB; Myeloid cells = APOE, LYZ, CD72; T & NK cells = CD3D, GMZA, NKG7). Of note, the mesenchymal cell cluster was left broadly annotated due to varied gene expression, although it does demonstrate some features attributable to pericytes. In instances where cells expressing SIGLEC genes were enumerated on a per sample basis, immune cells were first gated by virtue of them having PTPRC (CD45) expression > 0.5 and then the resulting cells were enumerated using SIGLEC expression > 0. In analyses where the epithelial cells were counted for their expression of SiaSynthesis genes, we first gated the cells via KRT19 expression > 0.5 and next quantified those expressing individual SiaSynthesis genes > 0. The analysis of the normal mammary gland samples proceeded in a manner akin to our tumor analysis.

Immunoflourescence staining

Frozen OCT tissue 10 μm sections were fixed in 4% PFA for 10 min at RT, and then washed three times with PBS for 5 min each. Tissue sections were permeabilized with 0.25% v/v Triton-X-100 in PBS for 5 min at room temperature. Tissues sections were then blocked with 1x Carbo-Free blocking solution (Vector Laboratories # SP-5040–125) for 1 h at room temperature. Primary antibodies were diluted in 1x Carbo-Free blocking solution and incubated overnight at 4 °C. Tissue sections were washed three times with PBS and stained with fluorescently labelled secondary antibodies diluted in 1x Carbo-Free blocking solution for 1 h at room temperature. Tissue sections were washed three times with PBS, counterstained with DAPI, mounted, and imaged. Primary antibodies used and dilution ratios are: anti-panCK (Biolegend #914204; 1:100), anti-CMAS (Sigma-Aldrich #HPA039905; 1:300), SNA-biotin (Vector Laboratories #B-1305–2; 1:200), anti-SMA (Cell Signaling Technology #19245 s; 1:200), MAL-II biotin (Vector Laboratories #B-1265–1; 1:100). For Siglec-Fc reagents, which were used to image Siglec ligands, a pre-complexing protocol [38] was used where 1 μg/mL Siglec-Fc reagent was incubated with 1 μg/mL donkey anti-human-DyLight488 (Thermo-Fisher #PISA510126) in 1x Carbo-Free blocking solution before being added to the tissue sections at the secondary labeling step. Siglec-Fc reagents

were purchase from R&D Systems: Siglec-7-Fc (#1138SL050) Siglec-9-Fc (#1139SL050), and Siglec-10-Fc (#2130SL050).

Immunofluorescence imaging and analysis

IF-stained breast tumor sections were imaged on an inverted Nikon Ti2-E microscope equipped with a CREST X-Light V2 large field of view spinning disk confocal. For each slide, 3–6 representative images were collected for each high and low fibrosis regions. Images were collected using a 20x or 40x objective. IF micrographs were batch analyzed using custom pipelines built using the NIS-Elements General Analysis (GA3) tool.

Analyses of RNAseq data deposited in TCGA database

For RNAseq analysis, HTseq count files were acquired from the TCGA-BRCA repository from 1,222 patient samples. Lowly expressed genes were filtered out if average expression was less than 1 CPM, which resulted in inclusion of 16,974 genes. Normalization was performed using calcNormFactors in edgeR. Pathway enrichment was done using GSVA. Pearson correlation 'r' and 'p' values are reported.

7.3 Chapter 4

Antibodies and chemicals

Antibodies employed in this study: Rabbit phospho-EIF2a (Ser51) (Cell Signaling Technology, #3398), Rabbit total EIF2a (Cell Signaling Technology, #9722), rabbit α-tubulin (Cell Signaling Technology, #2125), mouse anti-β-Actin (Sigma, A5441), mouse anti-GFP (Thermo Fisher, MA5-15256), mouse anti-myc (Sigma, SAB1305535), rabbit anti-myc (Cell Signaling Technology, #2278), FLAG M2 (Sigma, F3165), mouse anti-filamin (Millipore, MAB1678 for Western blotting; Millipore, MAB1680 for immunofluorescence staining), mouse anti-α-actinin (Santa Cruz, sc17829) rabbit anti-Annexin A2 (Cell Signaling Technology, #8235), rabbit anti-S100A14 (Sigma, HPA027613), rabbit anti-V5 (Cell Signaling, #13202), rabbit cleaved caspase-3 antibody (Asp175) (Cell Signaling, #9661), Rabbit phospho-myosin light chain 2 (Ser19) (Cell Signaling, #3675), mouse anti-laminin 5 (Developmental Studies Hybridoma Bank, P3H9), rabbit

anti-integrinβ4 (Cell Signaling, #14803), HRP-conjugated goat anti-rabbit (Advansta, R-05072-500), HRP-conjugated goat anti-mouse (Advansta, R-05071-500), and Streptavidin-HRP (Sigma, S2438).

Chemicals/reagents employed in this study

Blebbistatin (Sigma, B0560), Pluronic acid (Sigma, P2443), CF-dye phalloidin conjugates (Biotium), recombinant basement membrane (BD Biosciences, #356234), Cultrex 3D Culture Matrix Laminin I (R&D Systems, #3446-005-01), Polyethylenimine (Polyplus Transfection, #24765-1), doxycycline (Alfa Aesar, J60579), Isopropyl β-d-1-thiogalactopyranoside (IPTG) (Sigma, #10724815001), 4-hydroxytamoxifen (Sigma, H6278), Biotin-phenol (IRIS Technologies International GmbH, LS-3500), FURA (Abcam, Ab120873), Thapsigargin (Adipogen, AG-CN2-0003), Paclitaxel (TSZCHEM, RS036), TRAIL (BioMol Research Laboratories Inc., T8180-08.50), Doxorubicin (Sigma, D2975000), Duolink® In Situ Red Kit (mouse/rabbit; Sigma, DUO92102).

Cell culture

MCF10A MECs were cultured in DMEM/F12 Ham's mixture (Invitrogen) supplemented with 5% horse serum (Invitrogen), 20 ng/ml EGF (PeproTech), 10 μg/ml insulin (Sigma), 100 ng/ml cholera toxin (Sigma), and 0.5 mg/ml hydrocortisone (Sigma) as described previously ([362]). HEK293T cells were cultured in DMEM (Genesee Scientific) supplemented with 10% FBS (Gemini Bio-Products). HMT-3522 S-1 MECs were cultured in chemically defined medium as previously described ([188]). All cell lines were derived from authenticated sources and tested for mycoplasma. All cells and derivative stable cell lines were maintained at 37°C and 5% CO2.

2D and 3D culture models

2D monolayer cultures were plated on rBM-laminated glass coverslips overnight. For fully embedded 3D culture, cells were resuspended in an ice-chilled solution composed of 50% rBM and 50% growth media and immediately placed at 37°C for matrix gelation for 1 h. Regular growth media were supplemented 45 min after rBM polymerization. Polyacrylamide (PA) gels were prepared as described previously ([352]). Briefly, compliant PA gels were polymerized on

silanized coverslips and were either functionalized with rBM (50 μg/ml) or laminin (40 μg/ml) overnight. PA gels were washed three times and equilibrated overnight at 37°C prior to cell seeding. Cells that remained unattached 1 h post-seeding were removed by replacing the supernatant with regular growth media. In 2D conditions, the supernatant was replaced with fresh media, whereas in 3D conditions, the supernatant was replaced with fresh media supplemented with 2% rBM or 100 μg/ml laminin, generating a 3D scaffold around cells. Micropatterned surfaces were prepared as described previously ([363]). Briefly, a thin film of round perforations (microwells) 10 μm in diameter were fabricated and adhered to tissue culture-treated coverslips. Alexa-647 conjugated laminin-111 (40 μg/ml) was used to coat the surface overnight at 4°C. After two washes with PBS, the thin microwell film was subsequently removed. PEG-PLL (100 μg/ml) was used to passivate the unpatterned glass surface for 1 h. The fluorescent signal of laminin-111 on the coverslips was used to ensure proper patterning prior to cell plating. Cells were trypsinized and incubated on the micropatterned surface for 15 min. For 2D conditions, unattached cells were removed by aspiration and replaced with fresh media. In 3D conditions, unattached cells were similarly removed and replaced with fresh media supplemented with 40 μg/ml of laminin.

Microarray experiments

Total RNA for microarray analysis was extracted from three independent culture preparations using TRIzol™ (Life Technologies) and RNA was purified using a RNeasy Mini Kit and a DNase treatment (Qiagen). To prevent apoptosis induction, organoid cultures were pretreated with caspase inhibitors DEVD-CHO and Ac-IETD-CHO (1 μM, respectively) at least 2 h before stimulation and inhibition was maintained throughout the duration of TRAIL treatment. Gene expression analysis was performed on an Affymetrix GeneChipTM Human Genome U133A 2.0 platform containing 22,283 probes according to the manufacturer's protocol. Biotinylated cRNA was produced from total RNA from each sample. After hybridization, washing and staining, arrays were scanned using a confocal scanner. The hybridization intensity data were processed using GeneChip Operating software. Affymetrix.cel files (probe intensity files) were processed with the Transcriptome Analysis Console (TAC) software. A filtering criterion (P ¡ 0.05 by empirical Bayes test, fold-

change $>$ 2.0-fold) was used to select differentially expressed genes within a comparison group. Gene ontology (GO) analysis was performed using GAGE on RMA-normalized microarray data with the "affy_hg_u133a" and "name_1006" attributes from the "ensembl" biomaRt. The microarray data can be download from NCBI Gene Expression Omnibus Website (GEO: GSE138900).

RNA purification, RNA-seq library preparation, sequencing, and analysis

RNA was isolated using TRIzol™ (Life Technologies) followed by chloroform extraction. RNA pellets were washed three times in 75% isopropanol and resuspended in RNAse-free water. The integrity of total RNA was examined by formaldehyde-agarose gel electrophoresis. RNA-seq libraries were constructed using a combination of KAPA mRNA HyperPrep Kit (Illumina) and NEBNext RNA Library Prep Kit (New England Biolabs) protocols. The poly-A-containing mRNA (500 ng) were purified using oligo(dT) beads and fragmented into 200–300 bp fragments using heat and magnesium. The cleaved RNA fragments were reversed transcribed into first strand cDNA using random primers. Second strand synthesis and an A-tailing step were performed according to Kapa kit instructions. NEBNextAdaptor was ligated to dA-tailed DNA and the end products were gel purified to remove excess unligated adaptors. USER enzyme was used to cleave at uracil incorporation sites followed by library amplification using NEBNext index primers for multiplexing. At the final stage, the cDNA library was again purified using gel electrophoresis. Libraries were quantified on a Bioanalyzer and sequenced via HiSeq4000 (Illumina) at the Vincent J. Coates Genomics Sequencing Laboratory, University of California, Berkeley. We performed 50-bp single-end sequencing on all samples and sequencing reads were aligned to the Gencode human genome primary assembly (v31) using STAR (v2.7.1a). Aligned reads were counted for each gene using the analyzeRepeats.pl function in HOMER (v4.9.1). Low expression genes were filtered out if they did not have at least one count per million (CPM) in at least three samples and normalized using the calcNormFactors function in edgeR with the "TMM" method. Clustering was performed on log2(CPM) values using Limma's plotMDS function. Differential expression analysis was made using Limma-Voom. GO analysis was applied to log2(CPM) values using GAGE with the "ensembl_gene_id_version" and "name_1006" attributes from the "ensembl" mart

on biomaRt. RNA-seq data were deposited in the National Center for Biotechnology Information Gene Expression Omnibus database under the accession number GSE150695.

Quantitative RT-PCR

Total RNA was harvested using a TRIzol™ (Life Technologies) method as described above. Samples were reverse transcribed using random hexamer primers. PerfeCTa SYBR Green FastMix (Quantibio, 95072-05k) and gene-specific primers were then added to cDNA samples. The primers employed in this study include GAPDH-For: 5'-CAGCCTCAAGATCATCAGCA-3'; GAPDH-Rev: 5'-TGTGGTCATGAGTCCTTCCA-3'; SEC61B-For: 5'-TCATCTCCAATATGCCTGGTC-3'; SEC61B-Rev: 5'-TTTGAGCCCAGGTGAATCTT-3'; ATF3-For: 5'-CGCTGGAATCAGTCACTGTCAG-3'; ATF3-Rev: 5'-CTTGTTTCGGCACTTTGCAGCTG-3'; CRACR2B-For: 5'-CTGATGAGGCCCAGGAGGAGGA-3'; CRACR2B_Rev: 5'-AGCCTCCTTGTCACACAGCAGAAA-3'. Thermal cycling conditions were 10 min at 95°C, followed by 40 cycles of 15 s at 95°C and 45 s at 65°C. Melting curve analysis was performed at the end of each PCR to verify the specificity of each primer. Relative mRNA expression was determined by the δ δ CT method with normalization to GAPDH.

Generation of expression constructs

A detailed description of cDNA constructs and their construction is provided in the section Construct source and molecular cloning.

Viral packaging, infection and selection and transfection

To generate retrovirus (pBabe and pBMN vectors), Phoenix cells were seeded and transfected with the indicated vectors using polyethylenimine (PEI). For lentivirus packaging (farnsylated mcherry, mCherry-GalT, Exo70-GFP, shRNAs, and FLAG-FLNIg21-Ig23, APEX-CAAX vectors), HEK293T cells were seeded and co-transfected with psPAX2 and pMD2.G and indicated lentiviral vectors using PEI. Virus-containing supernatant was collected 48 h post transfection, and the supernatant was centrifuged twice to remove residual Phoenix or HEK293T cells in suspension. The supernatant was supplemented with 8 μg/ml of polybrene prior to infection. Cells were infected with virus overnight, recovered from viral infection for 24 h followed by either puromycin,

G418 or blasticidin selection until all uninfected control cells were eliminated by the antibiotic. To generate MECs with doxycycline-inducible filamin, cells stably expressing the synthetic reverse Tet transcriptional transactivator rtTAs-M2 were transiently co-transfected with a transposon pPB-Puro-Tet vector encoding filamin and a vector with the hyperactive piggyBac transposase (pCMV-HAhyPBase) using Lipofectamine 3000 Reagents. Cells were allowed to recover from transfection for 24 h prior to puromycin selection. Doxycycline (0.5 μg/ml) was used to pre-induce filamin expression in MECs for 24 h prior to experimental use. To generate MCF10A MECs with doxycycline-inducible GFP-MAPPER, myc-tagged FLNIg21-Ig23 and myc-tagged PERK, cells were transiently transfected with these Sleeping Beauty (SB) transposon constructs using JetOPTIMUS® DNA Transfection Reagent. Cells were allowed to recover from transfection for 24 h prior to blasticidin selection. Doxycycline (0.5 μg/ml) was used to induce GFP-MAPPER after cells were plated on PA gels. Doxycycline (0.5 μg/ml) was used to induce myc-tagged FLNIg21-Ig23 for 3 h prior to cell plating on PA gels. To generate knockdown cells, MECs were infected with virus particles packaged with vectors expressing either shRNAs targeting luciferase, filamin, or actinin. The expression of shRNAs in MECs was induced using IPTG (100 μM) for 5 days prior to experiments.

Immunofluorescence

Cells on compliant PA gels or micropatterned surfaces were rinsed twice with PBS prior to fixation using 4% formaldehyde for 15 min. Cells were subsequently permeabilized with 0.2% Triton X-100, quenched in 10 mM glycine/PBS, blocked in 10% goat serum/1% BSA, and incubated with primary and secondary antibodies in 1% goat serum overnight. Secondary antibodies were conjugated to either Alexa 488, Alexa 555, or Alexa 647. Immmunofluorescence and live cell imaging was performed on an inverted microscope (Eclipse Ti-E; Nikon) with spinning disk confocal (CSU-X1; Yokogawa Electric Corporation), 405, 488, 561, 635 nm lasers; an Apo TIRF 100XNA 1.49 objective; electronic shutters; a charge-coupled device camera (Clara; Andor) and controlled by Metamorph. Fully embedded spheroid staining was conducted as above except that spheroids were fixed using 4% formaldehyde supplemented with 0.5% glutaraldehyde to prevent

rBM depolymerization during fixation. For samples with weaker fluorescent signals, stacks of images were acquired on a confocal microscope using a 100× 1.49 NA oil immersion objective and were deconvolved using Huygens Essential (Scientific Volume Imaging). All live-cell image stacks were acquired with 0.1-μm or 0.15-μm z-steps. Image deconvolution was performed to remove noise via the classic maximum likelihood estimation deconvolution algorithm in Huygens Essential imaging software.

Proximity ligation assay

Proximity ligation assay (PLA) experiments were performed using Duolink® In Situ Red Kit (mouse/rabbit; Sigma DUO92102) according to the manufacturer's instructions with minor modifications. Doxycycline-inducible myc-tagged PERK-expressing MECs ligated to rBM in 2D or 3D were incubated in 37°C humidified incubator overnight. The following day, the expression of myc-tagged PERK was induced for 7 h with doxycycline. Cells were subsequently fixed in 4% formaldehyde, permeabilized with 0.2% Triton X-100, quenched in 10 mM glycine/PBS, blocked in 10% goat serum/1% BSA, and incubated in the absence (negative control) or presence of mouse anti-filamin and rabbit anti-myc in 1% goat serum overnight at 4°C. Samples were incubated with anti-rabbit PLUS and anti-mouse MINUS PLA probes diluted in 1% BSA for 1 h at 37°C humidified chamber. Cells were washed twice for 5 min with buffer A (provided in the kit), incubated with the PLA reaction mix for 30 min at 37°C and washed again twice for 2 min with buffer A. The amplification reaction was performed by incubating cells with polymerase reaction mix for 100 min at 37°C in a humidified chamber. Cells were then washed twice for 10 min with buffer B (from kit) and once for 10 min with 0.01x buffer B. Prior to imaging, samples were counterstained with phalloidin and DAPI to visualize actin and nuclei. All image stacks were acquired with a 0.1-μm z-steps. The PLA signals were quantified using Fiji software and reported as total number of puncta per cell (as the sum of punctate above a defined signal threshold in the confocal image stack). Cortical PLA signal were quantified by the total number of puncta present at the actin cortex.

For PLA experiments measuring PERK and filamin interaction, MCF10A MECs with doxycycline-inducible myc-PERK were ligated with rBM in 2D (with or without blebbistatin) or 3D. The next day, myc-PERK expression was induced for 7 h and cells were then fixed and processed using the PLA staining protocol outlined above. For PLA experiments assessing the functional impact of FLNIg21-Ig23, MCF10A MECs with doxycycline-inducible myc-PERK were transduced with IRES-GFP vectors encoding FLAG-tag alone (control) or FLAG-FLNIg21-Ig23. Subsequently, cells with doxycycline-inducible myc-PERK and FLAG alone or myc-PERK and FLAG-FLNIg21-Ig23 were ligated with rBM in 2D or 3D overnight. The next day, myc-PERK expression was induced for 7 h by the addition of doxycycline and cells were fixed and PLA stained.

Intracellular calcium imaging

Cytosolic Ca2+ signals were measured as described previously with some modifications ([364]). MCF10A MECs were loaded with 2 μM Fura-AM in extracellular buffer (125 mM NaCl, 5 mM KCl, 1.5 mM MgCl2, 20 mM HEPES, 10 mM glucose, 1 mM CaCl2, 0.04% pluronic acid) for 30 min at 37°C for 30 min. Loaded cells were washed twice with extracellular buffer and 3 mM EGTA was added to chelate the extracellular calcium for 10 min. Fura-AM fluorescence is acquired by illuminating cells with alternating 340/380 nm light every 5 s and fluorescent intensity is collected at 510 nm. Cells were imaged for a few minutes and 2 μM Thapsigargin was added to the bath solution to stimulate ER Ca2+ release. After about 10 min, 4 mM CaCl2 was added back to the cells to allow for calcium influx from the bath solution.

Traction force microscopy

Cells were plated sparsely on rBM-laminated compliant 400 Pa PA gels containing 100 nm fluorescent beads. The gel was mounted on a microscope chamber to maintain 37°C and 5% CO2. Phase contrast images were taken to record cell position and fluorescent images of beads embedded in the gel just below the cells were taken to determine gel deformation. Images of MECs were collected before and after 0.5% SDS treatment using a Nikon Inverted Eclipse TE300 microscope and a Photometric Cool Snap HQ camera (Roper Scientific). Images were exported to

ImageJ and aligned using the StackReg plugin (NIH). The bead displacement field and the force field were reconstructed using iterative Particle Image Velocimetry (PIV) and Fourier Transform Traction Cytometry (FTTC) plugins from Image J, respectively. The freely available package of traction force microscopy software is available at https://sites.google.com/site/qingzongtseng/tfm.

Atomic force microscopy

All atomic force microscopy (AFM) measurements were performed using a MFP3D-BIO inverted optical AFM (Asylum Research, Santa Barbara, CA) mounted on a Nikon TE200-U inverted microscope (Melville, NY) and placed on a vibration-isolation table (Herzan TS-150). A 2-μm beaded tip attached to a silicon nitride cantilever (Asylum Research, Santa Barbara, CA) was used for indentation. The spring constant of the cantilever was 0.06 N/m. For each session, cantilevers were calibrated using the thermal fluctuation method ([365]). AFM force maps were performed on 40 x 40 μm fields and obtained as a 12×12 raster series of indentation. Elastic modulus measurement was derived from the force curve obtained utilizing the FMAP function of the Igor Pro v. 6.22A (WaveMetrics, Lake Oswego, OR) supplied by Asylum Research. Cells were assumed to be incompressible and a Poisson's ratio of 0.5 was used in the calculation of the Young's elastic modulus. 2D measurements were conducted on MECs plated on a laminin-conjugated micropatterned surface with media overlay. 3D measurements were obtained using MECs incubated overnight with media containing laminin-111 (40 μg/ml).

Optical tweezer measurement

Mechanical properties of the cytoplasm were measured as described previously ([200]). Briefly, 0.5 μm latex beads were endocytosed by cells before they were seeded on compliant PA gels. Upon attachment, cells were cultured in either 2D or 3D conditions, as described above. The laser beam (10 W, 1064 nm) was focused through a series of Keplerian beam expanders and a 100x oil immersion objective. A high-resolution quadrant detector was used for position detection. The endocytosed bead was dragged at a constant velocity of 0.5 μm/s by the optical trap, and the force displacement curve of the local cytoplasm was recorded. The cytoplasmic modulus was calculated based on the slope in the linear range of a normalized force-displacement curve.

Laser ablation

Laser ablation experiments were performed as described previously ([366]). Live imaging for laser ablation was performed on an inverted microscope (Eclipse Ti-E; Nikon) with a spinning disk confocal (CSU-X1; Yokogawa Electric Corporation), head dichroic Semrock Di01-T405/488/561GFP, 488 nm (120 mW) and 561 nm (150 mW) diode lasers, emission filters ET525/36M (Chroma Technology Corp.) for GFP or ET630/75M for RFP, and an iXon3 camera (Andor Technology). Targeted laser ablation (20 3-ns pulses at 20 Hz at two target spots) using 551- (for GFP) or 514-nm (for RFP) light was performed using a galvo-controlled MicroPoint Laser System (Photonic Instruments) operated through Metamorph. Laser strength was calibrated before each experimental session based on minimum power necessary to ablate a kinetochore-fiber bundle of microtubules in mitotic cells.

MECs stably expressing LifeAct-RFP-T or inducible ROCK constructs ligated to 2D or 3D ECM were imaged for 20s prior to high-power ablation of the actin cortex and 5 min after laser ablation. The cellular response (bleb nucleation or no response) was quantified. Notably, acto-myosin contractility of MECs stably transduced with an inducible ROCK vector were stimulated overnight with 4-hydroxytamoxifen and the actin cortex of cells was labeled with SiR-actin dye (Cytoskeleton) according to the manufacturer's instructions prior to laser ablation.

Sample preparation for cellular tomography

We devised a workflow where compliant PA hydrogels of set elastic module were combined with electron microscopy-compatible surfaces functionalized with an ECM component of choice. To achieve that goal, we prepared two separate modules, one incorporating an electron microscopy compatible surface (EM grid) that could be treated with an ECM component such as rBM, and one with a PA hydrogel of set stiffness (i.e., cells cultured under 2D conditions). The two modules were combined right before seeding MCF10A cells expressing mCherry-CAAX (farnesylated mCherry). After a brief incubation, non-adherent cells were removed by gentle aspiration and fresh media containing DMSO (2D control) or blebbistatin (2D + Bleb, lower cortical tension) was added. Samples were closely monitored on an inverted microscope (Nikon), and as soon

as spreading was noticed, we applied the RCIA fixation protocol, a verified protocol that allows halting cell movement while maintaining the nanoscale integrity of the cell ultrastructure ([367]). Bright field images and the spatial position of non-spread cells expressing mCherry-CAAX were recorded. Samples that passed this screening stage were vitrified in liquid-nitrogen cooled liquefied ethane using manual plunger. Vitrification allows imaging these samples by a cryogenic electron microscope while maintaining the cells fully hydrated; averting structural collapse or shrinkage associated with dehydration ([368]). The vitrified samples were then transferred to a cryogenic transmission electron microscope (Tecnai Spirit T12, Thermo Fisher Scientific) for another round of screening. Here, we examined the quality of vitrification, and the number of cells and regions amenable for next step in our workflow, cryogenic cellular tomography (cryo-ET). The fluorescence images collected after fixation and before vitrification were aligned with images of the same region obtained through the cryo-TEM screening, using a fiducial-less approach we previously published ([209]; [369]) to identify regions slated for cryo-ET data acquisition.

Cellular tomography and image reconstruction

Cryo-ET data were acquired with an FEI Titan Krios equipped with a Falcon II or Falcon 3CE detector, operated at 300 kV, using Serial EM ([370]) or the Tomo packages (ThermoFisher Scientific) in batch model. The average dose for a complete tilt series was about 100–120 e$\sim$/Å2 and the defocus ranged between $\sim$8 and $\sim$14 μm. Magnification was chosen to result in a pixel size of 0.45 nm in the reconstructions. The fidelity and quality of the data collection was monitored with real-time automatic reconstruction protocols implemented in the pyCoAn package (github.com/pyCoAn/distro), an extended python version of the CoAn package([371]). Briefly, tilt series were aligned using the IMOD package with a combination of fiducial-based and patch-based approaches ([372]). Three-dimensional reconstructions were then generated using the simultaneous iterative reconstruction technique as implemented in Tomo3D ([373]). A total of 32 and 28 tomograms near the cell edges were analyzed for cells in the presence and absence of blebbistatin, respectively. Protrusion widths were measured in virtual slices of the 3D reconstructions every 100 nm along the center line of the protrusions. The assessment for filled versus empty was

done by visual inspection of the three-dimensional cryo-ET reconstructions. Compartments that contained discernible, individual macromolecules were counted as "filled." Compartments with somewhat smoother but very dense material were also counted as "filled." All others were counted as "empty." The process was repeated independently by three different cryo-EM experts (n = 3) to compile the statistics. The standard deviation of the assessment was 10.3%. Statistical significance of differences between the distributions was assessed using Mann–Whitney rank tests. The distance between actin filaments in the protrusions was analyzed using a modified version of the sliding-window Fourier amplitude averaging method that adds alignment and classification steps before calculating the Fourier transform ([374]).

Stable isotope labeling with amino acids in cell culture (SILAC), proximity-dependent biotinylation and affinity purification of plasma membrane-associated proteins

MCF10A MECs stably expressing farnesylated APEX2 (APEX2-CAAX) were cultured in lysine- and arginine-free DMEM/F12 media supplemented with dialyzed horse serum (Gemini Bio-Products), EGF, insulin, cholera toxin, hydrocortisone, light isotope labeled lysine and arginine or heavy isotope labeled lysine (K8) and arginine (R10). Cells were labeled in SILAC media for at least 8 passages prior to biotinylation assay. MCF10A were trypsinized and plated on compliant PA gels as described above (2D setup). During plating, cells were also preincubated with biotin-phenol overnight due to limited membrane permeability of the chemical in MCF10A cells. Cells were either treated with DMSO or 10 μM blebbistatin for 2 h prior to the biotinylation reaction. After incubating with H2O2 for 1 min, cells were washed three times with quenching solution and lysed directly in 2% SDS lysis buffer (2% SDS in 100 mM Tris–HCl, pH 8.0). The supernatant was diluted to 0.2% SDS and trichloroacetic acid (TCA) was added to a final concentration of 20% and incubated at 4°C overnight. After TCA precipitation, protein was pelleted by centrifugation at 13,000 g for 30 min. Pellets were washed with ice-cold 100% acetone, re-centrifuged at 13,000 g for 30 min and air-dried. Pellets were resuspended in 8 M guanidine-HCl (GnHCl; Sigma), 100 mM Tris–HCl pH 8.0 and incubated at room temperature for 1 h. Subsequently, samples from light and heavy labeled cells were mixed in equal proportion and the combined samples were diluted to

2.5 M GnHCl. Biotinylated proteins were captured on 100 μl of packed high-capacity NeutrAvidin sepharose beads (Thermo Fisher) overnight at 4°C. The affinity purified samples were washed five times with 1 ml of 2.5 M Gn-HCl, 100 mM Tris–HCl, pH 8.0 prior to mass spectrometry analysis. For immunoblotting, affinity-purified samples were washed an additional five times in 100 mM Tris–HCl followed by two washes in RIPA buffer (150 mM NaCl, 1% NP40, 0.5% sodium deoxycholate, 0.1% sodium dodecyl sulfate, 50 mM Tris–HCl, pH 8.0).

Identification of biotinylated proteins using mass spectrometry

NeutrAvidin sepharose beads and affinity purified proteins were resuspended and mildly denatured in 200 μl of 1 M GnHCl, 1 mM CaCl2, and 100 mM Tris pH 8.0, where we assumed 50% volume occupancy by the beads. Disulfide bonds were reduced with 10 mM tris (2-carboxyethyl) phosphine (Sigma, C4706), and free thiols were alkylated with 40 mM 2-chloroacetamide (Sigma, 22790-250G-F) in 100 mM Tris pH 8.0. Beads were heated to 80°C for 5 min to denature proteins and then kept at room temperature for 45 min in the dark for protein reduction and alkylation. After alkylation, 5 μg of mass spectrometry (MS) grade trypsin (Fisher, PI90057) dissolved in 5 μl 50 mM acetic acid (Sigma, 45754-100ML-F) was added to beads and proteins were digested at room temperature for 20 h in microcentrifuge tubes rotating on a rotisserie rack. The eluate was transferred to a new tube, acidified to a final concentration of 0.5% trifluoroacetic acid (pH ¡ 3, Sigma, AAA1219822) and desalted by reversed phase C18 solid phase extraction (SPE) cartridge, using a SOLA SPE (Fisher, 03150391). Peptides were eluted from the C18 SPE in 30 μl 50% acetonitrile (ACN, Sigma, 03150391) and 0.1% formic acid (FA, Honeywell, 94318-250ML-F) and then dried in a Genevac EZ-2 on an HPLC setting. Dried peptides were resuspended in 2% acetonitrile, 0.1% formic acid in a bath sonicator for 5 min to a concentration of 0.2 μg/μl before MS analysis. SILAC-labeled peptides (1 μg) were submitted for nano-LC–MS/MS analysis, using an 83 min reversed-phase curved gradient (2.4–32% acetonitrile, 0.1% formic acid with a concave curve number 7 in Chromeleon) with a 15 cm Acclaim PepMap 100 C18 analytical column (2 μm beads, 75 μm i.d., Fisher, DX164534), running at 200 nl/min on a Dionex Ultimate 3000 RSLCnano pump, in-line with a hybrid quadrupole-Orbitrap Q-Exactive

Plus mass spectrometer (ThermoFisher). The method includes a 13 min segment for the sample to load at 500 nl/min 2.4% ACN, 0.1% FA before the gradient and MS acquisition begins and a 6 min 80% ACN, 0.08% FA wash step at 500 nl/min after the gradient. For the MS analysis, a data-dependent method with a parent ion scan at a resolving power of 70,000 and a top 15 method was used for each replicate, selecting the top 15 most intense peaks for MS/MS using HCD fragmentation (normalized collision energy 27). Dynamic exclusion was activated such that parent ions are excluded from MS/MS fragmentation for 20s after initial selection.

For protein identification and quantification, RAW files were analyzed by Maxquant using default settings ([375]; [376]). The recorded spectra from two independent biological replicates were searched against the human reference proteome from UniProt (2017-11-15 release, with 71,544 entries in SwissProt/TrEMBL) using MaxQuant, version 1.6.2.1. Search parameters allowed two missed tryptic cleavages. Oxidation of methionine, phosphorylation of serine/threonine/tyrosines, and N-terminal acetylation were allowed as variable modifications, while carbamidomethylation of cysteines was selected as a constant modification and a threshold peptide spectrum match (PSM) false discovery rate (FDR) and protein FDR of 1% was allowed. Quantification of SILAC ratios was performed by Maxquant on the MS1 level and the resulting ratios for all replicates were compared using statistical tools found in the Perseus statistical analysis package ([377]). Proteins with ratio quantification in only one replicate were removed. Statistical significance was determined by applying a one-sample, two-sided Student's t-test to the replicates with a P-value cutoff of P = 0.1. The mass spectrometry proteomics data have been deposited to the ProteomeXchange Consortium via the PRIDE partner repository with the dataset identifier PXD018975 ([378]).

VSVG trafficking assay

MCF10A cells were transfected with the VSVGts045-GFP construct using JetOPTIMUS® DNA Transfection Reagent (Polyplus, #101000051) for 4 h and then seeded on compliant PA gels. MEC cultures on compliant PA gels were placed at 40°C overnight to trap the protein at the endoplasmic reticulum. VSVG-ts045-GFP Cells were fixed after 2-h incubation at 32°C in the

presence of cycloheximide to allow VSVG-ts045 trafficking from the ER to the plasma membrane. The subcellular localization of VSVG-ts045-GFP was examined using confocal microscopy. Cell surface VSVG and total VSVG fluorescent signals were measured using Fiji software as described in the Image Quantification section.

Image quantification

To examine the subcellular localization of GFP-MAPPER, MECs expressing doxycycline-inducible GFP-MAPPER were fixed and counterstained with phalloidin to visualize the actin cytoskeleton. The actin cortex was used as a proxy for plasma membrane. The amount of ER-PM contact sites was measured as GFP-MAPPER fluorescence at the actin cortex relative to total GFP-MAPPER fluorescence for the cell.

To evaluate the secretory efficiency of VSVGts045-GFP, MECs transiently expressing VSVGts045-GFP were fixed after 2-h incubation at 32°C and counterstained with phalloidin to visualize the actin cortex. The actin cortex (stained by phalloidin) was used as a proxy for plasma membrane. VSVG fluorescent signals overlapping with actin cortex (in the middle focal plane of each cell) was quantified as plasma membrane localized VSVG. The secretion efficiency was scored as VSVGts045-GFP fluorescence at the plasma membrane relative to total VSVG-ts045-GFP fluorescence for the whole cell.

To measure the subcellular localization of Exo70-GFP, MECs stably expressing GFP-Exo70 and farnesylated mCherry were fixed and imaged directly. The spatial distribution of Exo70GFP was reported as plasma membrane Exo70-GFP (Exo70-GFP co-localized with farnesylated mCherry) relative to cytoplasmic Exo70-GFP (Exo70-GFP that is not colocalized with farnesylated mCherry).

Immunoblotting

MECs on 2D and 3D PA gels were lysed directly using 2X protein sample buffer (2% sodium dodecyl sulfate, 0.1% bromophenol blue and 20% glycerol, and 5% β-mercaptoethanol) containing a protease inhibitor cocktail (Pierce). The lysate was sonicated by 10 short bursts with a stainless steel probe sonicator before boiling at 95°C for 5 min. Samples were centrifuged at 13,000

g for 10 min and resolved using SDS–PAGE gels and transferred onto polyvinylidene difluoride membranes (PVDF; BioRad). The membranes were blocked with 5% milk in TBST and probed with the indicated primary antibodies in 5% BSA/TBST and a 1:10,000 dilution of anti-rabbit or anti-mouse horseradish peroxidase-conjugated secondary antibodies in 5% BSA/TBST. Blots were developed using WesternBright Quantum (Advansta) and visualized on PXI 6 Touch (Syngene). The band intensity of all Western blots was quantified using Fiji software.

Live/dead assay

Live/Dead assays of MECs on compliant PA gels were performed using a viability/ cytotoxicity kit (Thermo Fisher, L3224). Briefly, single round MECs grown in 2D and 3D conditions were seeded for 48 h and were washed twice in PBS prior to live/dead quantification. Percent cell death measurements were calculated based on the number of dead cells/total cells. For the 2D monolayer and spheroid live/dead assay, cells were either cultured on 2D plastic surfaces (2D monolayer) or embedded within rBM and grown for 12 days to form 3D spheroids. Cells were treated in the absence or presence of recombinant, purified human or mouse TRAIL, Paclitaxel or doxorubicin. Percent live/dead cells in 2D monolayers and organoids were quantified by indirect immunofluorescence for active caspase-3 cells with total cells enumerated from nuclei counterstained with Hoechst 33342.

Statistical analyses

Statistical analyses were performed using Prism GraphPad 5 software. All quantitative results were assessed by paired or unpaired two-tailed Student's t-test where indicated or one-way ANOVA after confirming that the data met appropriate assumptions (normality, homogeneous variance, and independent sampling). All data were plotted with standard deviation or standard error bars as indicated in the figure legends. Sample size was chosen based upon the size of the effect and variance for the different experimental approaches. P-values less than or equal to 0.05 were considered to be significant.

Construct source and molecular cloning

The pCB6-VSV-G-ts045-GFP construct and cDNA encoding EGFP-Exo70 were provided by Wei Guo (University of Pennsylvania, USA). The retroviral pBABE-Puro construct with conditionally active human ROCK1 (ROCK1:ER) was provided by Michael Samuel (University of South Australia, Australia). The pcDNA3-myc-FLND21-D23 was provided by Dr. Peter Carmeliet (KU Leuven, Belgium). The cDNAs encoding APEX2, GFP-MAPPER, myc-tagged PERK and pSBtet-BB was acquired via Addgene (Plasmid #72480, #117721, #21814, and #60505, respectively). The cDNAs encoding mApple-golgi (GalT) and human filamin were obtained from Michael Davidson's plasmid collection at the UCSF Imaging Center (Plasmid #54907 and #54098). pLV-PGK-H2B-EGFP (Plasmid #21210). pCMV-HAhyPBase was kindly provided by Allan Bradley (The Wellcome Trust Sanger Institute, UK). pBMN-LifeAct-RFP-T was provided by Roy Duncan (Dalhousie University, Canada). pLV-PGK-mcherry-CAAX, pLV-rtTAs-M2-IRES-Neo, pLV-EEF1a-Integrin_IRES-mEmerald, pPB-SV40-pA-Puro-SV40-polyA-tet-IVS-MCS-BGH-polyA (expression vector), and pPB_U6_3xlacIbs_Luciferase_shRNA-IRES_Neo and pPB_U6_3xlacIbs_2kb_stuffer_shRNA-IRES_Neo (shRNA vector) constructs were made in our laboratory.

The open reading frame (ORF) of mApple-golgi (GalT) was PCR amplified using forward primer 5'-ACTACTAGATCTACCATGAGGCTTCGGGAGCCGCTC-3' and reverse primer 5'-TTACTTGTACAGCTCGTCCA-3' and digested with BglII/BsrGI. The resultant fragment was ligated to a pLV-PGK-H2B-EGFP vector backbone digested with BamHI/BsrGI. EGFP-Exo70 was subcloned into a vector backbone of pLV-PGK-H2B-EGFP digested with BamHI/SalI. A pLKO-cppt-PGK-APEX2-CAAX-IRES-Neomycin construct was generated by ligating three pieces of PCR fragments: (Fragment 1) BamHI-V5-APEX2-N22 (linker)-XhoI; (Fragment 2) XhoI-CAAX-PmeI, and (Fragment 3) pLKO-cppt-hPGK-MCS-IRES-Neomycin construct digested with BamHI/PmeI. The Filamin ORF was PCR amplified using forward primer (5'-ACTACTACTAGTACCATGAGTAGCTCCCACTCTCGGGCG-3') and reverse primer (5'-ACTACTGTTTAAACTTAGGGCACCACAACGCGGTAGG-3') and digested with SpeI/PmeI. The resultant fragment was ligated to a pPB-SV40 pA-Puro-SV40-polyA-tet-IVS-

vector digested with SpeI/PmeI. The ORF of myc-FLND21-D23 was PCR amplified using forward primer 5'-AGCTGGCCTCTGAGGCCACCATGGAGCAGAAGCTGATCAGC-3' and reverse primer 5'-AGCTGGCCTGACAGGCCTCACTTGAAGGGGCTGCCCCCAA-3' and digested with SfiI. The resultant fragment was ligated to a pSBtet-BB vector backbone digested with SfiI. The ORF of GFP-MAPPER was PCR amplified using forward primer 5'-AGCTGGCC TCTGAGGCCACCATGGATGTATGCGTCCGTCTTG-3' and reverse primer 5'-AGCT GGCCTGACAGGCCTCAAGTTACTGAATCTTTCTTCTTCCGGAATG-3' and digested with SfiI. The resultant fragment was ligated to a pSBtet-BB vector backbone digested with SfiI. The ORF of myc-tagged PERK was PCR amplified using forward primer 5'-AGCTGGCCTCTGAGGCCGAATTCGGCACGAGCGATGTCTGC-3' and reverse primer 5'-AGCTGGCCTGACAGGCCTCACAGATCCTCCTCAGAGAT CAGCTT-3' and digested with SfiI. The resultant fragment was ligated to a pSBtet-BB vector backbone digested with SfiI and SfiI-AgeI-BglII-EcoRI oligonucleotide fragment (GGCCTCTGAGGCCACCGGTA-GATCTGAATTC). pLV-EEF1a-FLAG-FLND21D23-IRES-mEmerald was generated by ligating three pieces of PCR fragments: (Fragment 1) BamHI-FLAG-EcoRI; (Fragment 2), PCR product of BamHI-myc-FLND21-D23-PmeI digested with EcoRI and PmeI, and (Fragment 3) pLV-EEF1a-Integrin_IRES-mEmerald digested with BamHI/PmeI. EGFP-Exo70 was subcloned into a vector backbone of pLV-PGK-H2B-EGFP digested with BamHI/SalI. pLKO-cppt-PGK-APEX2-CAAX-IRES-Neomycin was generated by ligating three PCR fragments: (Fragment 1) BamHI-V5-APEX2-N22 (linker)-XhoI; (Fragment 2) XhoI-CAAX-PmeI fragment, and (Fragment 3) pLKO-cppt-hPGK-MCS-IRES-Neomycin vector digested with BamHI/PmeI.

For knockdown studies, the shRNAs are cloned into vector pPB_U6_3xlacIbs_2kb_stuffer_shRNA-IRES_Neo digested with AgeI/EcoRI. Filamin shRNA used in this paper has been validated by Sigma Aldrich (TRCN0000230788) and the shRNA was assembled using forward primer 5'-CCGGGACCGCCAATAACGACAAGAACTCGAGTTCTTGTCGTTATTGGCGGTCTTTTT G-3' and reverse primer 5'-AATTCAAAAAGACCGCCAATAACGACAAGAACTCGAG TTCTTGTCGTTATTGGCGGTC-3', which yield duplexes with 5' AgeI and 3' EcoRI restriction

site overhangs that are ready for ligation reaction. ACTN shRNA was assembled using forward primer 5'-CCGGGCCACACTATCGGACATCAAACTCGAGTTTGATGTCCGATAGTGTGGCTTTTTG-3' and reverse primer 5'-AATTCAAAAAGCCACACTATCGGACATCAAACTCGAGTTTGATGTCCGATAGTGTGGC-3'. Exo70 shRNA was assembled using forward primer 5'-CCGGCGACCAGCTCACTAAGAACATCTCGAGATGTTCTTAGTGAGCTGGTCGTTTTTTG-3' and reverse primer 5'-AATTCAAAAAACGACCAGCTCACTAAGAACATCTCG AGATGTTCTTAGTGAGCTGGTCG-3'.

Computational modeling

The description of modeling methods used for the free energy of tubule formation and free energy landscape for protein recruitment on the cell membranes, as well as the subsequent analysis are detailed in the online version of this article.

Protrusion elongation studies Protrusion simulations are performed with several curvature-inducing membrane proteins present and with no other background spontaneous curvature field. In this study, membrane proteins diffuse around and are able to co-locate to produce tubule like structures. Once above a threshold density required for tubulation, the protrusion elongates. The threshold density of proteins required for tubulation and consequently the protrusion length and density are strongly dependent on membrane interfacial tension.

Parameters are detailed in Table 8.2.

Data availability The authors declare that all data supporting the findings of this study are available within the paper. The microarray data can be download from NCBI Gene Expression Omnibus website (GEO: GSE138900; http://www.ncbi.nlm.nih.gov/geo/query/acc.cgi?acc=GSE138900). RNA-seq data were deposited in the National Center for Biotechnology Information Gene Expression Omnibus database under the accession number GSE150695. The mass spectrometry proteomics data have been deposited to the ProteomeXchange Consortium via the PRIDE partner repository with the dataset identifier PXD018975.

7.4 Chapter 5

Western blotting

Cells were freeze-thaw lysed (-80 °C) with RIPA buffer (150 mM NaCl, 1% v/v NP-40, 0.5% w/v sodium deoxycholate, 0.1% w/v SDS, and 25 mM tris) containing protease and phosphatase inhibitor coctail (GenDepot, P3100 and P3200). Protein content was determined via BCA (Pierce, 23225) and 5-10 μg of protein was mixed with 5x Laemmli buffer to generate final 1x concentration (50 mM Tris-HCl (Fischer, AAJ2267636) pH 6.8, 4% w/v SDS (Sigma, L3771), 10% v/v glycerol (Fischer, BP229-1), 0.1% w/v bromophenol blue (Bio-Rad, 1610404), 2% v/v β-mercaptoethanol (Bio-Rad, 1610710) and heated to 95 °C for 5 min (no heating of the samples used for the total oxphos (abcam, ab110413) blots). 10%-gels (Bio-Rad, Bulletin_6201) were cast in a PROTEAN Plus multi casting chamer (Bio-Rad). Samples were loaded ($\sim$20 μL) and run to completion in Tris Glycine SDS running buffer (25 mM Tris, 192 mM glycine (Fischer, BP381), and 0.1% SDS, pH $\sim$8.6), wet transferred @ 100V for 60 min to methanol (Fischer, A412) activated PVDF (BioRad, 1620177) in Towbin transfer buffer containing (25 mM Tris, 192 mM Glycine, 20% v/v methanol, pH $\sim$8.3). Protein loaded PVDF membranes were washed 2x with TBST (20 mM tris, 150 mM NaCl (S271), 0.1% w/v Tween20) and blocked in 5% milk TBST buffer for 1 h at 22 °C on an orbital shaker.

Antibodies used

HSF1 (Cell Signaling, HSF1, 4356, AB_2120258), YME1L1 (Invitrogen, PA564299, AB_2649732) HSP60 (LK1, sc-59567, AB_783870), HSP70 (3A3, sc32239, AB_627759), mtHSP70 (D-9, sc-133137, AB_2120468), Total OXPHOS WB Antibody Cocktail (Abcam, ab110413, AB_2629281), β-Actin (Sigma, A5441, AB_476744), FAK pY397 (Invitrogen, 44-625G, AB_1500096), FAK (BD, 610088, AB_397495), and pMLCK (Cell Signaling, 3671, AB_330248).

V737N β1 integrin

Weaver lab generated (Dr. Jonathan Lakins) puromycin lentiviral transfer vector expressing 3x myc tagged V737N β1 integrin using the tetracycline rtTA2(S)-M2 ([379]) inducible pro-

moter for 24 h with doxycycline [200 ng/mL] (Sigma, D9891). No respiratory repression of MCF10A or MB-MDA-231 cells was observed with 200 ng/mL, 1 μg/mL, or 2 μg/mL doxycycline. Previous studies have demonstrated that 24 h of 30 μg/mL doxycycline treatment can suppress mitochondrial respiration ([380]).

WT β1 integrin

Weaver lab generated (Dr. Jonathan Lakins) puromycin lentiviral transfer vector expressing 3× myc tagged β1 integrin using the tetracycline rtTA2(S)-M2 ([379]) inducible promoter for 24 h with doxycycline [200 ng/mL] (Sigma, D9891).

YME1L1 CRISPR-I Using EF1a-dCas9-KRAB-Blast dCas9 vector and sgRNA lentiviral vectors generously provided by Dr. Michael T McManus and Broad institute GPP sgRNA Design identified sgRNAs targeting YME1L1 (1: 5'-TTCCGTTTCTGGGAGGAGTG, 2: 5'-GCAGTAGCTGTAGGAAGGGG, and 3:CTCCTCCCAGAAACGGAAAA-5') stable cell lines were generated via sequential selection of blasticidin (CRISPR-I) and puromycin (sgRNA), kill curve and qPCR validated.

***in vitro* respirometry**

Mitochondrial stress tests were performed with a Sea horse XF24e cellular respirometer on non-permeablized cells at $\sim$ 96% confluence (100-k cells/well) in V7 microplates, with XF assay medium supplemented with 1 mM pyruvate (Gibco), 2 mM glutamine (Gibco),and 5 or 25-mM glucose (Sigma) at pH 7.4 and sequential additions via injection ports of oligomycin [1-μM final], FCCP [1-μM final], and antimycin A/rotenone [1-μM final] during respirometry (concentrated stock solutions solubilized in 100% ethanol [2.5 mM] for mitochondrial stress test compounds). OCR values presented with non-mitochondrial oxygen consumption deducted.

Knockdown of HSF1

pLKO.1 puro (Addgene #8453) was modified to carry: Scr insert: 5'-CAACAAGATGAA GAGCACCAACTCGAGTTGGTGCTCTTCATCTTGTTGTTTTT, shRNA HSF1-1 TRCN00000-07481 (HSF1): 5'-CCGGGCAGGTTGTTCATAGTCAGAACTCGAGTTCTGACTATGAACAA

CCTGCTTTTT, shRNA HSF1-2 TRCN0000318652 (HSF1): 5'-CCGGGCACATTCCATGCCCA AGTATCTCGAGATACTTGGGCATGGAATGTGCTTTTT

Constitutively active HSF1

CD510B-1_pCDH-CMV-MCS-EF1-Puro (SystemBio) vector was modified to carry the hHSF1δRD (δ221–315) transgene ([381]) under the CMV promoter.

SLC9A1 KO

MCF10A cells were transfected via PEI (https://www.addgene.org/protocols/transfection) with pSpCas9(BB)-2A-GFP (PX458) - (Addgene #48138) carrying sgRNA for hSLC9A1 5'-GTTTGCCAACTACGAACACG (SLC9A1:HGLibA_45399) and H+-suicide selected ([382]) four separate times to isolate SCL9A1 KOs. $\sim$15% of the cells survived the first H+-suicide selection, $\sim$90% survived the subsequent 4 sections.

C. elegans compound microscopy of mitochondria

Transgenic animals carrying vha-6p::MLS::mRuby (MLS was derived from atp-1: ATGTTGTCCAAACGCATTGTTACCGCTCTTAACACCGCCGTCAAGGTCCAAAATGCCG-GAATCGCCACCACCGCCCGCGGA) were grown from L1 to desired stage of adulthood on standard RNAi plates as described above. Animals were aged by hand-picking adults away from progeny using a pick daily until desired stage of adulthood. For imaging, adult worms are mounted on a glass slide in M9 solution, covered with a cover slip, and imaged immediately for a maximum of 10 minutes per slide. Animals were imaged on a Zeiss AxioObserver 7 LSM900 Airyscan 2 equipped with a 63x/1.4 Plan Aprochromat objective, MA-PMT detector, diode lasers (488 nm, 10mW, laser class 3B; 561 nm, 10 mW, laser class 4B), driven by ZenBlack software. Images were processed using ZEN Module Airyscan for 3D using default software settings. Images were analyzed using MitoMAPR ([383]) across max projections keeping all parameters constant.

C. elegans Paraquat survival assay

Animals were grown to day 1 adulthood on standard RNAi plates as described above. 10 animals were picked into 75 μL of 100 mM paraquat solution prepared in M9 in a flat-bottom 96-well plate. $>$8 wells are used per condition for a minimum of 80 animals per replicate. Animals

were scored every 2 hours for death. Plates are tapped gently, and any trashing or bending movement is scored as alive. Paraquat survival assays are performed with the experimenter blinded to the strain conditions during scoring and are repeated a minimum of 3 replicates per experiment.

C. elegans stereomicroscopy for fluorescent transcriptional reporters

Transgenic animals carrying gst-4p::GFP were grown on standard RNAi plates as described above until the L4 stage. L4 animals were washed off of plates using M9, centrifuged to pellet, and M9 was replaced with 50 mM paraquat prepared in M9. Animals were incubated rotating in a 20 °C incubator for two hours, and subsequently washed 2x with M9 solution. Animals were then plated on OP50 plates and recovered for 2 hours at 20 °C. For imaging, worms were picked onto a standard NGM plate containing 5 μL of 100 mM sodium azide to paralyze worms. Paralyzed worms were lined up, and imaged immediately on a Leica M250FA automated fluorescent stereomicroscope equipped with a Hamamatsu ORCA-ER camera, standard GFP filter, and driven by LAS-X software.

C. elegans biosorter analysis

For large-scale quantification of fluorescent animals, a Union Biometrica complex object parameter analysis sorter (COPAS) was used (for full details, refer to [384]). Briefly, to quantify signal of gst-4p::GFP, animals treated as described above were washed off plates using M9, and run through the COPAS biosort using a 488 nm light source. Integrated fluorescence intensity normalized to the time of flight is collected automatically on the COPAS software, and then normalized again to the extinction to correct for both worm length and worm thickness.

ROCK:ER

pBABEpuro3 ROCK:ER ([248]) was generously provided by Dr. Michael F. Olson, packaged into retroviral particles with phoenix cells, and used to generate stable MCF10A cells lines which were activated with 1 μg/mL 4-hydroxytamoxifen (Sigma).

COX4L MTS tagged roGFP was expressed under the CMV promoter in a puromycin lentiviral transfer vector generated by the Dillin Lab (Dr. Brant Webster).

AFM and analyses were performed using an MFP3D-BIO inverted optical atomic force microscope mounted on a Nikon TE2000-U inverted fluorescence microscope (Asylum Research). 100k cells were seeded onto fibronectin coated 15 mm2 coverslips and cultured for 24 h. Coverslips were anchored with permanent adhesive dots (Scotch, 00051141908113) to a glass slide that was then magnet-anchored to the stage of the microscope. All samples were measured in media with contact mode using Novascan cantilevers (5 μm radius, Probe 58, k = 0.06 N per m), which were calibrated using the thermal tune method. 36 force measurements were collected over a 250 × 250 μm grid per sample. The resulting force data were converted to elastic modulus values using the Hertz Model program (tissue samples were assumed to be noncompressible, and a Poisson's ratio of 0.5 was used in the calculation of theYoung's elastic modulus values) in IgorPro v.6.22, supplied by Asylum Research

For JC-9 staining, day 1 adult animals were transferred to a plate containing JC-9-treated bacteria (OP50 bacteria were grown during mid-log phase for 4 hours in LB containing 50 μM JC-9 at 37 °C to incorporate JC-9 into bacteria; then bacteria were washed 2x with fresh LB to remove excess JC-9). Animals were grown on JC-9 bacteria for 2 hours at 20 °C to label. After labeling, worms were moved onto standard OP50 plates and grown for an additional 1 hour at 20 °C to remove excess JC-9 from the gut. Animals were then washed off plates and immediately run on a biosorter using a 488 and 561 nm light source. Worm profile data was collected, and run through an orientation and quantification algorithm, LAMPro ([384]). Briefly, integrated fluorescence intensity is measured throughout the entire profile of the worm and normalized to extinction throughout the length of the worm. Total integrated fluorescence of the entire worm was also calculated by normalizing to the time of flight and integrated extinction of the entire worm. JC-9 fluorescence at 515 nm was used to determine mitochondrial quantity, and the ratio of the fluorescence of 585 nm / 515 nm was used to determine mitochondrial membrane potential.

Lifespan assay Lifespan measurements were performed on solid NGM plates with RNAi bacteria. Worms were synchronized via bleaching/L1 arrested as described above. Adult animals were moved away from progeny by moving worms onto fresh RNAi plates every day until D7-10 when

progeny were no longer visible. Animals were then scored every 1-2 days for death until all animals were scored. Animals with bagging vulval explosion, or other age-unrelated deaths were censored and removed from quantification.

Lattice light sheet microscopy

We used a Custom build lattice light sheet microscope ([255]) to image MCF10A culture on polyacrylamide gels. Polyacrylamide gels (PA-gels) were formed on 5 mm round cover glass (Warner Instruments), coated with fibronectin and seeded with $\sim$ 1000 cells per gel. The samples were cultured for 24 h in MCF10A media prior to imaging in DMEM (5 mM glucose) without phenol red supplemented with 5% Fetal Bovine serum. Samples were illuminated by 561 nm diode laser (0.5W Coherent) or 639 nm diode laser (1W Coherent) using an excitation objective (Special Optics, 0.65 NA with a working distance of 3.74-mm) at 2% AOTF transmittance and output laser power of 100 mW. The measured powers at the back focal plane of the illumination objective were in the range of 0.15-0.2 mW. Order transfer functions were calculated by acquiring Point-spread functions using 200-nm TetraSpeck beads adhered freshly to 5-mm glass coverslips (Invitrogen T7280) for each excitation wavelength and each acquisition filter set. The LLSM was realigned before each experiment.

For illumination we displayed on the spatial light modulator (SLM) a Square lattice generated by an interference pattern of 59 bessels beams separated by 1.67 um and cropped to 0.22 with a 0.325 inner NA and 0.40 outer NA, or by a an interference pattern of 83 bessels beams separated by 1.23 um and cropped to 0.22 with a 0.44 inner NA and 0.55 outer NA The lattice light sheet was dithered 15-25 um to obtain an homogenous illumination with 5% of flyback time. Fluorescent signal was collected by a Nikon detection objective (CFI Apo LWD 25XW, 1.1 NA, 2-mm working distance (WD)), coupled with a 500 mm focal length tube lens (Thorlabs), a set of Semrock filters (BL02-561R-25, BLP01-647R-25, and NF03-405-488-561-635E-25), and a sCMOS camera (Hamamatsu Orca Flash 4.0 v2) with a 103 nm/pixel magnification.

Z-Stacks (Volumes) were acquired by moving the Z-piezo in scanning mode while leaving the lattice light sheet static. The slices of the stacks were taken with an interval of 100-235 nm (S-

axis) through ranges of 30-35 um at 20-100 ms exposuretime with 0 - 60 seconds intervals between volumes.

Raw data was flash corrected ([385]) and deconvolved using an iterative Richardson-Lucy algorithm ([255]) on two graphics processing units (GPU) (Nvidia, GeForce GTX Titan 4-Gb RAM). Flash calibration, flash correction, channel registration, Order transfer function calculation and Image deconvolution were done using the LLSpy open software (Lambert, 2019). Visualization of the images and volume inspection were done using Spimagine (https://github.com/maweigert/spimagine) and Clear volume ([386]).

For the glucose shock experiment, MCF10A cells were first localized under the LLSM. During the first 30 seconds of the acquisition, the glucose concentration was raised to a final concentration of 25 mM. The glucose infusion caused misalignment of the lattice light sheet microscope which was corrected manually during the first acquisition volume.

Fractal dimension and lacunarity

Due to the complex morphology of mitochondria networks, we chose to calculate the fractal dimension and lacunarity to describe its morphology. This analysis has been proven useful to characterize mitochondrial morphology in malignant mesothelioma ([387]). For the analysis regions of 276x276 pixels containing mitochondrial network were sampled randomly from 4 representative microscopy images for each experimental condition. Regions with more than 25% of its area contained nucleus were excluded from the analysis. Each data point in Extended Fig. 8.23E represent a sampled region. Each region was first low pass filtered with a radius of 8 pixels and a weight of 0.8 to enhance the mitochondria network signal. After each region was thresholded using the Huang Algorithm. For each binary-masked region we used FracLac (http://rsb.info.nih.gov/ij/plugins/fraclac/FLHelp/Introduction.htm) to calculate the fractal dimension (Db) and the lacunarity (lambda). For each region we increased linearly the sampled box until a maximum size of 50% of the region area the Db is calculated as the the average of Db from the Box scans. The fractal dimension was calculated using a regression to the logarithmic values of pixels with value 1 versus logarithm of the box size.

RNAseq

Total RNA was isolated using Trizol (Invitrogen), and RNAseq libraries (2 biological replicates per condition comprised of a pool of 4 PA-gel cultures each) prepared using KAPA mRNA HyperPrep Kit (Roche) and IDT dual indexed sequencing adaptors. Multiplexed libraries were sequenced on an Illumina HiSeq4000, and reads were aligned to the human genome (hg19) using RNA STAR ([388]). Aligned reads were counted using HOMER ([389]), and hierarchical clustering was performed using Cluster ([390]) and visualized with Java TreeView. Gene Ontology analysis was performed using Metascape ([391]).

Mitochondrial ETC proteomics timsTOF

1 million cells were seeded on 50 mM2 varied stiffness ECM coated PA-gels cultured for 24 h. Cells were washed with sterile PBS once, then cells were detached with cold PBS and a cell scraper (rubber policeman). Cell pellets were then suspended in 100 μL urea lysis buffer (ULB: 8M urea, 100 mM Tris, and 75 mM NaCl at pH 8). Probe sonicated 5 times for 2 s on ice. Protein concentrations were determined via BCA, and 100 μg of each sample was alkylated and reduced for 1 h at $\sim$22 °C (protected from light) via the addition of a 10X concentrated stock (ARB: 400 mM 2-Chloroacetamide and 100 mM Tris(2-carboxyethyl)phosphine (TCEP) dissolved in ULB) yielding a final concentration of 40 mM 2-Chloroacetamide and 10 mM TCEP. Samples were then diluted, with a Tris/NaCl buffer (100 mM Tris and 75 mM NaCl at pH 8) containing 1 μg LysC (Promega, Va11A) per sample, to yield a final concertation of 2M urea during a 4 h digestion at $\sim$22 °C (protected from light). Following the LysC digestion, 2 μg of Trypsin (Pierce, 1862746) was added and allowed to react with the sample overnight at 37 °C. The samples were then acidified with Trifluoroacetic acid (TFA) [$\sim$1% final] to yield a sample pH of 2. Samples were then desalted on C18 tips (Nest Group), the eluant was lyophilized, and then resuspended in 4% formic acid, 3% acetonitrile at 200 fmol/μL concentration. For each MS analysis, 1 μL of sample was separated over a 25 cm column packed with 1.9 μm Reprosil C18 particles (Dr. Maisch HPLC GmbH) by a nanoElute HPLC (Bruker). Separation was performed at 50 °C at a flow rate of 400 μL/min by the following gradient in 0.1% formic acid: 2% to 17% acetonitrile from 0 to 60 min, followed by

17% to 28% acetonitrile from 60 to 105 min. The eluant was directed electrospray ionized into a Bruker timsTOF Pro mass spectrometer and data was collected using data-dependent PASEF acquisition ([392]). Database searching and extraction of MS1 peptide abundances was performed using the MaxQuant algorithm ([375]), and all peptide and protein identifications were filtered to a 1% false-discovery rate. Searches were performed against a protein database of the human proteome (downloaded from Uniprot on 3/21/2018). Lastly quality control analysis was performed via artMS (http://artms.org) and statistical testing was performed with MSstats ([393]).

LC-MS/MS deuterium incorporation proteomics

1 million cells were seeded on 50 mM2 varied stiffness PA-gels cultured for 24 h in 6% D2O culture media in a 5% CO2 incubator humidified with 5% D2O. D2O labeled cells were detached with cold PBS and a cell scraper (rubber policeman), pelleted with centrifugation, and mitochondrial fractions were isolated with the Mitochondria Isolation Kit for Cultured Cells (Thermo, 89874). Protein was isolated by flash freezing and sonication in PBS with 1 mM PMSF, 5 mM EDTA, and 1x Halt protease inhibitor (Thermo, 78440). Protein content was quantified via BCA (Pierce, 23225) and 100 μg of protein from each sample was trypsin (Pierce, 90057) digested overnight after reduction and alkylation with DTT, TFE, and iodoactamide ([394]). Trypsin-digested peptides were analyzed on a 6550 quadropole time of flight (Q-ToF) mass spectrometer equipped with Chip Cube nano ESI source (Agilent Technologies). High performance liquid chromatography (HPLC) separated the peptides using capillary and nano binary flow. Mobile phases were 95% acetonitrile/0.1% formic acid in LC-MS grade water. Peptides were eluted at 350 nL/minute flow rate with an 18 minute LC gradient. Each sample was analyzed once for protein/peptide identification in data-dependent MS/MS mode and once for peptide isotope analysis in MS mode. Acquired MS/MS spectra were extracted and searched using Spectrum Mill Proteomics Workbench software (Agilent Technologies) and a human protein database (https://www.uniprot.org/). Search results were validated with a global false discovery rate of 1%. A filtered list of peptides was collapsed into a nonredundant peptide formula database containing peptide elemental composition, mass, and retention time. This was used to extract mass isotope

abundances (M0-M3) of each peptide from MS-only acquisition files with Mass Hunter Qualitative Analysis software (Agilent Technologies). Mass isotopomer distribution analysis (MIDA) was used to calculate peptide elemental composition and curve-fit parameters for predicting peptide isotope enrichment based on precursor body water enrichment (p) and the number (n) of amino acid C-H positions per peptide actively incorporating hydrogen (H) and deuterium (D) from body water. Subsequent data handling was performed using python-based scripts, with input of precursor body water enrichment for each subject, to yield fractional synthesis rate (FSR) data at the protein level. FSR data were filtered to exclude protein measurements with fewer than 2 peptide isotope measurements per protein.

LC-MS metabolomics

1 million cells were seeded on 50 mm2 varied stiffness ECM coated PA-gels cultured for 24 h. Cells were dissolved in 100% methanol doped with N-Ethylmaleimide (NEM) [8 mM,1 mg/mL] (Sigma-Aldrich, E1271) ([395]). Protein concentrations of the methanol extract was determined via BCA (Pierce, 23225) (5 uL transferred into 45 uL RIPA buffer, 5 uL of the RIPA dissolved solution assayed). Data was normalized to 100 μg per sample and polar metabolites were extracted in a total volume of 275 μl of 40:40:20 (acetonitrile:methanol:water) with inclusion of internal standard d3N15-serine (Cambridge Isotope Laboratories, #DNLM-6863). Extracted samples were centrifuged at 10,000 x g for 10 min and an aliquot of the supernatant was injected onto LC/MS where metabolites were separated by liquid chromatography. Analysis was performed with an electrospray ionization (ESI) source on an Agilent 6430 QQQ LC-MS/MS (Agilent Technologies). The capillary voltage was set to 3.0 kV, and the fragmentor voltage was set to 100 V, the drying gas temperature was 350 °C, the drying gas flow rate was 10 L/min, and the nebulizer pressure was 35 PSI. Polar metabolites were identified by SRM of the transition from precursor to product ions at associated optimized collision energies and retention times ([396]). Quantification of metabolites was performed by integrating the area under the curve and then normalizing to internal standard values. All metabolite levels are expressed as relative abundances compared to the control group.

13C6-glucose LC-MS metabolomics

1 million cells were seeded on 50 mm2 varied stiffness ECM coated PA-gels cultured for 22 h in 5 mM glucose DMEM based MCF10A media. The media was exchanged for media with 5 mM 13C6-Glucose (Cambridge Isotope Laboratories, CLM-1396) DMEM based MCF10A media Cells for 2 h. Cells were washed twice with PBS and extracted with mass spectrometry grade 80% methanol (ThermoFisher, A456-1) and 20% water (ThermoFisher, W6500) supplemented with 5 nmol DL-Norvaline (Sigma, N7502). Protein concentrations of the methanol extract was determined via BCA (Pierce, 23225) with no significant variability assessed (5 uL transferred into 45 uL RIPA buffer, 5 uL of the RIPA dissolved solution assayed). Insoluble material was pelleted in a 4°C centrifuge at 16k x g, supernatant was transferred and dried in a Speedvac. Dried metabolites were resuspended in 50% ACN:water and 1/10th of the volume was loaded onto a Luna 3 um NH2 100A (150 × 2.0 mm) column (Phenomenex). The chromatographic separation was performed on a Vanquish Flex (Thermo Scientific) with mobile phases A (5 mM NH4AcO pH 9.9) and B (ACN) and a flow rate of 200 μL/min. A linear gradient from 15% A to 95% A over 18 min was followed by 9 min isocratic flow at 95% A and reequilibration to 15% A. Metabolites were detected with a Thermo Scientific Q Exactive mass spectrometer run with polarity switching (+3.5 kV / -3.5 kV) in full scan mode with an m/z range of 65-975. TraceFinder 4.1 (Thermo Scientific) was used to quantify the targeted metabolites by area under the curve using expected retention time and accurate mass measurements (¡ 5 ppm). Values were normalized to cell number and sample protein concentration. Relative amounts of metabolites were calculated by summing up the values for all isotopologues of a given metabolite. Fractional contributional (FC) of 13C carbons to total carbon for each metabolite was calculated. Data analysis was accomplished using in-house developed R scripts.

Paraquat survival

10 mM paraquat (Acros Organics, 227320010) was dissolved into media and added to cell culture vessels and allowed to affect the cells for 24 h, experiments were always performed with a

fresh suspension of paraquat. After 24 h of paraquat treatment cells were fixed with 4% PFA and stained for cleaved caspase 3 (Cell Signaling, 9661).

Quantification and statistical analysis

Data displayed represent at least three independent experiments, unless otherwise specified. Figure legends contain biological and technical replicate information. Plots include each data point, mean, and SEM. Student's t test with 95% confidence interval was used to determine differences between two comparable groups. ANOVA with 95% confidence interval was used to compare three or more comparable groups. Grubb's test was used to detect distributions for outliers. Statistical comparisons were completed Graphpad Prism 6 software

8 Extended Data

8.1 Chapter 2

Table 8.1: AutoAFM Bill of Materials

List of components required to implement an AutoAFM system on an existing MFP 3D Bio AFM (Asylum Research).

ITEM NO.	SW-File Name(File Name)	DESCRIPTION	PROCESS	SUPPLIER	MATERIAL	PART NUMBER	QTY.	Package Qty	Unit Price ($)	Order Qty	Extended Price ($)
1	Microscope Stage_base	AFM Stage Base	INCLUDED				1				
2	Microscope Stage_X	AFM Stage X Translation	INCLUDED				1				
3	Microscope Stage_Y	AFM Stage Y Transation	INCLUDED				1				
4	Microscope Stage_X_knob	AFM X Knob	INCLUDED				1				
5	Microscope Stage_Y_knob	AFM Y Knob	INCLUDED				1				
6	clamp_screw_91290A190	Screws frame_main into frame_clamp	PURCHASED	MCMASTER		91290A190	4	10	7.11	1	7.11
7	clamp_nut_90576A103	Screws frame_main into frame_clamp	PURCHASED	MCMASTER		90576A103	4	100	4.27	1	4.27
8	clamp_washer_93475A230	Screws frame_main into frame_clamp	PURCHASED	MCMASTER		93475A230	4	100	1.86	1	1.86
9	X_frame_main	Stage Frame_x	3D PRINTED				1				
10	NEMA 17	Motor	INCLUDED			NEMA 17	2				
11	motor_faceplate	Motor Bracket	3D PRINTED				2				
12	slider	Motor Frame	3D PRINTED				2				
13	wedge_1	Bracket Adjuster_front	3D PRINTED				2				
14	wedge_2	Bracket Adjuster_back	3D PRINTED				2				
15	wedge_spring_5108N271	Springs holding Motor Bracket with Motor Frame	PURCHASED	MCMASTER		9044K113	4	3	5.26	2	10.52
16	wedge_pin_m3x36_91595A140	Tensioning Pin	PURCHASED	MCMASTER		91595A140	4	25	9.91	1	9.91
17	wedge_screw_92000A077	Bracket Adjusting Screws	PURCHASED	MCMASTER		92000A077	4	50	9.94	1	9.94
18	wedge_nut_90591A250	Used with Bracket Adjusting Screws	PURCHASED	MCMASTER		90591A250	4	100	2.33	1	2.33
19	wedge_washer_97310A111	Used with Bracket Adjusting Screws	PURCHASED	MCMASTER		97310A111	4	100	2.86	1	2.86
20	slider_pin_91585A389	Alignment Rod	PURCHASED	MCMASTER		91585A389	4	1	4.14	4	16.56
21	motor_screw_91290A111	Screws Motor into Motor Bracket	PURCHASED	MCMASTER		91290A111	4	100	8.71	1	8.71
22	X_frame_clamp	Clamps Stage Frame_x onto AFM Stage	3D PRINTED				1				
23	knob_cap	Knob Adapter	3D PRINTED				2				
24	knob_screw_90044A247	Adapter Screw	PURCHASED	MCMASTER		90044A247	2	5	7.44	1	7.44
25	5mm_hub_9889T106	Motor Coupling	PURCHASED	MCMASTER		9889T106	2	1	16.08	2	32.16
26	8mm_Hub_9889T109	Motor Coupling	PURCHASED	MCMASTER		9889T109	2	1	16.08	2	32.16
27	Acetal_disk_59985K620	Motor Coupling	PURCHASED	MCMASTER		59985K62	2	1	3.22	2	6.44
28	rubber pad_X	Between X_frame_main and X_frame_clamp	INCLUDED				1				
29	Yframe_main	Stage Frame_y	3D PRINTED				1				
30	Yframe_clamp	Clamps Stage Frame_y onto AFM Stage	3D PRINTED				1				
31	rubber pad_Y	Between Y_frame_main and Y_frame_clamp	INCLUDED				1				
32	rollers_1	Screw into Y_frame_main from above	PURCHASED	MCMASTER		3668K22	2	1	18.63	2	37.26
33	rollers_2	Screw into Y_frame_main from below	PURCHASED	MCMASTER		3659K11	2	1	36.88	2	73.76
										TOTAL	263.29

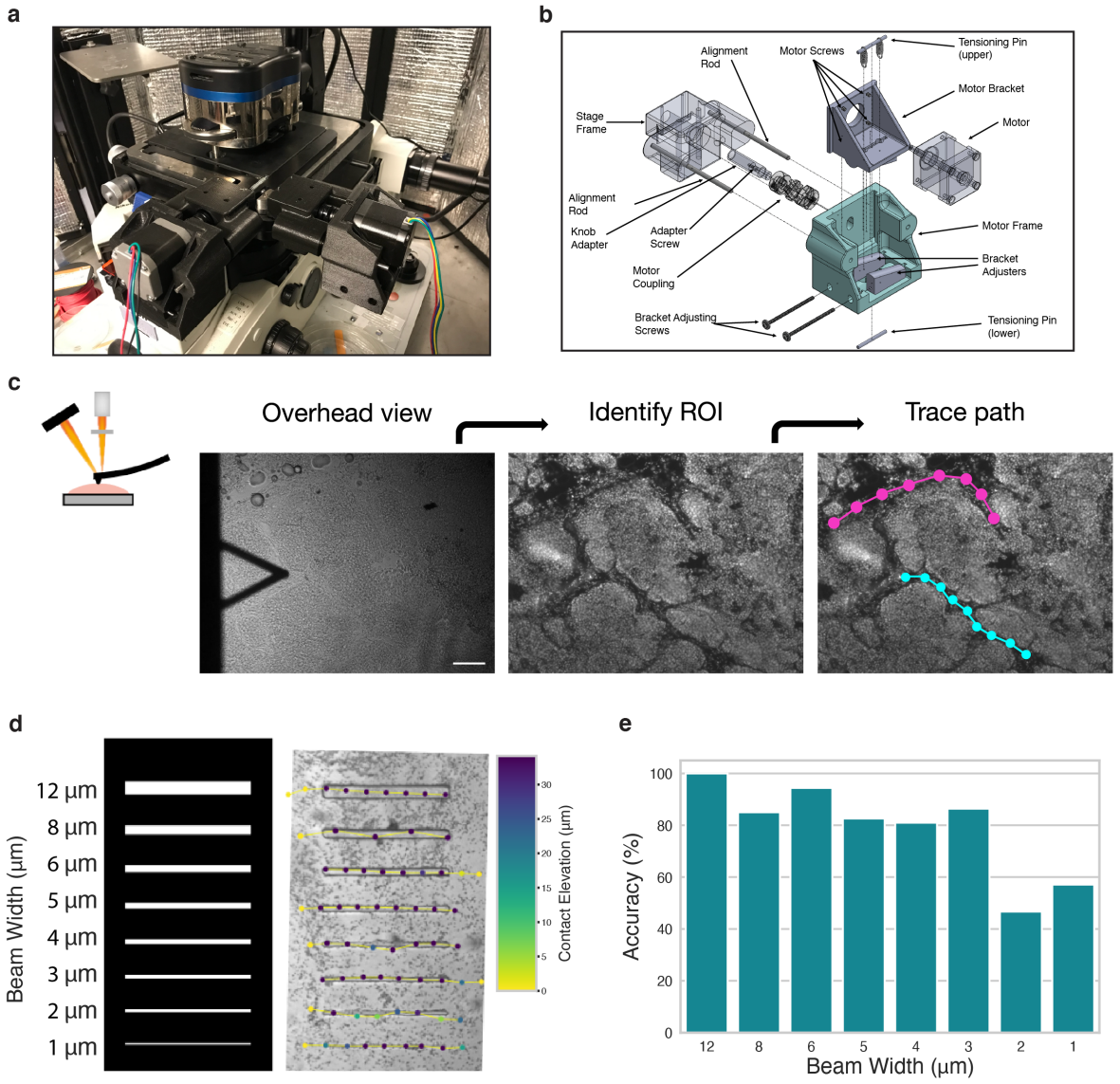

Figure 8.1: AutoAFM Principle and Validation.

a, Photo of AutoAFM assembly. b, Technical drawing of all main components of the AutoAFM system. c, AutoAFM workflow. d, Overview of PDMS balance beam design (left) and actual fabrication (right) with points overlaid. e, Accuracy of AutoAFM movements along each PDMS beam. Scale bar, 100μm.

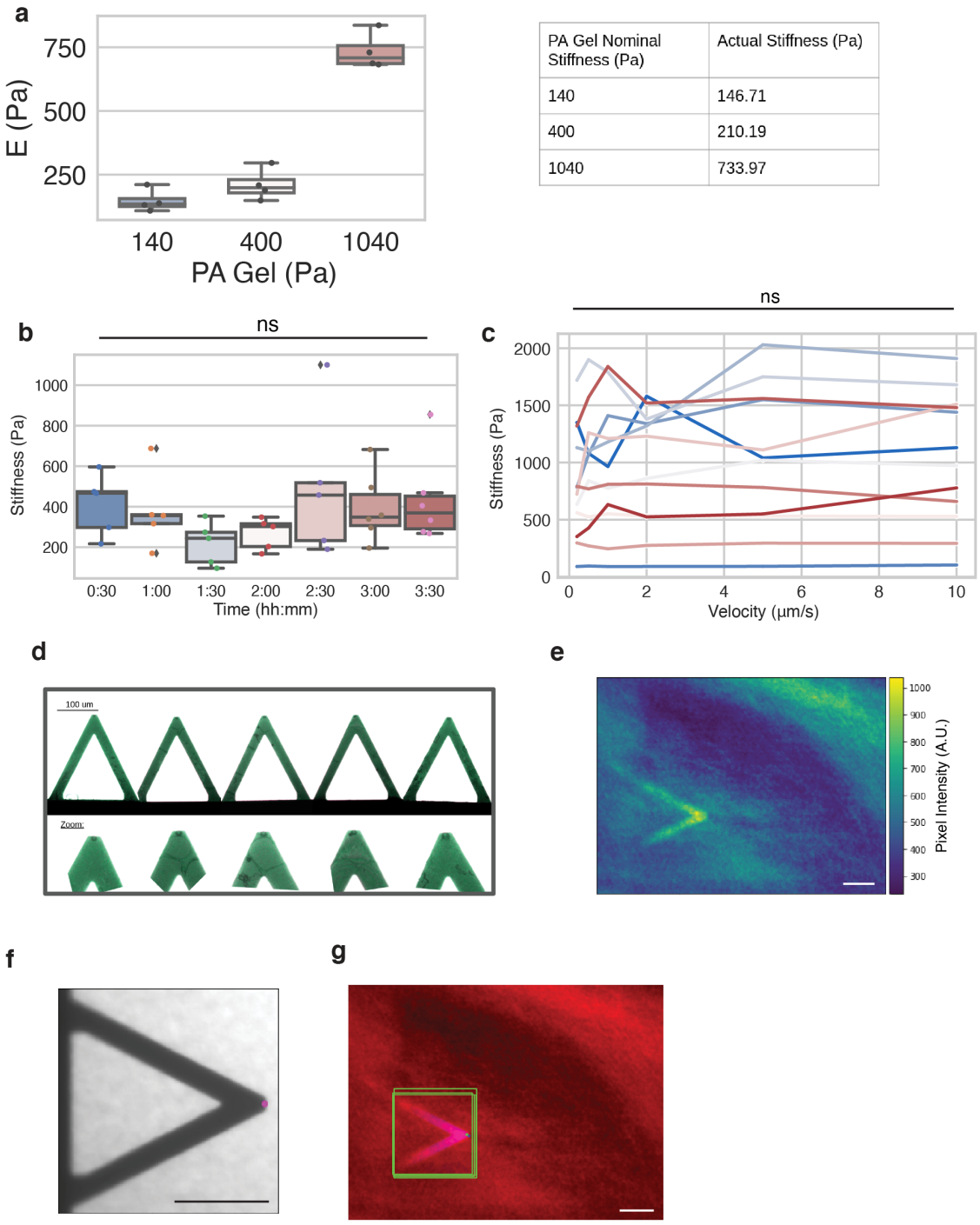

PA Gel Nominal Stiffness (Pa)	Actual Stiffness (Pa)
140	146.71
400	210.19
1040	733.97

Figure 8.2: AFM Control Experiments.

a, Young's Moduli of polyacrylamide (PA) gels of different nominal elasticities measured using shear rheology. n = 4 gels of each elasticity. b, Time course of the same tissue region probed with AFM every thirty minutes for 3.5 hours. c, Elasticity of different tissue positions probed with AFM at different velocities. n = 12 positions. d, Representative images of AFM cantilevers used.

e, AFM cantilever artifact in the average image for an AutoAFM scan. f, 5 μm ball position on the end of an AFM cantilever. g, AFM cantilever ball positions fit onto the AFM artifact from an average image (e). Statistical analyses used were performed using Mann-Whitney U test, ns=non-significant. Scale bar, 100μm.

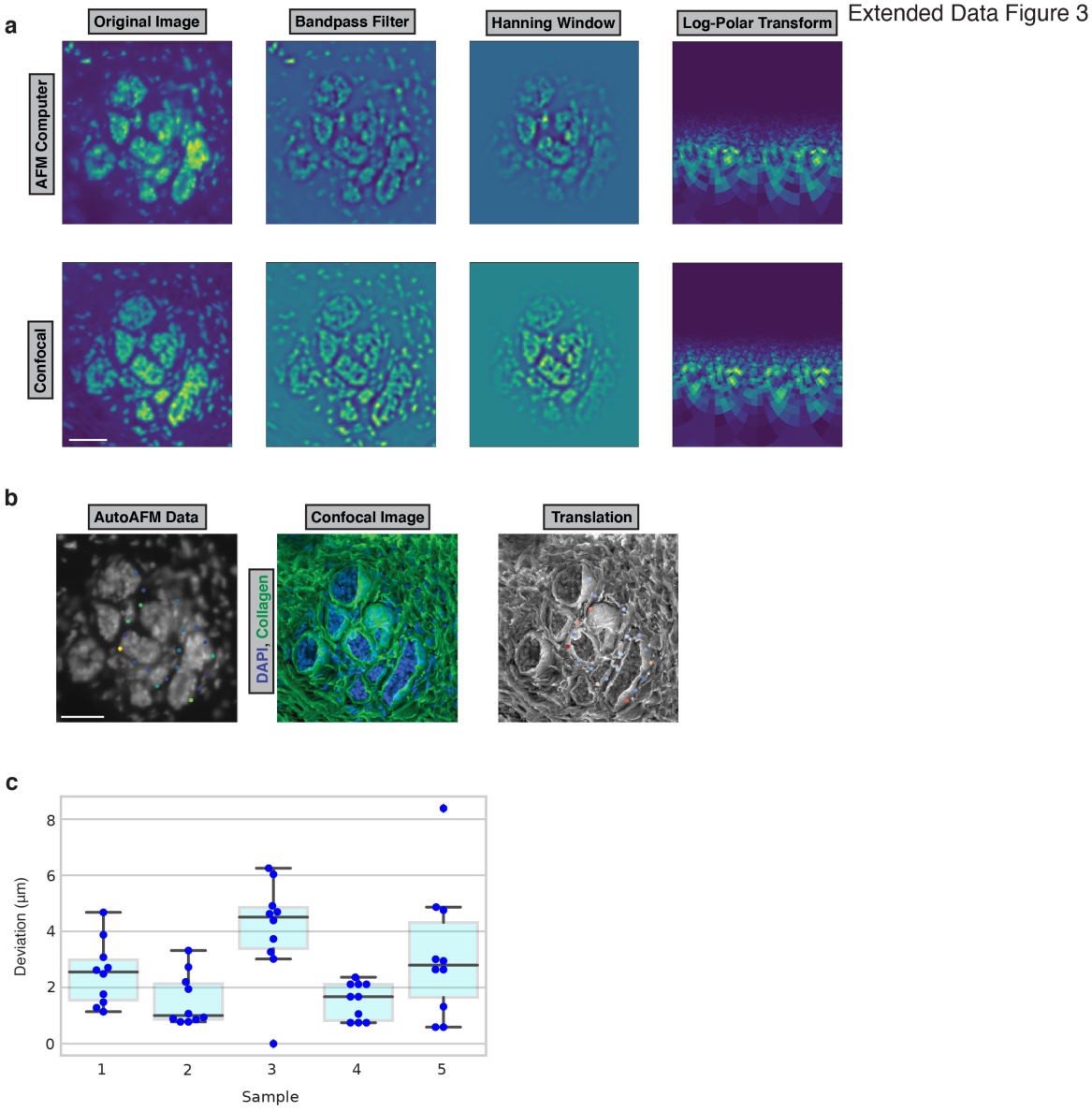

Figure 8.3: Image Stitching and Overlaying.

a, Pipeline for Fourier-Mellin Transformation. The confocal DAPI image was downsampled (bottom left) to better resemble the AFM image (top left). Then, both images were processed with a Bandpass Filter, Hanning Window, and Log-Polar Transformation. Translational differences between the final images were converted into scaling and rotation differences in the original images. b, Overall translation of AutoAFM data from a low-resolution AFM microscope image onto the

high-resolution confocal image. c, Deviation in cell positions after transformation. n = 50 cell positions from five samples. Scale bar, 50μm.

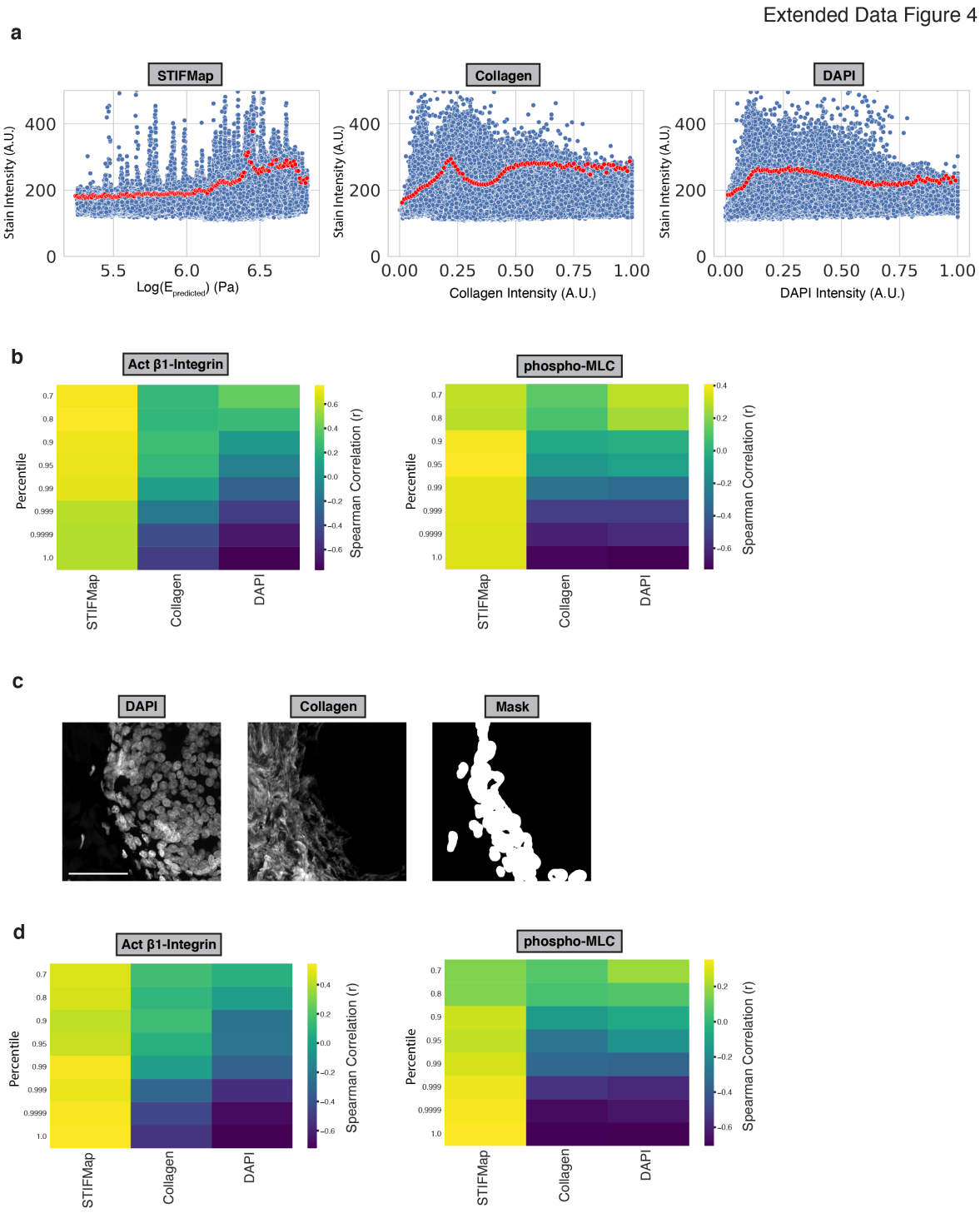

Figure 8.4: Imaging Sensitivity Analysis.

a, Scatterplots of stain intensity vs predicted stiffness (left), collagen intensity (middle), or DAPI intensity (right) shown for all pixels (blue) or aggregated to show the 99th percentile of stain intensity for each percentile of the indicated independent variable (red) for the representative pMLC stain shown in Fig. 2.3c. Aggregating data into percentiles is necessary to limit the influence of image regions where cells are not interacting with the ECM. b, Sensitivity analysis of the average Spearman correlation coefficient as shown in (a) for stain intensity compared to DAPI, collagen, and STIFMap depending on the stain threshold used. n = 60 FOVs from 10 patient tumor samples. c, Representative FOV indicating pixels that are at the interface between cells and collagen. d, Sensitivity analysis of the average Spearman correlation coefficient depending on the stain threshold used when only masked pixels are included. n = 60 FOVs from 10 patient tumor samples. Scale bar, 50μm.

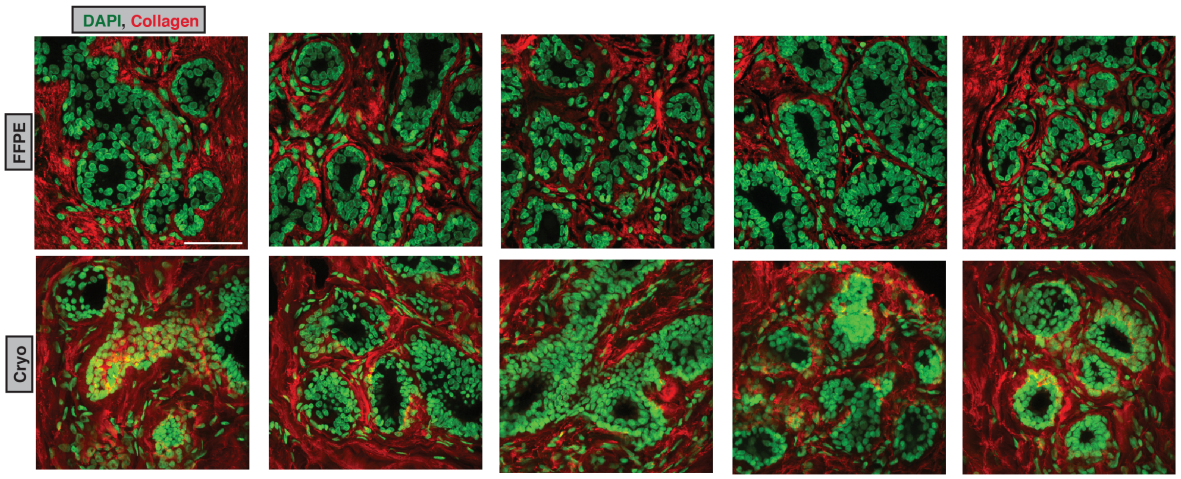

Figure 8.5: Collagen Morphology Validation in FFPE Tissue.
Five FOVs for an FFPE (top) or cryopreserved tissue (bottom) taken from the same patient stained with DAPI and CNA35. Scale bar, 50μm.

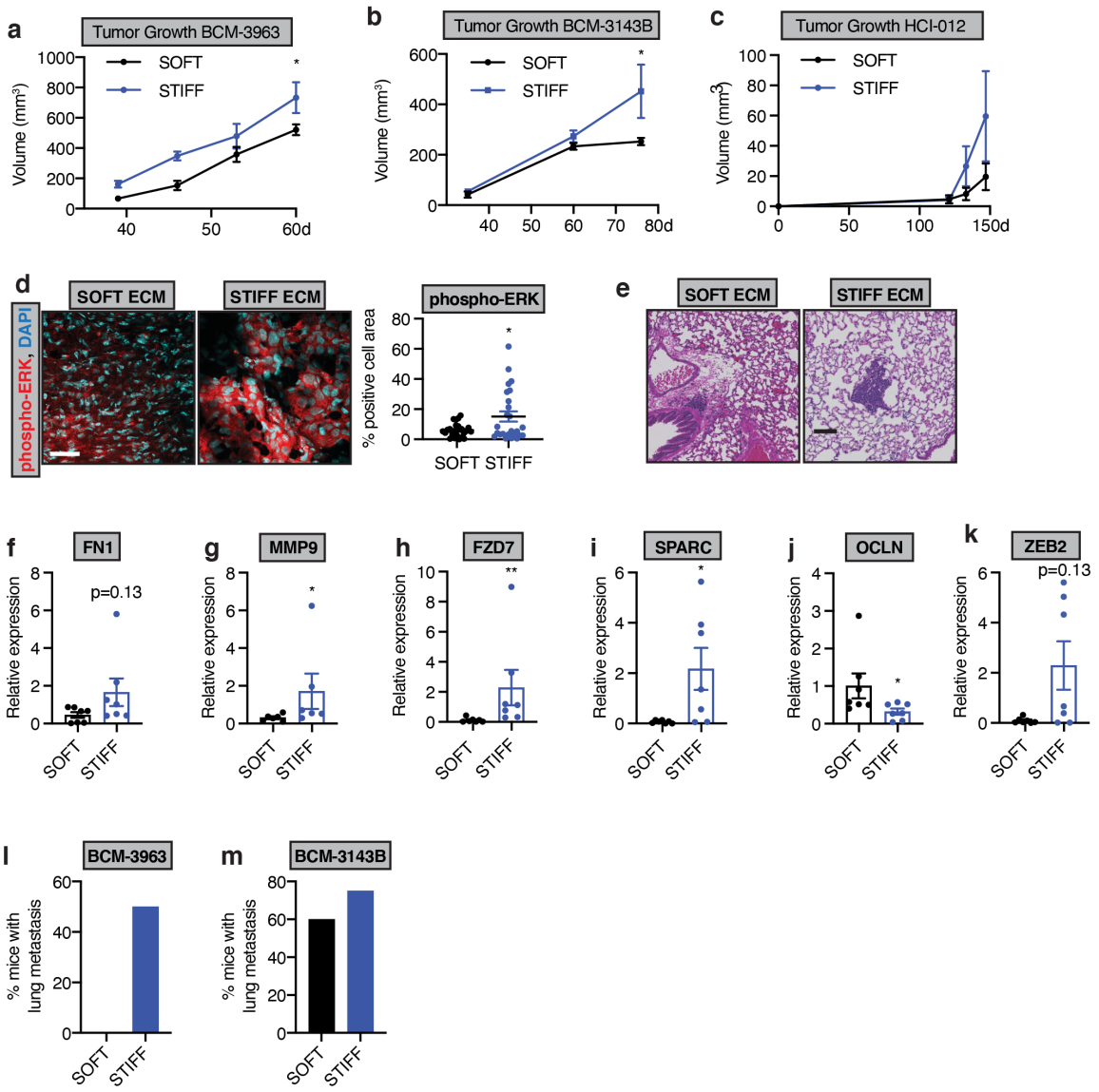

Figure 8.6: A stiff stroma enhances mechanosignaling, tumor growth, metastasis, and mesenchymal gene expression in HER2-positive breast cancer patient-derived xenografts.
a-c, Graphs showing average tumor growth in SOFT and STIFF matrices for the HER2-positive PDX models indicated as determined by caliper measurement. SOFT and STIFF, n=10 each for BCM-3963 and BCM3143B, n=4 each for HCI-012. d, Representative images of immunofluorescence staining of phospho-ERK in SOFT and STIFF HER2-positive PDX tumors (left). Scale bar, 50μm. Quantification of average phospho-ERK positive cell area for all HER2-positive PDX tumors (right). SOFT; n = 6, STIFF; n = 6. e, Representative images of lung metastases for mice bearing BCM-3143B PDX tumors in SOFT and STIFF ECM stroma. Scale bar, 100 μm. f-k, Graphs showing RT-PCR analysis of RNA extracted from HER2-positive PDX tumors with SOFT and STIFF matrices showing relative gene expression for the indicated mesenchymal and epithelial genes. SOFT; n = 7, STIFF; n = 7. l,m, Percentage of mice bearing HER2-positive PDX tumors with SOFT and STIFF matrices presenting detectable lung metastases. SOFT and STIFF, n=10

each for BCM-3963 and BCM3143B. All graphs are presented as mean +/- S.E.M. Statistical tests used were Mann-Whitney U test (f-k), unpaired t-test (d) and two-way ANOVA (with Bonferroni's multiple comparisons test) (a-c). *P¡0.03, **P¡0.002, ***P¡0.0002, ns=non-significant.

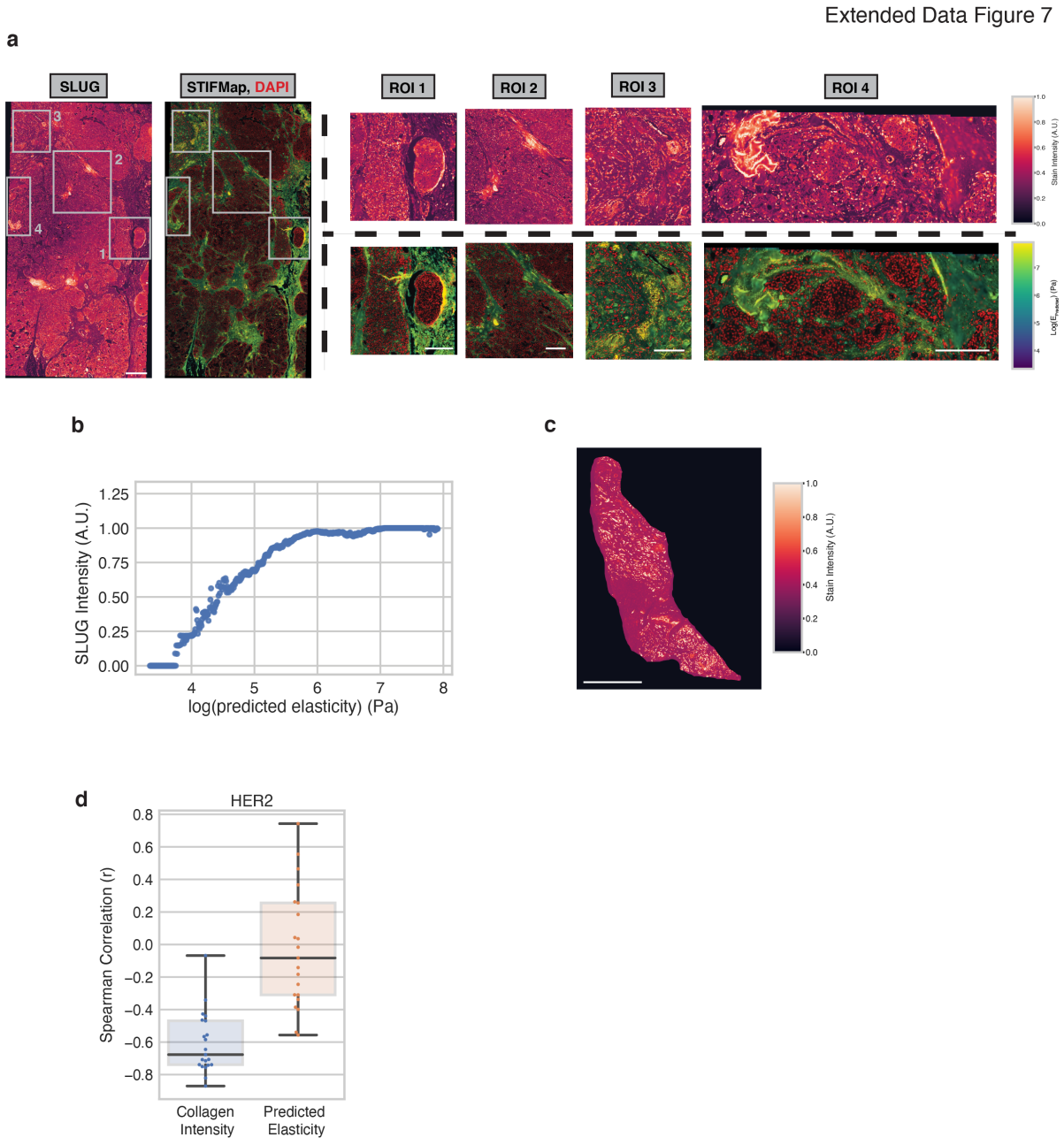

Figure 8.7: Additional Patient EMT Staining Data.

a, Representative WSI and ROIs for immunofluorescence staining of SLUG in a TNBC sample. Scale bar (WSI), 100 μm. Scale bar (ROIs), 50 μm. b, Quantification of the 99th percentile of SLUG staining intensity for each percentile of predicted matrix elasticity for the image shown in (a). c, Representative HER2 stain from the HER2+ breast cancer cohort. Scale bar, 1 mm.

d, Correlation between HER2 intensity and either collagen intensity or predicted stiffness in the HER2+ cohort. n = 21 patient tumor samples.

8.2 Chapter 3

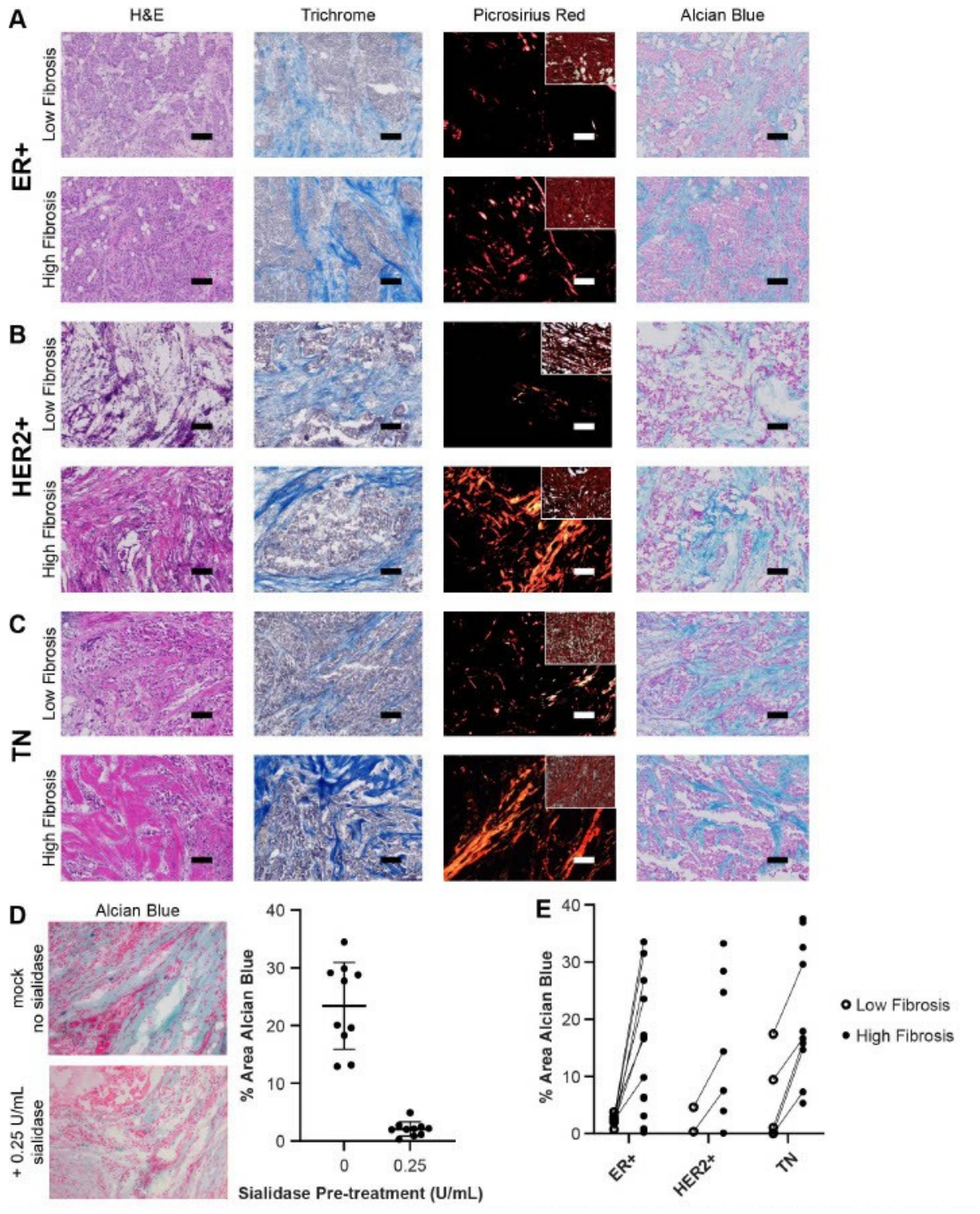

Figure 8.8: Acidic glycoprotein content is elevated in high fibrosis regions and associates with aggression in breast tumors.

A-C. Representative images of staining of all breast cancer subtypes. Scale bar represents 100 um. D. Representative images of Alcian blue staining with or without sialidase pretreatment. In the adjacent plot, each point represents one field of view from a HER2+ tumor. The mean is plotted and the error bards represent one standard deviation. E. Plots of % area Alcian blue in low and high fibrosis regions by breast cancer subtype.

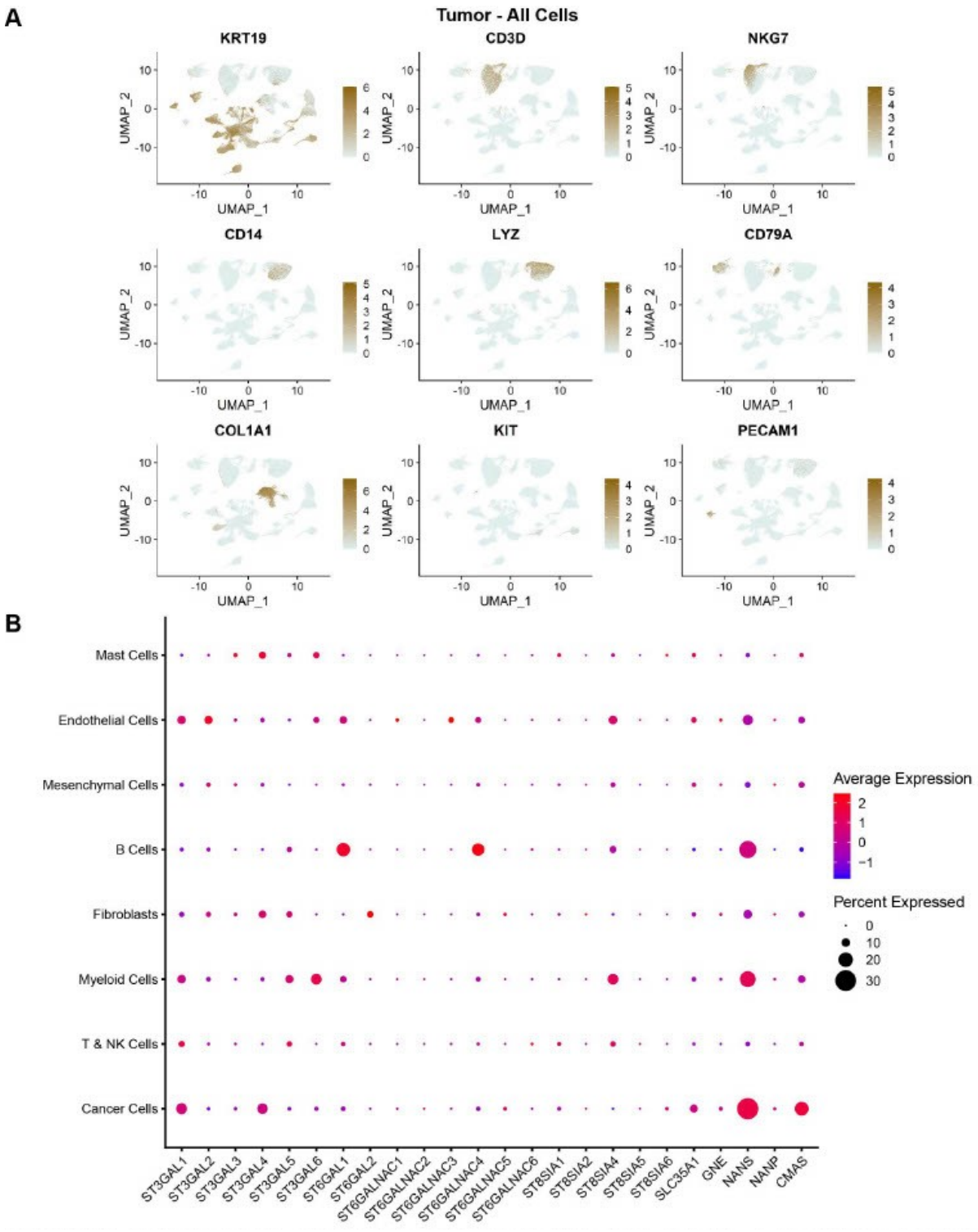

Figure 8.9: Analysis of scRNAseq of 34 tumor samples from Pal et al., EMBO 2021.
A. Feature plots for cluster assigments. B. Dot plot of sialic acid biosynthetic gene expression for each cell type.

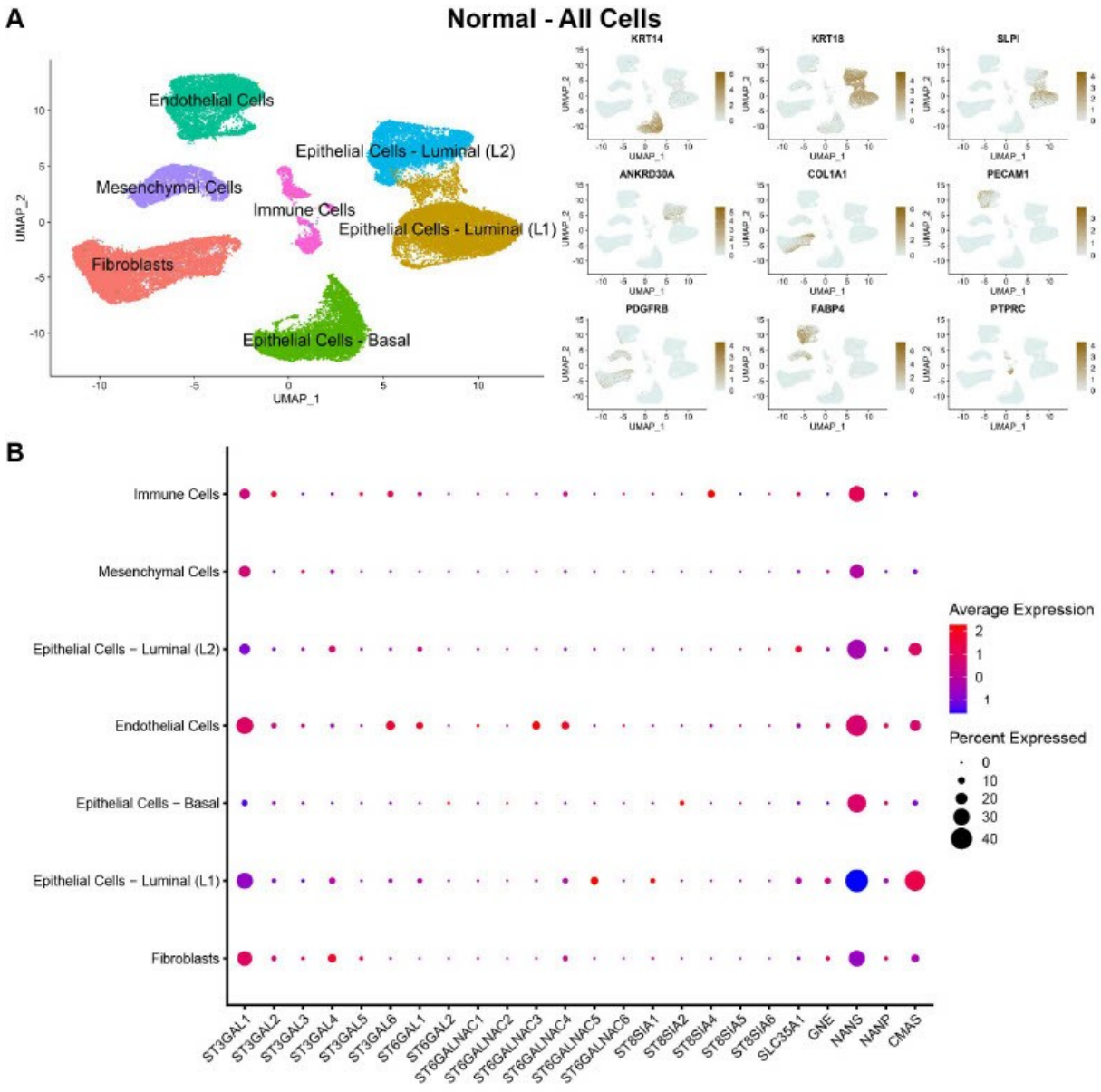

Figure 8.10: Clustering of normal breast samples from Pal et al., EMBO 2021.

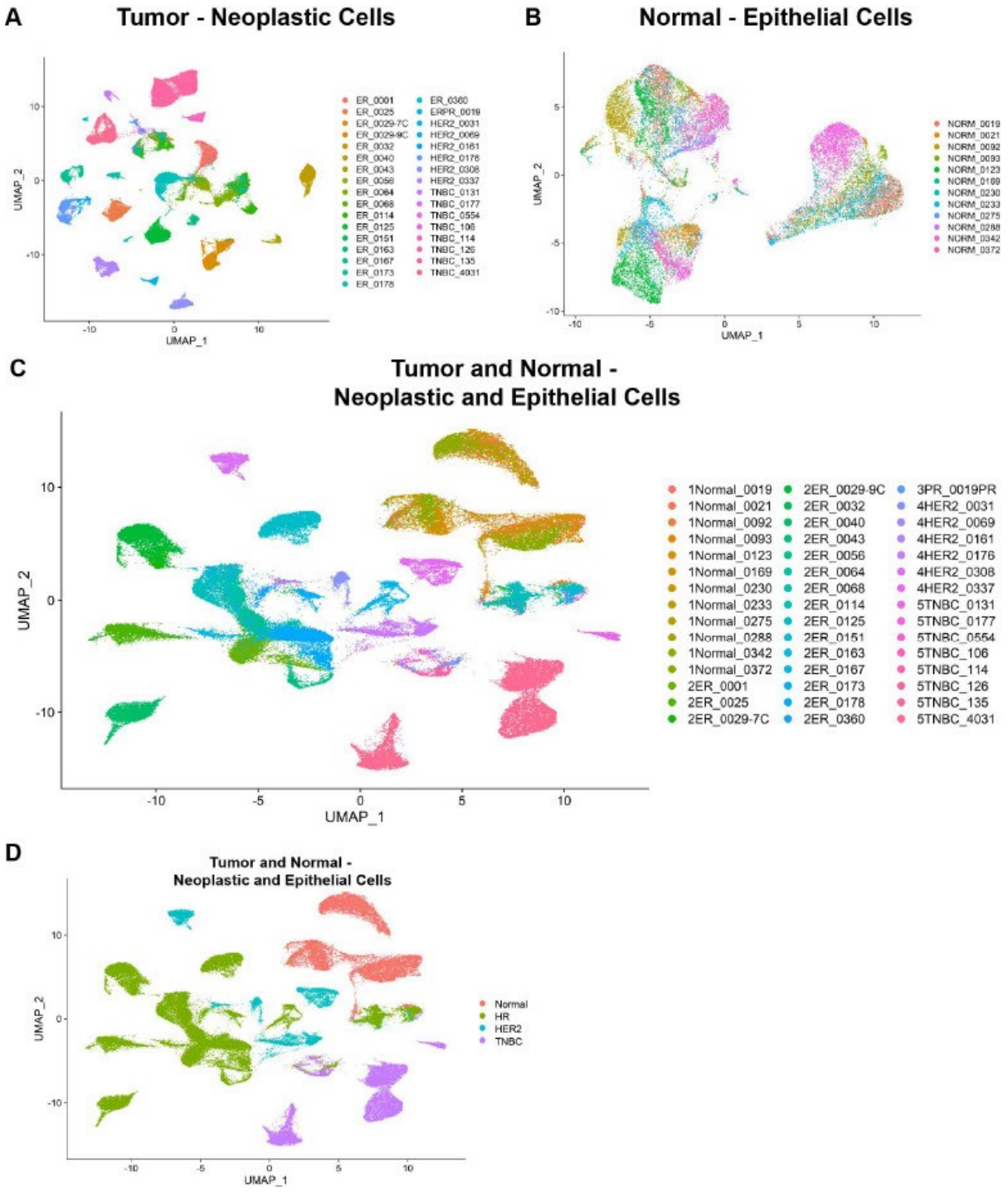

Figure 8.11: Analysis of extracted epithelial cells from tumor and normal breast.
A. UMAP plot of cancer cells colored by patient. B. UMAP plot of epithelial cells colored by patient. C-D. UMAP plot of epithelial cells from tumors and normal breast colored by C. patient and D. subtype.

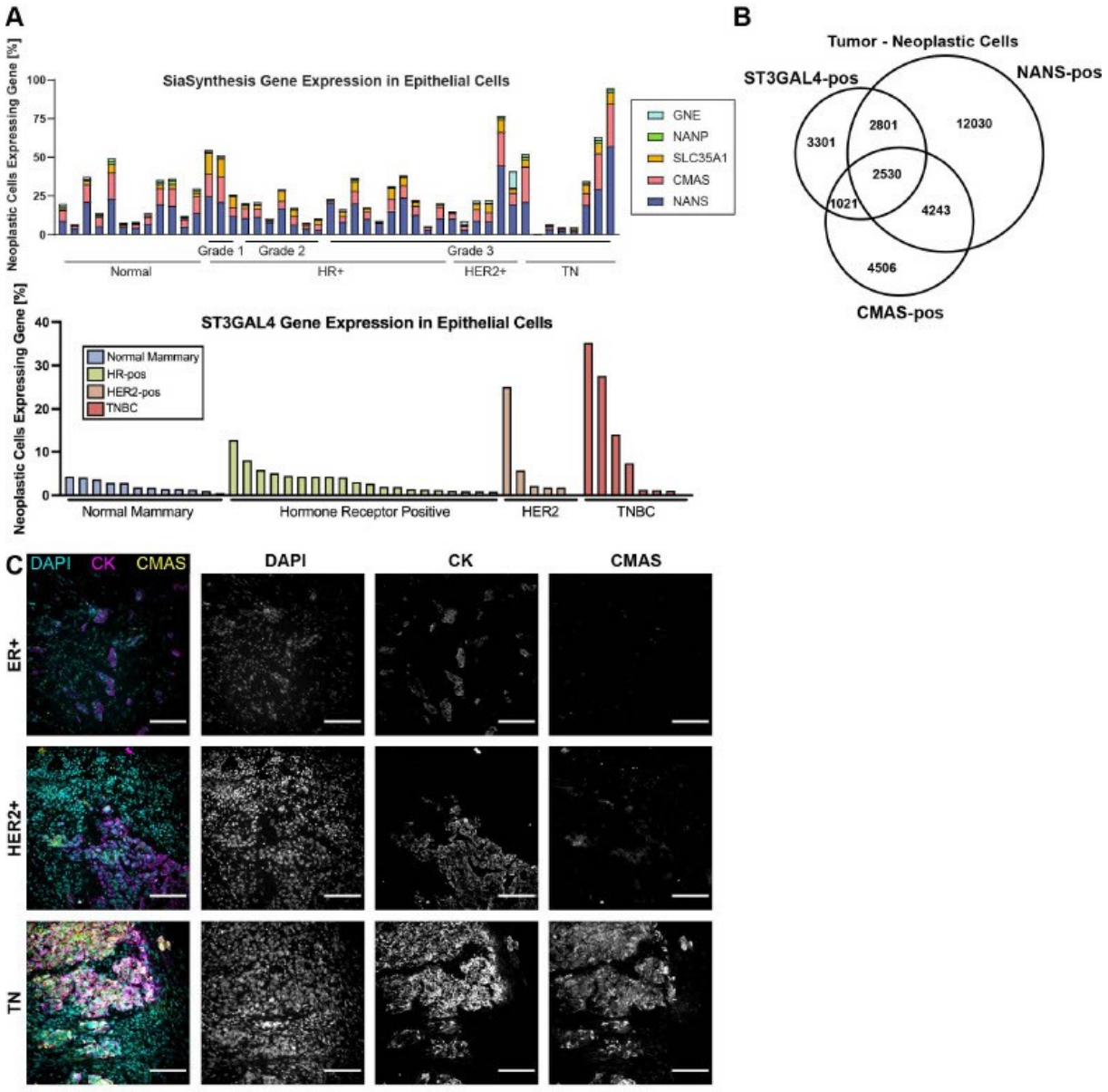

Figure 8.12: Analysis of sialoglycoprotein biosynthetic gene expression.
A. Bar plot of (top) sialic acid biosynthetic genes and (bottom) ST3GAL4 expression in epithelial cells from breast tumors and normal breast from scRNAseq dataset from Pal et al., EMBO 2021. B. Venn diagram of individual cell expression of ST3GAL4, NANS, and CMAS from breast tumor scRNAseq data. C. Representative images of breast tumors stained with DAPI, anti-pan-cytokeratin (CK), and anti-CMAS.

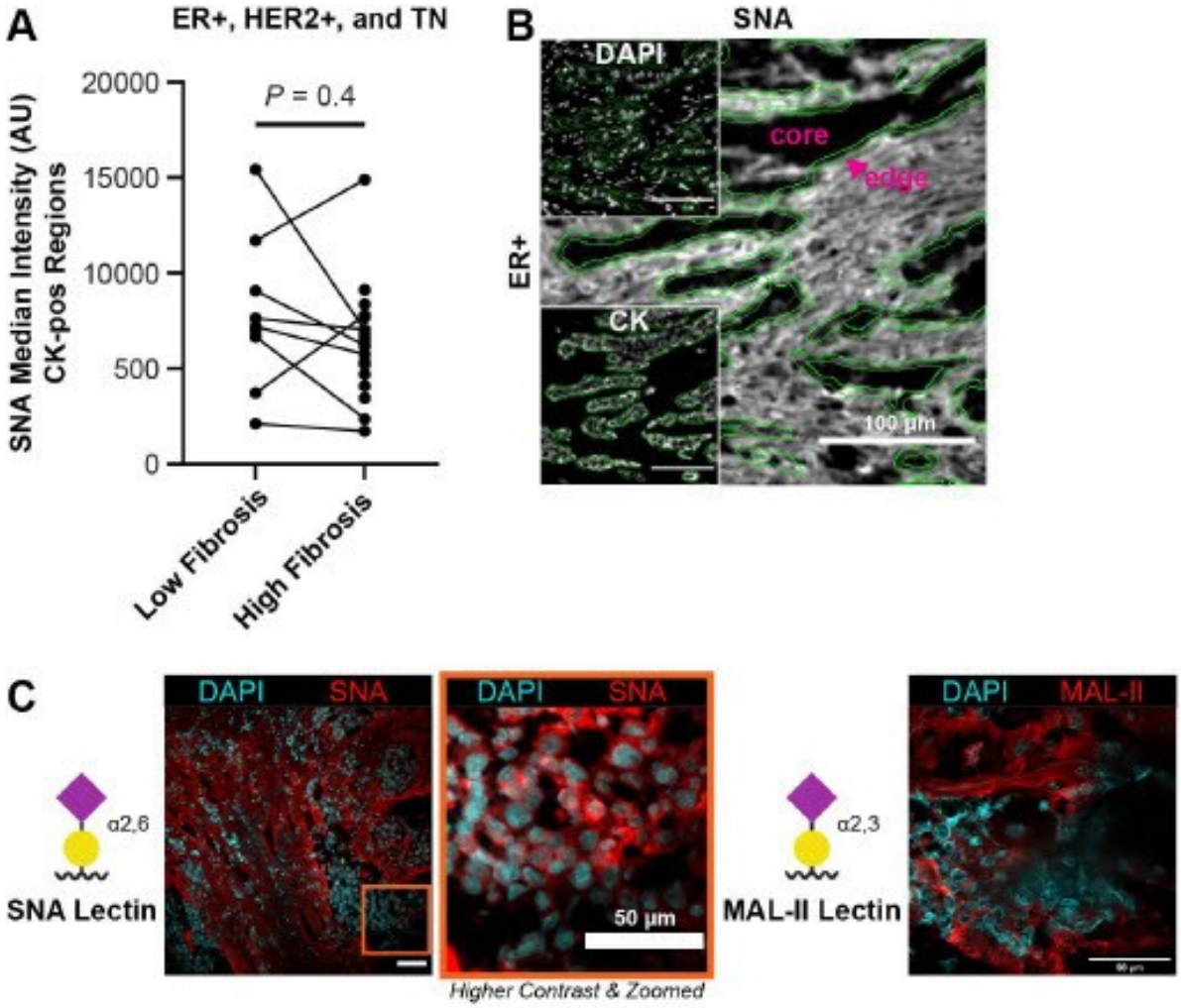

Figure 8.13: Analysis of lectin staining in breast tumors.

A. Plot of SNA lectin median intensity staining in anti-pan-cytokeratin-positive regions (CK-pos) by local fibrosis. B. Representative IF images used for quantification of SNA lectin staining of cancer cell region edge and core. Cancer cell regions were identified as CK-pos regions. C. Representative IF images of SNA lecting and MAL-II lectin.

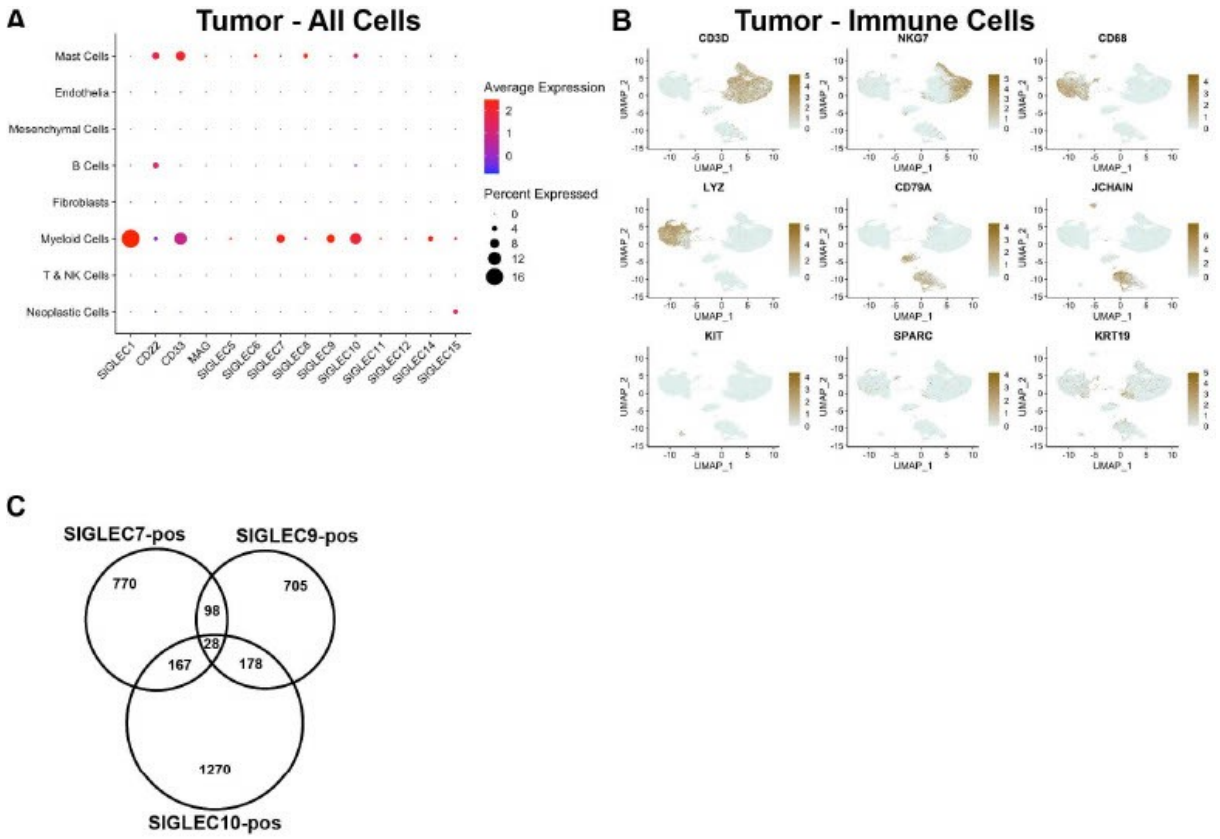

Figure 8.14: Analysis of SIGLEC expression in breast tumors from scRNAseq dataset from Pal et al., EMBO 2021.

A. Dot plot for all 14 human SIGLECs. B. Feature plots for cluster assignments. C. Venn diagram of individual cell expression of SIGLEC7, SIGLEC9, and SIGLEC10.

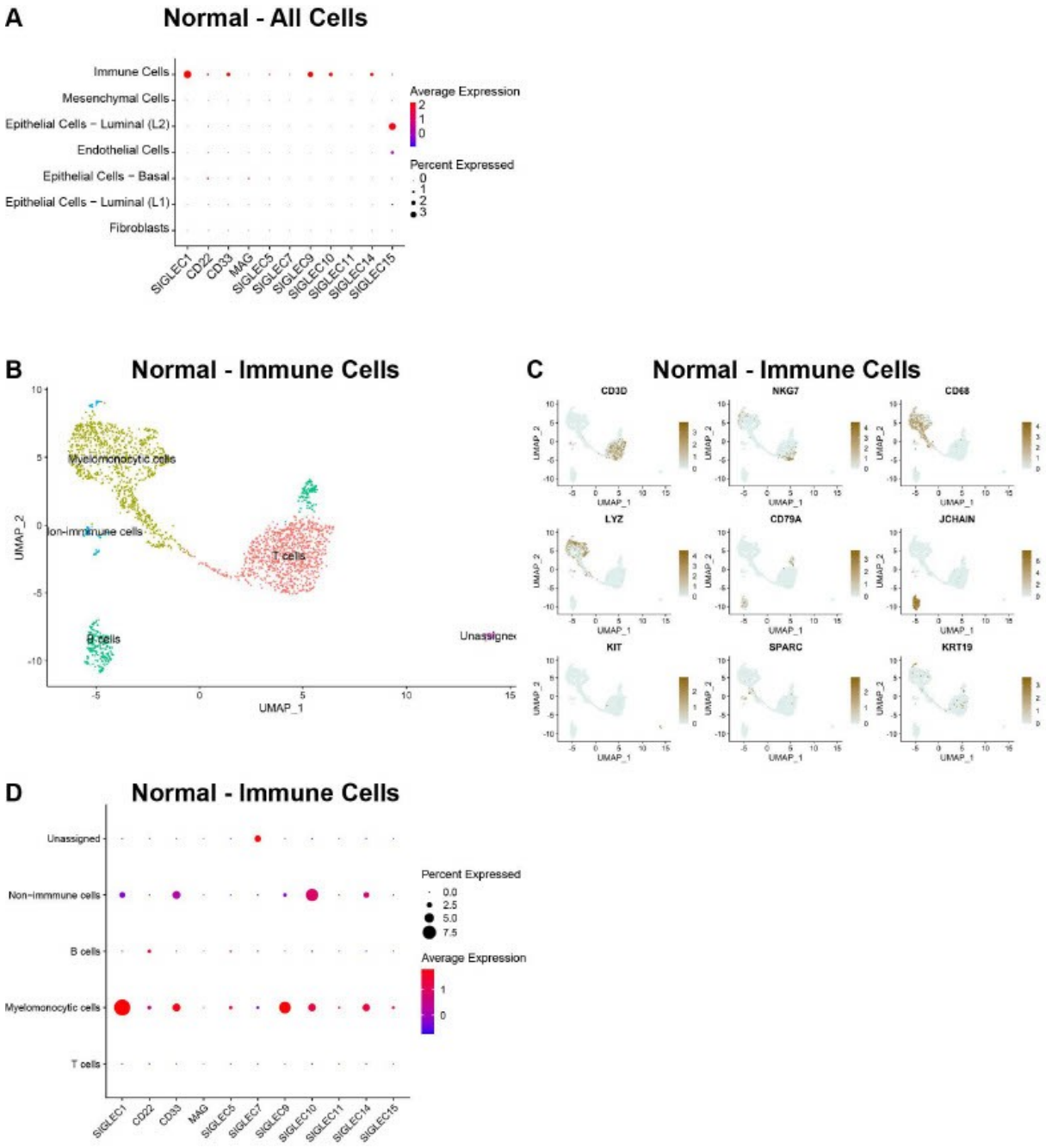

Figure 8.15: Analysis of SIGLEC expression in normal breast tissues from scRNAseq dataset from Pal et al., EMBO 2021.

A. Dot plot for all 14 human SIGLECs in all cell types. B. UMAP plot of extracted immune cells. C. Feature plots for cluster assignments. D. Dot plot for all 14 human SIGLECs in immune cell types.

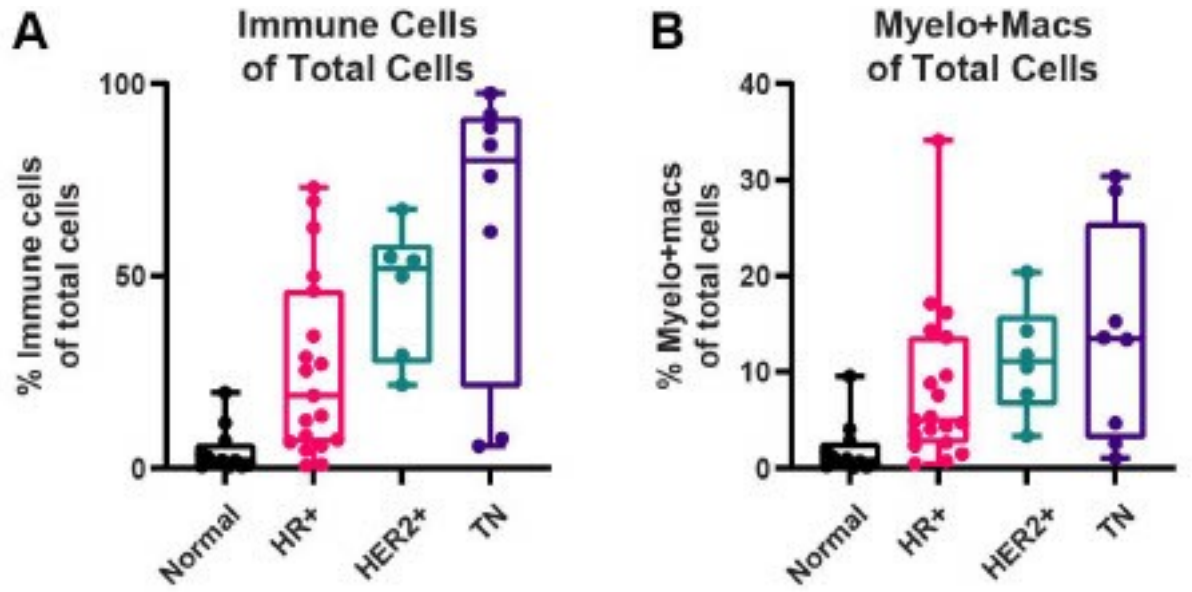

Figure 8.16: Analysis of inflammation in breast tumors and normal breast tissue from scRNAseq dataset from Pal et al., EMBO 2021.
A. Quantification of percent immune cells of total cells by subtype. B. Quantification of percent myelomonocytic cells and macrophages of total cells by subtype.

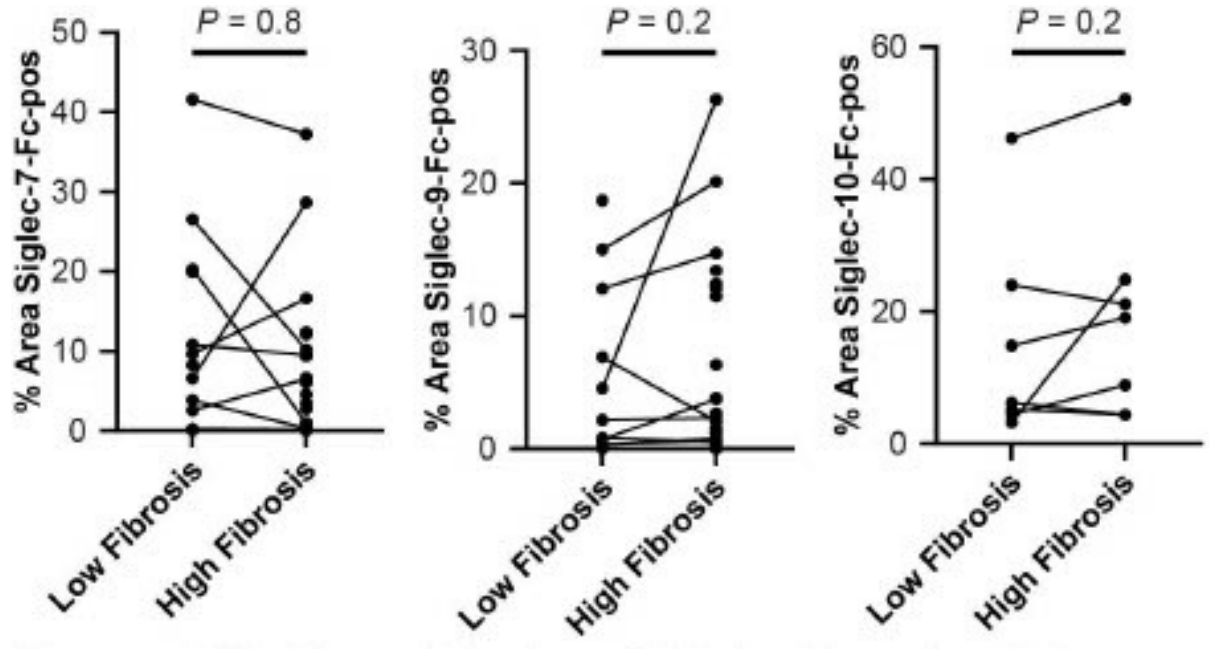

Figure 8.17: Quantification of Siglec ligand staining percent area in low and high fibrosis regions.

8.3 Chapter 4

Table 8.2: Membrane excess area and renormalized surface tension.

Initial link length	A/Ap	Renormalized σ ($k_B T/ a0^2$)	Renormalized σ (μN/m) a_0 = 10 nm
1.27	1.0754	0.165312855	6.794358356
1.3	1.0295	0.51881372	21.32324391
1.33	1.0156	0.85017139	34.94204415
1.35	1.0132	1.066002153	43.81268848
1.38	1.0117	1.390551811	57.15167943
1.4	1.0112	1.619003582	66.54104724

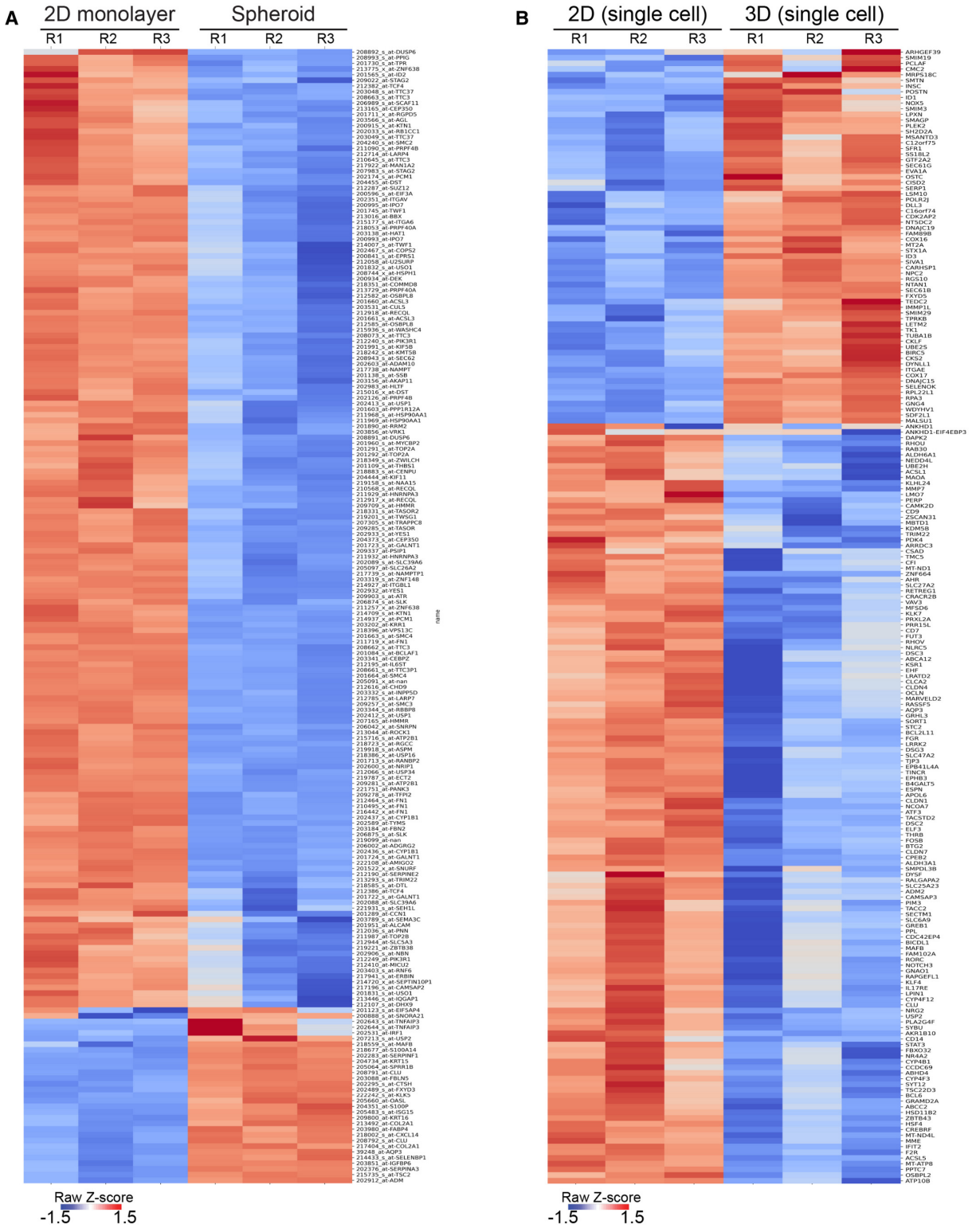

Figure 8.18: Ligation of rBM in 2D versus 3D alters cellular gene expression profiles

A. Heatmap of microarray analysis of gene expression in HMT-3522 S-1 MECs cultured either as a 2D monolayer or as spheroids. The top 200 differentially expressed genes are shown (n = 3 independent biological replicates). B. Heatmap of RNA-seq experiment from MCF10A MECs

ligated with rBM in 2D and 3D at 12 h post-plating. The top 200 genes differentially expressed between the 2D and 3D rBM conditions are shown (n = 3 independent biological replicates).

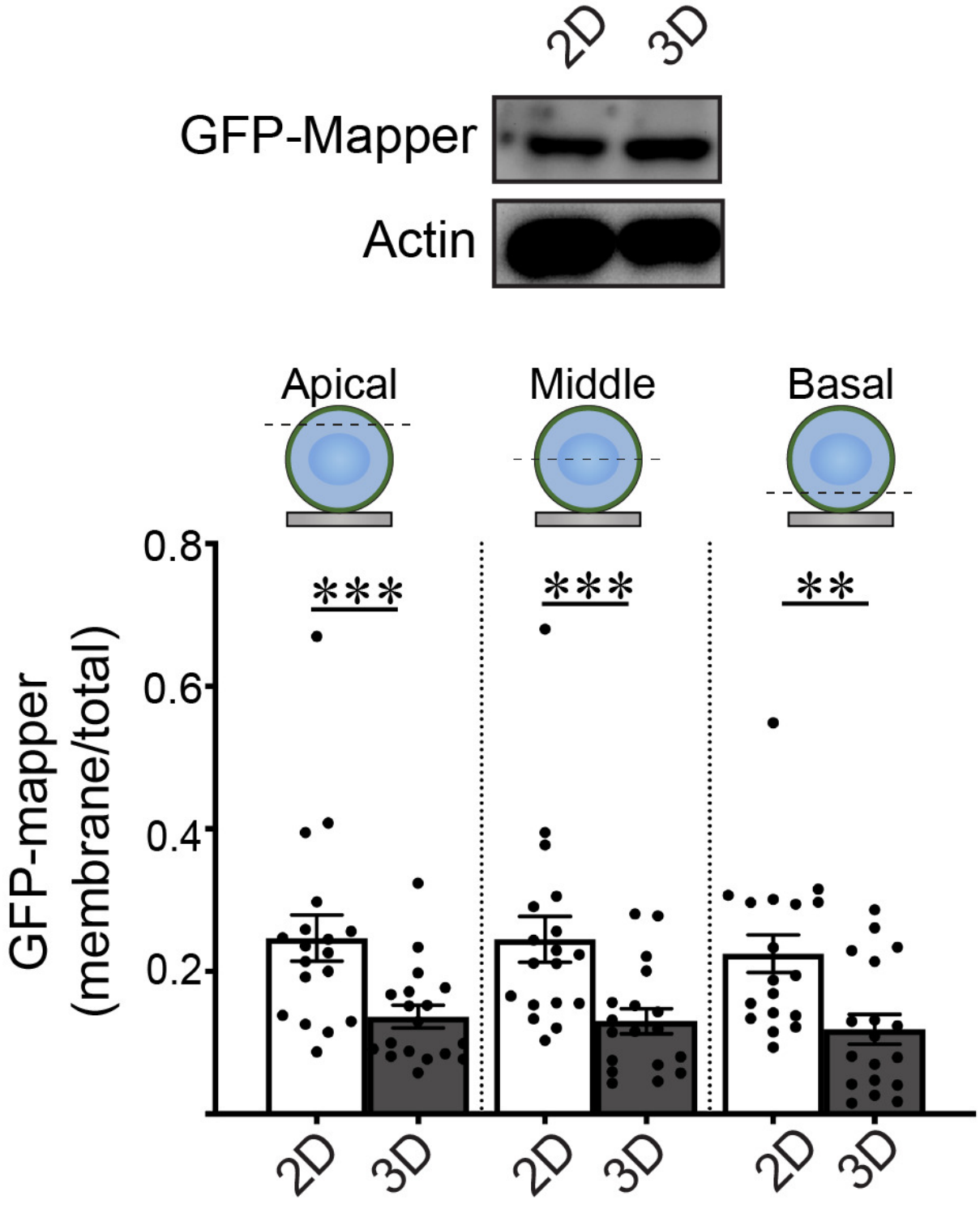

Figure 8.19: rBM ligation in 3D decreases ER-PM contact site formation

(Top) Expression levels of GFP-MAPPER in MCF10A MECs ligated with rBM in 2D or 3D was assessed by immunoblotting. Actin was used as the loading control. (Bottom) Quantification of levels of plasma membrane-proximal GFP-MAPPER in different focal planes (apical, middle, and basal) in MCF10A MECs ligated with rBM in 2D or 3D. The abundance of ER-PM contact sites in MECs was quantified as plasma membrane fluorescence relative to total fluorescence (mean ± SEM; 2D, n = 18; 3D, n = 18 cells from two independent experiments). Statistical analysis by one-way ANOVA followed by Uncorrected Fisher's LSD. Apical 2D versus 3D, ***P = 0.0007; middle 2D versus 3D, ***P = 0.0004; basal 2D versus 3D, **P = 0.0011.

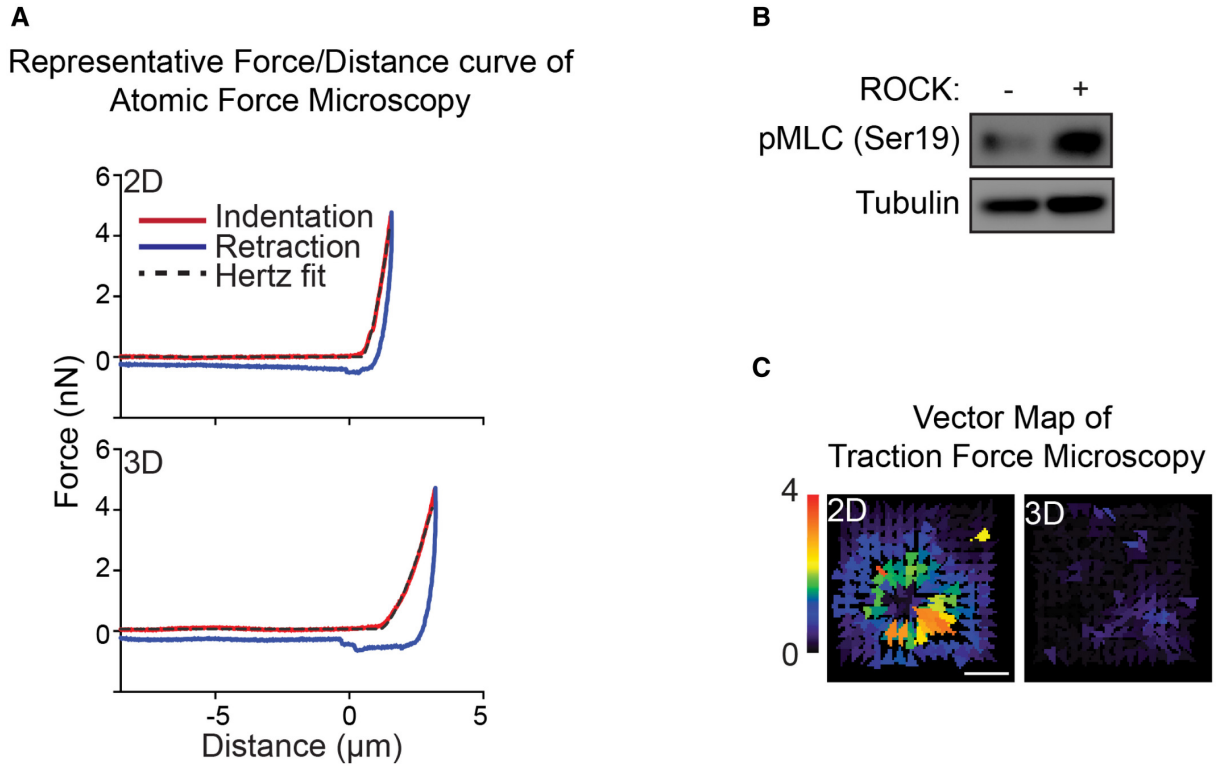

Figure 8.20: Representative AFM force curve and TFM force map

A. Representative AFM force-distance curve of MECs interacting with either laminin-111 in 2D or 3D. The indentation curve (red), retraction curve (blue), and Hertz model fit of the indentation curve (black dash line) are shown. The indentation curve of MECs ligated to rBM in 3D exhibits a similar pattern of classical AFM indentation curve. B. ROCK activity in MCF10A MECs ligated to rBM in 3D for 18 h was assessed via immunoblot for Ser19 phosphorylated myosin light chain (pMLC) relative to alpha-tubulin loading control. C. Bead displacement field of MECs ligated to a rBM in 2D or 3D is displayed as a color-coded vector map. Scale bar, 10 μm.

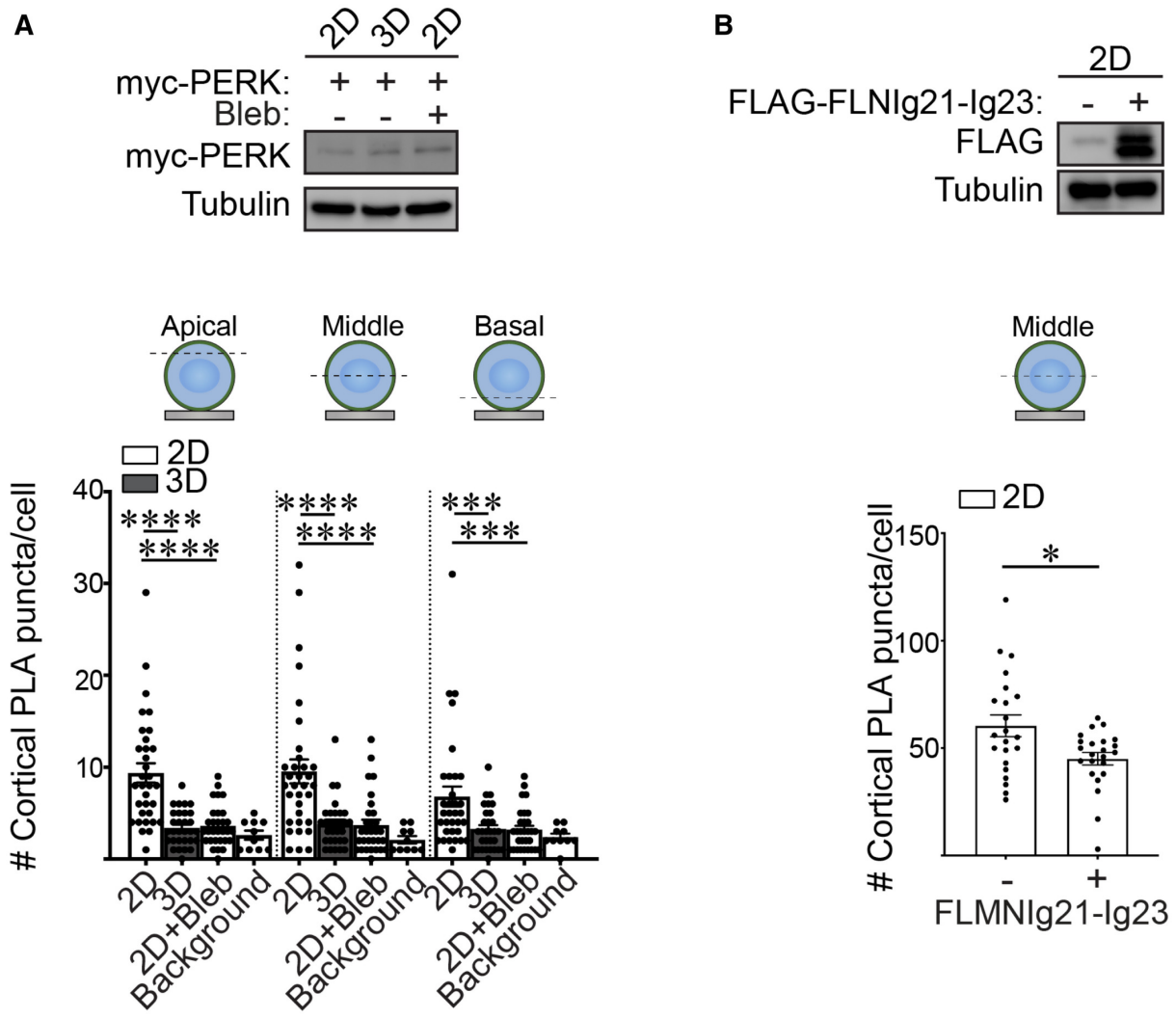

Figure 8.21: FLMNIg21-Ig23 domain regulates PERK-filamin interaction at the cell cortex
A. (Top) Immunoblots of myc-PERK and alpha-tubulin (control) in lysate from MCF10A MECs harboring doxycycline-inducible myc-PERK. MCF10A MECs were ligated with rBM in 2D or 3D for 18 h and treated with doxycycline for 7 h. (Bottom) Quantification of PLA signals within the actin cortex (cortical PLA puncta) at different focal planes (apical, middle, and basal) in MCF10A MECs expressing doxycycline-inducible myc-PERK. MECs were ligated with rBM in 2D or 3D in the absence or presence of blebbistatin (2D + Bleb) for 18 h and myc-PERK was induced for 7 h prior to PLA. The number of PLA puncta per cell were quantified to measure of the levels of interaction between filamin and PERK. Background PLA signal was measured from cells that were stained in the absence of primary antibodies (mean ± SEM; 2D, n = 33; 3D, n = 30 cells; 2D + Bleb, n = 30; background, n = 10 cells from three independent experiments). Statistical analysis by one-way ANOVA followed by Uncorrected Fisher's LSD. ****P ¡ 0.0001; basal 2D versus 3D, ***P = 0.0010; basal 2D versus 2D + Bleb, ***P = 0.0008. B. (Top) Immunoblots of FLAG-FLMNIg21-Ig23 and alpha-tubulin (control) in MCF10A MECs expressing doxycycline-inducible myc-PERK. (Bottom) Quantification of cortical PLA signals in the middle focal plane of myc-PERK expressing MCF10A MECs transduced with vector encoding FLAG alone (control) or

FLAG-FLMNIg21-Ig23 domain (mean ± SEM; 2D, n = 22; 3D, n = 23 cells from two independent experiments). *P = 0.0176 (Student's t-test).

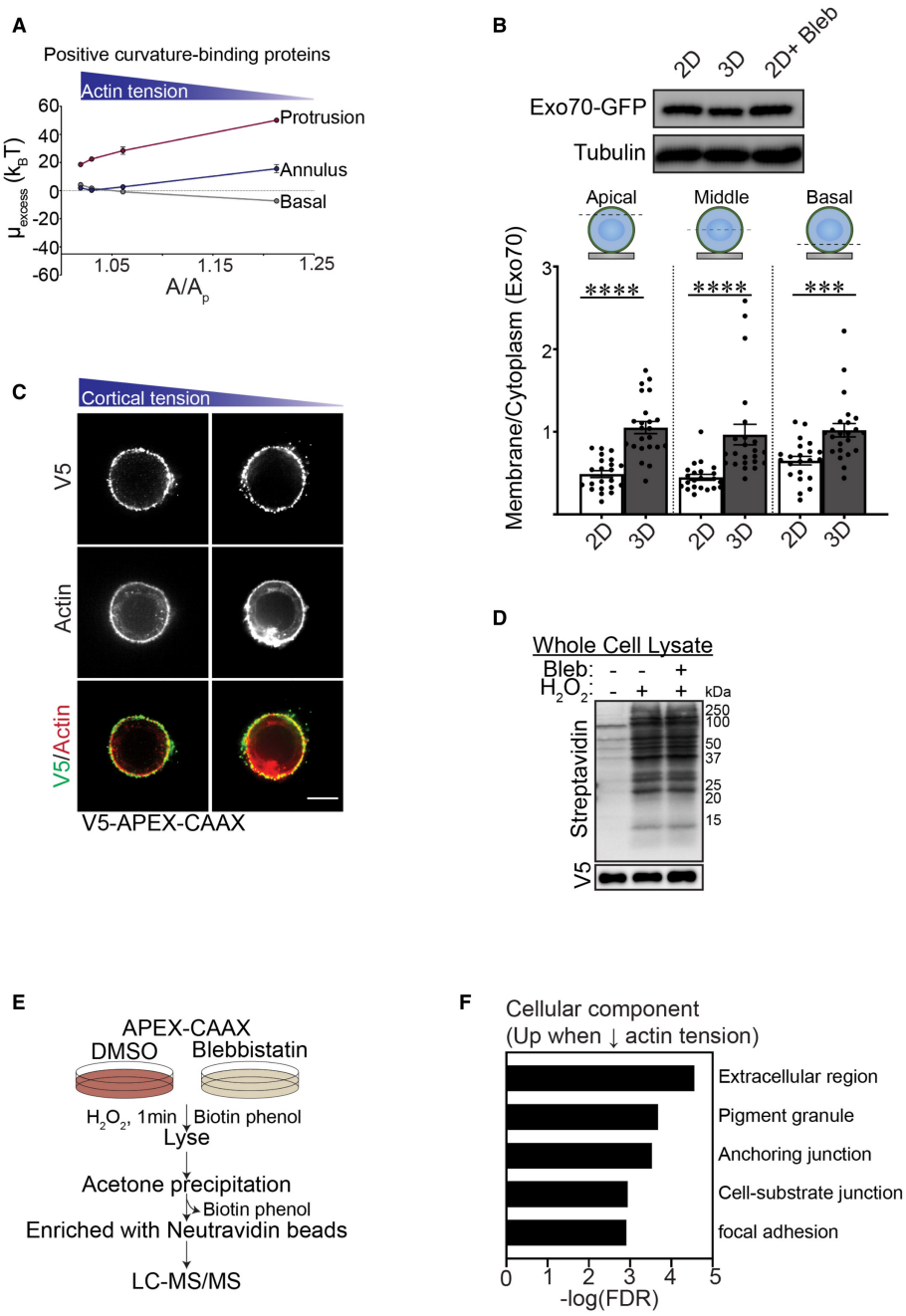

Figure 8.22: Cortical actin tension modulates plasma membrane protein composition
A. Excess chemical potential required for the recruitment of positive curvature sensing domains in basal, annulus, and protrusion regions of the plasma membrane plotted as a function of A/Ap. B. Immunoblots of Exo70-GFP and alpha-tubulin (control) in MCF10A MECs ligated with rBM in 2D or 3D. Quantification of the levels of plasma membrane-proximal Exo70 at different focal planes (apical, middle, and basal) in MCF10A MECs ligated with rBM in 2D or 3D. The levels

of plasma membrane-proximal Exo70 in MECs were quantified as plasma membrane fluorescence (GFP colocalization with farnesylated mCherry) relative to total cellular Exo70-GFP fluorescence (mean ± SEM; 2D, n = 22; 3D, n = 23 cells from two independent experiments). Statistical analysis by one-way ANOVA followed by Uncorrected Fisher's LSD. Apical and middle 2D versus 3D, ****P ¡ 0.0001; basal 2D versus 3D, ***P = 0.0007. C. Representative fluorescence microscopy images of MCF10A MECs stably expressing recombinant V5-APEX2-CAAX and ligated to rBM in 2D in the absence and presence of blebbistatin. MECs were immunostained with antibodies targeting V5 (green) and counterstained with phalloidin (red). Scale bar, 10 μm. D. MECs ligated to rBM in 2D with and without 2 h of blebbistatin treatment were harvested for immunoblotting. The activity of APEX2-CAAX (V5) was examined via immunoblot for biotinylated proteins with streptavidin-HRP. E. Schematic of the strategy used for the two-state SILAC experiment. MECs expressing APEX-CAAX were treated with biotin-phenol overnight followed by 1 min of H2O2 exposure. MECs labeled with heavy isotope amino acids were treated with blebbistatin to reduce myosin II activity, whereas those labeled with light amino acids were treated with DMSO (vehicle). Cells were lysed and excess biotin phenol trapped in the polyacrylamide gels was removed using acetone precipitation. The resuspended protein was purified using streptavidin beads and identified by mass spectrometry. For each protein, the H/L SILAC ratio reflects the extent of its biotinylation by APEX2-CAAX in the presence/absence of blebbistatin. F. GO Cellular Component analysis of proteins enriched at the plasma membrane of cells with low cortical tension (Fig 7I) using PANTHER online database.

8.4 Chapter 5

Table 8.3: Stress response gene signatures

Stiffness				Hyperglycemia			
ISR	**HSR**	**OSR**	**UPR$_{mito}$**	**ISR**	**HSR**	**OSR**	**UPR$_{mito}$**
ASNS	BAG3	GCLM	AFG3L2	ASNS	BAG3	GCLM	AFG3L2
ATF3	CRYAB	HMOXI	CLPP	ATF3	CRYAB	HMOXI	CLPP
ATF4	CLU	PRDX1	DNAJA3	ATF4	CLU	PRDX1	DNAJA3
ATF6	DNAJB1	SOD1	ENDOG	ATF6	DNAJB1	SOD1	ENDOG
CARS	ONAJB4	SQSTMI	HSPA9	CARS	ONAJB4	SQSTMI	HSPA9
CEBPB	GADD45B	TXNRD1	LONPI	CEBPB	GADD45B	TXNRD1	LONPI
DDIT3	HBA2	GCLC	TXN2	DDIT3	HBA2	GCLC	TXN2
DDIT4	HSP90AA1	NQO1	YME1L1	DDIT4	HSP9OAA1	NQO1	YME1L1
GADD45A	HSPAIA	ME1	HSPD1	GADD45A	HSPAIA	ME1	HSPD1
PPP1R15A	HSPA1B	TXN		PPP1R15A	HSPA1B	TXN	
SARS	HSPA4L			SARS	HSPA4L		
SLC1A4	HSPB1			SLC1A4	HSPB1		
TRIB3	HSPH1			TR1B3	HSPH1		
WARS	IER5			WARS	IER5		
YARS	RGS2			YARS	RGS2		
ABCF2	SERP1NH1			ABCF2	SERP1NH1		
MTHFR				MTHFR			
PON2				PON2			
LMO4				LMO4			
CBX4				CBX4			

Blue = Downregulated **Red = Upregulated**

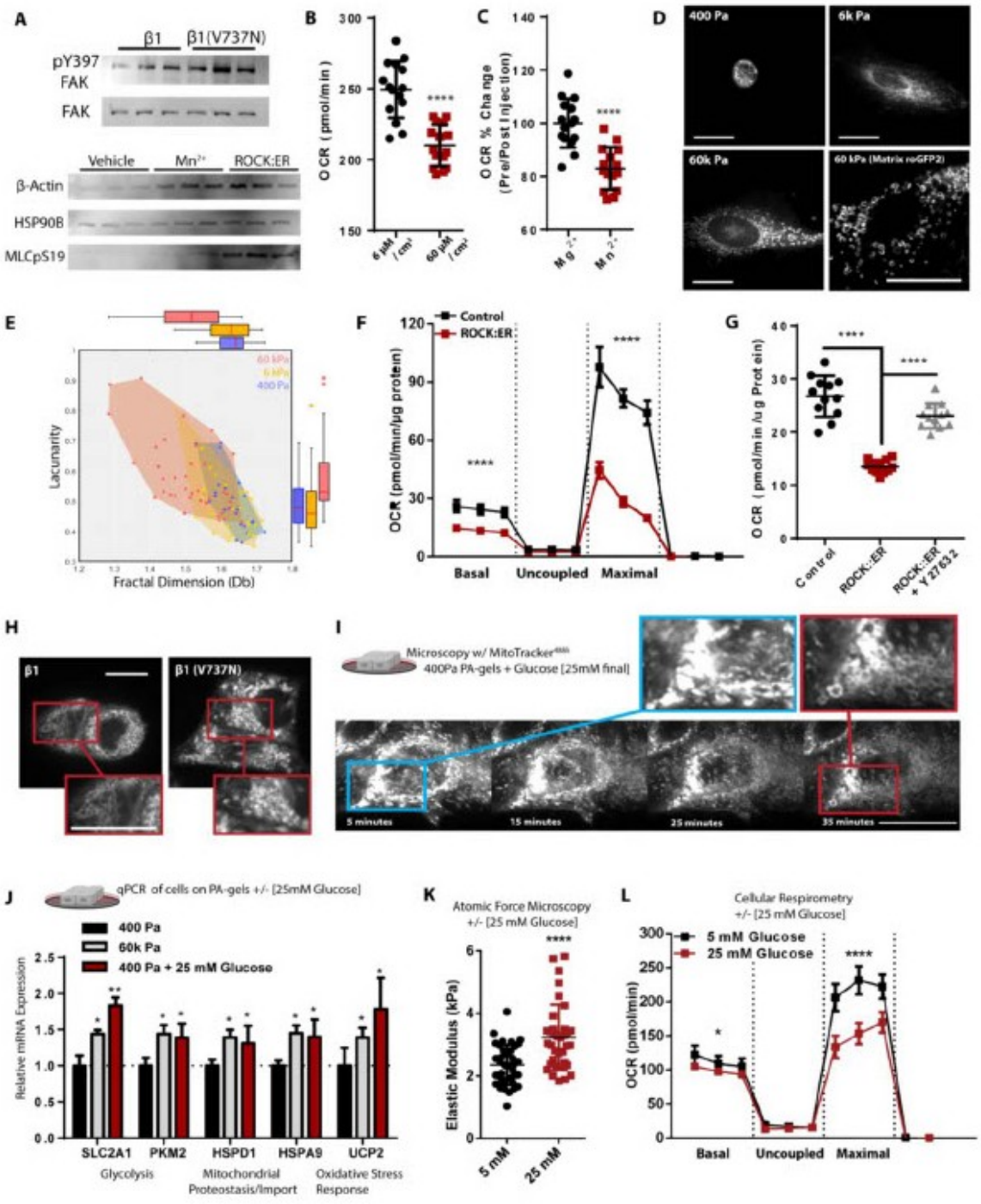

Figure 8.23: Integrin mechanosignaling via ROCK alters mitochondrial structure and function

A. Western blot depicting relative protein abundance of focal adhesion kinase (FAK) and phosphorylated/active FAK-pY397 within 5 μg of total protein derived from lysates of β1-integrin or β1(V7373N) expressing cells (n=3 separate experiments). Western blot depicting relative protein abundance of β-actin, HSP90B, and ROCK phosphorylated myosin light chain (MLC-pS19)

within 5 μg of total protein derived from lysates of ROCK:ER fusion protein expressing cells activated via 4HT [1 μM] treatment for 48 h or vehicle +/- 30 min of Mn2+ [1 μM]. (n=3 separate experiments). B. OCR of cells cultured for 24 h on varied fibronectin surface coating density (n=5 wells, 3 replicate measures). C. OCR 15 min before and a 15 minutes after the addition of Mn2+ or Mg2+ [1 μM] via injection port (n=5 wells, 3 replicate measures, repeated 3 times). D. Microscopy depicting mitochondrial network structure in PFA-fixed single cells cultured on soft-to-stiff fibronectin [6 μM/cm2] coated polyacrylamide hydrogels, mitotracker (deep red FM) [100 nM]. Mitochondrial matrix targeted roGFP2 expressing MEC cultured on stiff ECM for structure assessment of genetically encoded fluorophore relative to mitotracker staining (Scale Bar: 10 μm) E. Fractal dimension and lacunarity of mitochondrial morphology of MECs cultured on 400, 6k, and 60k Pa PA-hydrogels. Each point represents a randomly sampled 275 x 275-pixel region from 4 separate 1600 x 1600-pixel images of cells representatively depicted in Figure 1D F. Mitochondrial stress test of ROCK:ER fusion protein expressing cells activated via 4HT [1 μM] treatment for 48 h or vehicle (n=5 wells, 3 replicate measures, repeated 3 times). G. OCR of ROCK:ER fusion protein expressing cells activated via 4HT [1 μM] treatment for 48 h or vehicle, +/- y27632 [10 μM] (n=4 wells, 3 replicate measures, repeated 3 times). H. Confocal microscopy depicting mitochondrial network structure of β1-integrin or β1(V7373N) expressing PFA-fixed cells cultured on 400 Pa ECM for 24 h, stained with mitotracker (deep red FM) [100 nM]. (Scale Bar: 10 μm) I. Representative microscopy of the mitochondrial network structure in live cells cultured in 5 mM glucose on 400 Pa ECM with a lattice light sheet microscope, monitoring structural changes after infusion of glucose [200 mM], rendering a final concentration of 25 mM glucose, mitotracker (Green FM) [100 nM]. J. Relative gene expression of MECs grown of soft (400 PA) or stiff (60k Pa) ECM +/- glucose [5 or 25 mM] media normalized to low glucose media [5 mM], qPCR-δ δCT (housekeeping gene: 18s) (n=5 or 4 separate experiments). K. Cellular elasticity of MECs exposed to 24 h glucose [5 or 25 mM] on fibronectin [6 μM/cm2] coated glass coverslips, atomic force microscopy (n=36 indentations across 3 discrete samples). L. OCR of cells in either 5 or 25 mM Seahorse XF assay media, previously cultured in 25 mM glucose MCF10A media (n=5 wells, 3 replicate measures, repeated 3 times).

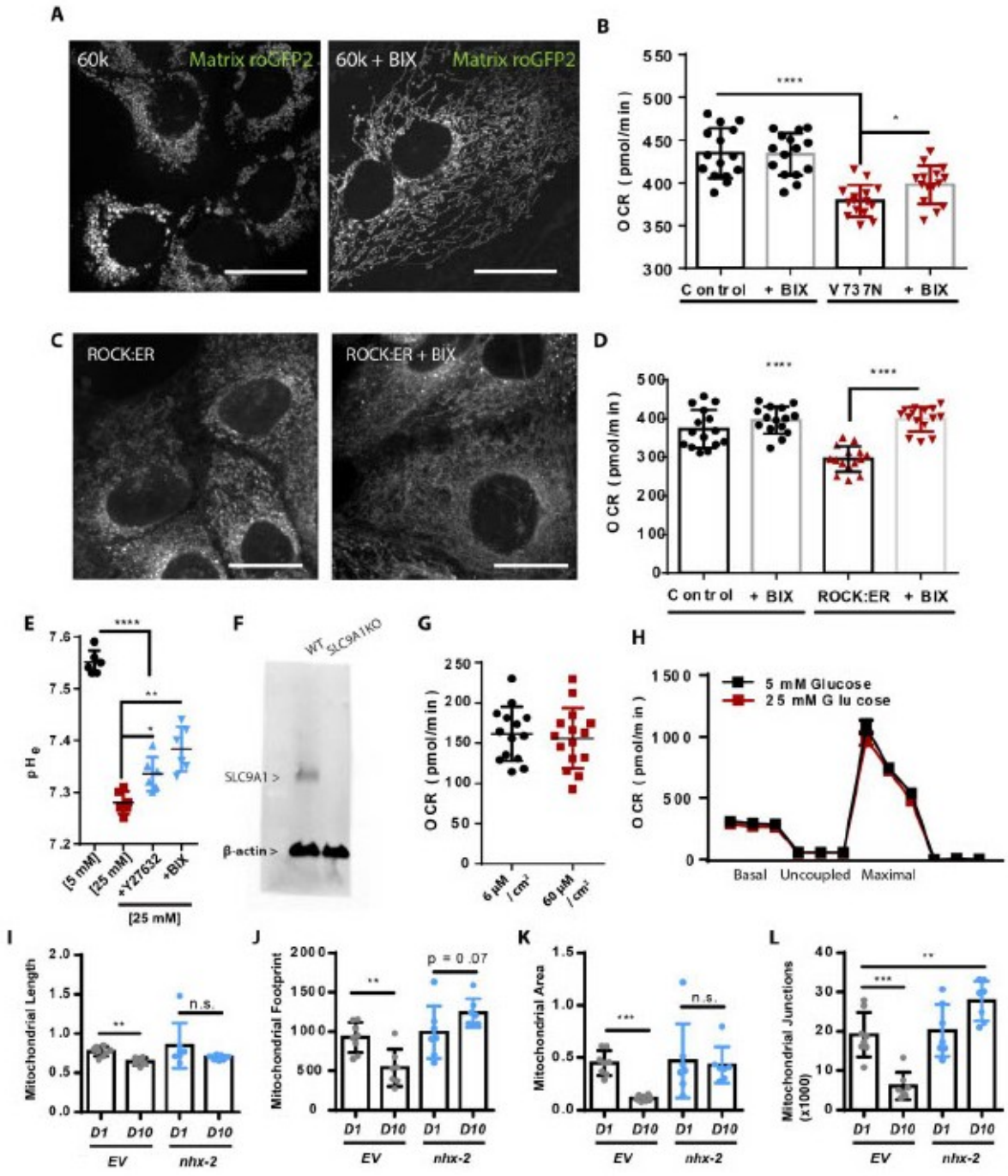

Figure 8.24: SLC9A1 contributes to mechanosignaling induced mitochondrial programming A. Confocal microscopy depicting mitochondrial network structure in cells expressing mitochondrial matrix targeted roGFP2 cultured on 60k Pa PA-gel surfaces +/- BIX [500 nM]. (Scale Bar: 10 μm). MitoMAPR Quantification: 60 kPa (8) and 60 kPa + BIX (12) junctions per network B. OCR of β1(V7373N) expressing cells via tetracycline inducible promoter for 24 h with doxycycline [200 ng/mL] +/- BIX [500 nM], (n=5 wells, 3 replicate measures, repeated 3 times). C. Confocal microscopy depicting mitochondrial network structure in ROCK:ER fusion protein ex-

pressing cells activated via 4HT [1 μM] treatment for 48 h or vehicle +/- BIX [500 nM]. (Scale Bar: 10 μm). MitoMAPR Quantification: ROCK:ER (7) and ROCK:ER + BIX (14) junctions per network. D. OCR of ROCK:ER fusion protein expressing cells activated via 4HT [1 μM] treatment for 48 h or vehicle, +/- BIX [500 nM] (n=5 wells, 3 replicate measures, repeated 3 times). E. pH of media surrounding MCF10A cells cultured in glucose [5 or 25 mM] +/- DMSO, Y27632 [10 μM], or BIX [500 nM] with 200k cells/well of 12 well plate after 48 h (n=3 repeated 2 times, shown together). F. Western blot depicting WT and SLC9A1 protein content (probed for SLC9A1 and β-actin on the same membrane). G. Oxygen consumption rate (OCR) of SLC9A1 KO cells in response to glucose [5 or 25 mM] (n=5 wells, 3 replicate measures). H. Mitochondrial stress test of SLC9A1 KO cells in response to 24 h of varied fibronectin surface coating density (n=5 wells, 3 replicate measures). I-L. MitoMAPR ([383]) quantitation of mitochondrial morphology depicted in Figure 2I (n=7 d1 wt, n=6 d10 wt, d1 nhx-2, and d10 nhx-2 images from separate animals).

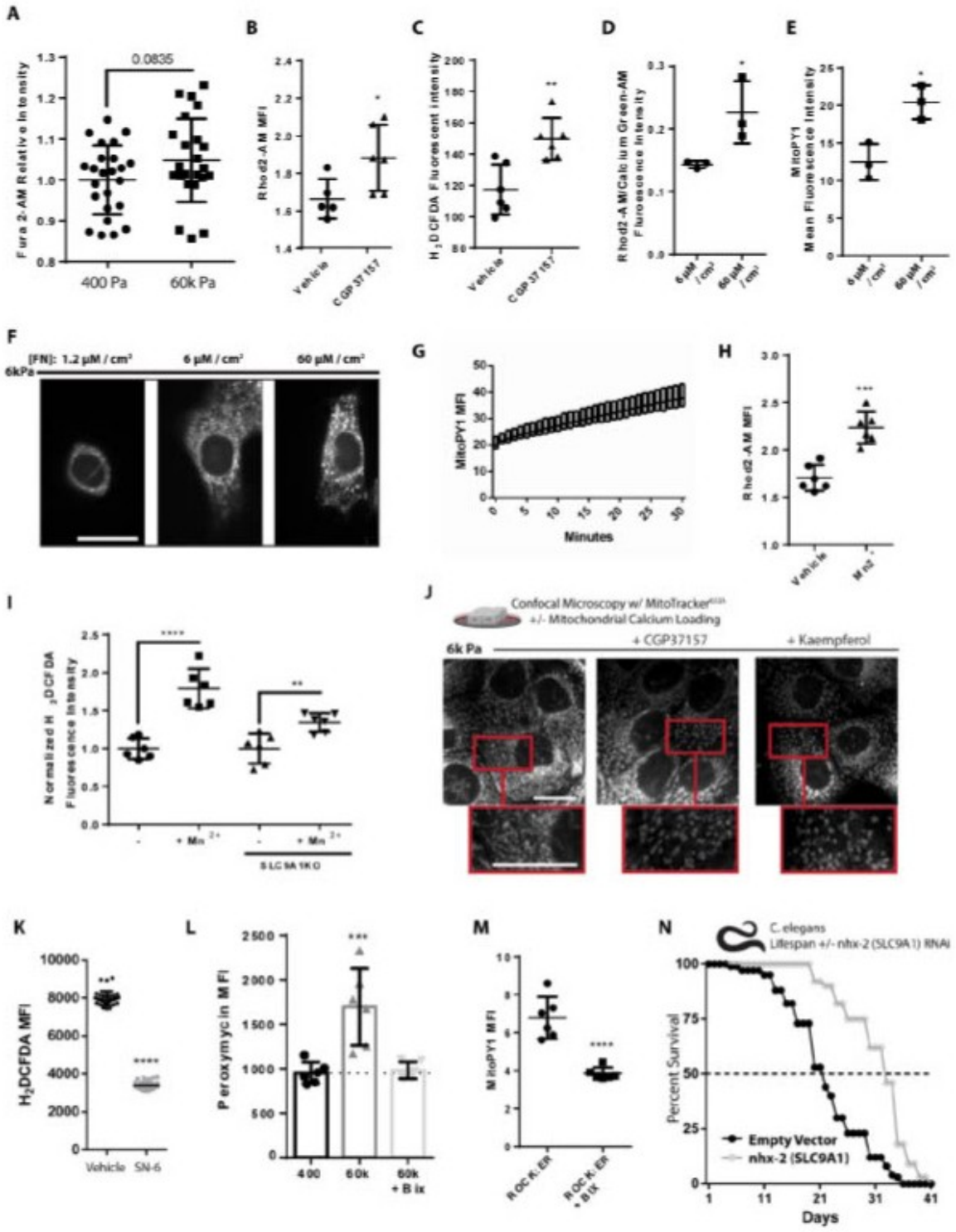

Figure 8.25: SLC9A1 activity promotes oxidative stress

A. Cellular calcium content of MECs cultured on 400 Pa or 60k Pa PA-gels for 24h, measured with Fura-2 AM [1 μM] (n=8 PA gels, repeated 3 times). B. Mitochondrial calcium content of cells treated with CGP37157 [1 μM] for 1 h, Rhod2-AM [2 μM] (n=6 wells, repeated 2 times). C.

Oxidative stress indicator intensity of cells treated with CGP37157 [1 μM] for 1 h, measured with 2',7'- dichlorodihydrofluorescein diacetate (H2DCFDA) [2 μM] (n=6 wells, repeated 2 times). D. Calcium content of MCF10A cells cultured for 24 h of varied fibronectin surface coating density, treated with Rhod2-AM [2 μM] (mitochondrial) and Calcium Green-1-AM [2 μM] (intracellular). (n=4 replicates, repeated 2 times). E. Mitochondrial H2O2 production of MCF10A cells cultured for 24 h of varied fibronectin surface coating density, MitoPy1 [5 μM] (n=4 replicates, repeated 2 times). F. Representative mitochondrial morphology of PFA fixed cells grown on 6k Pa PA-gels coated with varied fibronectin surface coating density for 24 h, stained with mitotracker (deep red FM) [100 nM] prior to fixation. G. Mitochondrial H2O2 production of MCF10A cells in response to increased glucose concentration [25 mM], measured over 30 minutes after glucose concentration was increased from 5 to 25 mM, MitoPy1 [5 μM] (n=6, repeated 2 times). H. Mitochondrial calcium content of cells treated with Mn2+ [1 μM] for 30 min, Rhod2-AM [2 μM] (n=6 wells, repeated 2 times). I. Oxidative stress indicator intensity of WT or SLC9A1 KO cells treated with Mn2+ [1 μM] for 30 min, measured with 2',7'-dichlorodihydrofluorescein diacetate (H2DCFDA) [2 μM] (n=6 wells, repeated 2 times). J. Confocal microscopy depicting mitochondrial network structure of PFA-fixed cells cultured on 6k Pa surfaces treated with CGP37157 [1 μM], kaempferol [10 μM], or vehicle for 1 h, mitotracker (deep red FM) [100 nM]. MitoMAPR Quantification: 6k (11), CGP37157 (6), and kaempferol (6) junctions per network. K. Oxidative stress indicator intensity MECs treated with SN-6 [10 μM] or vehicle for 24 h, measured with 2',7'-dichlorodihydrofluorescein diacetate (H2DCFDA) [2 μM] (n=12 wells, repeated 2 times). L H2O2 production of cells cultured on 400 Pa or 60k Pa ECM +/- BIX [500 nM] for 24 h measured with peroxymycin fluorescent intensity (n=6 separate samples). M. Mitochondrial H2O2 production of ROCK:ER fusion protein expressing cells activated via 4HT [1 μM] treatment for 48 h +/- BIX [500nM] or vehicle for 24 h and then MitoPy1 [5 μM] (n=6 wells, repeated 2 times). N. Lifespan of C. elegans grown on nhx-2 (SLC9A1 orthologue) or empty vector RNAi, (n=120 animals, repeated 3 times)

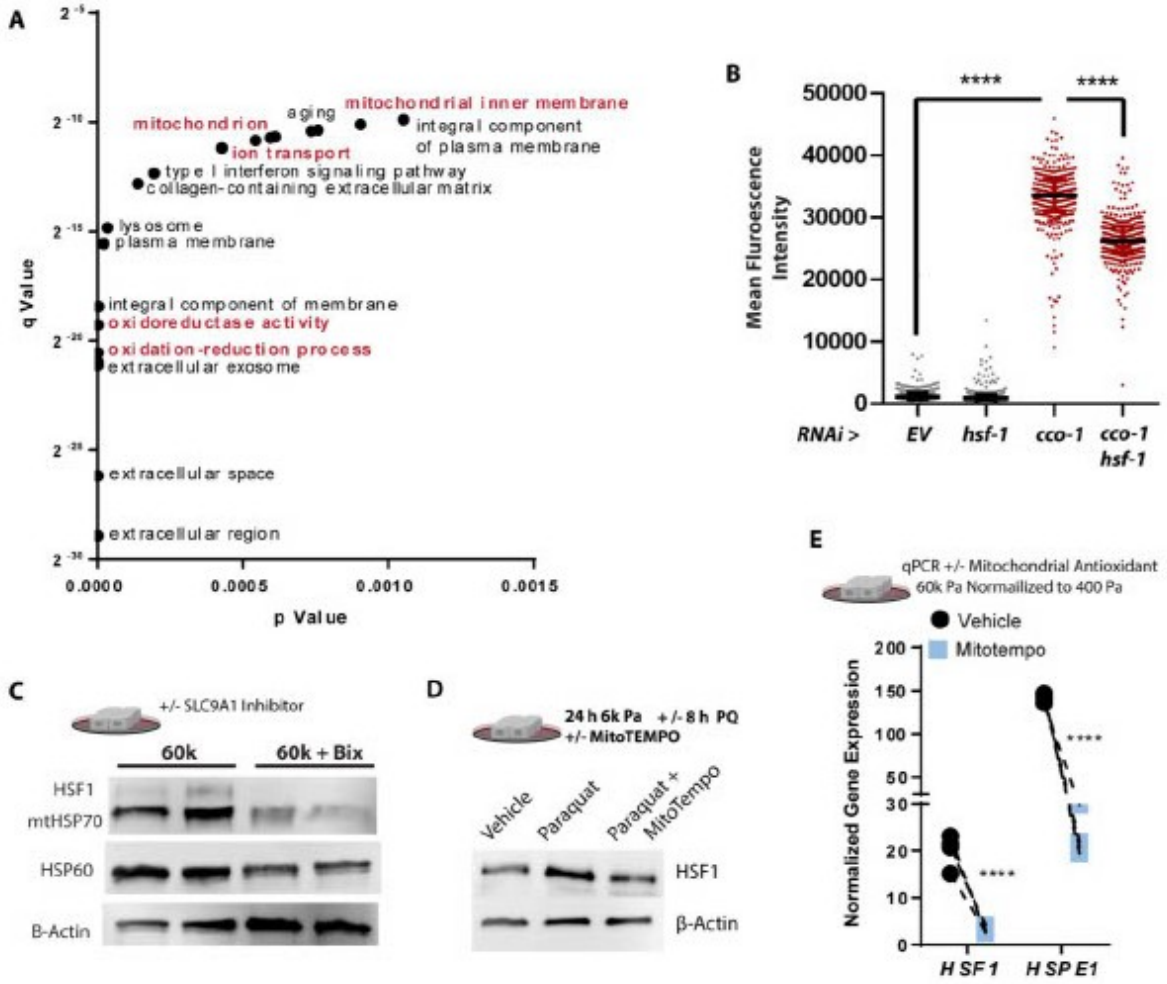

Figure 8.26: Mechanosignaling influences the mitochondrial stress response

A. Gene ontology of categories more highly represented in cells cultured on 400 Pa ECM than 60k Pa ECM (n=2 duplicate libraries of 3 biological replicates, 10 million reads per library). B. hsp-6::gfp reporter fluorescent intensity of C.elegans measured with a large particle cytometer, +/- cco-1 RNAi +/- HSF1 RNAi (1:1 ratio) (n=213, 263, 295, and 285 animals in order left to right), repeated 3 times. C. Western blot depicting relative protein abundance of 60k Pa ECM +/- 24 h Bix [500 nM] treatment (n=2 two biological replicates shown, repeated 3 times). D. Western blot depicting relative protein abundance of HSF1 and β-actin within 5 μg of total protein derived from lysates of cells cultured 6k Pa ECM +/- MitoTempo treatment for 24 h +/- paraquat [10 mM] treatment for 4 additional hours. E. Relative HSF1 and HSPE1 (HSF1 target gene) mRNA expression of cells grown 60k Pa ECM normalized to 400 Pa ECM, qPCR-δ δCT (housekeeping gene: 18s) (n= 4 separate experiments).

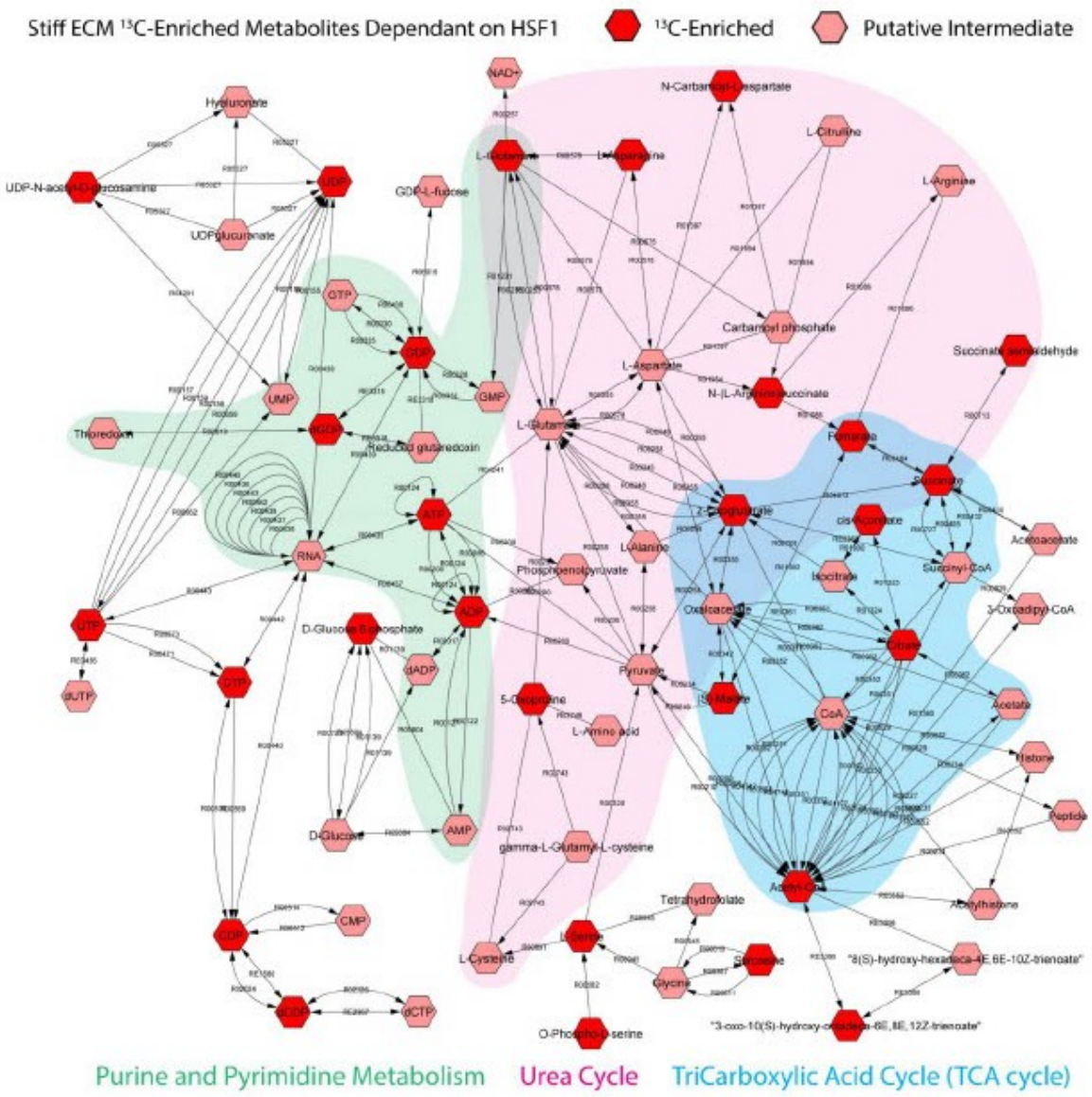

Figure 8.27: HSF1 facilitates mechano-metabolic programing

A. Network model of 13C6-glucose fractional contribution to significantly stiff ECM enhanced HSF1 dependent metabolic flux. Corresponding to Figure 5, generated with Cytoscape/Metscape.

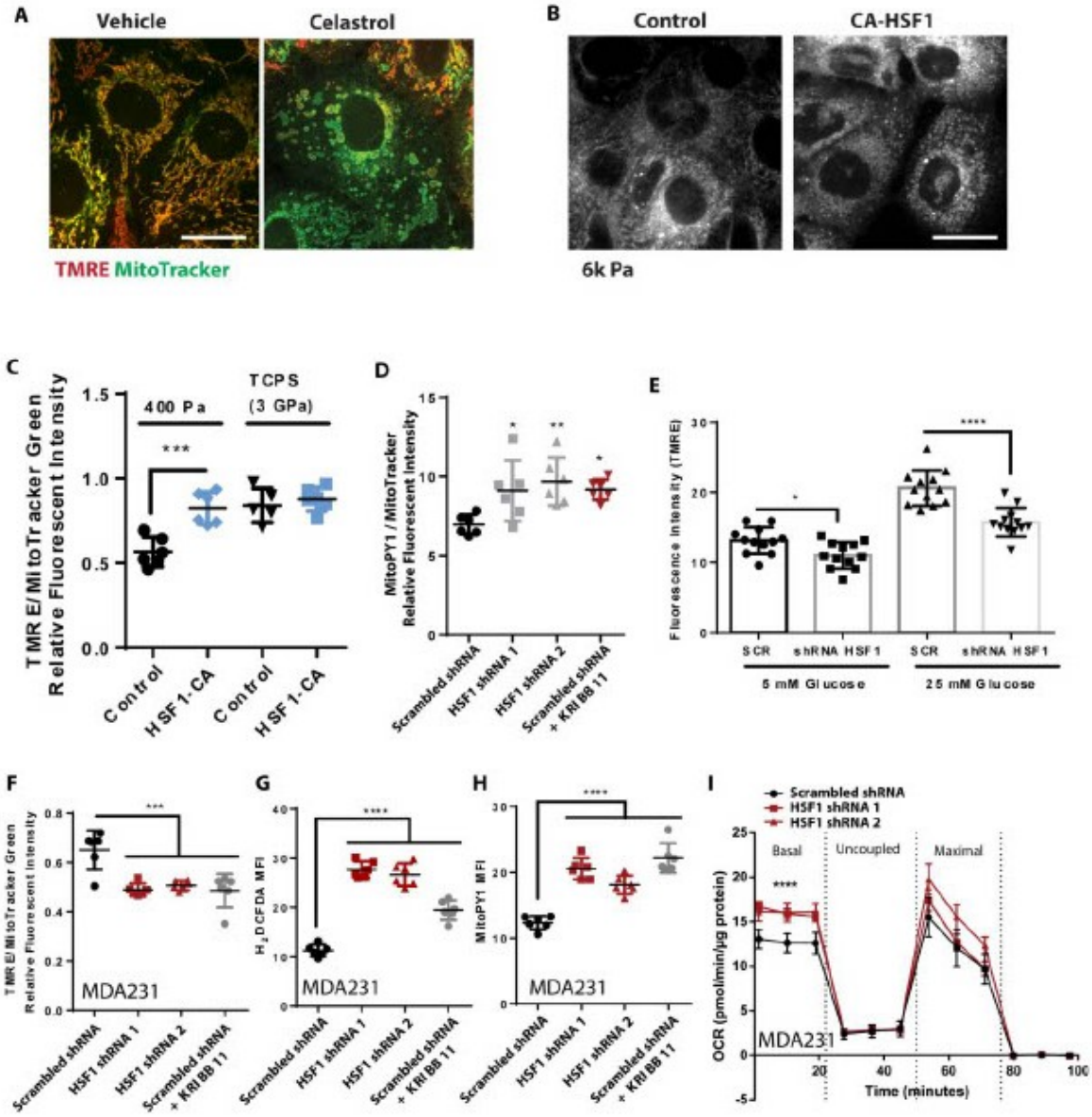

Figure 8.28: Mitochondrial reprogramming via HSF1

A. Representative microscopy depicting morphology and mitochondrial membrane potential staining of live cells via TMRE [10 nM] staining and mitotracker (green FM) [100 nM] +/- vehicle or Celastrol [2 μM] treatment for 40 minutes prior to imaging. (Scale Bar: 10 μm) B. Representative microscopy depicting mitochondrial network structure of cells cultured on 6k Pa ECM expressing constitutively active HSF1 or empty vector control, mitotracker (deep red FM) [100 nM]. (Scale Bar: 10 μm) C. Mitochondrial membrane potential MCF10A cells expressing CA-HSF1 on 400 Pa ECM or tissue culture polystyrene (TCPS) surfaces, measured with TMRE [10 nM] after 1 h staining (n=6) (n=6 wells, repeated 3 times). D. Mitochondrial hydrogen peroxide production of MCF10A cells expressing a scrambled shRNA +/- KRIBB11 [2 μM] or two different shRNAs targeting HSF1, measured with MitoPY1 [5 μM] normalized to Mitotracker green

staining [100nM] (n=6 wells, repeated 3 times). E. Mitochondrial membrane potential of MDA-231 cells cultured on TCPS expressing a scrambled shRNA +/- shRNAs targeting HSF1 (HSF1 shRNA 1) +/- glucose [5 or 25 mM], measured with TMRE [10 nM] after 1 h staining (n=6 wells, repeated 3 times). F. Mitochondrial hydrogen peroxide production of MDA-231 cells cultured on TCPS expressing a scrambled shRNA +/- KRIBB11 [2 μM] or two different shRNAs targeting HSF1, measured with MitoPY1 [5 μM] normalized to Mitotracker green staining [100nM] (n=6 wells, repeated 3 times). G. Oxidative stress indicator intensity of of MDA-231 cells expressing a scrambled shRNA +/- KRIBB11 [2 μM] or two different shRNAs targeting HSF1, measured with H2DCFDA [2 μM] H. Mitochondrial membrane potential of MDA-231 cells expressing a scrambled shRNA +/- KRIBB11 [2 μM] or shRNAs targeting HSF1 +/- glucose [5 or 25 mM], measured with TMRE [10 nM] after 1 h staining (n=6 wells, repeated 3 times). I. OCR of MDA-231 cells expressing a scrambled shRNA or two different shRNAs targeting HSF1 (n=5 wells, 3 replicate measures, repeated 3 times)

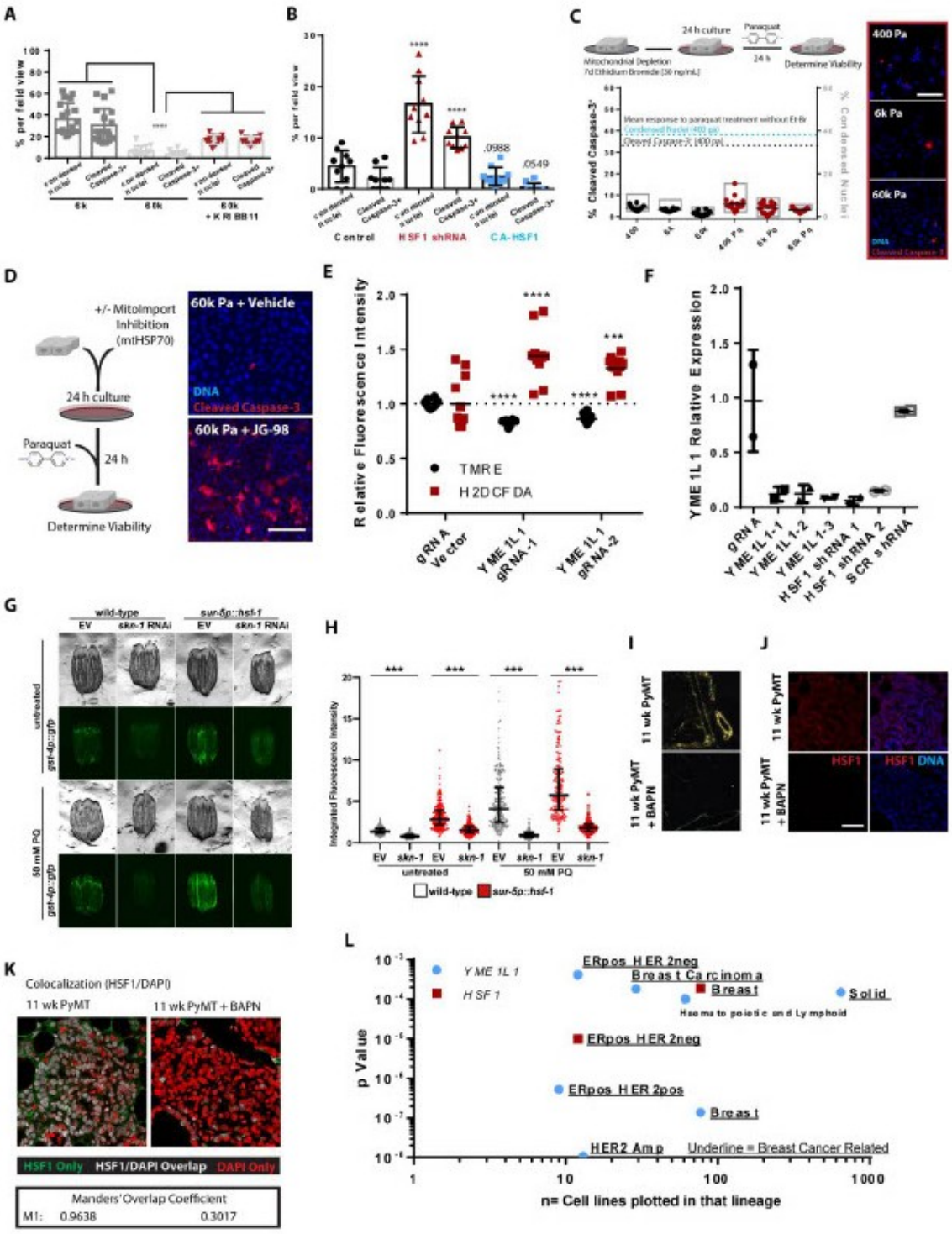

Figure 8.29: Mechanosignaling controls OxSR via HSF1 and YME1L1

A. Cleaved caspase 3 staining (red) and nuclear condensation (dapi) of cells cultured on 6 or 60 Pa PAgel surfaces for 24 h +/- vehicle or KRIBB11 [2 μM] followed by 24 h paraquat treatment [10 mM], (n=16 field views 600 cells per condition, repeated 3 times) B. Quantitation of

MCF10A cells expressing HSF1 shRNA 1 or CA-HSF1 from 10 field views for condensed nuclei and cleaved caspase-3 positive cells, cultured on fibronectin coated glass coverslips (800 cells counted per condition, repeated 3 times). C. Representative microscopy and quantitation of indicators of apoptosis with cleaved caspase 3 staining (red) and nuclear condensation (dapi) of MCF10A cells previously cultured for 7 d with 30 ng/mL ethidium bromide in the culture media, then transferred and cultured on 400, 6k, 60k Pa PA-gel surfaces for 24 h with another 24 h +/- paraquat treatment [10 mM]. 100k cells/well of 24 well plate. EtBr maintained in media during paraquat challenge. (600 cells counted per condition). Repeated 3 times (Scale Bar: 100 μm) D. Confocal microscopy of indicators of apoptosis with cleaved caspase 3 staining (red) and nuclear condensation (dapi) of cells cultured 60k Pa ECM surfaces for 24 h +/- JG98 [1 μM] followed by 24 h paraquat treatment [10 mM]. 100k cells/well of 24 well plate, repeated 2 times. E. Relative mitochondrial membrane potential and oxidative stress indicator intensity of MCF10A cells expressing YME1L1 knockdown via CRISPR-I compared to CRISPR-I and empty guide vector expressing cells on fibronectin coated TCPS, measured with TMRE [10 nM] and H2DCFDA [2 μM] for 1 h (n= 6 wells, repeated 2 times, both included) F. YME1L1 gene expression of pertinent cell lines. qPCR-δ δCT (housekeeping gene: 18s) (n=2 biological replicates). G-H. gst-4p::gfp reporter fluorescent intensity of C.elegans measured with a large particle cytometer, +/- paraquat [50 mM] (n=230, 190, 219, 222, 206, 215, 190, and 235 - from left to right), representative images (G) of C. elegans quantified (H), repeated 3 times. I. Representative polarized light microscopy of picrosirius red stained collagen of PyMT murine mammary tumors derived from mice treated with BAPN or vehicle. J-K. Representative immunofluorescence microscopy (J) and colocalization (K) of PyMT murine mammary tumors derived from mice treated with BAPN or vehicle, immunofluorescence microscopy for HSF1 (red) and DNA (blue). (Scale Bar: 100 μm). L. Cancer cell line/type dependency of HSF1 and YME1L1, all statistically represented values presented, determined with the Cancer Dependency Map produced by the Broad Institute (Boston, MA, USA) in collaboration with the Wellcome Sanger Institute (Hinxton, UK) (https://depmap.org/portal/depmap/)

9 References

[1] J. G. Jackson and J. W. Orr. The ducts of carcinomatous breasts, with particular reference to connectivetissue changes. *The Journal of Pathology and Bacteriology*, 74(2):265–273, 1957.

[2] F. Liu, J. D. Mih, B. S. Shea, A. T. Kho, A. S. Sharif, A. M. Tager, and D. J. Tschumperlin. Feedback amplification of fibrosis through matrix stiffening and COX-2 suppression. *J Cell Biol*, 190(4):693–706, Aug 2010.

[3] A. J. Booth, R. Hadley, A. M. Cornett, A. A. Dreffs, S. A. Matthes, J. L. Tsui, K. Weiss, J. C. Horowitz, V. F. Fiore, T. H. Barker, B. B. Moore, F. J. Martinez, L. E. Niklason, and E. S. White. Acellular normal and fibrotic human lung matrices as a culture system for in vitro investigation. *Am J Respir Crit Care Med*, 186(9):866–876, Nov 2012.

[4] A. C. Brown, V. F. Fiore, T. A. Sulchek, and T. H. Barker. Physical and chemical microenvironmental cues orthogonally control the degree and duration of fibrosis-associated epithelial-to-mesenchymal transitions. *J Pathol*, 229(1):25–35, Jan 2013.

[5] P. C. Georges, J. J. Hui, Z. Gombos, M. E. McCormick, A. Y. Wang, M. Uemura, R. Mick, P. A. Janmey, E. E. Furth, and R. G. Wells. Increased stiffness of the rat liver precedes matrix deposition: implications for fibrosis. *Am J Physiol Gastrointest Liver Physiol*, 293(6):G1147–1154, Dec 2007.

[6] F. Degos, P. Perez, B. Roche, A. Mahmoudi, J. Asselineau, H. Voitot, and P. Bedossa. Diagnostic accuracy of FibroScan and comparison to liver fibrosis biomarkers in chronic viral hepatitis: a multicenter prospective study (the FIBROSTIC study). *J Hepatol*, 53(6):1013–1021, Dec 2010.

[7] X. Chen, S. Wanggou, A. Bodalia, M. Zhu, W. Dong, J. J. Fan, W. C. Yin, H. K. Min, M. Hu, D. Draghici, W. Dou, F. Li, F. J. Coutinho, H. Whetstone, M. M. Kushida, P. B.

Dirks, Y. Song, C. C. Hui, Y. Sun, L. Y. Wang, X. Li, and X. Huang. A Feedforward Mechanism Mediated by Mechanosensitive Ion Channel PIEZO1 and Tissue Mechanics Promotes Glioma Aggression. *Neuron*, 100(4):799–815, 11 2018.

[8] I. Acerbi, L. Cassereau, I. Dean, Q. Shi, A. Au, C. Park, Y. Y. Chen, J. Liphardt, E. S. Hwang, and V. M. Weaver. Human breast cancer invasion and aggression correlates with ECM stiffening and immune cell infiltration. *Integr Biol (Camb)*, 7(10):1120–1134, Oct 2015.

[9] G. Finak, N. Bertos, F. Pepin, S. Sadekova, M. Souleimanova, H. Zhao, H. Chen, G. Omeroglu, S. Meterissian, A. Omeroglu, M. Hallett, and M. Park. Stromal gene expression predicts clinical outcome in breast cancer. *Nat Med*, 14(5):518–527, May 2008.

[10] S. S. Mujtaba, Y. B. Ni, J. Y. Tsang, S. K. Chan, R. Yamaguchi, M. Tanaka, P. H. Tan, and G. M. Tse. Fibrotic focus in breast carcinomas: relationship with prognostic parameters and biomarkers. *Ann Surg Oncol*, 20(9):2842–2849, Sep 2013.

[11] C. J. Whatcott, C. H. Diep, P. Jiang, A. Watanabe, J. LoBello, C. Sima, G. Hostetter, H. M. Shepard, D. D. Von Hoff, and H. Han. Desmoplasia in Primary Tumors and Metastatic Lesions of Pancreatic Cancer. *Clin Cancer Res*, 21(15):3561–3568, Aug 2015.

[12] H. Laklai, Y. A. Miroshnikova, M. W. Pickup, E. A. Collisson, G. E. Kim, A. S. Barrett, R. C. Hill, J. N. Lakins, D. D. Schlaepfer, J. K. Mouw, V. S. LeBleu, N. Roy, S. V. Novitskiy, J. S. Johansen, V. Poli, R. Kalluri, C. A. Iacobuzio-Donahue, L. D. Wood, M. Hebrok, K. Hansen, H. L. Moses, and V. M. Weaver. Genotype tunes pancreatic ductal adenocarcinoma tissue tension to induce matricellular fibrosis and tumor progression. *Nat Med*, 22(5):497–505, 05 2016.

[13] J. M. O'Rourke, V. M. Sagar, T. Shah, and S. Shetty. Carcinogenesis on the background of liver fibrosis: Implications for the management of hepatocellular cancer. *World J Gastroenterol*, 24(39):4436–4447, Oct 2018.

[14] J. Park, D. S. Kim, T. S. Shim, C. M. Lim, Y. Koh, S. D. Lee, W. S. Kim, W. D. Kim, J. S. Lee, and K. S. Song. Lung cancer in patients with idiopathic pulmonary fibrosis. *Eur Respir J*, 17(6):1216–1219, Jun 2001.

[15] D. W. Kamp. Asbestos-induced lung diseases: an update. *Transl Res*, 153(4):143–152, Apr 2009.

[16] B. Stengel. Chronic kidney disease and cancer: a troubling connection. *J Nephrol*, 23(3):253–262, 2010.

[17] B. D. Humphreys. Mechanisms of Renal Fibrosis. *Annu Rev Physiol*, 80:309–326, 02 2018.

[18] G. R. Cunha, S. W. Hayward, and Y. Z. Wang. Role of stroma in carcinogenesis of the prostate. *Differentiation*, 70(9-10):473–485, Dec 2002.

[19] P. Taroni, G. Quarto, A. Pifferi, F. Abbate, N. Balestreri, S. Menna, E. Cassano, and R. Cubeddu. Breast tissue composition and its dependence on demographic risk factors for breast cancer: non-invasive assessment by time domain diffuse optical spectroscopy. *PLoS One*, 10(6):e0128941, 2015.

[20] M. Chan, S. Lonie, S. Mackay, and K. MacGill. Reduction Mammaplasty: What Cup Size Will I Be? *Plast Reconstr Surg Glob Open*, 7(6):e2273, Jun 2019.

[21] M. W. Conklin, J. C. Eickhoff, K. M. Riching, C. A. Pehlke, K. W. Eliceiri, P. P. Provenzano, A. Friedl, and P. J. Keely. Aligned collagen is a prognostic signature for survival in human breast carcinoma. *Am J Pathol*, 178(3):1221–1232, Mar 2011.

[22] J. Mütze, V. Iyer, J. J. Macklin, J. Colonell, B. Karsh, Z. Petrášek, P. Schwille, L. L. Looger, L. D. Lavis, and T. D. Harris. Excitation spectra and brightness optimization of two-photon excited probes. *Biophys J*, 102(4):934–944, Feb 2012.

[23] M. Drobizhev, N. S. Makarov, S. E. Tillo, T. E. Hughes, and A. Rebane. Two-photon absorption properties of fluorescent proteins. *Nat Methods*, 8(5):393–399, May 2011.

[24] J. D. Humphries, A. Byron, and M. J. Humphries. Integrin ligands at a glance. *J Cell Sci*, 119(Pt 19):3901–3903, Oct 2006.

[25] J. H. Wang. Pull and push: talin activation for integrin signaling. *Cell Res*, 22(11):1512–1514, Nov 2012.

[26] A. Elosegui-Artola, E. Bazellières, M. D. Allen, I. Andreu, R. Oria, R. Sunyer, J. J. Gomm, J. F. Marshall, J. L. Jones, X. Trepat, and P. Roca-Cusachs. Rigidity sensing and adaptation through regulation of integrin types. *Nat Mater*, 13(6):631–637, Jun 2014.

[27] R. Oria, T. Wiegand, J. Escribano, A. Elosegui-Artola, J. J. Uriarte, C. Moreno-Pulido, I. Platzman, P. Delcanale, L. Albertazzi, D. Navajas, X. Trepat, J. M. García-Aznar, E. A. Cavalcanti-Adam, and P. Roca-Cusachs. Force loading explains spatial sensing of ligands by cells. *Nature*, 552(7684):219–224, 12 2017.

[28] R. G. Hodge and A. J. Ridley. Regulating Rho GTPases and their regulators. *Nat Rev Mol Cell Biol*, 17(8):496–510, 08 2016.

[29] S. T. Lim, X. L. Chen, Y. Lim, D. A. Hanson, T. T. Vo, K. Howerton, N. Larocque, S. J. Fisher, D. D. Schlaepfer, and D. Ilic. Nuclear FAK promotes cell proliferation and survival through FERM-enhanced p53 degradation. *Mol Cell*, 29(1):9–22, Jan 2008.

[30] G. Kadaré, N. Gervasi, K. Brami-Cherrier, H. Blockus, S. El Messari, S. T. Arold, and J. A. Girault. Conformational dynamics of the focal adhesion targeting domain control specific functions of focal adhesion kinase in cells. *J Biol Chem*, 290(1):478–491, Jan 2015.

[31] A. R. Hess, L. M. Postovit, N. V. Margaryan, E. A. Seftor, G. B. Schneider, R. E. Seftor, B. J. Nickoloff, and M. J. Hendrix. Focal adhesion kinase promotes the aggressive melanoma phenotype. *Cancer Res*, 65(21):9851–9860, Nov 2005.

[32] T. R. Johnson, L. Khandrika, B. Kumar, S. Venezia, S. Koul, R. Chandhoke, P. Maroni, R. Donohue, R. B. Meacham, and H. K. Koul. Focal adhesion kinase controls aggressive

phenotype of androgen-independent prostate cancer. *Mol Cancer Res*, 6(10):1639–1648, Oct 2008.

[33] A. L. Lark, C. A. Livasy, L. Dressler, D. T. Moore, R. C. Millikan, J. Geradts, M. Iacocca, D. Cowan, D. Little, R. J. Craven, and W. Cance. High focal adhesion kinase expression in invasive breast carcinomas is associated with an aggressive phenotype. *Mod Pathol*, 18(10):1289–1294, Oct 2005.

[34] R. R. Valiathan, M. Marco, B. Leitinger, C. G. Kleer, and R. Fridman. Discoidin domain receptor tyrosine kinases: new players in cancer progression. *Cancer Metastasis Rev*, 31(1-2):295–321, Jun 2012.

[35] E. Henriet, M. Sala, A. Abou Hammoud, A. Tuariihionoa, J. Di Martino, M. Ros, and F. Saltel. Multitasking discoidin domain receptors are involved in several and specific hallmarks of cancer. *Cell Adh Migr*, 12(4):363–377, 2018.

[36] D. Barbouri, N. Afratis, C. Gialeli, D. H. Vynios, A. D. Theocharis, and N. K. Karamanos. Syndecans as modulators and potential pharmacological targets in cancer progression. *Front Oncol*, 4:4, 2014.

[37] K. Kessenbrock, V. Plaks, and Z. Werb. Matrix metalloproteinases: regulators of the tumor microenvironment. *Cell*, 141(1):52–67, Apr 2010.

[38] B. Jang, A. Kim, J. Hwang, H. K. Song, Y. Kim, and E. S. Oh. Emerging Role of Syndecans in Extracellular Matrix Remodeling in Cancer. *J Histochem Cytochem*, 68(12):863–870, 12 2020.

[39] K. Kunzelmann. Ion channels and cancer. *J Membr Biol*, 205(3):159–173, Jun 2005.

[40] DaeYong Lee, JongHoon Ha, Minjeong Kang, Zhaogang Yang, Wen Jiang, and Betty Y. S. Kim. Strategies of perturbing ion homeostasis for cancer therapy. *Advanced Therapeutics*, 5(2):2100189, 2022.

[41] K. E. Scott, S. I. Fraley, and P. Rangamani. A spatial model of YAP/TAZ signaling reveals how stiffness, dimensionality, and shape contribute to emergent outcomes. *Proc Natl Acad Sci U S A*, 118(20), 05 2021.

[42] A. Pocaterra, P. Romani, and S. Dupont. YAP/TAZ functions and their regulation at a glance. *J Cell Sci*, 133(2), 01 2020.

[43] R. K. Jain, J. D. Martin, and T. Stylianopoulos. The role of mechanical forces in tumor growth and therapy. *Annu Rev Biomed Eng*, 16:321–346, Jul 2014.

[44] G. Helmlinger, P. A. Netti, H. C. Lichtenbeld, R. J. Melder, and R. K. Jain. Solid stress inhibits the growth of multicellular tumor spheroids. *Nat Biotechnol*, 15(8):778–783, Aug 1997.

[45] A. Bagaev, N. Kotlov, K. Nomie, V. Svekolkin, A. Gafurov, O. Isaeva, N. Osokin, I. Kozlov, F. Frenkel, O. Gancharova, N. Almog, M. Tsiper, R. Ataullakhanov, and N. Fowler. Conserved pan-cancer microenvironment subtypes predict response to immunotherapy. *Cancer Cell*, 39(6):845–865, 06 2021.

[46] C. Hatzis, L. Pusztai, V. Valero, D. J. Booser, L. Esserman, A. Lluch, T. Vidaurre, F. Holmes, E. Souchon, H. Wang, M. Martin, J. Cotrina, H. Gomez, R. Hubbard, J. I. Chacón, J. Ferrer-Lozano, R. Dyer, M. Buxton, Y. Gong, Y. Wu, N. Ibrahim, E. Andreopoulou, N. T. Ueno, K. Hunt, W. Yang, A. Nazario, A. DeMichele, J. O'Shaughnessy, G. N. Hortobagyi, and W. F. Symmans. A genomic predictor of response and survival following taxane-anthracycline chemotherapy for invasive breast cancer. *JAMA*, 305(18):1873–1881, May 2011.

[47] M. Itoh, T. Iwamoto, J. Matsuoka, T. Nogami, T. Motoki, T. Shien, N. Taira, N. Niikura, N. Hayashi, S. Ohtani, K. Higaki, T. Fujiwara, H. Doihara, W. F. Symmans, and L. Pusztai. Estrogen receptor (ER) mRNA expression and molecular subtype distribu-

tion in ER-negative/progesterone receptor-positive breast cancers. *Breast Cancer Res Treat*, 143(2):403–409, Jan 2014.

[48] D. Ribatti, R. Tamma, and T. Annese. Epithelial-Mesenchymal Transition in Cancer: A Historical Overview. *Transl Oncol*, 13(6):100773, Jun 2020.

[49] S. C. Wei, L. Fattet, J. H. Tsai, Y. Guo, V. H. Pai, H. E. Majeski, A. C. Chen, R. L. Sah, S. S. Taylor, A. J. Engler, and J. Yang. Matrix stiffness drives epithelial-mesenchymal transition and tumour metastasis through a TWIST1-G3BP2 mechanotransduction pathway. *Nat Cell Biol*, 17(5):678–688, May 2015.

[50] K. Zhang, C. A. Corsa, S. M. Ponik, J. L. Prior, D. Piwnica-Worms, K. W. Eliceiri, P. J. Keely, and G. D. Longmore. The collagen receptor discoidin domain receptor 2 stabilizes SNAIL1 to facilitate breast cancer metastasis. *Nat Cell Biol*, 15(6):677–687, Jun 2013.

[51] P. P. Provenzano, K. W. Eliceiri, J. M. Campbell, D. R. Inman, J. G. White, and P. J. Keely. Collagen reorganization at the tumor-stromal interface facilitates local invasion. *BMC Med*, 4(1):38, Dec 2006.

[52] A. H. Mekhdjian, F. Kai, M. G. Rubashkin, L. S. Prahl, L. M. Przybyla, A. L. McGregor, E. S. Bell, J. M. Barnes, C. C. DuFort, G. Ou, A. C. Chang, L. Cassereau, S. J. Tan, M. W. Pickup, J. N. Lakins, X. Ye, M. W. Davidson, J. Lammerding, D. J. Odde, A. R. Dunn, and V. M. Weaver. Integrin-mediated traction force enhances paxillin molecular associations and adhesion dynamics that increase the invasiveness of tumor cells into a three-dimensional extracellular matrix. *Mol Biol Cell*, 28(11):1467–1488, Jun 2017.

[53] O. Maller, A. P. Drain, A. S. Barrett, S. Borgquist, B. Ruffell, I. Zakharevich, T. T. Pham, T. Gruosso, H. Kuasne, J. N. Lakins, I. Acerbi, J. M. Barnes, T. Nemkov, A. Chauhan, J. Gruenberg, A. Nasir, O. Bjarnadottir, Z. Werb, P. Kabos, Y. Y. Chen, E. S. Hwang, M. Park, L. M. Coussens, A. C. Nelson, K. C. Hansen, and V. M. Weaver. Tumour-

associated macrophages drive stromal cell-dependent collagen crosslinking and stiffening to promote breast cancer aggression. *Nat Mater*, 20(4):548–559, 04 2021.

[54] K. R. Levental, H. Yu, L. Kass, J. N. Lakins, M. Egeblad, J. T. Erler, S. F. Fong, K. Csiszar, A. Giaccia, W. Weninger, M. Yamauchi, D. L. Gasser, and V. M. Weaver. Matrix crosslinking forces tumor progression by enhancing integrin signaling. *Cell*, 139(5):891–906, Nov 2009.

[55] D. H. Munn and V. Bronte. Immune suppressive mechanisms in the tumor microenvironment. *Curr Opin Immunol*, 39:1–6, Apr 2016.

[56] J. Wang, D. Li, H. Cang, and B. Guo. Crosstalk between cancer and immune cells: Role of tumor-associated macrophages in the tumor microenvironment. *Cancer Med*, 8(10):4709–4721, 08 2019.

[57] K. L. Singel and B. H. Segal. Neutrophils in the tumor microenvironment: trying to heal the wound that cannot heal. *Immunol Rev*, 273(1):329–343, 09 2016.

[58] A. V. Ponomarev and I. Z. Shubina. Insights Into Mechanisms of Tumor and Immune System Interaction: Association With Wound Healing. *Front Oncol*, 9:1115, 2019.

[59] T. Gruosso, M. Gigoux, V. S. K. Manem, N. Bertos, D. Zuo, I. Perlitch, S. M. I. Saleh, H. Zhao, M. Souleimanova, R. M. Johnson, A. Monette, V. M. Ramos, M. T. Hallett, J. Stagg, R. Lapointe, A. Omeroglu, S. Meterissian, L. Buisseret, G. Van den Eynden, R. Salgado, M. C. Guiot, B. Haibe-Kains, and M. Park. Spatially distinct tumor immune microenvironments stratify triple-negative breast cancers. *J Clin Invest*, 129(4):1785–1800, 04 2019.

[60] B. Erdogan and D. J. Webb. Cancer-associated fibroblasts modulate growth factor signaling and extracellular matrix remodeling to regulate tumor metastasis. *Biochem Soc Trans*, 45(1):229–236, 02 2017.

[61] V. Syed. TGF-β Signaling in Cancer. *J Cell Biochem*, 117(6):1279–1287, Jun 2016.

[62] I. Fabregat, J. Fernando, J. Mainez, and P. Sancho. TGF-beta signaling in cancer treatment. *Curr Pharm Des*, 20(17):2934–2947, 2014.

[63] Z. Li, M. Seehawer, and K. Polyak. Untangling the web of intratumour heterogeneity. *Nat Cell Biol*, 24(8):1192–1201, 08 2022.

[64] M. Janiszewska, S. Stein, O. Metzger Filho, J. Eng, N. L. Kingston, N. W. Harper, I. H. Rye, M. Alečković, A. Trinh, K. C. Murphy, E. Marangoni, S. Cristea, B. Oakes, E. P. Winer, I. E. Krop, H. G. Russnes, P. T. Spellman, E. Bucher, Z. Hu, K. Chin, J. W. Gray, F. Michor, and K. Polyak. The impact of tumor epithelial and microenvironmental heterogeneity on treatment responses in HER2+ breast cancer. *JCI Insight*, 6(11), 06 2021.

[65] I. H. Rye, A. Trinh, A. B. Saetersdal, D. Nebdal, O. C. Lingjaerde, V. Almendro, K. Polyak, A. L. Børresen-Dale, Å. Helland, F. Markowetz, and H. G. Russnes. Intratumor heterogeneity defines treatment-resistant HER2+ breast tumors. *Mol Oncol*, 12(11):1838–1855, 11 2018.

[66] E. Azizi, A. J. Carr, G. Plitas, A. E. Cornish, C. Konopacki, S. Prabhakaran, J. Nainys, K. Wu, V. Kiseliovas, M. Setty, K. Choi, R. M. Fromme, P. Dao, P. T. McKenney, R. C. Wasti, K. Kadaveru, L. Mazutis, A. Y. Rudensky, and D. Pe'er. Single-Cell Map of Diverse Immune Phenotypes in the Breast Tumor Microenvironment. *Cell*, 174(5):1293–1308, 08 2018.

[67] Q. Xu, S. Chen, Y. Hu, and W. Huang. Landscape of Immune Microenvironment Under Immune Cell Infiltration Pattern in Breast Cancer. *Front Immunol*, 12:711433, 2021.

[68] N. Rohani, L. Hao, M. S. Alexis, B. A. Joughin, K. Krismer, M. N. Moufarrej, A. R. Soltis, D. A. Lauffenburger, M. B. Yaffe, C. B. Burge, S. N. Bhatia, and F. B. Gertler. Acidification of Tumor at Stromal Boundaries Drives Transcriptome Alterations Associated with Aggressive Phenotypes. *Cancer Res*, 79(8):1952–1966, 04 2019.

[69] M. Bartoschek, N. Oskolkov, M. Bocci, J. Lövrot, C. Larsson, M. Sommarin, C. D. Madsen, D. Lindgren, G. Pekar, G. Karlsson, M. Ringnér, J. Bergh, Å. Björklund, and K. Pietras. Spatially and functionally distinct subclasses of breast cancer-associated fibroblasts revealed by single cell RNA sequencing. *Nat Commun*, 9(1):5150, 12 2018.

[70] R. E. Vandenbroucke and C. Libert. Is there new hope for therapeutic matrix metalloproteinase inhibition? *Nat Rev Drug Discov*, 13(12):904–927, Dec 2014.

[71] L. M. Coussens, B. Fingleton, and L. M. Matrisian. Matrix metalloproteinase inhibitors and cancer: trials and tribulations. *Science*, 295(5564):2387–2392, Mar 2002.

[72] V. B. Lokeshwar, S. Mirza, and A. Jordan. Targeting hyaluronic acid family for cancer chemoprevention and therapy. *Adv Cancer Res*, 123:35–65, 2014.

[73] V. M. Platt and F. C. Szoka. Anticancer therapeutics: targeting macromolecules and nanocarriers to hyaluronan or CD44, a hyaluronan receptor. *Mol Pharm*, 5(4):474–486, 2008.

[74] M. Schmitt, A. Schmitt, M. T. Rojewski, J. Chen, K. Giannopoulos, F. Fei, Y. Yu, M. Götz, M. Heyduk, G. Ritter, D. E. Speiser, S. Gnjatic, P. Guillaume, M. Ringhoffer, R. F. Schlenk, P. Liebisch, D. Bunjes, H. Shiku, H. Dohner, and J. Greiner. RHAMM-R3 peptide vaccination in patients with acute myeloid leukemia, myelodysplastic syndrome, and multiple myeloma elicits immunologic and clinical responses. *Blood*, 111(3):1357–1365, Feb 2008.

[75] D. Ciardiello, E. Elez, J. Tabernero, and J. Seoane. Clinical development of therapies targeting TGFβ: current knowledge and future perspectives. *Ann Oncol*, 31(10):1336–1349, 10 2020.

[76] D. Padua, X. H. Zhang, Q. Wang, C. Nadal, W. L. Gerald, R. R. Gomis, and J. Massagué. TGFbeta primes breast tumors for lung metastasis seeding through angiopoietin-like 4. *Cell*, 133(1):66–77, Apr 2008.

[77] A. Bruna, R. S. Darken, F. Rojo, A. Ocaña, S. Peñuelas, A. Arias, R. Paris, A. Tortosa, J. Mora, J. Baselga, and J. Seoane. High TGFbeta-Smad activity confers poor prognosis in glioma patients and promotes cell proliferation depending on the methylation of the PDGF-B gene. *Cancer Cell*, 11(2):147–160, Feb 2007.

[78] R. K. Kelley, E. Gane, E. Assenat, J. Siebler, P. R. Galle, P. Merle, I. O. Hourmand, A. Cleverly, Y. Zhao, I. Gueorguieva, M. Lahn, S. Faivre, K. A. Benhadji, and G. Giannelli. A Phase 2 Study of Galunisertib (TGF-β1 Receptor Type I Inhibitor) and Sorafenib in Patients With Advanced Hepatocellular Carcinoma. *Clin Transl Gastroenterol*, 10(7):e00056, 07 2019.

[79] L. Paz-Ares, T. M. Kim, D. Vicente, E. Felip, D. H. Lee, K. H. Lee, C. C. Lin, M. J. Flor, M. Di Nicola, R. M. Alvarez, I. Dussault, C. Helwig, L. S. Ojalvo, J. L. Gulley, and B. C. Cho. Bintrafusp Alfa, a Bifunctional Fusion Protein Targeting TGF-β and PD-L1, in Second-Line Treatment of Patients With NSCLC: Results From an Expansion Cohort of a Phase 1 Trial. *J Thorac Oncol*, 15(7):1210–1222, 07 2020.

[80] Ben Adams. Gsk, german merck's $4.2b bintrafusp alfa drug flops again, but companies squint to see glimmers of hope, Mar 2021.

[81] C. R. Gil Del Alcazar, M. Alečković, and K. Polyak. Immune Escape during Breast Tumor Progression. *Cancer Immunol Res*, 8(4):422–427, 04 2020.

[82] L. K. Huynh, C. J. Hipolito, and P. Ten Dijke. A Perspective on the Development of TGF-β Inhibitors for Cancer Treatment. *Biomolecules*, 9(11), 11 2019.

[83] A. Marusyk, M. Janiszewska, and K. Polyak. Intratumor Heterogeneity: The Rosetta Stone of Therapy Resistance. *Cancer Cell*, 37(4):471–484, 04 2020.

[84] G. Turashvili and E. Brogi. Tumor Heterogeneity in Breast Cancer. *Front Med (Lausanne)*, 4:227, 2017.

[85] G. Biffi and D. A. Tuveson. Diversity and Biology of Cancer-Associated Fibroblasts. *Physiol Rev*, 101(1):147–176, 01 2021.

[86] D. R. Caswell and C. Swanton. The role of tumour heterogeneity and clonal cooperativity in metastasis, immune evasion and clinical outcome. *BMC Med*, 15(1):133, 07 2017.

[87] D. A. Lawson, K. Kessenbrock, R. T. Davis, N. Pervolarakis, and Z. Werb. Tumour heterogeneity and metastasis at single-cell resolution. *Nat Cell Biol*, 20(12):1349–1360, 12 2018.

[88] R. Fisher, L. Pusztai, and C. Swanton. Cancer heterogeneity: implications for targeted therapeutics. *Br J Cancer*, 108(3):479–485, Feb 2013.

[89] K. L. McNamara, J. L. Caswell-Jin, R. Joshi, Z. Ma, E. Kotler, G. R. Bean, M. Kriner, Z. Zhou, M. Hoang, J. Beechem, J. Zoeller, M. F. Press, D. J. Slamon, S. A. Hurvitz, and C. Curtis. Spatial proteomic characterization of HER2-positive breast tumors through neoadjuvant therapy predicts response. *Nat Cancer*, 2(4):400–413, 04 2021.

[90] R. Gyanchandani, Y. Lin, H. M. Lin, K. Cooper, D. P. Normolle, A. Brufsky, M. Fastuca, W. Crosson, S. Oesterreich, N. E. Davidson, R. Bhargava, D. J. Dabbs, and A. V. Lee. Intratumor Heterogeneity Affects Gene Expression Profile Test Prognostic Risk Stratification in Early Breast Cancer. *Clin Cancer Res*, 22(21):5362–5369, Nov 2016.

[91] L. Keren, M. Bosse, S. Thompson, T. Risom, K. Vijayaragavan, E. McCaffrey, D. Marquez, R. Angoshtari, N. F. Greenwald, H. Fienberg, J. Wang, N. Kambham, D. Kirkwood, G. Nolan, T. J. Montine, S. J. Galli, R. West, S. C. Bendall, and M. Angelo. MIBI-TOF: A multiplexed imaging platform relates cellular phenotypes and tissue structure. *Sci Adv*, 5(10):eaax5851, 10 2019.

[92] R. Moncada, D. Barkley, F. Wagner, M. Chiodin, J. C. Devlin, M. Baron, C. H. Hajdu, D. M. Simeone, and I. Yanai. Integrating microarray-based spatial transcriptomics and single-cell

RNA-seq reveals tissue architecture in pancreatic ductal adenocarcinomas. *Nat Biotechnol*, 38(3):333–342, 03 2020.

[93] D. Phillips, C. M. Schürch, M. S. Khodadoust, Y. H. Kim, G. P. Nolan, and S. Jiang. Highly Multiplexed Phenotyping of Immunoregulatory Proteins in the Tumor Microenvironment by CODEX Tissue Imaging. *Front Immunol*, 12:687673, 2021.

[94] D. C. Belisario, J. Kopecka, M. Pasino, M. Akman, E. De Smaele, M. Donadelli, and C. Riganti. Hypoxia Dictates Metabolic Rewiring of Tumors: Implications for Chemoresistance. *Cells*, 9(12), 12 2020.

[95] J. Winkler, A. Abisoye-Ogunniyan, K. J. Metcalf, and Z. Werb. Concepts of extracellular matrix remodelling in tumour progression and metastasis. *Nat Commun*, 11(1):5120, 10 2020.

[96] F. Kai, A. P. Drain, and V. M. Weaver. The Extracellular Matrix Modulates the Metastatic Journey. *Dev Cell*, 49(3):332–346, 05 2019.

[97] T. Stylianopoulos, J. D. Martin, V. P. Chauhan, S. R. Jain, B. Diop-Frimpong, N. Bardeesy, B. L. Smith, C. R. Ferrone, F. J. Hornicek, Y. Boucher, L. L. Munn, and R. K. Jain. Causes, consequences, and remedies for growth-induced solid stress in murine and human tumors. *Proc Natl Acad Sci U S A*, 109(38):15101–15108, Sep 2012.

[98] A. Nicolas-Boluda, J. Vaquero, L. Vimeux, T. Guilbert, S. Barrin, C. Kantari-Mimoun, M. Ponzo, G. Renault, P. Deptula, K. Pogoda, R. Bucki, I. Cascone, J. Courty, L. Fouassier, F. Gazeau, and E. Donnadieu. Tumor stiffening reversion through collagen crosslinking inhibition improves T cell migration and anti-PD-1 treatment. *Elife*, 10, 06 2021.

[99] M. Egeblad, M. G. Rasch, and V. M. Weaver. Dynamic interplay between the collagen scaffold and tumor evolution. *Curr Opin Cell Biol*, 22(5):697–706, Oct 2010.

[100] E. Lundberg and G. H. H. Borner. Spatial proteomics: a powerful discovery tool for cell biology. *Nat Rev Mol Cell Biol*, 20(5):285–302, 05 2019.

[101] A. Rao, D. Barkley, G. S. França, and I. Yanai. Exploring tissue architecture using spatial transcriptomics. *Nature*, 596(7871):211–220, 08 2021.

[102] S. Xie, X. F. Shan, V. Yau, J. Y. Zhang, X. Y. Zhang, Y. P. Yan, and Z. G. Cai. Hyperion imaging system reveals heterogeneous tumor microenvironment of oral squamous cell carcinoma patients at T1N0M0 stage. *Ann Transl Med*, 8(22):1513, Nov 2020.

[103] X. Chen, O. Nadiarynkh, S. Plotnikov, and P. J. Campagnola. Second harmonic generation microscopy for quantitative analysis of collagen fibrillar structure. *Nat Protoc*, 7(4):654–669, Mar 2012.

[104] R. Lattouf, R. Younes, D. Lutomski, N. Naaman, G. Godeau, K. Senni, and S. Changotade. Picrosirius red staining: a useful tool to appraise collagen networks in normal and pathological tissues. *J Histochem Cytochem*, 62(10):751–758, Oct 2014.

[105] M. Plodinec and R. Y. Lim. Nanomechanical characterization of living mammary tissues by atomic force microscopy. *Methods Mol Biol*, 1293:231–246, 2015.

[106] R. G. Barr. The Role of Sonoelastography in Breast Lesions. *Semin Ultrasound CT MR*, 39(1):98–105, Feb 2018.

[107] C. D. Madsen and T. R. Cox. Relative Stiffness Measurements of Tumour Tissues by Shear Rheology. *Bio Protoc*, 7(9):e2265, May 2017.

[108] N. G. Ramião, P. S. Martins, R. Rynkevic, A. A. Fernandes, M. Barroso, and D. C. Santos. Biomechanical properties of breast tissue, a state-of-the-art review. *Biomech Model Mechanobiol*, 15(5):1307–1323, 10 2016.

[109] P. K. Viji Babu and M. Radmacher. Mechanics of Brain Tissues Studied by Atomic Force Microscopy: A Perspective. *Front Neurosci*, 13:600, 2019.

[110] X. Deng, F. Xiong, X. Li, B. Xiang, Z. Li, X. Wu, C. Guo, X. Li, Y. Li, G. Li, W. Xiong, and Z. Zeng. Application of atomic force microscopy in cancer research. *J Nanobiotechnology*, 16(1):102, Dec 2018.

[111] M. Plodinec, M. Loparic, C. A. Monnier, E. C. Obermann, R. Zanetti-Dallenbach, P. Oertle, J. T. Hyotyla, U. Aebi, M. Bentires-Alj, R. Y. Lim, and C. A. Schoenenberger. The nanomechanical signature of breast cancer. *Nat Nanotechnol*, 7(11):757–765, Nov 2012.

[112] B. Du and J. S. Shim. Targeting Epithelial-Mesenchymal Transition (EMT) to Overcome Drug Resistance in Cancer. *Molecules*, 21(7), Jul 2016.

[113] B. N. Smith and N. A. Bhowmick. Role of EMT in Metastasis and Therapy Resistance. *J Clin Med*, 5(2), Jan 2016.

[114] M. Li, N. Xi, Y. C. Wang, and L. Q. Liu. Atomic force microscopy for revealing micro/nanoscale mechanics in tumor metastasis: from single cells to microenvironmental cues. *Acta Pharmacol Sin*, 42(3):323–339, Mar 2021.

[115] A. Stylianou and T. Stylianopoulos. Atomic Force Microscopy Probing of Cancer Cells and Tumor Microenvironment Components. *BioNanoSci*, 6:33–46, 2016.

[116] O. Chaudhuri, L. Gu, D. Klumpers, M. Darnell, S. A. Bencherif, J. C. Weaver, N. Huebsch, H. P. Lee, E. Lippens, G. N. Duda, and D. J. Mooney. Hydrogels with tunable stress relaxation regulate stem cell fate and activity. *Nat Mater*, 15(3):326–334, Mar 2016.

[117] J. I. Lopez, I. Kang, W. K. You, D. M. McDonald, and V. M. Weaver. In situ force mapping of mammary gland transformation. *Integr Biol (Camb)*, 3(9):910–921, Sep 2011.

[118] B. S. Reddy and B. N. Chatterji. An FFT-based technique for translation, rotation, and scale-invariant image registration. *IEEE Trans Image Process*, 5(8):1266–1271, 1996.

[119] E. T. Goddard, R. C. Hill, A. Barrett, C. Betts, Q. Guo, O. Maller, V. F. Borges, K. C. Hansen, and P. Schedin. Quantitative extracellular matrix proteomics to study mammary and liver tissue microenvironments. *Int J Biochem Cell Biol*, 81(Pt A):223–232, 12 2016.

[120] P. M. Angel, K. Schwamborn, S. Comte-Walters, C. L. Clift, L. E. Ball, A. S. Mehta, and R. R. Drake. Extracellular Matrix Imaging of Breast Tissue Pathologies by MALDI-Imaging Mass Spectrometry. *Proteomics Clin Appl*, 13(1):e1700152, 01 2019.

[121] B. R. Seo, X. Chen, L. Ling, Y. H. Song, A. A. Shimpi, S. Choi, J. Gonzalez, J. Sapudom, K. Wang, R. C. Andresen Eguiluz, D. Gourdon, V. B. Shenoy, and C. Fischbach. Collagen microarchitecture mechanically controls myofibroblast differentiation. *Proc Natl Acad Sci U S A*, 117(21):11387–11398, 05 2020.

[122] F. Bestvater, E. Spiess, G. Stobrawa, M. Hacker, T. Feurer, T. Porwol, U. Berchner-Pfannschmidt, C. Wotzlaw, and H. Acker. Two-photon fluorescence absorption and emission spectra of dyes relevant for cell imaging. *J Microsc*, 208(Pt 2):108–115, Nov 2002.

[123] A. Chopra, L. Shan, W. C. Eckelman, K. Leung, M. Latterner, S. H. Bryant, and A. Menkens. Molecular Imaging and Contrast Agent Database (MICAD): evolution and progress. *Mol Imaging Biol*, 14(1):4–13, Feb 2012.

[124] K. N. Krahn, C. V. Bouten, S. van Tuijl, M. A. van Zandvoort, and M. Merkx. Fluorescently labeled collagen binding proteins allow specific visualization of collagen in tissues and live cell culture. *Anal Biochem*, 350(2):177–185, Mar 2006.

[125] Y. Zong, Y. Xu, X. Liang, D. R. Keene, A. Höök, S. Gurusiddappa, M. Höök, and S. V. Narayana. A 'Collagen Hug' model for Staphylococcus aureus CNA binding to collagen. *EMBO J*, 24(24):4224–4236, Dec 2005.

[126] S. J. Aper, A. C. van Spreeuwel, M. C. van Turnhout, A. J. van der Linden, P. A. Pieters, N. L. van der Zon, S. L. de la Rambelje, C. V. Bouten, and M. Merkx. Colorful protein-based fluorescent probes for collagen imaging. *PLoS One*, 9(12):e114983, 2014.

[127] W. Rawat and Z. Wang. Deep Convolutional Neural Networks for Image Classification: A Comprehensive Review. *Neural Comput*, 29(9):2352–2449, 09 2017.

[128] Utku Ozbulak. Pytorch cnn visualizations. https://github.com/utkuozbulak/pytorch-cnn-visualizations, 2019.

[129] Ramprasaath R. Selvaraju, Michael Cogswell, Abhishek Das, Ramakrishna Vedantam, Devi Parikh, and Dhruv Batra. Grad-cam: Visual explanations from deep networks via gradient-based localization. In *2017 IEEE International Conference on Computer Vision (ICCV)*, pages 618–626, 2017.

[130] Haofan Wang, Zifan Wang, Mengnan Du, Fan Yang, Zijian Zhang, Sirui Ding, Piotr Mardziel, and Xia Hu. Score-cam: Score-weighted visual explanations for convolutional neural networks, 2020.

[131] Jost Tobias Springenberg, Alexey Dosovitskiy, Thomas Brox, and Martin Riedmiller. Striving for simplicity: The all convolutional net, 2015.

[132] M. J. Paszek, N. Zahir, K. R. Johnson, J. N. Lakins, G. I. Rozenberg, A. Gefen, C. A. Reinhart-King, S. S. Margulies, M. Dembo, D. Boettiger, D. A. Hammer, and V. M. Weaver. Tensional homeostasis and the malignant phenotype. *Cancer Cell*, 8(3):241–254, Sep 2005.

[133] M. G. Rubashkin, L. Cassereau, R. Bainer, C. C. DuFort, Y. Yui, G. Ou, M. J. Paszek, M. W. Davidson, Y. Y. Chen, and V. M. Weaver. Force engages vinculin and promotes tumor progression by enhancing PI3K activation of phosphatidylinositol (3,4,5)-triphosphate. *Cancer Res*, 74(17):4597–4611, Sep 2014.

[134] K. V. Nguyen-Ngoc, K. J. Cheung, A. Brenot, E. R. Shamir, R. S. Gray, W. C. Hines, P. Yaswen, Z. Werb, and A. J. Ewald. ECM microenvironment regulates collective migration and local dissemination in normal and malignant mammary epithelium. *Proc Natl Acad Sci U S A*, 109(39):E2595–2604, Sep 2012.

[135] R. S. Stowers, A. Shcherbina, J. Israeli, J. J. Gruber, J. Chang, S. Nam, A. Rabiee, M. N. Teruel, M. P. Snyder, A. Kundaje, and O. Chaudhuri. Matrix stiffness induces a tumorigenic phenotype in mammary epithelium through changes in chromatin accessibility. *Nat Biomed Eng*, 3(12):1009–1019, 12 2019.

[136] J. K. Mouw, Y. Yui, L. Damiano, R. O. Bainer, J. N. Lakins, I. Acerbi, G. Ou, A. C. Wijekoon, K. R. Levental, P. M. Gilbert, E. S. Hwang, Y. Y. Chen, and V. M. Weaver. Tissue mechanics modulate microRNA-dependent PTEN expression to regulate malignant progression. *Nat Med*, 20(4):360–367, Apr 2014.

[137] Y. S. DeRose, K. M. Gligorich, G. Wang, A. Georgelas, P. Bowman, S. J. Courdy, A. L. Welm, and B. E. Welm. Patient-derived models of human breast cancer: protocols for in vitro and in vivo applications in tumor biology and translational medicine. *Curr Protoc Pharmacol*, Chapter 14:Unit14.23, Mar 2013.

[138] X. Zhang, S. Claerhout, A. Prat, L. E. Dobrolecki, I. Petrovic, Q. Lai, M. D. Landis, L. Wiechmann, R. Schiff, M. Giuliano, H. Wong, S. W. Fuqua, A. Contreras, C. Gutierrez, J. Huang, S. Mao, A. C. Pavlick, A. M. Froehlich, M. F. Wu, A. Tsimelzon, S. G. Hilsenbeck, E. S. Chen, P. Zuloaga, C. A. Shaw, M. F. Rimawi, C. M. Perou, G. B. Mills, J. C. Chang, and M. T. Lewis. A renewable tissue resource of phenotypically stable, biologically and ethnically diverse, patient-derived human breast cancer xenograft models. *Cancer Res*, 73(15):4885–4897, Aug 2013.

[139] C. Wels, S. Joshi, P. Koefinger, H. Bergler, and H. Schaider. Transcriptional activation of ZEB1 by Slug leads to cooperative regulation of the epithelial-mesenchymal transition-like phenotype in melanoma. *J Invest Dermatol*, 131(9):1877–1885, Sep 2011.

[140] T. M. Kiio and S. Park. Nano-scientific Application of Atomic Force Microscopy in Pathology: from Molecules to Tissues. *Int J Med Sci*, 17(7):844–858, 2020.

[141] J. M. Barnes, S. Kaushik, R. O. Bainer, J. K. Sa, E. C. Woods, F. Kai, L. Przybyla, M. Lee, H. W. Lee, J. C. Tung, O. Maller, A. S. Barrett, K. V. Lu, J. N. Lakins, K. C. Hansen, K. Obernier, A. Alvarez-Buylla, G. Bergers, J. J. Phillips, D. H. Nam, C. R. Bertozzi, and V. M. Weaver. A tension-mediated glycocalyx-integrin feedback loop promotes mesenchymal-like glioblastoma. *Nat Cell Biol*, 20(10):1203–1214, 10 2018.

[142] H. Y. Chang, C. K. Jung, J. I. Woo, S. Lee, J. Cho, S. W. Kim, and T. Y. Kwak. Artificial Intelligence in Pathology. *J Pathol Transl Med*, 53(1):1–12, Jan 2019.

[143] M. K. K. Niazi, A. V. Parwani, and M. N. Gurcan. Digital pathology and artificial intelligence. *Lancet Oncol*, 20(5):e253–e261, 05 2019.

[144] M. Cui and D. Y. Zhang. Artificial intelligence and computational pathology. *Lab Invest*, 101(4):412–422, 04 2021.

[145] A. Saito, H. Toyoda, M. Kobayashi, Y. Koiwa, H. Fujii, K. Fujita, A. Maeda, Y. Kaneoka, S. Hazama, H. Nagano, A. H. Mirza, H. P. Graf, E. Cosatto, Y. Murakami, and M. Kuroda. Prediction of early recurrence of hepatocellular carcinoma after resection using digital pathology images assessed by machine learning. *Mod Pathol*, 34(2):417–425, 02 2021.

[146] D. Komura and S. Ishikawa. Machine Learning Methods for Histopathological Image Analysis. *Comput Struct Biotechnol J*, 16:34–42, 2018.

[147] J. van der Laak, G. Litjens, and F. Ciompi. Deep learning in histopathology: the path to the clinic. *Nat Med*, 27(5):775–784, 05 2021.

[148] M. Cohen, M. Elkabets, M. Perlmutter, A. Porgador, E. Voronov, R. N. Apte, and R. G. Lichtenstein. Sialylation of 3-methylcholanthrene-induced fibrosarcoma determines antitumor immune responses during immunoediting. *J Immunol*, 185(10):5869–5878, Nov 2010.

[149] J. M. Tarbell and L. M. Cancel. The glycocalyx and its significance in human medicine. *J Intern Med*, 280(1):97–113, 07 2016.

[150] M. J. Paszek, C. C. DuFort, O. Rossier, R. Bainer, J. K. Mouw, K. Godula, J. E. Hudak, J. N. Lakins, A. C. Wijekoon, L. Cassereau, M. G. Rubashkin, M. J. Magbanua, K. S. Thorn, M. W. Davidson, H. S. Rugo, J. W. Park, D. A. Hammer, G. Giannone, C. R. Bertozzi, and V. M. Weaver. The cancer glycocalyx mechanically primes integrin-mediated growth and survival. *Nature*, 511(7509):319–325, Jul 2014.

[151] E. C. Woods, F. Kai, J. M. Barnes, K. Pedram, M. W. Pickup, M. J. Hollander, V. M. Weaver, and C. R. Bertozzi. A bulky glycocalyx fosters metastasis formation by promoting G1 cell cycle progression. *Elife*, 6, 12 2017.

[152] P. R. C. Imbert, A. Saric, K. Pedram, C. R. Bertozzi, S. Grinstein, and S. A. Freeman. An Acquired and Endogenous Glycocalyx Forms a Bidirectional "Don't Eat" and "Don't Eat Me" Barrier to Phagocytosis. *Curr Biol*, 31(1):77–89, 01 2021.

[153] J. Munkley and D. J. Elliott. Hallmarks of glycosylation in cancer. *Oncotarget*, 7(23):35478–35489, Jun 2016.

[154] C. Jandus, K. F. Boligan, O. Chijioke, H. Liu, M. Dahlhaus, T. Démoulins, C. Schneider, M. Wehrli, R. E. Hunger, G. M. Baerlocher, H. U. Simon, P. Romero, C. Münz, and S. von Gunten. Interactions between Siglec-7/9 receptors and ligands influence NK cell-dependent tumor immunosurveillance. *J Clin Invest*, 124(4):1810–1820, Apr 2014.

[155] M. A. Stanczak, S. S. Siddiqui, M. P. Trefny, D. S. Thommen, K. F. Boligan, S. von Gunten, A. Tzankov, L. Tietze, D. Lardinois, V. Heinzelmann-Schwarz, M. von Bergwelt-Baildon, W. Zhang, H. J. Lenz, Y. Han, C. I. Amos, M. Syedbasha, A. Egli, F. Stenner, D. E. Speiser, A. Varki, A. Zippelius, and H. Läubli. Self-associated molecular patterns mediate cancer immune evasion by engaging Siglecs on T cells. *J Clin Invest*, 128(11):4912–4923, 11 2018.

[156] J. E. Hudak, S. M. Canham, and C. R. Bertozzi. Glycocalyx engineering reveals a Siglec-based mechanism for NK cell immunoevasion. *Nat Chem Biol*, 10(1):69–75, Jan 2014.

[157] I. Ibarlucea-Benitez, P. Weitzenfeld, P. Smith, and J. V. Ravetch. Siglecs-7/9 function as inhibitory immune checkpoints in vivo and can be targeted to enhance therapeutic antitumor immunity. *Proc Natl Acad Sci U S A*, 118(26), 06 2021.

[158] H. Läubli, O. M. Pearce, F. Schwarz, S. S. Siddiqui, L. Deng, M. A. Stanczak, L. Deng, A. Verhagen, P. Secrest, C. Lusk, A. G. Schwartz, N. M. Varki, J. D. Bui, and A. Varki. Engagement of myelomonocytic Siglecs by tumor-associated ligands modulates the innate immune response to cancer. *Proc Natl Acad Sci U S A*, 111(39):14211–14216, Sep 2014.

[159] A. A. Barkal, R. E. Brewer, M. Markovic, M. Kowarsky, S. A. Barkal, B. W. Zaro, V. Krishnan, J. Hatakeyama, O. Dorigo, L. J. Barkal, and I. L. Weissman. CD24 signalling through macrophage Siglec-10 is a target for cancer immunotherapy. *Nature*, 572(7769):392–396, 08 2019.

[160] J. Wang, J. Sun, L. N. Liu, D. B. Flies, X. Nie, M. Toki, J. Zhang, C. Song, M. Zarr, X. Zhou, X. Han, K. A. Archer, T. O'Neill, R. S. Herbst, A. N. Boto, M. F. Sanmamed, S. Langermann, D. L. Rimm, and L. Chen. Siglec-15 as an immune suppressor and potential target for normalization cancer immunotherapy. *Nat Med*, 25(4):656–666, 04 2019.

[161] E. Rodriguez, K. Boelaars, K. Brown, R. J. Eveline Li, L. Kruijssen, S. C. M. Bruijns, T. van Ee, S. T. T. Schetters, M. H. W. Crommentuijn, J. C. van der Horst, N. C. T. van Grieken, S. J. van Vliet, G. Kazemier, E. Giovannetti, J. J. Garcia-Vallejo, and Y. van Kooyk. Sialic acids in pancreatic cancer cells drive tumour-associated macrophage differentiation via the Siglec receptors Siglec-7 and Siglec-9. *Nat Commun*, 12(1):1270, 02 2021.

[162] O. J. Adams, M. A. Stanczak, S. von Gunten, and H. Läubli. Targeting sialic acid-Siglec interactions to reverse immune suppression in cancer. *Glycobiology*, 28(9):640–647, 09 2018.

[163] B. Piersma, M. K. Hayward, and V. M. Weaver. Fibrosis and cancer: A strained relationship. *Biochim Biophys Acta Rev Cancer*, 1873(2):188356, 04 2020.

[164] T. M. J. Evers, L. J. Holt, S. Alberti, and A. Mashaghi. Publisher Correction: Reciprocal regulation of cellular mechanics and metabolism. *Nat Metab*, 3(6):876–877, Jun 2021.

[165] B. Pal, Y. Chen, F. Vaillant, B. D. Capaldo, R. Joyce, X. Song, V. L. Bryant, J. S. Penington, L. Di Stefano, N. Tubau Ribera, S. Wilcox, G. B. Mann, A. T. Papenfuss, G. J. Lindeman, G. K. Smyth, and J. E. Visvader. A single-cell RNA expression atlas of normal, preneoplastic and tumorigenic states in the human breast. *EMBO J*, 40(11):e107333, 06 2021.

[166] Q. H. Nguyen, N. Pervolarakis, K. Blake, D. Ma, R. T. Davis, N. James, A. T. Phung, E. Willey, R. Kumar, E. Jabart, I. Driver, J. Rock, A. Goga, S. A. Khan, D. A. Lawson, Z. Werb, and K. Kessenbrock. Profiling human breast epithelial cells using single cell RNA sequencing identifies cell diversity. *Nat Commun*, 9(1):2028, 05 2018.

[167] A. Haque, J. Engel, S. A. Teichmann, and T. Lönnberg. A practical guide to single-cell RNA-sequencing for biomedical research and clinical applications. *Genome Med*, 9(1):75, 08 2017.

[168] S. S. Pinho and C. A. Reis. Glycosylation in cancer: mechanisms and clinical implications. *Nat Rev Cancer*, 15(9):540–555, Sep 2015.

[169] A. J. Combes, B. Samad, J. Tsui, N. W. Chew, P. Yan, G. C. Reeder, D. Kushnoor, A. Shen, B. Davidson, A. J. Barczak, M. Adkisson, A. Edwards, M. Naser, K. C. Barry, T. Courau, T. Hammoudi, R. J. Argüello, A. A. Rao, A. B. Olshen, C. Cai, J. Zhan, K. C. Davis, R. K. Kelley, J. S. Chapman, C. E. Atreya, A. Patel, A. I. Daud, P. Ha, A. A. Diaz, J. R. Kratz, E. A. Collisson, G. K. Fragiadakis, D. J. Erle, A. Boissonnas, S. Asthana, V. Chan, M. F. Krummel, M. Spitzer, L. Fong, A. Nelson, R. Kumar, J. Lee, A. Burra, J. Hsu, C. Hackett, K. Tolentino, J. Sjarif, P. Johnson, E. Shao, D. Abrau, L. Lupin, C. Shaw, Z. Collins, T. Lea, C. Corvera, E. Nakakura, J. Carnevale, M. Alvarado, K. Loo, L. Chen, M. Chow,

J. Grandis, W. Ryan, I. El-Sayed, D. Jablons, G. Woodard, M. W. Meng, S. P. Porten, H. Okada, M. Tempero, A. Ko, K. Kirkwood, S. Vandenberg, D. Guevarra, E. Oropeza, C. Cyr, P. Glenn, J. Bolen, A. Morton, and W. Eckalbar. Discovering dominant tumor immune archetypes in a pan-cancer census. *Cell*, 185(1):184–203, 01 2022.

[170] M. S. Macauley, P. R. Crocker, and J. C. Paulson. Siglec-mediated regulation of immune cell function in disease. *Nat Rev Immunol*, 14(10):653–666, Oct 2014.

[171] R. Beatson, V. Tajadura-Ortega, D. Achkova, G. Picco, T. D. Tsourouktsoglou, S. Klausing, M. Hillier, J. Maher, T. Noll, P. R. Crocker, J. Taylor-Papadimitriou, and J. M. Burchell. The mucin MUC1 modulates the tumor immunological microenvironment through engagement of the lectin Siglec-9. *Nat Immunol*, 17(11):1273–1281, Nov 2016.

[172] B. A. H. Smith and C. R. Bertozzi. The clinical impact of glycobiology: targeting selectins, Siglecs and mammalian glycans. *Nat Rev Drug Discov*, 20(3):217–243, 03 2021.

[173] L. Cassetta and J. W. Pollard. Tumor-associated macrophages. *Curr Biol*, 30(6):R246–R248, 03 2020.

[174] H. Gonzalez, C. Hagerling, and Z. Werb. Roles of the immune system in cancer: from tumor initiation to metastatic progression. *Genes Dev*, 32(19-20):1267–1284, 10 2018.

[175] S. Wisnovsky, L. Möckl, S. A. Malaker, K. Pedram, G. T. Hess, N. M. Riley, M. A. Gray, B. A. H. Smith, M. C. Bassik, W. E. Moerner, and C. R. Bertozzi. Genome-wide CRISPR screens reveal a specific ligand for the glycan-binding immune checkpoint receptor Siglec-7. *Proc Natl Acad Sci U S A*, 118(5), 02 2021.

[176] M. S. Alphey, H. Attrill, P. R. Crocker, and D. M. van Aalten. High resolution crystal structures of Siglec-7. Insights into ligand specificity in the Siglec family. *J Biol Chem*, 278(5):3372–3377, Jan 2003.

[177] S. Ohno, Y. Ohno, H. Nakada, N. Suzuki, G. Soma, and M. Inoue. Expression of Tn and sialyl-Tn antigens in endometrial cancer: its relationship with tumor-produced cyclooxygenase-2, tumor-infiltrated lymphocytes and patient prognosis. *Anticancer Res*, 26(6A):4047–4053, 2006.

[178] M. A. Gray, M. A. Stanczak, N. R. Mantuano, H. Xiao, J. F. A. Pijnenborg, S. A. Malaker, C. L. Miller, P. A. Weidenbacher, J. T. Tanzo, G. Ahn, E. C. Woods, H. Läubli, and C. R. Bertozzi. Targeted glycan degradation potentiates the anticancer immune response in vivo. *Nat Chem Biol*, 16(12):1376–1384, 12 2020.

[179] V. M. Weaver, S. Lelièvre, J. N. Lakins, M. A. Chrenek, J. C. Jones, F. Giancotti, Z. Werb, and M. J. Bissell. beta4 integrin-dependent formation of polarized three-dimensional architecture confers resistance to apoptosis in normal and malignant mammary epithelium. *Cancer Cell*, 2(3):205–216, Sep 2002.

[180] J. Roignot, X. Peng, and K. Mostov. Polarity in mammalian epithelial morphogenesis. *Cold Spring Harb Perspect Biol*, 5(2), Feb 2013.

[181] K. Han, S. E. Pierce, A. Li, K. Spees, G. R. Anderson, J. A. Seoane, Y. H. Lo, M. Dubreuil, M. Olivas, R. A. Kamber, M. Wainberg, K. Kostyrko, M. R. Kelly, M. Yousefi, S. W. Simpkins, D. Yao, K. Lee, C. J. Kuo, P. K. Jackson, A. Sweet-Cordero, A. Kundaje, A. J. Gentles, C. Curtis, M. M. Winslow, and M. C. Bassik. CRISPR screens in cancer spheroids identify 3D growth-specific vulnerabilities. *Nature*, 580(7801):136–141, 04 2020.

[182] L. H. Chen and M. J. Bissell. A novel regulatory mechanism for whey acidic protein gene expression. *Cell Regul*, 1(1):45–54, Nov 1989.

[183] C. H. Streuli, N. Bailey, and M. J. Bissell. Control of mammary epithelial differentiation: basement membrane induces tissue-specific gene expression in the absence of cell-cell interaction and morphological polarity. *J Cell Biol*, 115(5):1383–1395, Dec 1991.

[184] C. D. Roskelley, P. Y. Desprez, and M. J. Bissell. Extracellular matrix-dependent tissue-specific gene expression in mammary epithelial cells requires both physical and biochemical signal transduction. *Proc Natl Acad Sci U S A*, 91(26):12378–12382, Dec 1994.

[185] J. Krebs, L. B. Agellon, and M. Michalak. Ca(2+) homeostasis and endoplasmic reticulum (ER) stress: An integrated view of calcium signaling. *Biochem Biophys Res Commun*, 460(1):114–121, Apr 2015.

[186] R. S. Lewis. Store-operated calcium channels: new perspectives on mechanism and function. *Cold Spring Harb Perspect Biol*, 3(12), Dec 2011.

[187] O. W. Petersen, L. Rønnov-Jessen, A. R. Howlett, and M. J. Bissell. Interaction with basement membrane serves to rapidly distinguish growth and differentiation pattern of normal and malignant human breast epithelial cells. *Proc Natl Acad Sci U S A*, 89(19):9064–9068, Oct 1992.

[188] V. M. Weaver, O. W. Petersen, F. Wang, C. A. Larabell, P. Briand, C. Damsky, and M. J. Bissell. Reversion of the malignant phenotype of human breast cells in three-dimensional culture and in vivo by integrin blocking antibodies. *J Cell Biol*, 137(1):231–245, Apr 1997.

[189] M. H. Barcellos-Hoff, J. Aggeler, T. G. Ram, and M. J. Bissell. Functional differentiation and alveolar morphogenesis of primary mammary cultures on reconstituted basement membrane. *Development*, 105(2):223–235, Feb 1989.

[190] A. Yamaguchi, O. Hori, D. M. Stern, E. Hartmann, S. Ogawa, and M. Tohyama. Stress-associated endoplasmic reticulum protein 1 (SERP1)/Ribosome-associated membrane protein 4 (RAMP4) stabilizes membrane proteins during stress and facilitates subsequent glycosylation. *J Cell Biol*, 147(6):1195–1204, Dec 1999.

[191] S. Z. Jia, X. W. Xu, Z. H. Zhang, C. Chen, Y. B. Chen, S. L. Huang, Q. Liu, P. R. Hoffmann, and G. L. Song. Selenoprotein K deficiency-induced apoptosis: A role for calpain and the ERS pathway. *Redox Biol*, 47:102154, 11 2021.

[192] D. Ito, J. R. Walker, C. S. Thompson, I. Moroz, W. Lin, M. L. Veselits, A. M. Hakim, A. A. Fienberg, and G. Thinakaran. Characterization of stanniocalcin 2, a novel target of the mammalian unfolded protein response with cytoprotective properties. *Mol Cell Biol*, 24(21):9456–9469, Nov 2004.

[193] S. Srikanth, H. J. Jung, K. D. Kim, P. Souda, J. Whitelegge, and Y. Gwack. A novel EF-hand protein, CRACR2A, is a cytosolic Ca2+ sensor that stabilizes CRAC channels in T cells. *Nat Cell Biol*, 12(5):436–446, May 2010.

[194] A. Read and M. Schröder. The Unfolded Protein Response: An Overview. *Biology (Basel)*, 10(5), Apr 2021.

[195] S. Preissler, C. Rato, Y. Yan, L. A. Perera, A. Czako, and D. Ron. Calcium depletion challenges endoplasmic reticulum proteostasis by destabilising BiP-substrate complexes. *Elife*, 9, 12 2020.

[196] C. L. Chang, Y. J. Chen, and J. Liou. ER-plasma membrane junctions: Why and how do we study them? *Biochim Biophys Acta Mol Cell Res*, 1864(9):1494–1506, Sep 2017.

[197] A. R. van Vliet, F. Giordano, S. Gerlo, I. Segura, S. Van Eygen, G. Molenberghs, S. Rocha, A. Houcine, R. Derua, T. Verfaillie, J. Vangindertael, H. De Keersmaecker, E. Waelkens, J. Tavernier, J. Hofkens, W. Annaert, P. Carmeliet, A. Samali, H. Mizuno, and P. Agostinis. The ER Stress Sensor PERK Coordinates ER-Plasma Membrane Contact Site Formation through Interaction with Filamin-A and F-Actin Remodeling. *Mol Cell*, 65(5):885–899, Mar 2017.

[198] Z. Razinia, T. Mäkelä, J. Ylänne, and D. A. Calderwood. Filamins in mechanosensing and signaling. *Annu Rev Biophys*, 41:227–246, 2012.

[199] M. Guo, A. F. Pegoraro, A. Mao, E. H. Zhou, P. R. Arany, Y. Han, D. T. Burnette, M. H. Jensen, K. E. Kasza, J. R. Moore, F. C. Mackintosh, J. J. Fredberg, D. J. Mooney,

J. Lippincott-Schwartz, and D. A. Weitz. Cell volume change through water efflux impacts cell stiffness and stem cell fate. *Proc Natl Acad Sci U S A*, 114(41):E8618–E8627, 10 2017.

[200] Y. L. Han, A. F. Pegoraro, H. Li, K. Li, Y. Yuan, G. Xu, Z. Gu, J. Sun, Y. Hao, S. K. Gupta, Y. Li, W. Tang, X. Tang, L. Teng, J. J. Fredberg, and M. Guo. Cell swelling, softening and invasion in a three-dimensional breast cancer model. *Nat Phys*, 16(1):101–108, Jan 2020.

[201] J. Y. Tinevez, U. Schulze, G. Salbreux, J. Roensch, J. F. Joanny, and E. Paluch. Role of cortical tension in bleb growth. *Proc Natl Acad Sci U S A*, 106(44):18581–18586, Nov 2009.

[202] M. Kitamura and N. Hiramatsu. Real-time monitoring of ER stress in living cells and animals using ESTRAP assay. *Methods Enzymol*, 490:93–106, 2011.

[203] A. Bisaria, A. Hayer, D. Garbett, D. Cohen, and T. Meyer. Membrane-proximal F-actin restricts local membrane protrusions and directs cell migration. *Science*, 368(6496):1205–1210, 06 2020.

[204] I. K. Jarsch, F. Daste, and J. L. Gallop. Membrane curvature in cell biology: An integration of molecular mechanisms. *J Cell Biol*, 214(4):375–387, 08 2016.

[205] N. Ramakrishnan, P. B. Sunil Kumar, and R. Radhakrishnan. Mesoscale computational studies of membrane bilayer remodeling by curvature-inducing proteins. *Phys Rep*, 543(1):1–60, Oct 2014.

[206] R. W. Tourdot, R. P. Bradley, N. Ramakrishnan, and R. Radhakrishnan. Multiscale computational models in physical systems biology of intracellular trafficking. *IET Syst Biol*, 8(5):198–213, Oct 2014.

[207] R. W. Tourdot, N. Ramakrishnan, and R. Radhakrishnan. Defining the free-energy landscape of curvature-inducing proteins on membrane bilayers. *Phys Rev E Stat Nonlin Soft Matter Phys*, 90(2):022717, Aug 2014.

[208] N. Volkmann, D. DeRosier, P. Matsudaira, and D. Hanein. An atomic model of actin filaments cross-linked by fimbrin and its implications for bundle assembly and function. *J Cell Biol*, 153(5):947–956, May 2001.

[209] K. L. Anderson, C. Page, M. F. Swift, P. Suraneni, M. E. W. Janssen, T. D. Pollard, R. Li, N. Volkmann, and D. Hanein. Nano-scale actin-network characterization of fibroblast cells lacking functional Arp2/3 complex. *J Struct Biol*, 197(3):312–321, 03 2017.

[210] H. T. McMahon and E. Boucrot. Membrane curvature at a glance. *J Cell Sci*, 128(6):1065–1070, Mar 2015.

[211] N. Ramakrishnan, K. K. Sreeja, A. Roychoudhury, D. M. Eckmann, P. S. Ayyaswamy, T. Baumgart, T. Pucadyil, S. Patil, V. M. Weaver, and R. Radhakrishnan. Excess area dependent scaling behavior of nano-sized membrane tethers. *Phys Biol*, 15(2):026002, 01 2018.

[212] Y. Zhao, J. Liu, C. Yang, B. R. Capraro, T. Baumgart, R. P. Bradley, N. Ramakrishnan, X. Xu, R. Radhakrishnan, T. Svitkina, and W. Guo. Exo70 generates membrane curvature for morphogenesis and cell migration. *Dev Cell*, 26(3):266–278, Aug 2013.

[213] E. Umbrecht-Jenck, V. Demais, V. Calco, Y. Bailly, M. F. Bader, and S. Chasserot-Golaz. S100A10-mediated translocation of annexin-A2 to SNARE proteins in adrenergic chromaffin cells undergoing exocytosis. *Traffic*, 11(7):958–971, Jul 2010.

[214] T. L. Boye, J. C. Jeppesen, K. Maeda, W. Pezeshkian, V. Solovyeva, J. Nylandsted, and A. C. Simonsen. Annexins induce curvature on free-edge membranes displaying distinct morphologies. *Sci Rep*, 8(1):10309, 07 2018.

[215] P. Walter and D. Ron. The unfolded protein response: from stress pathway to homeostatic regulation. *Science*, 334(6059):1081–1086, Nov 2011.

[216] H. Xu, Y. Jiao, S. Qin, W. Zhao, Q. Chu, and K. Wu. Organoid technology in disease modelling, drug development, personalized treatment and regeneration medicine. *Exp Hematol Oncol*, 7:30, 2018.

[217] A. Papadopulos, V. M. Tomatis, R. Kasula, and F. A. Meunier. The cortical acto-Myosin network: from diffusion barrier to functional gateway in the transport of neurosecretory vesicles to the plasma membrane. *Front Endocrinol (Lausanne)*, 4:153, Oct 2013.

[218] T. Lang, I. Wacker, I. Wunderlich, A. Rohrbach, G. Giese, T. Soldati, and W. Almers. Role of actin cortex in the subplasmalemmal transport of secretory granules in PC-12 cells. *Biophys J*, 78(6):2863–2877, Jun 2000.

[219] Y. Zhu, B. Wu, and W. Guo. The role of Exo70 in exocytosis and beyond. *Small GTPases*, 10(5):331–335, 09 2019.

[220] T. J. Kim, C. Joo, J. Seong, R. Vafabakhsh, E. L. Botvinick, M. W. Berns, A. E. Palmer, N. Wang, T. Ha, E. Jakobsson, J. Sun, and Y. Wang. Distinct mechanisms regulating mechanical force-induced Ca^{2+} signals at the plasma membrane and the ER in human MSCs. *Elife*, 4:e04876, Feb 2015.

[221] N. S. Lee, C. W. Yoon, Q. Wang, S. Moon, K. M. Koo, H. Jung, R. Chen, L. Jiang, G. Lu, A. Fernandez, R. H. Chow, A. C. Weitz, P. M. Salvaterra, F. Pinaud, and K. K. Shung. Focused Ultrasound Stimulates ER Localized Mechanosensitive PANNEXIN-1 to Mediate Intracellular Calcium Release in Invasive Cancer Cells. *Front Cell Dev Biol*, 8:504, 2020.

[222] M. M. Nava, Y. A. Miroshnikova, L. C. Biggs, D. B. Whitefield, F. Metge, J. Boucas, H. Vihinen, E. Jokitalo, X. Li, J. M. García Arcos, B. Hoffmann, R. Merkel, C. M. Niessen, K. N. Dahl, and S. A. Wickström. Heterochromatin-Driven Nuclear Softening Protects the Genome against Mechanical Stress-Induced Damage. *Cell*, 181(4):800–817, 05 2020.

[223] J. L. Maiers and H. Malhi. Endoplasmic Reticulum Stress in Metabolic Liver Diseases and Hepatic Fibrosis. *Semin Liver Dis*, 39(2):235–248, May 2019.

[224] S. J. Sequeira, A. C. Ranganathan, A. P. Adam, B. V. Iglesias, E. F. Farias, and J. A. Aguirre-Ghiso. Inhibition of proliferation by PERK regulates mammary acinar morphogenesis and tumor formation. *PLoS One*, 2(7):e615, Jul 2007.

[225] R. S. Balaban, S. Nemoto, and T. Finkel. Mitochondria, oxidants, and aging. *Cell*, 120(4):483–495, Feb 2005.

[226] Colleen R. Reczek and Navdeep S. Chandel. The two faces of reactive oxygen species in cancer. *Annual Review of Cancer Biology*, 1(1):79–98, 2017.

[227] F. Scialò, A. Sriram, D. Fernández-Ayala, N. Gubina, M. Lõhmus, G. Nelson, A. Logan, H. M. Cooper, P. Navas, J. A. Enríquez, M. P. Murphy, and A. Sanz. Mitochondrial ROS Produced via Reverse Electron Transport Extend Animal Lifespan. *Cell Metab*, 23(4):725–734, Apr 2016.

[228] D. C. Wallace. Mitochondria and cancer. *Nat Rev Cancer*, 12(10):685–698, Oct 2012.

[229] M. Fane and A. T. Weeraratna. How the ageing microenvironment influences tumour progression. *Nat Rev Cancer*, 20(2):89–106, 02 2020.

[230] W. Ladiges, J. Wanagat, B. Preston, L. Loeb, and P. Rabinovitch. A mitochondrial view of aging, reactive oxygen species and metastatic cancer. *Aging Cell*, 9(4):462–465, Aug 2010.

[231] N. Sun, R. J. Youle, and T. Finkel. The Mitochondrial Basis of Aging. *Mol Cell*, 61(5):654–666, Mar 2016.

[232] S. Vyas, E. Zaganjor, and M. C. Haigis. Mitochondria and Cancer. *Cell*, 166(3):555–566, Jul 2016.

[233] Y. A. Miroshnikova, J. K. Mouw, J. M. Barnes, M. W. Pickup, J. N. Lakins, Y. Kim, K. Lobo, A. I. Persson, G. F. Reis, T. R. McKnight, E. C. Holland, J. J. Phillips, and V. M. Weaver. Tissue mechanics promote IDH1-dependent HIF1α-tenascin C feedback to regulate glioblastoma aggression. *Nat Cell Biol*, 18(12):1336–1345, Dec 2016.

[234] J. M. Northcott, I. S. Dean, J. K. Mouw, and V. M. Weaver. Feeling Stress: The Mechanics of Cancer Progression and Aggression. *Front Cell Dev Biol*, 6:17, 2018.

[235] M. J. Oudin and V. M. Weaver. Physical and Chemical Gradients in the Tumor Microenvironment Regulate Tumor Cell Invasion, Migration, and Metastasis. *Cold Spring Harb Symp Quant Biol*, 81:189–205, 2016.

[236] V. Papalazarou, T. Zhang, N. R. Paul, A. Juin, M. Cantini, O. D. K. Maddocks, M. Salmeron-Sanchez, and L. M. Machesky. The creatine-phosphagen system is mechanoresponsive in pancreatic adenocarcinoma and fuels invasion and metastasis. *Nat Metab*, 2(1):62–80, 01 2020.

[237] J. S. Park, C. J. Burckhardt, R. Lazcano, L. M. Solis, T. Isogai, L. Li, C. S. Chen, B. Gao, J. D. Minna, R. Bachoo, R. J. DeBerardinis, and G. Danuser. Mechanical regulation of glycolysis via cytoskeleton architecture. *Nature*, 578(7796):621–626, 02 2020.

[238] V. Anesti and L. Scorrano. The relationship between mitochondrial shape and function and the cytoskeleton. *Biochim Biophys Acta*, 1757(5-6):692–699, 2006.

[239] P. Schedin and P. J. Keely. Mammary gland ECM remodeling, stiffness, and mechanosignaling in normal development and tumor progression. *Cold Spring Harb Perspect Biol*, 3(1):a003228, Jan 2011.

[240] S. C. J. Helle, Q. Feng, M. J. Aebersold, L. Hirt, R. R. Grüter, A. Vahid, A. Sirianni, S. Mostowy, J. G. Snedeker, A. Šarić, T. Idema, T. Zambelli, and B. Kornmann. Mechanical force induces mitochondrial fission. *Elife*, 6, 11 2017.

[241] U. Manor, S. Bartholomew, G. Golani, E. Christenson, M. Kozlov, H. Higgs, J. Spudich, and J. Lippincott-Schwartz. A mitochondria-anchored isoform of the actin-nucleating spire protein regulates mitochondrial division. *Elife*, 4, Aug 2015.

[242] A. S. Moore, Y. C. Wong, C. L. Simpson, and E. L. Holzbaur. Dynamic actin cycling through mitochondrial subpopulations locally regulates the fission-fusion balance within mitochondrial networks. *Nat Commun*, 7:12886, Sep 2016.

[243] K. M. Tharp, M. S. Kang, G. A. Timblin, J. Dempersmier, G. E. Dempsey, P. H. Zushin, J. Benavides, C. Choi, C. X. Li, A. K. Jha, S. Kajimura, K. E. Healy, H. S. Sul, K. Saijo, S. Kumar, and A. Stahl. Actomyosin-Mediated Tension Orchestrates Uncoupled Respiration in Adipose Tissues. *Cell Metab*, 27(3):602–615, 03 2018.

[244] G. L. Lin, D. M. Cohen, R. A. Desai, M. T. Breckenridge, L. Gao, M. J. Humphries, and C. S. Chen. Activation of beta 1 but not beta 3 integrin increases cell traction forces. *FEBS Lett*, 587(6):763–769, Mar 2013.

[245] S. R. Caliari and J. A. Burdick. A practical guide to hydrogels for cell culture. *Nat Methods*, 13(5):405–414, 04 2016.

[246] K. M. Tharp and V. M. Weaver. Modeling Tissue Polarity in Context. *J Mol Biol*, 430(19):3613–3628, 09 2018.

[247] D. T. Butcher, T. Alliston, and V. M. Weaver. A tense situation: forcing tumour progression. *Nat Rev Cancer*, 9(2):108–122, Feb 2009.

[248] D. R. Croft and M. F. Olson. Conditional regulation of a ROCK-estrogen receptor fusion protein. *Methods Enzymol*, 406:541–553, 2006.

[249] C. Yik-Sham Chung, G. A. Timblin, K. Saijo, and C. J. Chang. Versatile Histochemical Approach to Detection of Hydrogen Peroxide in Cells and Tissues Based on Puromycin Staining. *J Am Chem Soc*, 140(19):6109–6121, 05 2018.

[250] M. Sciacovelli, E. Gonçalves, T. I. Johnson, V. R. Zecchini, A. S. da Costa, E. Gaude, A. V. Drubbel, S. J. Theobald, S. R. Abbo, M. G. Tran, V. Rajeeve, S. Cardaci, S. Foster, H. Yun, P. Cutillas, A. Warren, V. Gnanapragasam, E. Gottlieb, K. Franze, B. Huntly, E. R. Maher,

P. H. Maxwell, J. Saez-Rodriguez, and C. Frezza. Fumarate is an epigenetic modifier that elicits epithelial-to-mesenchymal transition. *Nature*, 537(7621):544–547, 08 2016.

[251] A. Barasa, G. Godina, P. Buffa, and I. Pasquali-Ronchetti. Biochemical lesions of respiratory enzymes and configurational changes of mitochondria in vivo. I. The effect of fluoroacetate: a study by phase-contrast microscopy and time-lapse cinemicrography. *Z Zellforsch Mikrosk Anat*, 138(2):187–210, Mar 1973.

[252] D. Jimenez-Blasco, A. Busquets-Garcia, E. Hebert-Chatelain, R. Serrat, C. Vicente-Gutierrez, C. Ioannidou, P. Gómez-Sotres, I. Lopez-Fabuel, M. Resch-Beusher, E. Resel, D. Arnouil, D. Saraswat, M. Varilh, A. Cannich, F. Julio-Kalajzic, I. Bonilla-Del Río, A. Almeida, N. Puente, S. Achicallende, M. L. Lopez-Rodriguez, C. Jollé, N. Déglon, L. Pellerin, C. Josephine, G. Bonvento, A. Panatier, B. Lutz, P. V. Piazza, M. Guzmán, L. Bellocchio, A. K. Bouzier-Sore, P. Grandes, J. P. Bolaños, and G. Marsicano. Glucose metabolism links astroglial mitochondria to cannabinoid effects. *Nature*, 583(7817):603–608, 07 2020.

[253] P. Lindström and J. Sehlin. Effect of glucose on the intracellular pH of pancreatic islet cells. *Biochem J*, 218(3):887–892, Mar 1984.

[254] Q. Wang, M. Zhang, G. Torres, S. Wu, C. Ouyang, Z. Xie, and M. H. Zou. Metformin Suppresses Diabetes-Accelerated Atherosclerosis via the Inhibition of Drp1-Mediated Mitochondrial Fission. *Diabetes*, 66(1):193–205, Jan 2017.

[255] B. C. Chen, W. R. Legant, K. Wang, L. Shao, D. E. Milkie, M. W. Davidson, C. Janetopoulos, X. S. Wu, J. A. Hammer, Z. Liu, B. P. English, Y. Mimori-Kiyosue, D. P. Romero, A. T. Ritter, J. Lippincott-Schwartz, L. Fritz-Laylin, R. D. Mullins, D. M. Mitchell, J. N. Bembenek, A. C. Reymann, R. Böhme, S. W. Grill, J. T. Wang, G. Seydoux, U. S. Tulu, D. P. Kiehart, and E. Betzig. Lattice light-sheet microscopy: imaging molecules to embryos at high spatiotemporal resolution. *Science*, 346(6208):1257998, Oct 2014.

[256] J. E. Aldridge, T. Horibe, and N. J. Hoogenraad. Discovery of genes activated by the mitochondrial unfolded protein response (mtUPR) and cognate promoter elements. *PLoS One*, 2(9):e874, Sep 2007.

[257] Y. F. Lin and C. M. Haynes. Metabolism and the UPR(mt). *Mol Cell*, 61(5):677–682, Mar 2016.

[258] H. G. Sprenger and T. Langer. The Good and the Bad of Mitochondrial Breakups. *Trends Cell Biol*, 29(11):888–900, 11 2019.

[259] R. J. Youle and A. M. van der Bliek. Mitochondrial fission, fusion, and stress. *Science*, 337(6098):1062–1065, Aug 2012.

[260] X. Liu and G. Hajnóczky. Altered fusion dynamics underlie unique morphological changes in mitochondria during hypoxia-reoxygenation stress. *Cell Death Differ*, 18(10):1561–1572, Oct 2011.

[261] Y. Miyazono, S. Hirashima, N. Ishihara, J. Kusukawa, K. I. Nakamura, and K. Ohta. Uncoupled mitochondria quickly shorten along their long axis to form indented spheroids, instead of rings, in a fission-independent manner. *Sci Rep*, 8(1):350, 01 2018.

[262] G. Twig and O. S. Shirihai. The interplay between mitochondrial dynamics and mitophagy. *Antioxid Redox Signal*, 14(10):1939–1951, May 2011.

[263] S. W. Perry, J. P. Norman, J. Barbieri, E. B. Brown, and H. A. Gelbard. Mitochondrial membrane potential probes and the proton gradient: a practical usage guide. *Biotechniques*, 50(2):98–115, Feb 2011.

[264] C. H. Choi, B. A. Webb, M. S. Chimenti, M. P. Jacobson, and D. L. Barber. pH sensing by FAK-His58 regulates focal adhesion remodeling. *J Cell Biol*, 202(6):849–859, Sep 2013.

[265] T. Tominaga and D. L. Barber. Na-H exchange acts downstream of RhoA to regulate integrin-induced cell adhesion and spreading. *Mol Biol Cell*, 9(8):2287–2303, Aug 1998.

[266] T. Tominaga, T. Ishizaki, S. Narumiya, and D. L. Barber. p160ROCK mediates RhoA activation of Na-H exchange. *EMBO J*, 17(16):4712–4722, Aug 1998.

[267] K. Nehrke and J. E. Melvin. The NHX family of Na+-H+ exchangers in Caenorhabditis elegans. *J Biol Chem*, 277(32):29036–29044, Aug 2002.

[268] M. Ristow and S. Schmeisser. Extending life span by increasing oxidative stress. *Free Radic Biol Med*, 51(2):327–336, Jul 2011.

[269] P. S. Brookes, Y. Yoon, J. L. Robotham, M. W. Anders, and S. S. Sheu. Calcium, ATP, and ROS: a mitochondrial love-hate triangle. *Am J Physiol Cell Physiol*, 287(4):C817–833, Oct 2004.

[270] C. Giorgi, S. Marchi, and P. Pinton. The machineries, regulation and cellular functions of mitochondrial calcium. *Nat Rev Mol Cell Biol*, 19(11):713–730, 11 2018.

[271] P. Hernansanz-Agustín, C. Choya-Foces, S. Carregal-Romero, E. Ramos, T. Oliva, T. Villa-Piña, L. Moreno, A. Izquierdo-Álvarez, J. D. Cabrera-García, A. Cortés, A. V. Lechuga-Vieco, P. Jadiya, E. Navarro, E. Parada, A. Palomino-Antolín, D. Tello, R. Acín-Pérez, J. C. Rodríguez-Aguilera, P. Navas, Á. Cogolludo, I. López-Montero, Á. Martínez-Del-Pozo, J. Egea, M. G. López, J. W. Elrod, J. Ruíz-Cabello, A. Bogdanova, J. A. Enríquez, and A. Martínez-Ruiz. controls hypoxic signalling by the mitochondrial respiratory chain. *Nature*, 586(7828):287–291, 10 2020.

[272] P. R. Castello, D. A. Drechsel, and M. Patel. Mitochondria are a major source of paraquat-induced reactive oxygen species production in the brain. *J Biol Chem*, 282(19):14186–14193, May 2007.

[273] Q. Ma. Role of nrf2 in oxidative stress and toxicity. *Annu Rev Pharmacol Toxicol*, 53:401–426, 2013.

[274] M. Ristow. Unraveling the truth about antioxidants: mitohormesis explains ROS-induced health benefits. *Nat Med*, 20(7):709–711, Jul 2014.

[275] J. Yun and T. Finkel. Mitohormesis. *Cell Metab*, 19(5):757–766, May 2014.

[276] M. P. Mattson. Hormesis defined. *Ageing Res Rev*, 7(1):1–7, Jan 2008.

[277] S. E. Calvo, K. R. Clauser, and V. K. Mootha. MitoCarta2.0: an updated inventory of mammalian mitochondrial proteins. *Nucleic Acids Res*, 44(D1):D1251–1257, Jan 2016.

[278] J. Labbadia, R. M. Brielmann, M. F. Neto, Y. F. Lin, C. M. Haynes, and R. I. Morimoto. Mitochondrial Stress Restores the Heat Shock Response and Prevents Proteostasis Collapse during Aging. *Cell Rep*, 21(6):1481–1494, Nov 2017.

[279] J. M. D. Grandjean, L. Plate, R. I. Morimoto, M. J. Bollong, E. T. Powers, and R. L. Wiseman. Deconvoluting Stress-Responsive Proteostasis Signaling Pathways for Pharmacologic Activation Using Targeted RNA Sequencing. *ACS Chem Biol*, 14(4):784–795, 04 2019.

[280] D. Reichmann, W. Voth, and U. Jakob. Maintaining a Healthy Proteome during Oxidative Stress. *Mol Cell*, 69(2):203–213, 01 2018.

[281] A. M. Nargund, M. W. Pellegrino, C. J. Fiorese, B. M. Baker, and C. M. Haynes. Mitochondrial import efficiency of ATFS-1 regulates mitochondrial UPR activation. *Science*, 337(6094):587–590, Aug 2012.

[282] C. J. Fiorese, A. M. Schulz, Y. F. Lin, N. Rosin, M. W. Pellegrino, and C. M. Haynes. The Transcription Factor ATF5 Mediates a Mammalian Mitochondrial UPR. *Curr Biol*, 26(15):2037–2043, 08 2016.

[283] A. Katiyar, M. Fujimoto, K. Tan, A. Kurashima, P. Srivastava, M. Okada, R. Takii, and A. Nakai. HSF1 is required for induction of mitochondrial chaperones during the mitochondrial unfolded protein response. *FEBS Open Bio*, 10(6):1135–1148, 06 2020.

[284] F. Boos, L. Krämer, C. Groh, F. Jung, P. Haberkant, F. Stein, F. Wollweber, A. Gackstatter, E. Zöller, M. van der Laan, M. M. Savitski, V. Benes, and J. M. Herrmann. Mitochondrial protein-induced stress triggers a global adaptive transcriptional programme. *Nat Cell Biol*, 21(4):442–451, 04 2019.

[285] S. G. Ahn and D. J. Thiele. Redox regulation of mammalian heat shock factor 1 is essential for Hsp gene activation and protection from stress. *Genes Dev*, 17(4):516–528, Feb 2003.

[286] S. Paul, S. Ghosh, S. Mandal, S. Sau, and M. Pal. promoter under oxidative stress and affects survival and migration potential of MCF7 cells. *J Biol Chem*, 293(50):19303–19316, 12 2018.

[287] N. Wiedemann and N. Pfanner. Mitochondrial Machineries for Protein Import and Assembly. *Annu Rev Biochem*, 86:685–714, 06 2017.

[288] A. E. Charos, B. D. Reed, D. Raha, A. M. Szekely, S. M. Weissman, and M. Snyder. A highly integrated and complex PPARGC1A transcription factor binding network in HepG2 cells. *Genome Res*, 22(9):1668–1679, Sep 2012.

[289] M. L. Mendillo, S. Santagata, M. Koeva, G. W. Bell, R. Hu, R. M. Tamimi, E. Fraenkel, T. A. Ince, L. Whitesell, and S. Lindquist. HSF1 drives a transcriptional program distinct from heat shock to support highly malignant human cancers. *Cell*, 150(3):549–562, Aug 2012.

[290] S. E. LeBoeuf, W. L. Wu, T. R. Karakousi, B. Karadal, S. R. Jackson, S. M. Davidson, K. K. Wong, S. B. Koralov, V. I. Sayin, and T. Papagiannakopoulos. Activation of Oxidative Stress Response in Cancer Generates a Druggable Dependency on Exogenous Non-essential Amino Acids. *Cell Metab*, 31(2):339–350, 02 2020.

[291] C. Jang, L. Chen, and J. D. Rabinowitz. Metabolomics and Isotope Tracing. *Cell*, 173(4):822–837, 05 2018.

[292] D. R. Crooks, N. Maio, M. Lang, C. J. Ricketts, C. D. Vocke, S. Gurram, S. Turan, Y. Y. Kim, G. M. Cawthon, F. Sohelian, N. De Val, R. M. Pfeiffer, P. Jailwala, M. Tandon, B. Tran, T. W. Fan, A. N. Lane, T. Ried, D. Wangsa, A. A. Malayeri, M. J. Merino, Y. Yang, J. L. Meier, M. W. Ball, T. A. Rouault, R. Srinivasan, and W. M. Linehan. Mitochondrial DNA alterations underlie an irreversible shift to aerobic glycolysis in fumarate hydratase-deficient renal cancer. *Sci Signal*, 14(664), 01 2021.

[293] X. Ma, L. Xu, A. T. Alberobello, O. Gavrilova, A. Bagattin, M. Skarulis, J. Liu, T. Finkel, and E. Mueller. Celastrol Protects against Obesity and Metabolic Dysfunction through Activation of a HSF1-PGC1α Transcriptional Axis. *Cell Metab*, 22(4):695–708, Oct 2015.

[294] C. R. Reczek, K. Birsoy, H. Kong, I. Martínez-Reyes, T. Wang, P. Gao, D. M. Sabatini, and N. S. Chandel. A CRISPR screen identifies a pathway required for paraquat-induced cell death. *Nat Chem Biol*, 13(12):1274–1279, Dec 2017.

[295] O. Schmidt, N. Pfanner, and C. Meisinger. Mitochondrial protein import: from proteomics to functional mechanisms. *Nat Rev Mol Cell Biol*, 11(9):655–667, Sep 2010.

[296] C. C. Deocaris, S. C. Kaul, and R. Wadhwa. On the brotherhood of the mitochondrial chaperones mortalin and heat shock protein 60. *Cell Stress Chaperones*, 11(2):116–128, 2006.

[297] H. C. Schneider, J. Berthold, M. F. Bauer, K. Dietmeier, B. Guiard, M. Brunner, and W. Neupert. Mitochondrial Hsp70/MIM44 complex facilitates protein import. *Nature*, 371(6500):768–774, Oct 1994.

[298] X. Li, S. R. Srinivasan, J. Connarn, A. Ahmad, Z. T. Young, A. M. Kabza, E. R. Zuiderweg, D. Sun, and J. E. Gestwicki. Analogs of the Allosteric Heat Shock Protein 70 (Hsp70) Inhibitor, MKT-077, as Anti-Cancer Agents. *ACS Med Chem Lett*, 4(11), Nov 2013.

[299] S. R. Srinivasan, L. C. Cesa, X. Li, O. Julien, M. Zhuang, H. Shao, J. Chung, I. Maillard, J. A. Wells, C. S. Duckett, and J. E. Gestwicki. Heat Shock Protein 70 (Hsp70) Suppresses

RIP1-Dependent Apoptotic and Necroptotic Cascades. *Mol Cancer Res*, 16(1):58–68, 01 2018.

[300] T. MacVicar and T. Langer. OPA1 processing in cell death and disease - the long and short of it. *J Cell Sci*, 129(12):2297–2306, 06 2016.

[301] T. MacVicar, Y. Ohba, H. Nolte, F. C. Mayer, T. Tatsuta, H. G. Sprenger, B. Lindner, Y. Zhao, J. Li, C. Bruns, M. Krüger, M. Habich, J. Riemer, R. Schwarzer, M. Pasparakis, S. Henschke, J. C. Brüning, N. Zamboni, and T. Langer. Lipid signalling drives proteolytic rewiring of mitochondria by YME1L. *Nature*, 575(7782):361–365, 11 2019.

[302] S. Santagata, R. Hu, N. U. Lin, M. L. Mendillo, L. C. Collins, S. E. Hankinson, S. J. Schnitt, L. Whitesell, R. M. Tamimi, S. Lindquist, and T. A. Ince. High levels of nuclear heat-shock factor 1 (HSF1) are associated with poor prognosis in breast cancer. *Proc Natl Acad Sci U S A*, 108(45):18378–18383, Nov 2011.

[303] R. Scherz-Shouval, S. Santagata, M. L. Mendillo, L. M. Sholl, I. Ben-Aharon, A. H. Beck, D. Dias-Santagata, M. Koeva, S. M. Stemmer, L. Whitesell, and S. Lindquist. The reprogramming of tumor stroma by HSF1 is a potent enabler of malignancy. *Cell*, 158(3):564–578, Jul 2014.

[304] J. R. Cantor, M. Abu-Remaileh, N. Kanarek, E. Freinkman, X. Gao, A. Louissaint, C. A. Lewis, and D. M. Sabatini. Physiologic Medium Rewires Cellular Metabolism and Reveals Uric Acid as an Endogenous Inhibitor of UMP Synthase. *Cell*, 169(2):258–272, Apr 2017.

[305] P. DelNero, B. D. Hopkins, L. C. Cantley, and C. Fischbach. Cancer metabolism gets physical. *Sci Transl Med*, 10(442), 05 2018.

[306] D. C. Radisky, D. D. Levy, L. E. Littlepage, H. Liu, C. M. Nelson, J. E. Fata, D. Leake, E. L. Godden, D. G. Albertson, M. A. Nieto, Z. Werb, and M. J. Bissell. Rac1b and reactive oxygen species mediate MMP-3-induced EMT and genomic instability. *Nature*, 436(7047):123–127, Jul 2005.

[307] Z. T. Schafer, A. R. Grassian, L. Song, Z. Jiang, Z. Gerhart-Hines, H. Y. Irie, S. Gao, P. Puigserver, and J. S. Brugge. Antioxidant and oncogene rescue of metabolic defects caused by loss of matrix attachment. *Nature*, 461(7260):109–113, Sep 2009.

[308] E. Werner and Z. Werb. Integrins engage mitochondrial function for signal transduction by a mechanism dependent on Rho GTPases. *J Cell Biol*, 158(2):357–368, Jul 2002.

[309] K. A. Dill. Dominant forces in protein folding. *Biochemistry*, 29(31):7133–7155, Aug 1990.

[310] K. A. Dill and J. L. MacCallum. The protein-folding problem, 50 years on. *Science*, 338(6110):1042–1046, Nov 2012.

[311] R. Higuchi-Sanabria, P. A. Frankino, J. W. Paul, S. U. Tronnes, and A. Dillin. A Futile Battle? Protein Quality Control and the Stress of Aging. *Dev Cell*, 44(2):139–163, Jan 2018.

[312] B. A. Hassell, G. Goyal, E. Lee, A. Sontheimer-Phelps, O. Levy, C. S. Chen, and D. E. Ingber. Human Organ Chip Models Recapitulate Orthotopic Lung Cancer Growth, Therapeutic Responses, and Tumor Dormancy In Vitro. *Cell Rep*, 21(2):508–516, Oct 2017.

[313] J. Irianto, C. R. Pfeifer, R. R. Bennett, Y. Xia, I. L. Ivanovska, A. J. Liu, R. A. Greenberg, and D. E. Discher. Nuclear constriction segregates mobile nuclear proteins away from chromatin. *Mol Biol Cell*, 27(25):4011–4020, 12 2016.

[314] P. Isermann and J. Lammerding. Consequences of a tight squeeze: Nuclear envelope rupture and repair. *Nucleus*, 8(3):268–274, 05 2017.

[315] M. S. Samuel, J. I. Lopez, E. J. McGhee, D. R. Croft, D. Strachan, P. Timpson, J. Munro, E. Schröder, J. Zhou, V. G. Brunton, N. Barker, H. Clevers, O. J. Sansom, K. I. Anderson, V. M. Weaver, and M. F. Olson. Actomyosin-mediated cellular tension drives increased tissue stiffness and β-catenin activation to induce epidermal hyperplasia and tumor growth. *Cancer Cell*, 19(6):776–791, Jun 2011.

[316] B. Faubert, A. Solmonson, and R. J. DeBerardinis. Metabolic reprogramming and cancer progression. *Science*, 368(6487), 04 2020.

[317] C. Dai and S. B. Sampson. HSF1: Guardian of Proteostasis in Cancer. *Trends Cell Biol*, 26(1):17–28, Jan 2016.

[318] P. Ostling, J. K. Björk, P. Roos-Mattjus, V. Mezger, and L. Sistonen. Heat shock factor 2 (HSF2) contributes to inducible expression of hsp genes through interplay with HSF1. *J Biol Chem*, 282(10):7077–7086, Mar 2007.

[319] J. R. Cantor. The Rise of Physiologic Media. *Trends Cell Biol*, 29(11):854–861, 11 2019.

[320] N. J. Rossiter, K. S. Huggler, C. H. Adelmann, H. R. Keys, R. W. Soens, D. M. Sabatini, and J. R. Cantor. CRISPR screens in physiologic medium reveal conditionally essential genes in human cells. *Cell Metab*, 33(6):1248–1263, 06 2021.

[321] J. S. Miller, K. R. Stevens, M. T. Yang, B. M. Baker, D. H. Nguyen, D. M. Cohen, E. Toro, A. A. Chen, P. A. Galie, X. Yu, R. Chaturvedi, S. N. Bhatia, and C. S. Chen. Rapid casting of patterned vascular networks for perfusable engineered three-dimensional tissues. *Nat Mater*, 11(9):768–774, Sep 2012.

[322] L. Cassereau, Y. A. Miroshnikova, G. Ou, J. Lakins, and V. M. Weaver. A 3D tension bioreactor platform to study the interplay between ECM stiffness and tumor phenotype. *J Biotechnol*, 193:66–69, Jan 2015.

[323] S. Pradhan, J. M. Clary, D. Seliktar, and E. A. Lipke. A three-dimensional spheroidal cancer model based on PEG-fibrinogen hydrogel microspheres. *Biomaterials*, 115:141–154, 01 2017.

[324] J. N. Lakins, A. R. Chin, and V. M. Weaver. Exploring the link between human embryonic stem cell organization and fate using tension-calibrated extracellular matrix functionalized polyacrylamide gels. *Methods Mol Biol*, 916:317–350, 2012.

[325] K. J. Wolf and S. Kumar. Hyaluronic Acid: Incorporating the Bio into the Material. *ACS Biomater Sci Eng*, 5(8):3753–3765, Aug 2019.

[326] O. Chaudhuri, S. T. Koshy, C. Branco da Cunha, J. W. Shin, C. S. Verbeke, K. H. Allison, and D. J. Mooney. Extracellular matrix stiffness and composition jointly regulate the induction of malignant phenotypes in mammary epithelium. *Nat Mater*, 13(10):970–978, Oct 2014.

[327] G. Cheng, J. Tse, R. K. Jain, and L. L. Munn. Micro-environmental mechanical stress controls tumor spheroid size and morphology by suppressing proliferation and inducing apoptosis in cancer cells. *PLoS One*, 4(2):e4632, 2009.

[328] T. Risom, D. R. Glass, I. Averbukh, C. C. Liu, A. Baranski, A. Kagel, E. F. McCaffrey, N. F. Greenwald, B. Rivero-Gutiérrez, S. H. Strand, S. Varma, A. Kong, L. Keren, S. Srivastava, C. Zhu, Z. Khair, D. J. Veis, K. Deschryver, S. Vennam, C. Maley, E. S. Hwang, J. R. Marks, S. C. Bendall, G. A. Colditz, R. B. West, and M. Angelo. Transition to invasive breast cancer is associated with progressive changes in the structure and composition of tumor stroma. *Cell*, 185(2):299–310, 01 2022.

[329] N. Kanyo, K. D. Kovacs, A. Saftics, I. Szekacs, B. Peter, A. R. Santa-Maria, F. R. Walter, A. Dér, M. A. Deli, and R. Horvath. Glycocalyx regulates the strength and kinetics of cancer cell adhesion revealed by biophysical models based on high resolution label-free optical data. *Sci Rep*, 10(1):22422, 12 2020.

[330] M. J. Paszek, D. Boettiger, V. M. Weaver, and D. A. Hammer. Integrin clustering is driven by mechanical resistance from the glycocalyx and the substrate. *PLoS Comput Biol*, 5(12):e1000604, Dec 2009.

[331] A. Buffone and V. M. Weaver. Don't sugarcoat it: How glycocalyx composition influences cancer progression. *J Cell Biol*, 219(1), 01 2020.

[332] J. Chin-Hun Kuo, J. G. Gandhi, R. N. Zia, and M. J. Paszek. Physical biology of the cancer cell glycocalyx. *Nat Phys*, 14(7):658–669, 2018.

[333] P. Brossart, A. Schneider, P. Dill, T. Schammann, F. Grünebach, S. Wirths, L. Kanz, H. J. Bühring, and W. Brugger. The epithelial tumor antigen MUC1 is expressed in hematological malignancies and is recognized by MUC1-specific cytotoxic T-lymphocytes. *Cancer Res*, 61(18):6846–6850, Sep 2001.

[334] D. Pardoll. Cancer and the Immune System: Basic Concepts and Targets for Intervention. *Semin Oncol*, 42(4):523–538, Aug 2015.

[335] Y. Zhang and Z. Zhang. The history and advances in cancer immunotherapy: understanding the characteristics of tumor-infiltrating immune cells and their therapeutic implications. *Cell Mol Immunol*, 17(8):807–821, 08 2020.

[336] G. T. Motz, S. P. Santoro, L. P. Wang, T. Garrabrant, R. R. Lastra, I. S. Hagemann, P. Lal, M. D. Feldman, F. Benencia, and G. Coukos. Tumor endothelium FasL establishes a selective immune barrier promoting tolerance in tumors. *Nat Med*, 20(6):607–615, Jun 2014.

[337] M. Ostroukhova, Z. Qi, T. B. Oriss, B. Dixon-McCarthy, P. Ray, and A. Ray. Treg-mediated immunosuppression involves activation of the Notch-HES1 axis by membrane-bound TGF-beta. *J Clin Invest*, 116(4):996–1004, Apr 2006.

[338] G. Wick, A. Backovic, E. Rabensteiner, N. Plank, C. Schwentner, and R. Sgonc. The immunology of fibrosis: innate and adaptive responses. *Trends Immunol*, 31(3):110–119, Mar 2010.

[339] C. Chandler, T. Liu, R. Buckanovich, and L. G. Coffman. The double edge sword of fibrosis in cancer. *Transl Res*, 209:55–67, 07 2019.

[340] H. Jiang, S. Hegde, and D. G. DeNardo. Tumor-associated fibrosis as a regulator of tumor immunity and response to immunotherapy. *Cancer Immunol Immunother*, 66(8):1037–1048, Aug 2017.

[341] B. Wu, Q. H. Sodji, and A. K. Oyelere. Inflammation, Fibrosis and Cancer: Mechanisms, Therapeutic Options and Challenges. *Cancers (Basel)*, 14(3), Jan 2022.

[342] K. K. Tsai, S. S. Huang, J. J. Northey, W. Y. Liao, C. C. Hsu, L. H. Cheng, M. E. Werner, C. P. Chuu, C. Chatterjee, J. N. Lakins, and V. M. Weaver. Screening of organoids derived from patients with breast cancer implicates the repressor NCOR2 in cytotoxic stress response and antitumor immunity. *Nat Cancer*, 3(6):734–752, 06 2022.

[343] R. A. Gatenby and R. J. Gillies. Why do cancers have high aerobic glycolysis? *Nat Rev Cancer*, 4(11):891–899, Nov 2004.

[344] M. V. Liberti and J. W. Locasale. The Warburg Effect: How Does it Benefit Cancer Cells? *Trends Biochem Sci*, 41(3):211–218, Mar 2016.

[345] J. W. Wojtkowiak, D. Verduzco, K. J. Schramm, and R. J. Gillies. Drug resistance and cellular adaptation to tumor acidic pH microenvironment. *Mol Pharm*, 8(6):2032–2038, Dec 2011.

[346] V. Estrella, T. Chen, M. Lloyd, J. Wojtkowiak, H. H. Cornnell, A. Ibrahim-Hashim, K. Bailey, Y. Balagurunathan, J. M. Rothberg, B. F. Sloane, J. Johnson, R. A. Gatenby, and R. J. Gillies. Acidity generated by the tumor microenvironment drives local invasion. *Cancer Res*, 73(5):1524–1535, Mar 2013.

[347] V. Huber, C. Camisaschi, A. Berzi, S. Ferro, L. Lugini, T. Triulzi, A. Tuccitto, E. Tagliabue, C. Castelli, and L. Rivoltini. Cancer acidity: An ultimate frontier of tumor immune escape and a novel target of immunomodulation. *Semin Cancer Biol*, 43:74–89, 04 2017.

[348] E. Cambria, S. Brunner, S. Heusser, P. Fisch, W. Hitzl, S. J. Ferguson, and K. Wuertz-Kozak. Cell-Laden Agarose-Collagen Composite Hydrogels for Mechanotransduction Studies. *Front Bioeng Biotechnol*, 8:346, 2020.

[349] R. Edgar, M. Domrachev, and A. E. Lash. Gene Expression Omnibus: NCBI gene expression and hybridization array data repository. *Nucleic Acids Res*, 30(1):207–210, Jan 2002.

[350] A. D. Edelstein, M. A. Tsuchida, N. Amodaj, H. Pinkard, R. D. Vale, and N. Stuurman. Advanced methods of microscope control using μManager software. *J Biol Methods*, 1(2), 2014.

[351] S. van der Walt, J. L. Schönberger, J. Nunez-Iglesias, F. Boulogne, J. D. Warner, N. Yager, E. Gouillart, and T. Yu. scikit-image: image processing in Python. *PeerJ*, 2:e453, 2014.

[352] L. Przybyla, J. N. Lakins, R. Sunyer, X. Trepat, and V. M. Weaver. Monitoring developmental force distributions in reconstituted embryonic epithelia. *Methods*, 94:101–113, Feb 2016.

[353] K. M. Wisdom, K. Adebowale, J. Chang, J. Y. Lee, S. Nam, R. Desai, N. S. Rossen, M. Rafat, R. B. West, L. Hodgson, and O. Chaudhuri. Matrix mechanical plasticity regulates cancer cell migration through confining microenvironments. *Nat Commun*, 9(1):4144, 10 2018.

[354] Toshikazu Takigawa, Yoshiro Morino, Kenji Urayama, and Toshiro Masuda. Poisson's ratio of polyacrylamide (paam) gels. *Polymer Gels and Networks*, 4(1):1–5, 1996.

[355] Q. Shi, R. P. Ghosh, H. Engelke, C. H. Rycroft, L. Cassereau, J. A. Sethian, V. M. Weaver, and J. T. Liphardt. Rapid disorganization of mechanically interacting systems of mammary acini. *Proc Natl Acad Sci U S A*, 111(2):658–663, Jan 2014.

[356] J. J. Northey, A. S. Barrett, I. Acerbi, M. K. Hayward, S. Talamantes, I. S. Dean, J. K. Mouw, S. M. Ponik, J. N. Lakins, P. J. Huang, J. Wu, Q. Shi, S. Samson, P. J. Keely, R. A. Mukhtar,

J. T. Liphardt, J. A. Shepherd, E. S. Hwang, Y. Y. Chen, K. C. Hansen, L. E. Littlepage, and V. M. Weaver. Stiff stroma increases breast cancer risk by inducing the oncogene ZNF217. *J Clin Invest*, 130(11):5721–5737, 11 2020.

[357] P. Bankhead, M. B. Loughrey, J. A. Fernández, Y. Dombrowski, D. G. McArt, P. D. Dunne, S. McQuaid, R. T. Gray, L. J. Murray, H. G. Coleman, J. A. James, M. Salto-Tellez, and P. W. Hamilton. QuPath: Open source software for digital pathology image analysis. *Sci Rep*, 7(1):16878, 12 2017.

[358] J. Schindelin, I. Arganda-Carreras, E. Frise, V. Kaynig, M. Longair, T. Pietzsch, S. Preibisch, C. Rueden, S. Saalfeld, B. Schmid, J. Y. Tinevez, D. J. White, V. Hartenstein, K. Eliceiri, P. Tomancak, and A. Cardona. Fiji: an open-source platform for biological-image analysis. *Nat Methods*, 9(7):676–682, Jun 2012.

[359] S. Davis and P. S. Meltzer. GEOquery: a bridge between the Gene Expression Omnibus (GEO) and BioConductor. *Bioinformatics*, 23(14):1846–1847, Jul 2007.

[360] M. E. Ritchie, B. Phipson, D. Wu, Y. Hu, C. W. Law, W. Shi, and G. K. Smyth. limma powers differential expression analyses for RNA-sequencing and microarray studies. *Nucleic Acids Res*, 43(7):e47, Apr 2015.

[361] A. Liberzon, C. Birger, H. Thorvaldsdóttir, M. Ghandi, J. P. Mesirov, and P. Tamayo. The Molecular Signatures Database (MSigDB) hallmark gene set collection. *Cell Syst*, 1(6):417–425, Dec 2015.

[362] J. Debnath, S. K. Muthuswamy, and J. S. Brugge. Morphogenesis and oncogenesis of MCF-10A mammary epithelial acini grown in three-dimensional basement membrane cultures. *Methods*, 30(3):256–268, Jul 2003.

[363] T. Masters, W. Engl, Z. L. Weng, B. Arasi, N. Gauthier, and V. Viasnoff. Easy fabrication of thin membranes with through holes. Application to protein patterning. *PLoS One*, 7(8):e44261, 2012.

[364] T. Verfaillie, N. Rubio, A. D. Garg, G. Bultynck, R. Rizzuto, J. P. Decuypere, J. Piette, C. Linehan, S. Gupta, A. Samali, and P. Agostinis. PERK is required at the ER-mitochondrial contact sites to convey apoptosis after ROS-based ER stress. *Cell Death Differ*, 19(11):1880–1891, Nov 2012.

[365] Jeffrey L. Hutter and John Bechhoefer. Calibration of atomic-force microscope tips. *Review of Scientific Instruments*, 64(7):1868–1873, 1993.

[366] A. F. Long, D. B. Udy, and S. Dumont. Hec1 Tail Phosphorylation Differentially Regulates Mammalian Kinetochore Coupling to Polymerizing and Depolymerizing Microtubules. *Curr Biol*, 27(11):1692–1699, Jun 2017.

[367] G. Gaietta, M. F. Swift, N. Volkmann, and D. Hanein. Rapid tool for cell nanoarchitecture integrity assessment. *J Struct Biol*, 213(4):107801, 12 2021.

[368] J. Dubochet. Cryo-EM–the first thirty years. *J Microsc*, 245(3):221–224, Mar 2012.

[369] D. J. Marston, K. L. Anderson, M. F. Swift, M. Rougie, C. Page, K. M. Hahn, N. Volkmann, and D. Hanein. High Rac1 activity is functionally translated into cytosolic structures with unique nanoscale cytoskeletal architecture. *Proc Natl Acad Sci U S A*, 116(4):1267–1272, 01 2019.

[370] D. N. Mastronarde. Automated electron microscope tomography using robust prediction of specimen movements. *J Struct Biol*, 152(1):36–51, Oct 2005.

[371] N. Volkmann and D. Hanein. Quantitative fitting of atomic models into observed densities derived by electron microscopy. *J Struct Biol*, 125(2-3):176–184, 1999.

[372] D. N. Mastronarde and S. R. Held. Automated tilt series alignment and tomographic reconstruction in IMOD. *J Struct Biol*, 197(2):102–113, 02 2017.

[373] J. I. Agulleiro and J. J. Fernandez. Fast tomographic reconstruction on multicore computers. *Bioinformatics*, 27(4):582–583, Feb 2011.

[374] A. Kumar, K. L. Anderson, M. F. Swift, D. Hanein, N. Volkmann, and M. A. Schwartz. Local Tension on Talin in Focal Adhesions Correlates with F-Actin Alignment at the Nanometer Scale. *Biophys J*, 115(8):1569–1579, 10 2018.

[375] J. Cox and M. Mann. MaxQuant enables high peptide identification rates, individualized p.p.b.-range mass accuracies and proteome-wide protein quantification. *Nat Biotechnol*, 26(12):1367–1372, Dec 2008.

[376] S. Tyanova, T. Temu, and J. Cox. The MaxQuant computational platform for mass spectrometry-based shotgun proteomics. *Nat Protoc*, 11(12):2301–2319, Dec 2016.

[377] S. Tyanova, T. Temu, P. Sinitcyn, A. Carlson, M. Y. Hein, T. Geiger, M. Mann, and J. Cox. The Perseus computational platform for comprehensive analysis of (prote)omics data. *Nat Methods*, 13(9):731–740, 09 2016.

[378] Y. Perez-Riverol, A. Csordas, J. Bai, M. Bernal-Llinares, S. Hewapathirana, D. J. Kundu, A. Inuganti, J. Griss, G. Mayer, M. Eisenacher, E. Pérez, J. Uszkoreit, J. Pfeuffer, T. Sachsenberg, S. Yilmaz, S. Tiwary, J. Cox, E. Audain, M. Walzer, A. F. Jarnuczak, T. Ternent, A. Brazma, and J. A. Vizcaíno. The PRIDE database and related tools and resources in 2019: improving support for quantification data. *Nucleic Acids Res*, 47(D1):D442–D450, 01 2019.

[379] S. Urlinger, U. Baron, M. Thellmann, M. T. Hasan, H. Bujard, and W. Hillen. Exploring the sequence space for tetracycline-dependent transcriptional activators: novel mutations yield expanded range and sensitivity. *Proc Natl Acad Sci U S A*, 97(14):7963–7968, Jul 2000.

[380] P. M. Quirós, M. A. Prado, N. Zamboni, D. D'Amico, R. W. Williams, D. Finley, S. P. Gygi, and J. Auwerx. Multi-omics analysis identifies ATF4 as a key regulator of the mitochondrial stress response in mammals. *J Cell Biol*, 216(7):2027–2045, 07 2017.

[381] A. Nakai, M. Suzuki, and M. Tanabe. Arrest of spermatogenesis in mice expressing an active heat shock transcription factor 1. *EMBO J*, 19(7):1545–1554, Apr 2000.

[382] J. Pouysségur, C. Sardet, A. Franchi, G. L'Allemain, and S. Paris. A specific mutation abolishing Na+/H+ antiport activity in hamster fibroblasts precludes growth at neutral and acidic pH. *Proc Natl Acad Sci U S A*, 81(15):4833–4837, Aug 1984.

[383] Y. Zhang, A. Lanjuin, S. R. Chowdhury, M. Mistry, C. G. Silva-García, H. J. Weir, C. L. Lee, C. C. Escoubas, E. Tabakovic, and W. B. Mair. . *Elife*, 8, 08 2019.

[384] J. R. Daniele, D. J. Esping, G. Garcia, L. S. Parsons, E. A. Arriaga, and A. Dillin. "High-Throughput Characterization of Region-Specific Mitochondrial Function and Morphology". *Sci Rep*, 7(1):6749, 07 2017.

[385] S. Liu, M. J. Mlodzianoski, Z. Hu, Y. Ren, K. McElmurry, D. M. Suter, and F. Huang. sCMOS noise-correction algorithm for microscopy images. *Nat Methods*, 14(8):760–761, 07 2017.

[386] L. A. Royer, M. Weigert, U. Günther, N. Maghelli, F. Jug, I. F. Sbalzarini, and E. W. Myers. ClearVolume: open-source live 3D visualization for light-sheet microscopy. *Nat Methods*, 12(6):480–481, Jun 2015.

[387] F. E. Lennon, G. C. Cianci, R. Kanteti, J. J. Riehm, Q. Arif, V. A. Poroyko, E. Lupovitch, W. Vigneswaran, A. Husain, P. Chen, J. K. Liao, M. Sattler, H. L. Kindler, and R. Salgia. Unique fractal evaluation and therapeutic implications of mitochondrial morphology in malignant mesothelioma. *Sci Rep*, 6:24578, Apr 2016.

[388] A. Dobin, C. A. Davis, F. Schlesinger, J. Drenkow, C. Zaleski, S. Jha, P. Batut, M. Chaisson, and T. R. Gingeras. STAR: ultrafast universal RNA-seq aligner. *Bioinformatics*, 29(1):15–21, Jan 2013.

[389] Y. C. Lin, S. Jhunjhunwala, C. Benner, S. Heinz, E. Welinder, R. Mansson, M. Sigvardsson, J. Hagman, C. A. Espinoza, J. Dutkowski, T. Ideker, C. K. Glass, and C. Murre. A global network of transcription factors, involving E2A, EBF1 and Foxo1, that orchestrates B cell fate. *Nat Immunol*, 11(7):635–643, Jul 2010.

[390] M. B. Eisen, P. T. Spellman, P. O. Brown, and D. Botstein. Cluster analysis and display of genome-wide expression patterns. *Proc Natl Acad Sci U S A*, 95(25):14863–14868, Dec 1998.

[391] Y. Zhou, B. Zhou, L. Pache, M. Chang, A. H. Khodabakhshi, O. Tanaseichuk, C. Benner, and S. K. Chanda. Metascape provides a biologist-oriented resource for the analysis of systems-level datasets. *Nat Commun*, 10(1):1523, 04 2019.

[392] F. Meier, A. D. Brunner, S. Koch, H. Koch, M. Lubeck, M. Krause, N. Goedecke, J. Decker, T. Kosinski, M. A. Park, N. Bache, O. Hoerning, J. Cox, O. Räther, and M. Mann. Online Parallel Accumulation-Serial Fragmentation (PASEF) with a Novel Trapped Ion Mobility Mass Spectrometer. *Mol Cell Proteomics*, 17(12):2534–2545, 12 2018.

[393] M. Choi, C. Y. Chang, T. Clough, D. Broudy, T. Killeen, B. MacLean, and O. Vitek. MSstats: an R package for statistical analysis of quantitative mass spectrometry-based proteomic experiments. *Bioinformatics*, 30(17):2524–2526, Sep 2014.

[394] W. K. Russell, Z. Y. Park, and D. H. Russell. Proteolysis in mixed organic-aqueous solvent systems: applications for peptide mass mapping using mass spectrometry. *Anal Chem*, 73(11):2682–2685, Jun 2001.

[395] D. Giustarini, I. Dalle-Donne, A. Milzani, P. Fanti, and R. Rossi. Analysis of GSH and GSSG after derivatization with N-ethylmaleimide. *Nat Protoc*, 8(9):1660–1669, Sep 2013.

[396] S. M. Louie, E. A. Grossman, L. A. Crawford, L. Ding, R. Camarda, T. R. Huffman, D. K. Miyamoto, A. Goga, E. Weerapana, and D. K. Nomura. GSTP1 Is a Driver of Triple-Negative Breast Cancer Cell Metabolism and Pathogenicity. *Cell Chem Biol*, 23(5):567–578, 05 2016.

Publishing Agreement

It is the policy of the University to encourage open access and broad distribution of all theses, dissertations, and manuscripts. The Graduate Division will facilitate the distribution of UCSF theses, dissertations, and manuscripts to the UCSF Library for open access and distribution. UCSF will make such theses, dissertations, and manuscripts accessible to the public and will take reasonable steps to preserve these works in perpetuity.

I hereby grant the non-exclusive, perpetual right to The Regents of the University of California to reproduce, publicly display, distribute, preserve, and publish copies of my thesis, dissertation, or manuscript in any form or media, now existing or later derived, including access online for teaching, research, and public service purposes.

DocuSigned by:
Connor Stasluka
1A95F1DF258C426...
Author Signature

11/17/2022
Date